学位論文

Evolution of Kinematic Properties of Early-Type Galaxies Investigated by Surface Photometry

(表面測光で探る早期型銀河の運動学的性質の進化)

平成 29 年12月博士(理学)申請

東京大学大学院理学系研究科

天文学専攻

満田　和真

Evolution of Kinematic Properties of Early-Type Galaxies Investigated by Surface Photometry

a dissertation presented
by
Kazuma Mitsuda
to
The Department of Astronomy

in partial fulfillment of the requirements
for the degree of
Doctor of Philosophy
in the subject of
Astronomy

The University of Tokyo
Bunkyo-ku, Tokyo
March 2018

Thesis advisor: Professor Mamoru Doi Kazuma Mitsuda

Evolution of Kinematic Properties of Early-Type Galaxies Investigated by Surface Photometry

Abstract

Understanding formation and evolution of galaxies is one of the most important goals in modern astronomy. Early-type galaxies (ETGs), ellipticals and S0s, play an important role. Because of the prominence of random motion of stars, they are thought to carry information of spin-down mechanisms of galaxies which is a key to understand how galaxies obtain their morphology. Observations of local ETGs have revealed that they can be classified into two kinematical families. One is fast rotator which rotates fast and tends to be less massive, and the other is slow rotator which rotates slowly and tend to be massive. Observational studies at high redshifts have revealed dramatic size growth of massive ETGs. Cosmological simulations show that a two-phase formation scenario would explain these observational results. However, the dominant processes are not clear mainly because of complexity in the formation and evolutionary processes. Observations of kinematic properties of high-redshift ETGs would provide critical constraints. In spite of the importance, crucial difficulty of absorption line spectroscopy at high redshifts prevents us from studying kinematics. Surface photometry measurement is an important and less observationally expensive tool with which kinematical properties could be indirectly investigated. In this study, we find a photometric parameter which can be used as a good proxy for the kinematics of ETGs. Then, we measure the parameters for high-redshift and low-redshift ETGs, in order to investigate the evolution of kinematic properties of ETGs.

First, we investigate relation between photometric parameters and kinematic properties. We prepare a sample of 166 non-barred ETGs in the local Universe which have high-quality kinematic measurements in ATLAS^{3D} survey and have imaging data of Sloan Digital Sky Survey (SDSS). We find that the r-band radial light profiles of slow rotators are more extended in the outer region than fast rotators. We define a photometric parameter, $\Delta\mathrm{Slope}$, in order to evaluate the difference of the outer light profile. If $\Delta\mathrm{Slope}$ is negative, this indicates that the light profiles is more extended than pure Sérsic profile, and vice versa. We find that slow rotators have smaller $\Delta\mathrm{Slope}$ than fast rotators at a

fixed stellar mass. Almost all slow rotators have negative $\Delta\mathrm{Slope}$, while majority of fast rotators have $\Delta\mathrm{Slope} \gtrsim 0$. We find a significant correlation between $\Delta\mathrm{Slope}$ and spin parameters, λ and V/σ. The correlation is also found for round galaxies for which other parameters such as Sérsic index do not show significant correlation to the spin parameters. We obtain an approximate linear relation between $\Delta\mathrm{Slope}$ and the spin parameters.

Second, we analyze and compare the light profiles of ETGs in massive clusters at redshift $z \sim 1$ and 0. We construct a sample of $\sim$ 600 quiescent ETGs at each redshift selected by a rest-frame optical color-magnitude diagram and morphological parameters. We make use of Hubble Space Telescope (HST) imaging data as well as ground-based spectroscopic data obtained in the HST Cluster Supernovae Survey for the high-redshift sample. We use SDSS imaging and spectroscopic data for the low-redshift comparison sample. We measure $\Delta\mathrm{Slope}$ with appropriate correction for the effects of point spread function (PSF). We find that the high-redshift ETGs have significantly larger $\Delta\mathrm{Slope}$ than the low-redshift ones, indicating that the high-redshift ETGs are more truncated in the outer region. The difference of $\Delta\mathrm{Slope}$ between the two samples is considered to be intrinsic and unlikely to originate from artifacts such as the PSF correction, sample selection, and contamination of foreground and background galaxies.

Finally, we address the evolution mechanisms of ETGs. We first discuss formation and evolution processes of fast and slow rotators. The relation between $\Delta\mathrm{Slope}$ and the spin parameter provides us with new insights. The outer profile evolution, together with other observational evidence, favors minor mergers as a likely contributor for the size growth of cluster ETGs at $z < 1$. We derive the spin parameters of the high-redshift ETGs from $\Delta\mathrm{Slope}$, and compare them to cosmological simulations as well as observations. We find that the spin parameter is largely consistent with that of $z \sim 1$ ETGs directly measured by a previous study. Although we have found significant evolution of $\Delta\mathrm{Slope}$, massive ETGs already have $\Delta\mathrm{Slope} < 0$ (i.e., extended outer profiles) at $z \sim 1$, which indicates that the dominant spin-down processes for massive slow rotators is working efficiently at $z > 1$.

Contents

The work in this dissertation is based on research carried out at the Department of Astronomy, the University of Tokyo, Japan. No part of this thesis has been submitted elsewhere for any other degree or qualification.

Kazuma Mitsuda
December 2017

Acknowledgments

First of all, I am deeply grateful to my supervisor, Mamoru Doi. He introduced me the world of galaxy formation and evolution as well as the surface photometry. He has always given me positive comments and advice. He has patiently supported me to carry out various research topics. I have learned a number of things about science from his great knowledge in astronomy and astrophysics. I would like to express the deepest appreciation to Tomoki Morokuma. His comments and advices have been important for me to broaden the knowledge of astronomy and to improve my researches. I would like to thank Mitsuru Kokubo for a number of exciting discussion and helpful advice. His interests in wide range of astrophysics have stimulated me to come up with various new ideas. I also would like to thank Masaki Yamaguchi and Jian Jiang for helpful comments and advice. I would like to express my gratitude to Shigeyuki Sako for a number of advice for my working on astronomical instruments. I would like to offer my special thanks to Yasuhito Hashiba, Yuki Kikuchi, Yuki Taniguchi, Makoto Ichiki, and Noriaki Arima for sharing the experience of observations.

I would like to thanks Nao Suzuki for kindly providing the calibrated and co-added images and the spectroscopic catalog of the Hubble Space Telescope Cluster Supernova Survey.

I want to thank may classmates. I especially thank Akio Taniguchi, Yuta Kato, and Yutaka Hirai for sharing precious memories in the campus life. I would like to express deep appreciation to all the staff members and students in the Institute of Astronomy for supporting the daily works in my Ph.D. course. I especially thank Yuki Yamaguchi for spending time as a roommate.

I would like to show my greatest appreciation to members of the Kyoto 3DII CCD upgrading project: Yosuke Minowa, Yutaka Hayano, Takashi Hattori, Hajime Sugai, Atsushi Shimono, Kazuya Matsubayashi, Yukiko Kamata, and Shinobu Ozaki. I was able to gain many valuable experiences of various experiments and observations.

I really appreciate the referees of this dissertation: Kazuhiro Shimasaku, Naoteru Goda, Eiichiro Kokubo, Kentaro Nagamine, and Kouji Ohta. Advice and comments given by them have been a great help in improving this work.

Finally, my deepest appreciation goes to my family who have supported me all the times.

1

Introduction

We begin the first chapter with a general introduction of scientific background of studying evolution of galaxies, focusing on early-type galaxies (ETGs). Then, we give a review of previous studies on the evolution of ETGs focusing on their kinematic properties based on recent observations as well as theoretical studies, describing unsolved issues that we would like to address in this study. In the end of this chapter, we provide outlines of the present paper.

1.1 Galaxies in the Universe

Galaxies are the one of the most important astronomical objects in the Universe. They are gravitationally bound systems consisting of various baryonic matters such as stars, gas, and dust as well as dark matter. Galaxies are the most common objects outside the Milky Way. They have been discovered at the distance from ~ 20 kpc for the nearest and out to redshifts $z \sim 11$ (Oesch et al., 2016) which correspond to the look-back time of ~ 13 Gyr. Although the universe is dominated by dark energy and dark matter in terms of energy or mass budget, various baryonic processes take place in galaxies. It is within a galaxy that stars form from gas, and various heavy elements are synthesized and re-distributed in the interstellar and intergalacic medium. Therefore, understanding how galaxies have formed and

evolved is of great importance as it is directly related to understanding how our world has formed.

Galaxies are complex systems and have great diversity because of their nature containing multiple components. Parameters characterizing galaxy properties have extremely wide distribution. For example, luminosity of a galaxy spans ~ 9 order of magnitude from 10^3 (Wiliam I) to 10^{12} $L_\odot$ where $L_\odot$ is the luminosity of the Sun.

Moreover, galaxies have diverse morphology which reflects wide variety of stellar distribution in a galaxy. The Hubble's classification scheme (Sandage, 1961) classifies galaxies into four broad classes with visible features. One is elliptical galaxies (Es). They have featureless smooth light distribution with almost elliptical isophotes. The second one is spiral galaxies. They have thin disks with star-forming spiral arms. They often have a central bulge. Another one is lenticular os S0 galaxies. This class is intermediate between Es and spirals. They have smooth profile with no star-forming spiral arms, like Es. They consist of a disk and a bulge, like spirals, but the bulge is more prominent than in spirals. The other is irregular galaxies. They have patchy structure and do not have smooth bulge or axisymmetric disk. In many studies, Es and S0s are classified as early-type galaxies (ETGs) while spiral and irregular galaxies as late-type galaxies (LTGs). In this study, we basically use this simple classification.

Galaxy morphology is related to properties such as gas fraction, angular momentum, and structure, and thought to be originated from evolution history of galaxies. Therefore, one goal of studying galaxy formation and evolution is to understand how such properties have evolved as a function of time and space as well as to understand what kind of physical processes are responsible for the evolution.

1.1.1 Early-type galaxie (ETGs)

In the context of galaxy formation and evolution, ETGs play an important role. Morphologically, ETGs are dominated by a spheroidal component, or bulge, unlike LTGs which are dominated by a disk component. This difference arises from different kinematics. While the stellar component of LTGs are dominated by rotation, that of ETGs is supported by a mixture of random motion (i.e., velocity dispersion) and rotation. Some ETGs have very little or almost no rotation. The kinematic properties of ETGs will be presented in the next section.

Also, ETGs tend to be massive $\log(M_*/M_\odot) \gtrsim 10$, where M_* indicate total mass of stars within a galaxy. The massive end of the stellar mass function ($\log(M_*/M_\odot) \gtrsim 11$) of galaxies are dominated

by ETGs in the local universe. The stars in ETGs are usually red and old. Their formation epoch is thought to be earlier than redshift $z > 2$ (Thomas et al., 2005), and thought to have passively evolved after they quench the star-forming activity, which indicates that ETGs carry information of the early universe as a fossil record.

ETGs are almost absent from gas and dust, which means the optical light distribution well traces the distribution of stars, and therefore, interpretation of observational results is more simple. Moreover, it is known that ETGs are more frequently found in high-density environments such as cores of galaxy clusters (Dressler, 1980). Therefore, formation and evolution of ETGs are thought to be affected from environments (environmental effects), which implies that their formation and evolution is tightly linked to the growth of the large scale structure. Thus, understanding formation and evolution of ETGs is necessary to understand the formation and evolution of all galaxy populations.

The observational properties of ETGs described above are thought to be the consequence of hierarchical formation of dark matter halos and galaxies in the ΛCDM framework. The most important aspect shaping their morphology, the prominence of velocity dispersion in kinematics, is thought to be the result of spin-down during assembly of ETGs.

The exact mechanisms of the spin-down, however, are far from being understood. This is partly because simulations of galaxy formation and evolution are complex as they deal not only with dark matter which is only influenced by gravitational interaction but also with various baryonic processes such as gas inflows and outflows, gas heating and cooling, star formation and supernova explosions, feedback from active galactic nuclei, and so on. Thus, observational constraints are essential for understanding formation and evolution of ETGs. In the following sections, we introduce recent important observational progress.

1.2 Kinematical Properties of Local ETGs

In this section, we present kinematical properties of ETGs mostly from recent integral-field spectroscopic surveys. After we mention an important scaling relation that is related to dynamics of ETGs, we introduce two kinematics families of ETGs.

1.2.1 Mass-Size Plane from the Fundamental Plane

Dynamics or kinematics* of ETGs provides crucial knowledge about their formation and evolution histories. There is a well-known parameter correlation between the luminosity, velocity dispersion, and size, i.e., the Fundamental Plane (Djorgovski & Davis, 1987), which combines the correlation between the total luminosity and velocity dispersion (Faber & Jackson, 1976), and that between the size and surface brightness (Kormendy, 1977, Kodaira et al., 1983).

The existence of the Fundamental Plane implies that ETGs are in virial equilibrium (e.g., Djorgovski & Davis, 1987, Prugniel & Simien, 1996, Forbes et al., 1998). In the meantime, the ***tilt*** of the Fundamental Plane also implies that there should be systematic variation of the mass-to-light ratio (M/L) as a function of velocity dispersion or mass (e.g., Djorgovski & Davis, 1987) or non-homology in the surface brightness profiles (e.g., Graham & Colless, 1997, Trujillo et al., 2004). Cappellari et al. (2013b) have obtained robust stellar mass estimator from two-dimensional stellar kinematics (see below) supported by dynamical modeling, confirmed the systematic M/L variation as a function of velocity dispersion, and shown that the Fundamental Plane can be interpreted as virial equilibrium. This indicates that the Fundamental Plane can be reduced into much simpler form, the mass-size plane (see Cappellari, 2015, for a review).

1.2.2 Two Kinematical Families of ETGs

Recent integral field spectroscopy (IFS)† have established a view in which ETGs can be classified in to two kinematical families Emsellem et al. (2007, 2011). One is so-called fast rotators which rotate fast and the system is supported by rotation, while the other is slow rotators which have very little

*The words, ***dynamics*** and ***kinematics***, have similar meaning. In this paper, we basically use ***kinematics*** when the topic is related to velocity and velocity dispersion fields but when we do not go deep into the origin of them, i.e., internal structure and gravitational potential, otherwise we use ***dynamics*** instead. We note that, however, we may sometimes use these words without distinction.

†Sometimes called integral field unit (IFU) spectroscopy

or no significant rotation and are supported by velocity dispersion (i.e., random motion of the stars in a galaxy). This dichotomy (e.g., Kormendy et al., 2009, Kormendy & Bender, 2012) actually has been known for $\gtrsim$ 30 years (Davies et al., 1983, Kormendy & Bender, 1996), i.e., much before the advent of IFS, but there have been significant updates thanks to large IFS surveys of nearby ETGs. We summarize the most updated views from IFS results (Cappellari, 2016, for a review).

1.2.2.1 Slow and fast rotator classifications based on velocity fields

IFS observations of galaxies provide line-of-sight velocity and velocity dispersion fields (i.e., two-dimensional or spatially-resolved kinematics). For ETGs, stellar kinematics are obtained from the stellar absorption features in the spectrum at each spatial position of a galaxy, spatial pixel or spatial bin, which are often called spaxel (Emsellem et al., 2004). Two-dimensional stellar kinematics of 48 local ETGs obtained in the SAURON project (Bacon et al., 2001, de Zeeuw et al., 2002), which is a pioneering IFS survey for ETGs, have shown that ETGs are broadly classified into two classes depending on large-scale rotation signature (Emsellem et al., 2007, Cappellari et al., 2007) although various types of velocity structure such as kinematically decoupled or counter-rotating cores, central disks, and twists of the rotation axis also exist in smaller scales (Emsellem et al., 2004, Krajnović et al., 2008) . In Figure 1.1, example of fast and slow rotators are shown. For the fast rotator (NGC4660), the two-dimensional line-of-sight velocity distribution shows clear sign of rotation with the left-hand side blue shifted and the other side red shifted. The two-dimensional line-of-sight velocity distribution of the slow rotator (NGC4486), on the other hand, does not have sign of rotation.

Emsellem et al. (2007) have introduced a spin parameter λ which can be used as a proxy for angular momentum of galaxies. The λ parameter is defined as

$$\lambda = \frac{< R|V| >}{< R\sqrt{V^2 + \sigma^2} >}, \tag{1.1}$$

where V and σ is the line-of-sight velocity and velocity dispersion at a position of a galaxy with a galactocentric radius of R while the brackets $<>$ corresponds to a luminosity-weighted average within a certain area such as within one effective radius. This dimensionless parameter represents the average angular momentum normalized by kinetic energy or mass. For the case of IFS data cube,

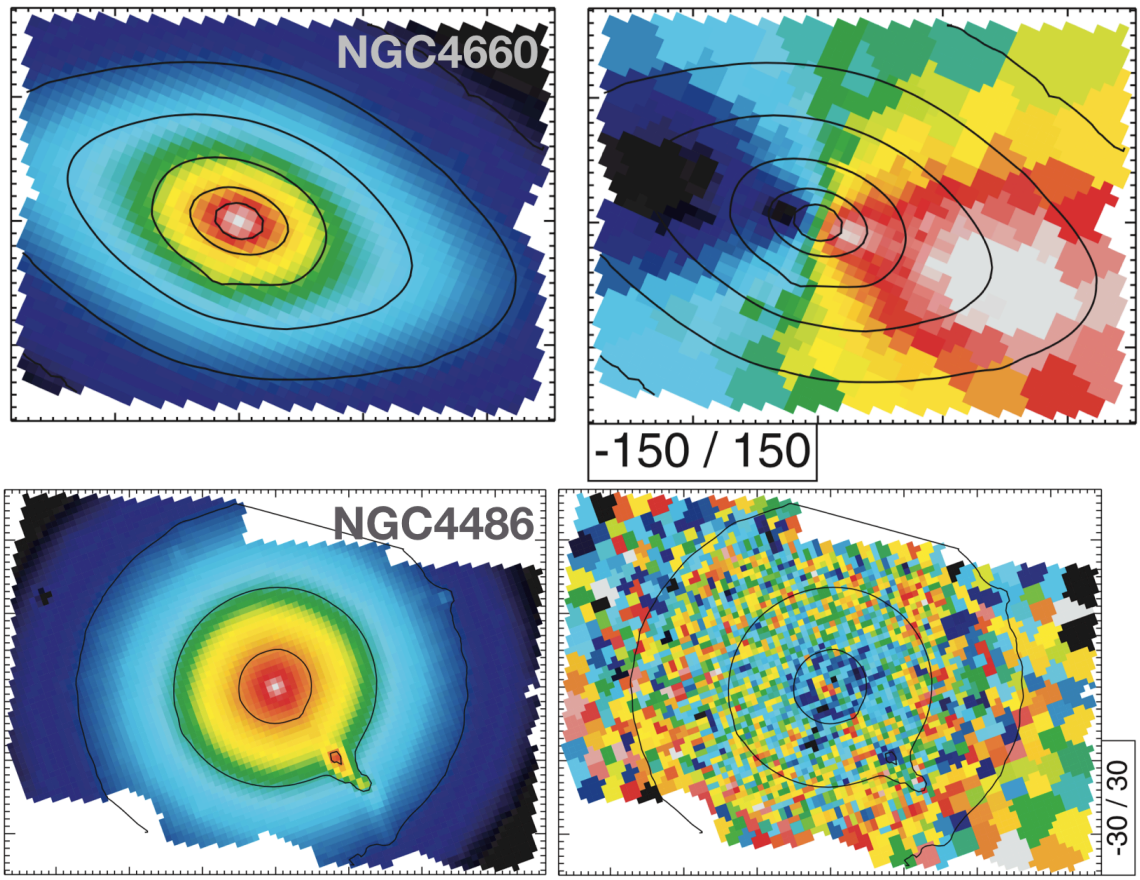

Figure 1.1 Example of fast (NGC4660; top) and slow (NGC4486; bottom) rotators, adopted from Figure 7 in Kuntschner et al. (2010). For each object, the two-dimensional distribution of intensity (left) and line-of-sight velocity (right) are presented by color code. The range for the line-of-sight velocity (white-red to blue-black) in km s^{-1} is shown in the box. The field of view is $\sim 44 \times 33$ arcsec and $\sim 74 \times 53$ arcsec for NGC4660 and NGC4486, respectively.

where V and σ are available at each spaxel, Equation 1.1 is written as

$$\lambda = \frac{\Sigma_{i=1}^{N} F_i R_i |V_i|}{\Sigma_{i=1}^{N} F_i R_i \sqrt{V_i^2 + \sigma_i^2}}, \tag{1.2}$$

where F_i, R_i, V_i, σ_i are flux, galactocentric distance, line-of-sight velocity, and velocity dispersion at a i-th spaxel, whereas the summation $\Sigma_{i=1}^{N}$ is taken within a certain region of a galaxy, e.g., one effective radius.

Based on spatially resolved stellar kinematics data of a complete sample of 260 ETGs obtained in a large IFU survey, the ATLAS^{3D} (Cappellari et al., 2011a), Emsellem et al. (2011) have introduced a λ_e-ϵ_e diagram (Figure 1.2) with which slow and fast rotators are classified. Here ϵ is ellipticity ($\epsilon = 1-b/a$ where a and b are semi-major and minor axes, respectively), while the suffix e indicates that the parameters are averaged within one effective radius r_e. On this diagram, galaxies that are elongated by rotation (i.e., rotationally supported systems) and by anisotropy of velocity dispersion (i.e., dispersion supported systems) occupy different regions (Emsellem et al., 2011). Emsellem et al. (2011) have proposed a classification threshold $\lambda_e = 0.31 \times \sqrt{\epsilon}$ while different thresholds are also proposed (e.g., Emsellem et al., 2007, Cappellari, 2016). We note that the λ_e-ϵ_e diagram is an improved version of traditional V/σ-ϵ diagram (Illingworth, 1977, Binney, 1978, Davies et al., 1983, Binney, 2005). There is a tight monotonic relation between λ_e and V/σ (Figure B1 in Emsellem et al., 2011), and with a first-order approximation the relation may be regarded as $\lambda_e \sim V/\sigma$, especially for $\lambda_e \lesssim 0.7$.

1.2.2.2 Properties of slow and fast rotators

One of the most important aspects of kinematics of ETGs is mass dependence. While fast rotators are the majority ($\gtrsim 80$ percent) of ETGs, the massive end is dominated by slow rotators (Emsellem et al., 2011)*. In the local Universe, the critical stellar mass above which slow rotators become dominant is $\log(M_*/M_\odot) = 11.3 - 11.5$ (Emsellem et al., 2011, Cappellari et al., 2013a).

Tridimensional structures are different between slow and fast rotators. Slow rotators are weakly triaxial while fast rotators can be regarded as axisymmetric oblate spheroids (Cappellari et al., 2007, Krajnović et al., 2011, Emsellem et al., 2011, Cappellari, 2016). This is the reason why these populations can be classified with the λ_e-ϵ_e diagram. We note that, however, the two populations, fast

*We note that the the variation of kinematic properties of ETGs as a function of the stellar mass has negligible contribution to the ***tilt*** of the Fundamental Plane (Ciotti et al., 1996, Lanzoni & Ciotti, 2003)

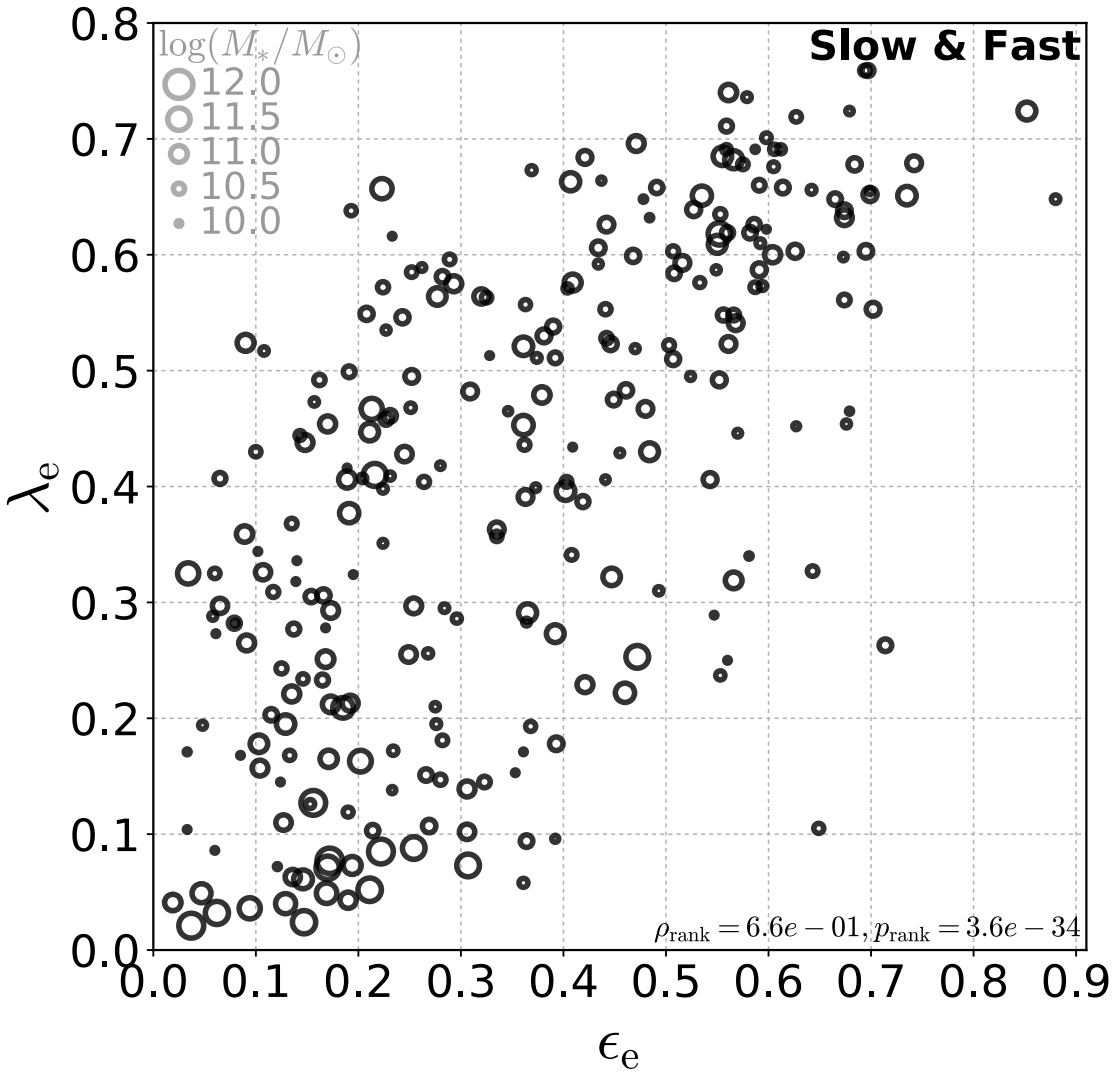

Figure 1.2 λ_e-ϵ_e diagram of 260 ETGs from ATLAS^{3D} (Cappellari et al., 2011a). The figure is created with publicly available data provided in the website of the ATLAS^{3D} ProjectThe size of symbols indicates the stellar mass noted in the upper left. We carry out Spearman's rank correlation test, and present the rank correlation efficiency ($\rho_{\rm rank}$) and p-value ($p_{\rm rank}$) in the lower right, which will be mentioned in Section 1.4.1.

to slow rotators, do not show well-separated dichotomy but continuous distributions on the λ_e-ϵ_e diagram. The transition is gradual from highly flattened fast rotators to the intermediate population, and then to round, slow rotators (see , e.g., Figure 14 in van de Sande et al., 2017).

Environmental dependence of the kinematics is also pointed out at first (Cappellari et al., 2011b, Houghton et al., 2013, D'Eugenio et al., 2013, Scott et al., 2014) but with rather small sample sizes. Cappellari et al. (2011b) proposed the kinematic morphology-density relation that massive slow rotators appear more frequently in high density regions, e.g., in the core of Virgo cluster. New large IFS surveys which are still on-going have been revealing that the apparent dependence of the fraction of slow rotators on environment may be a result of two correlations between masses and kinematics, and between masses and environments, although Scott et al. (2014) have pointed out that slow rotator fraction is higher compared at a fixed stellar mass. Brough et al. (2017) show that once the correlation between mass and kinematics is taken into account, no significant correlation could be found between kinematics and environments, using kinematic data of 293 ETGs residing in nearby galaxy clusters obtained in an on-going IFS survey, the Sydney-AAO Multi-object Integral field spectrograph (SAMI) Galaxy Survey (Bryant et al., 2015). The similar conclusion is also drawn by another large IFS survey (Greene et al., 2017b,a).

1.2.2.3 Relation to the Stellar Population Properties

The stellar population is also important to discuss the formation and evolution of ETGs. Local ETGs are known to populate a tight red sequence in the color-magnitude or color-stellar mass diagram (Baum, 1959, Faber, 1973, Visvanathan & Sandage, 1977, Baldry et al., 2004, 2006), which indicates they have very old and metal-rich stellar populations (e.g., Bower et al., 1992, Kodama & Arimoto, 1997). Studies based on stellar absorption line spectroscopy have revealed that more massive ETGs are older, more metal-rich, and have more α-element enhancement which is a sign of shorter star formation time-scales (Worthey et al., 1992, Thomas et al., 2005, 2010).

Considered on the mass-size plane, the stellar population parameters such as the stellar age, metallicity, and star formation timescales (McDermid et al., 2015) as well as molecular gas fraction (Young et al., 2011, Cappellari et al., 2013a) vary with increasing central velocity dispersion. With increasing velocity dispersion, i.e., as the system becomes more compact and denser, the stellar populations become older, more metal-rich and more α-element enhanced with shorter formation time-scales, and

galaxies have less molecular gas fraction (Cappellari et al., 2013a, McDermid et al., 2015). Conversely, at a fixed central velocity dispersion, the stellar population parameters do not strongly depend on the stellar mass (see Figures 6 and 7 in McDermid et al., 2015).

The variation of the spin parameter λ on the the mass-size plane, however, is different from that of the stellar population parameters. The spin parameter λ does not change with increasing central velocity dispersion, considered at a fixed stellar mass (see Figure 8 in Cappellari et al., 2013a). The tridimensional structures behave similarly on the mass-size plane (see Figure 7 in Cappellari et al., 2013a).

1.2.3 Formation Scenarios of Slow and Fast Rotators

To explain the different correlation of the dynamical and kinematical properties and stellar population parameters to the velocity dispersion, the two-phase formation scenario (Oser et al., 2010) is favored (see discussion in Cappellari et al., 2013a). In this scenario, a massive compact bulge is formed by dissipative processes such as rapid gas inflow or wet mergers at high redshift ($z > 2$) when the universe is much more gas rich (Dekel & Burkert, 2014), which is the first phase. The formed bulge rotates rapidly (Wuyts et al., 2010), probably as a consequence of non-zero angular momentum of the accreting gas. Also, this process forms old, metal-rich stellar populations with large α-element enhancements, and therefore can be an origin of the compact (i.e., with a large central velocity dispersion) fast rotators located in the bottom region in the mass-size plane (Cappellari et al., 2013a).

In the lower redshifts ($z < 2$), dissipationless processes such as dry minor or major mergers increase the galaxy size to evolve the compact bulge into local massive ETGs, which is the second phase. Dry mergers can reduce angular momentum of the fast-rotating bulge formed in the first phase, and alter it into slow rotators (Khochfar & Burkert, 2005, Naab et al., 2006) without changing the stellar population. As a result, the dependence of the kinematical properties and stellar population parameters on the stellar mass and velocity dispersion (see above). The two-phase formation scenario is also attractive for explaining the rapid size growth of ETGs which we will describe in the next section. However, physical mechanisms actually working on the kinematical evolution of ETGs are far from being clearly understood mainly because of the complexity of baryonic physics such as gas inflows and outflows, and feedback from supernovae and AGNs. We describe theoretical efforts which aim to reveal the mechanisms of the kinematical evolution, i.e., spin down, of ETGs in what follows.

1.2.3.1 Merger Simulations

For almost 40 years, many authors have tried to explain the origin of the slow and rotators by mergers. White (1979) suggested that it would be difficult to form slowly rotating ETGs by major mergers between spheroids. Mergers of cold disks were successful in reproducing progenitors which have properties consistent with slow rotators (e.g., Gerhard, 1981). Bekki & Shioya (1997) also showed that the time-scale of star-forming activity in gas-rich mergers are related to dynamical properties of ETGs. They showed that mergers with extended star formation tend to produce remnants more consistent with fast rotators while those with rapid star formation tend to produce those consistent with both fast and slow rotators.

The role of unequal mass mergers are also investigated (e.g., Bekki, 1998, Naab et al., 1999). Binary merger simulations have shown that nearly equal mass mergers between disk galaxies produce slow rotators whereas minor mergers result in fast rotators (Naab et al., 1999, Naab & Burkert, 2003, Jesseit et al., 2009, Bois et al., 2011). However, the simulated remnants are not consistent with observed ETGs in that the remnants of the merger simulations tend to be more flattened and do not have a kinematically distinct core (Jesseit et al., 2009, Bois et al., 2011).

Khochfar & Burkert (2005) and Naab et al. (2006) also show that gas-poor (dry) mergers can also produce slow rotators regardless of the progenitor mass ratios. The similar results are also shown by Taranu et al. (2013) but with more emphasis on multiple gas-poor minor mergers to form massive slow rotators. In contrast, Cox et al. (2006) have presented that gas-poor merger remnants become inconsistent with observed slow rotators. In summary, the consensus of the origin of slow and fast rotators has not yet been reached from merger simulations. This illustrates the difficulty for revealing mechanisms of the spin down of ETGs predicted in the two-phase formation scenario from theoretical studies alone.

1.2.3.2 Cosmological Simulations

Thanks to recent remarkable improvement of cosmological simulations of galaxy formation and evolution, some theoretical studies have been carried out in order to address the evolution of kinematics of ETGs in a cosmological context. Khochfar et al. (2011) have investigated the evolution of the ratio of fast to slow rotators using a semi-analytic galaxy formation model, and present that the ratio evolves at $z < 2$. They have shown that, as predicted in the two-phase formation scenario, fast rotators form

at high redshifts, and then they experience spin down due to dry mergers. Therefore, the fast-to-slow rotator ratio decreases with decreasing redshifts. However, Naab et al. (2014) have shown that there would be many path to form fast rotators as well as slow rotators. They have carried out cosmological hydrodynamical zoom-in simulations, and analyzed kinematic properties of 44 central galaxies.

A large step has been made by Penoyre et al. (2017) who investigate evolution history of thousands of ETGs in the Illustris simulation (Genel et al., 2014). They show that the observed kinematic properties of local ETGs could be reproduced in the simulation and that local slow rotators have originally been rotating rapidly and experienced spin down during evolution. They find that the main contributor of the spin down of ETGs is major mergers regardless of gas fraction, whereas minor mergers only have small effects with possibility of spin up or down depending on the gas fraction. Moreover, they examine the average amount of change of the spin parameter λ for each process and for different conditions which may be compared with observations. They also suggest that the environmental effect does not have a large impact on kinematics of ETGs.

In contrast, another simulation suggest the possible environmental effect on the kinematical evolution. Choi & Yi (2017) carry out cosmological hydrodynamical zoom-in simulations focusing on galaxy clusters. They present that while major and minor mergers cause spin down of ETGs, they are not the primary contributor at least in cluster environments. The implication is almost opposite to that in Penoyre et al. (2017).

Moreover, internal processes may also have influence on the kinematics of ETGs. Martizzi et al. (2014) have carried out cosmological hydrodynamical zoom-in simulations in order to investigate the effect of AGN feedback on masses, sizes, star formation rates and kinematics of brightest cluster galaxies (BCGs). They have presented that the observed properties of BCGs (Jimmy et al., 2013) could be reproduced when the AGN feedback is on while the simulated galaxies rotates too rapidly otherwise, which implies not only late gas-poor processes but also the processes such as gas inflow and outflows, cooling and heating may be related to the kinematics of ETGs.

Thus, although kinematical aspects of ETGs become able to be investigated by cosmological simulations, we have not reach a consensus about the dominant mechanisms of the possible spin down history. But significant improvement is that such cosmological simulations provide us observational parameters such as λ at each redshift and the amount of change of the parameters in each process (Penoyre et al., 2017). Therefore, comparing such parameters between simulations and observations would provide critical constraints on the kinematical evolution of ETGs. And it becomes inevitably

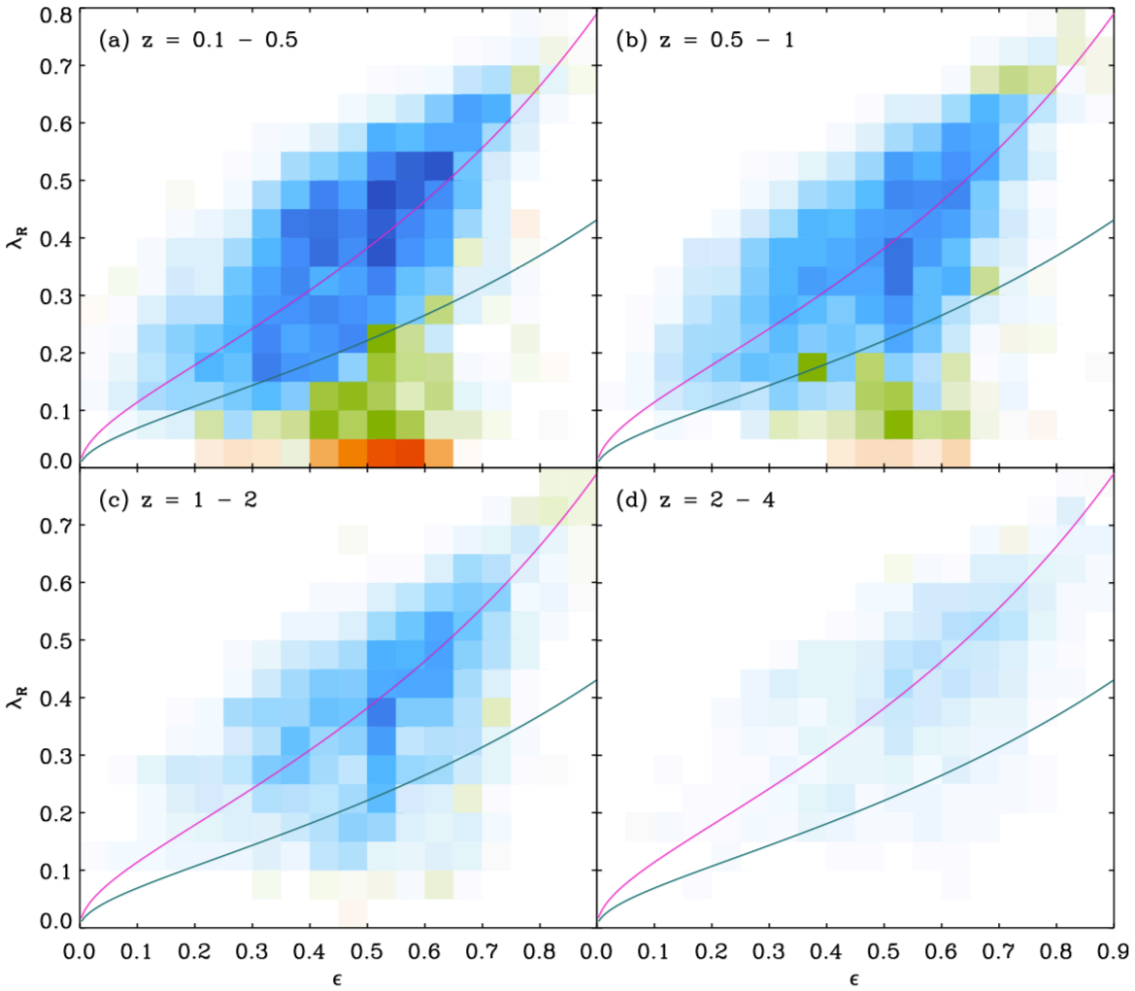

Figure 1.3 λ-ϵ diagram of simulated ETGs in Illustris from redshift $z = 4$ to 0, taken from Figure 6 in Penoyre et al. (2017). The λ and ϵ values are measured in edge-on projection. Color corresponds to the average stellar mass in the λ and ϵ bins Penoyre et al. (see Figure 4 in 2017). The distribution of the simulation at z=0 is in good agreement with that of the local ETGs in ATLAS^{3D} (see Figure 1.2).

important to obtain observational results on kinematics of distant ETGs, which is the main purpose of this study.

1.3 Observational Results of Distant ETGs

In this section, we present observational results of distant ETGs mostly about the strong size evolution in $z < 2$ which is closely related to the kinematical properties.

1.3.1 Rapid Size Evolution of ETGs in $z \lesssim 2$

Recent observations have revealed that massive ETGs ($\log(M_*/M_\odot) > 11$) have grown in the size by a factor of ~ 5 since $z \sim 2$ (Trujillo et al., 2007, van Dokkum et al., 2008). Compared at a stellar mass of $\log(M_*/M_\odot) \sim 11$, ETGs at $z \sim 2$ have an effective radius of $r_{\rm e} \sim 1$ kpc while the local ETGs have $r_{\rm e} \sim 5$ kpc (van Dokkum et al., 2008)*. The similar trend is also observed when high- and low-redshift ETGs are compared at a constant number density, which reveals that the stellar mass of massive ETGs have grown only by a factor of ~ 2 (van Dokkum et al., 2010). In the mean time, the $z \sim 2$ progenitors of local massive ETGs have the stellar mass density comparable to the core of the local counter parts (Bezanson et al., 2009, van Dokkum et al., 2010), which indicates that the local massive ETGs have developed their outer envelop at $z < 2$ (Hopkins et al., 2009).

The possible observational biasses such as flux loss in the outer region of a galaxy due to low signal to noise ratio (e.g., Mancini et al., 2010) as well as effect of color gradients in a galaxy (Daddi et al., 2005) are also taken into account in order to reveal that the observed size growth is real. Now a number of studies have established a consensus that the size growth is real and not due to observational biasses and artifacts such as the signal-to-noise ratios (e.g., van Dokkum et al., 2010), color gradients in galaxies (e.g., van der Wel et al., 2014), choice of the scale length, i.e., effective radius (e.g., van der Wel et al., 2014) or half-light radius (e.g., Andreon et al., 2016), method of profile fitting (Morishita et al., 2014), and the use of space-based (van der Wel et al., 2014) or grand-based telescopes (van Dokkum et al., 2010).

1.3.1.1 Possible Mechanisms of the Size Growth of ETGs

One caution is that the observed size evolution is the evolution of average sizes of ETGs. Therefore, the evolution can be explained by the size growth of individual galaxies (e.g., Bezanson et al., 2009) as well as different population mix in a ETG sample (e.g., Saglia et al., 2010). If the size evolution

*The smaller size of galaxies compared at a fixed mass means that the system is denser but not less massive.

is due to the growth of individual galaxies, the size growth can be explained by several mechanisms such as gas-poor major mergers, minor mergers, and adiabatic expansion. In gas-poor major mergers, a simple virial assumption shows that galaxies can grow in size roughly following the relation $r_{\rm e} \propto M_*$ (Bezanson et al., 2009). In contrast, gas-poor minor mergers can increase the galaxy size more efficiently with $r_{\rm e} \propto M_*^2$ (Bezanson et al., 2009). Another possible mechanism is the adiabatic expansion (Fan et al., 2008, 2010). At high-redshift, the gas fraction of galaxies at the central region is high. In such a situation, by blowing out a large amount of gas from the center by AGN feedback, stars and dark matter could be flown out as the central potential becomes less deep.

The fact that the effective radius grows much faster than the stellar mass favors gas-poor continuous minor mergers as a main channel of the evolution (Bezanson et al., 2009, Naab et al., 2009). Through high-resolution hydrodynamical simulations, Hopkins et al. (2010) have shown that the size growth alone could be explained by several mechanisms such as gas-poor major and minor mergers, adiabatic expansion (Fan et al., 2008, 2010), stellar age gradients in a galaxy, bias of the stellar mass estimates, and observational effects. Hopkins et al. (2010) have concluded that gas-poor minor mergers can reproduce velocity dispersions and central stellar mass densities and profile shape together with the size evolution.

On the other hand, a number of studies have pointed out the significant effect of different population mix (e.g., Saglia et al., 2010, Cimatti et al., 2012, Carollo et al., 2013), which is often called the ***progenitor bias*** (Franx & van Dokkum, 1996, van Dokkum et al., 2000). It has been shown that quenching of star-forming galaxies has been taking place from $z \sim 3$ to 0 (Ilbert et al., 2013, Muzzin et al., 2013, Tomczak et al., 2014), which indicates that quiescent galaxies are newly formed at the same time. As a result, low-redshift samples of quiescent galaxies or ETGs* contain larger fraction of newly quenched galaxies. The difference of morphology between star-forming galaxies which tend to be disks and quiescent galaxies which tend to be spheroidal (Wuyts et al., 2011) could be the origin of the apparent size evolution. As the size of disk galaxies is larger than spheroidal (e.g., Bernardi et al., 2014, van der Wel et al., 2014) due to the difference of the stellar density. Therefore, newly quenched galaxy from star-forming disks could have larger sizes than old, spheroidal galaxies if they do not experience morphological transformation (i.e., from disks to spheroids) during the quenching.

*The exact definition is different for quiescent and early-type galaxies. But as a result of correlation between morphology and colors, samples of quiescent and early-type galaxies are often become similar (but see discussion in Andreon et al., 2016, who discuss the impact of the ETG selection on the size evolution arguments).

The significant contribution of the progenitor bias for the size evolution is pointed out by van der Wel et al. (2009) who have shown that in the local Universe, more compact galaxies have older stellar populations compared at a fixed mass. Fagioli et al. (2016) have investigated relation between galaxy sizes and stellar population age by stacking a sample of spectroscopic quiescent galaxies at $0.2 < z < 0.8$ from the 20k zCOSMOS-bright spectroscopic survey (Lilly et al., 2007, 2009). They have shown that at lower stellar masses $10.5 < \log(M_*/M_\odot < 11)$, the stellar age is younger in large galaxies than small galaxies, which indicates that the progenitor bias can contribute the growth of average size of quiescent galaxies or ETGs.

By observationally estimating the minor merger rate in the redshift range of $0.4 < z < 2$ utilizing deep imaging data, Newman et al. (2012) have shown that while minor mergers may explain most of the size evolution at $z \lesssim 1$ assuming a short merger timescale, rapid size growth observed at higher redshifts may not be explained by minor mergers alone. The similar conclusion is drawn by Belli et al. (2015) who show that about one half of the increase of the average size of quiescent galaxies in $1.25 < z < 2$ may be explained by newly quenched galaxies. Carollo et al. (2013) investigate the change of the number density of small (i.e., compact) and large (i.e., diffuse) quiescent ETGs at $0.2 < z < 1$. For lower mass galaxies with $10.5 < \log(M_*/M_\odot) < 11$, while the number density of the compact ETGs is constant, that of large ETGs substantially increases in the redshift range, which indicates that the size growth there could be explained by the emerging large ETGs. Although Carollo et al. (2013) have not found such a phenomenon for massive galaxies, Gargiulo et al. (2017) have reached a similar conclusions for more massive ETGs than $\log(M_*/M_\odot) = 11$. These are another studies, however, that show conflicting results with those presented above. van der Wel et al. (2014) demonstrates that the number density of compact quiescent galaxies strongly decreases from $z \sim 1.5$.

1.3.1.2 Environmental Effect on the Size Growth of ETGs

Environmental effects may also be related to the size evolution of ETGs. At low redshifts, e.g., $z < 0.4$, the significant environmental effects on the average size of ETGs is not observed although the size of spiral galaxies tend to be smaller in the cluster environment (Weinmann et al., 2009, Maltby et al., 2010). Huertas-Company et al. (2013b) have shown that the size-mass relation of ETGs seems to be universal in the local Universe, regardless of environments such as field, groups, and clusters. Also no significant difference has been detected for the size at a fixed stellar mass between central and

satellite ETGs (Huertas-Company et al., 2013b). Thus, looking at the local Universe, it seems that the environment may not play a role for the size evolution of ETGs, although Poggianti et al. (2013) have presented that the average size of cluster ETGs is smaller than field counterpart due to the larger fraction of compact ETGs in clusters.

At high redshifts, the situation seems to be different. Cooper et al. (2012) have reported that ETGs at $0.4 < z < 1.2$ have larger effective radii in higher density regions, while Huertas-Company et al. (2013a) have shown that there is no significant environmental dependance of the size of ETGs as long as they compare groups ($\log(M_{\rm halo}/M_{\odot}) \lesssim 14$) and fields. At $z \sim 1$, Jørgensen & Chiboucas (2013) and Jørgensen et al. (2014) have investigated the Fundamental Plane of ETGs in four massive clusters between $0.5 < z < 1.3$, and shown that the amount of the size evolution tend to be smaller than field ETGs, i.e., larger sizes in clusters. Using a large sample of $\sim$ 400 ETGs drawn from 9 clusters at $0.8 < z < 1.5$, Delaye et al. (2014) have presented the larger average size for the cluster ETGs than the field counter part. They also have pointed out that the larger average size is due to skewed distribution tailing toward large sizes in the cluster sample. Using half-light radii instead of effective radii, Andreon et al. (2016) have shown that the size evolution of ETGs in the cluster environment is three-times gradual than in fields, which is in qualitative agreement with the findings in Delaye et al. (2014). Delaye et al. (2014) propose three possible mechanisms that may explain the larger sizes of the cluster ETGs at $z \sim 1$ but not at $z \sim 0$. The first one is the earlier quenching in cluster environment with which newly quenched galaxies make the average size bigger, i.e., the progenitor bias. The second is the different morphological mixing between clusters and fields, which is similar to the progenitor bias in that it explains the difference of the average size by the different fraction of galaxy population. In this case, we consider the fraction of S0s and Es. S0 galaxies with larger apparent ellipticity tend to be measure as more compact when the size is measured by the circularized radius (Huertas-Company et al., 2013a, Bernardi et al., 2014). Therefore, if a sample contains larger fraction of S0 galaxies, the average size of the sample would appear to be smaller. The third mechanism is enhanced major merger rates at higher redshifts in clusters. In massive clusters, major mergers are thought to be rare because the velocity dispersion of galaxies moving in a cluster is too large for them to slowly merge with each other (Binney & Tremaine, 2008). However, major merger rates may be higher in higher redshifts where the progenitors of massive clusters are less massive and have smaller velocity dispersion*.

*The velocity dispersion of galaxy clusters also depends on virial radius.

At even higher redshifts, e.g., $z \sim 2$, the size of ETGs seems to become comparable between clusters and field again. Newman et al. (2014) have shown that there is no significant difference in the size-mass relation between ETGs in a massive cluster at $z = 1.8$ and those in a coeval field. The similar conclusion is also drawn for other clusters at $z \sim 2$ (Allen et al., 2015, Wang et al., 2016).

As presented above, there are several possible mechanisms for explaining the size evolution of ETGs in $z < 2$. The main driver of the evolution may be different in different environments and different redshifts, which is far from being fully understood. Moreover, the mechanisms responsible for the size evolution of individual galaxies such as major and minor mergers as well as AGN feedback may also be responsible for the evolution of kinematics, i.e., possible spin down of ETGs. Thus, discriminating whether the size evolution is originated from the growth of individual galaxies or population mix such as the progenitor bias would provide important constraints on the spin down mechanisms of ETGs.

1.3.2 Observational Efforts on the Structures and Kinematics of Distant ETGs

It is inevitably important to observationally investigate kinematics of high-redshift ETGs. Unfortunately, with current telescope facilities, carrying out IFS observation to obtain spatially-resolved spectra with quality high enough for analyzing faint absorption lines of high-redshift ETGs. However, there have been a lot of efforts to investigate kinematics of distant ETGs with various methods.

1.3.2.1 Direct measurements of the kinematics of high-redshift ETGs

It is extremely difficult to investigate kinematical properties of distant ETGs though absorption line spectroscopy, because absorption lines are very faint for currently available 8-m class telescopes, and because the point spread function (PSF) affects the observed velocity and velocity dispersion fields. However, some authors have tried the direct measurement of kinematics making use of ultra-deep spectroscopy (van der Wel & van der Marel, 2008) as well as strong gravitational lensing (Newman et al., 2015, Toft et al., 2017). van der Wel & van der Marel (2008) have carried out ultra-deep optical slit spectroscopy (van der Wel et al., 2005) using an optical spectrograph, FORS2 mounted on 8-m Very Large Telescope (VLT). They have derived V/σ for 25 field ETGs in the redshift range $0.6 < z < 1.2$, applying dynamical modeling to take account of the PSF effects. While they have detected rotation for the majority of the sample, they have not found significant difference in the fraction

of fast rotators. Newman et al. (2015) have obtained high-quality near-infrared spectra of an ETG at $z = 2.6$, using strong gravitational lensing caused by a intermediate redshift cluster. From slit spectroscopic data taken by infrared spectrographs FIRE on the 6.5-m Magellan telescope and MOSFIRE on the 10.0-m Keck telescope, they extract velocity and velocity dispersion profiles along the semi-major axis from absorption lines in the spectra. The V/σ of the galaxy is large ($\sim 0.70 \pm 0.21$) compared to local ETGs which have similar stellar masses and ellipticity to the galaxy ($\log(M_*/M_\odot) = 11.24$ and $\epsilon = 0.12 \pm 0.06$). This result suggest that there may be a strong evolution from fast rotators to slow rotators in $z \sim 2$. Toft et al. (2017) also take advantage of strong lensing and obtain high-quality optical-to-near infrared spectra using XSHOOTER on VLT. They reveal that a massive ($\log(M_*/M_\odot) \sim 11.2$) quiescent disk galaxy at $z = 2.1$ is rotating very quickly with a large V/σ of > 3.3. If this galaxy would be a massive slowly rotating ETG, some mechanism should efficiently reduce the angular momentum of the system.

1.3.2.2 Indirect measurements of the kinematics of high-redshift ETGs

The direct measurements of kinematical properties of high-redshift ETGs are important. However, the sample size is limited due to difficulty in obtaining high-quality absorption spectra as well as the rareness of the strong lensing, which makes statistical comparison to state-of-art simulations difficult. Thus, indirect measurements which can be applied to a large sample is also indispensable.

The intermediate approach between direct and indirect is taken by Belli et al. (2017) who carry out deep spectroscopy and obtain ***unresolved*** kinematics. Belli et al. (2017) have investigated average V/σ of $z \sim 2$ ETGs, using ellipticity and line-of-sight velocity dispersion. Although they obtain deep spectroscopic data, the spatial resolution is too low to obtain V/σ which requires the spatially resolved velocity information at least along the slit. Therefore, they have applied a simple kinematical model to the distribution of ellipticity and line-of-sight velocity dispersion (i.e., unresolved velocity width) for the sample of 80 ETGs in $1.5 < z < 2.5$. They show that quiescent galaxies at $z \sim 2$ have a factor of two larger V/σ than $z \sim 0$.

One indirect approach only with imaging data is to use ellipticity. Intrinsic ellipticity (i.e., tridimensional shape) could be a proxy for rotation for axisymmetric system flattened by rotation (Binney & Tremaine, 2008). As apparent ellipticity is the projection of the tridimensional shape, the distribution of the apparent ellipticity can also be used as a proxy for kinematics. The advantage of using the

ellipticity is that it is relatively easy to obtain a large data set of ellipticity because it can be measured solely from imaging data. van der Wel et al. (2011) have found that the ellipticity of a significant fraction among 14 massive quiescent galaxies at $z \sim 2$ is extremely small and conclude that significant fraction (65 ± 15 percent) of the galaxies contain disks taking account of the viewing angle effect. Chang et al. (2013b) have measured ellipticity of ~ 400 ETGs at $0.6 < z < 1.8$, and found that the galaxies at $z > 1$ are significantly flatter than those at $z < 1$. Chang et al. (2013a) extend this study by fitting ellipticity distributions of oblate and triaxial models to the observed distribution and study the oblate-to-triaxial fraction at $0.5 < z < 2.5$ as well as in the local Universe. They show that while the fraction is a strong function of the stellar mass at $z \sim 0$ with the massive end $\log(M_*/M_\odot) \sim 1$ dominated by triaxial objects (oblate fraction ~ 0.2), such dependance vanishes at $z > 1$ with much larger oblate fraction (~ 0.6), which suggests that ETGs is more disk dominated fast rotators at high redshifts.

Besides ellipticity, there is another indirect method to investigate kinematics of ETGs. The isophote shape parameter a_4 can be a proxy for kinematics (Bender & Möllenhoff, 1987, Jedrzejewski, 1987). Around 1980s, several authors studied isophote shapes of E/S0s and found that the isophote shape of ETGs significantly deviates from a perfect ellipse (Lauer, 1985a,b,c, Bender & Möllenhoff, 1987, Jedrzejewski, 1987, Bender et al., 1988, 1989). Bender & Möllenhoff (1987) and Jedrzejewski (1987) evaluated the deviations using Fourier expansions in the polar angle. They found that most significant non-zero component of the Fourier analysis is the a_4 parameter, the coefficient of the $\cos(4\theta)$ term. As a_4 represents the lowest order symmetric deviation about the semi-major and minor axes, the negative sign of the parameter indicates that the isophote shape deviates into "boxy" whereas positive sign is indicative of "disky" deviation. It has been thought that boxy-disky dichotomy is closely linked to slow-fast rotator dichotomy of ETGs. (Kormendy & Bender, 1996) have shown correlation between the a_4 parameter and V/σ of local ETGs. They have presented that boxy ETGs tend to be brighter, supported by random motions with large velocity anisotropy (i.e., consistent with slow rotators), have significant radio and X-ray activities and core nuclear light profiles, while disky ETGs tend to be fainter, supported by ordered rotation with small velocity anisotropy (i.e., consistent with fast rotators), lack radio and X-ray activities and have coreless nuclear profiles (Kormendy et al., 2009, for a review)

Pasquali et al. (2006) have measured the a_4 parameter for 18 ETGs at $0.5 < z < 1.1$ using deep imaging data taken by Hubble Space Telescope (HST). They have shown that he percentages of disky

and boxy Es at $0.5 \lesssim z \lesssim 1.1$ are similar to that of the local counter parts. Mitsuda et al. (2017) also measure the a_4 parameter for 133 ETGs in massive clusters at $z \sim 1$ as well as a comparison sample of 355 ETGs residing in massive clusters at $z \sim 0$. In that study, we have shown that the disky galaxy fraction at a fixed stellar mass is comparable between the high- and low-redshift samples. The results from the a_4 parameter and from ellipticity distribution seem to be conflicting. However, Mitsuda et al. (2017) show that there is large uncertainty in measuring the a_4 parameter due to the effect of PSF as well as Eddington bias arising from lower signal-to-noise ratio for the high-redshift measurement (see Appendix in Mitsuda et al., 2017).

Moreover, recent updates about the kinematics of local ETGs from IFS surveys have revealed that the a_4 parameter may not be a good proxy for rotation of galaxies (Emsellem et al., 2011). As described in Krajnović et al. (2013), while a disk component in fast rotators could be detected by diskiness of isophotes when they are viewed closed to edge-on, the signature would be vanished in the noise for inclinations $\lesssim 60°$(90°for edge-on. See Figure 8 in Krajnović et al., 2013). Although the ellipticity is strongly correlated with the spin parameter (Figure 1.2), the use of ellipticity as a proxy for kinematics is also limited. As shown by (Newman et al., 2015), round objects may also rotate more rapidly at high redshifts than in the local universe. Therefore, it is important to assess the kinematical properties of round objects at high redshifts which may be progenitors of local round slow rotators.

1.4 Purpose of This Study

The purpose of this study is to observationally investigate the evolution of kinematics of ETGs. As we have shown in the previous sections, it is inevitably important to obtain kinematics of high-redshift ETGs and to compare the results with state-of-art cosmological simulation in order to investigate the mechanisms of kinematical evolution. However, it is difficult to directly measure the spatially-resolved kinematics for a statistically significant samples of high-redshift ETGs from absorption line spectroscopy as we have mentioned before. In this study, we take indirect approach to investigate kinematics of high-redshift ETGs. For this purpose, we (i) find out a photometric parameter that can be used as a proxy for kinematics of ETGs, and (ii) measure the parameter for a large sample of high-redshift ETGs by carrying out surface photometry.

1.4.1 Finding a Photometric Parameter as a Proxy for Kinematics

In the first part of this paper, Chapter 2, we investigate the relation between surface photometry and kinematics of ETGs in order to find out a photometric parameter which is significantly correlated to kinematic parameters such as λ and V/σ.

Radial light profiles are important aspects of ETGs. It is well known that radial light profiles of ETGs* can be well fitted by de Vaucouleurs (or $r^{1/4}$) profiles (de Vaucouleurs, 1948). More generally, the profiles of ETGs are often described by Sérsic profile (Sérsic, 1968) with which the intensity at a radius r is expressed as

$$I(r) = I_{\rm e} \exp\left\{-b_n \left[\left(\frac{r}{r_{\rm e}}\right)^{1/n} - 1\right]\right\}, \tag{1.3}$$

where $I_{\rm e}$ is the intensity at the effective radius $r_{\rm e}$, n is the Sérsic index, and b_n is a dimensionless scale factor depending on n ($b \sim 2n - 1/3$, Ciotti & Bertin, 1999). When $n = 4$, the Sérsic profile converges on the de Vaucouleurs. Luminous Es (e.g., B-band absolute magnitude brighter than $M_B \sim -20.5$) tend to have $n \sim 4$ or greater while less luminous Es have $n \sim 2 - 4$ (Caon et al., 1993, Graham &

* Strictly, the single component de Vaucouleurs or Séric profile fitting should be applied only for Es and bulge components. S0s should be fitted by multiple components because they have a disk and a bulge. But in many cases, a single Séric profile is enough. In this case, the Séric index n becomes ~ 4 when the galaxy is bulge-dominated, otherwise n becomes ~ 1. Especially for high-redshift galaxies, a single-component Séric profile is favored, because the spatial resolution and signal-to-noise ratio is not that high for carrying out robust two-component fitting (i.e., bulge-disk decomposition).

Guzmán, 2003, Kormendy et al., 2009).

Disk components*, on the other hand, have light profiles consistent with exponentially-declining profiles (exponential disk, Freeman, 1970) which can be described by $n = 1$ in the Sérsic profile. The exponential disk itself is more truncated than de Vaucouleurs profiles. Moreover, light profile of majority of disk-dominated galaxies are truncated in the outer region, deviating from pure exponential profiles (van der Kruit, 1979, Pohlen et al., 2004).

The light profile of ETGs are sometimes a fitted with two-component model including a bulge and a disk in order to carry out bulge-disk decomposition (Andredakis & Sanders, 1994, Andredakis et al., 1995). For ETGs, the bulge component is described either by a de Vaucouleurs or Sérsic profile while the other component by an exponential profile. This method is used to decompose multiple components in a galaxy (e.g., Fisher & Drory, 2008, Lang et al., 2014), and require higher spatial resolution and signal-to-noise ratio for robustly determining larger number of the fitting parameters.

Based on two-dimensional kinematics, Using the single-component Sérsic and two-component profile fitting, Krajnović et al. (2013) have presented that 83 per cent of 180 local non-barred ETGs in the ATLAS^{3D} sample show signs of disk components such as small single-component Sérsic index n and non-zero disk-to-total luminosity ratio D/T. They have suggested a criterion to ***photometrically*** classify slow and fast rotators using n and D/T. They propose to select fast rotators by disk-to-total light ratio $D/T > 0.5$ and total Sésic index $n < 3$ for those having $D/T \leq 0.05$, and slow rotators as remaining. Although this selection gives very high completeness for fast rotators (0.89), the contamination for fast rotators is as high as 0.29 and slow-rotator completeness is only 0.4 with the contamination of 0.29. In addition, although there are significant correlation between the Sésic parameters (total Sésic index n, bulge Sésic index $n_{\rm bulge}$, and D/T) and the kinematic parameter λ, the correlations almost vanish for round galaxies ($\epsilon < 0.4$).

In Figure 1.4, we show the total Sésic index as a function of $\lambda_{\rm e}$ for all non-barred ATLAS^{3D} ETGs and for round ETGs ($\epsilon < 0.4$). In this study, we gathered data from publicly available catalogs of the ATLAS^{3D} Project†. The details are described in Section 2.1.1. The left panel of Figure 1.4 describe significant correlation between n and $\lambda_{\rm e}$. We carry out the Spearman's rank correlation test, and the p-value‡ is small 2.6×10^{-10} which indicates that there is a significant correlation between the two

* LTGs are often fitted with a single exponential profile as well as Sésic profile with $n \sim 1$ as their bulge fraction is not large.

† http://www-astro.physics.ox.ac.uk/atlas3d/

‡ The p-value is the probability with which the observed distribution is drawn from random one.

parameters. If we select round galaxies, however, the significant correlation is no longer seen. The p-value of the rank correlation test is not small.

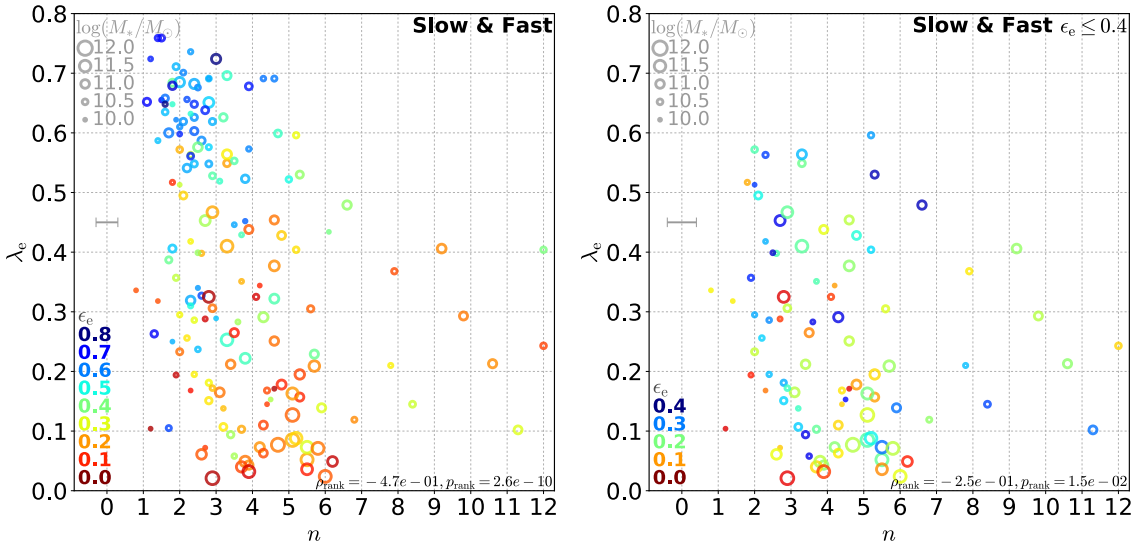

Figure 1.4 Spin parameter λ_e as a function of the Sésic index n for non-barred ETGs in the ATLAS^{3D} sample. Left: All galaxies. Right: Round galaxies with ellipticity $\epsilon < 0.4$. Color indicates ellipticity denoted in the lower left of each panel. Marker size indicate the stellar mass noted in the upper left of each panel. Error bar indicates median error for n. Results of the Spearman's rank correlation test, the correlation efficiency $\rho_{\rm rank}$ and p-value $p_{\rm rank}$ are also written in the lower right.

The situation is better for other Sésic parameters, $n_{\rm bulge}$, and D/T, which are described in Figures 1.5 and 1.6. The p-value of the rank correlation test between $n_{\rm bulge}$ and λ is 2.6×10^{-9} for all galaxies and 1.3×10^{-5} for round galaxies ($\epsilon \leq 0.4$). The p-value between D/T and λ is 1.0×10^{-12} for all galaxies and 2.5×10^{-3} for round galaxies. However, two-component fitting or bulge-disk profile decomposition is difficult for high-redshift galaxies for which signal-to-noise ratio and the spatial resolution of images is not very high (see Lang et al., 2014, who carried out the decomposition for high-redshift galaxies but with fixed $n_{\rm bulge} = 4$).

Among the Sésic parameters we find that the effective radius r_e and the surface brightness at the effective radius μ_e show significant correlation to λ_e. Figures 1.7 and 1.8 are the same plots as Figure 1.4 but for r_e and μ_e, respectively. For round galaxies, the p-value of the rank correlation test become 9.1×10^{-5} and 2.9×10^{-4}, respectively.

The problem in the parameters r_e and μ_e is that they are fitting parameters and are not always able to be interpreted as ***effective radius*** and ***surface brightness at the radius*** when a light profile of

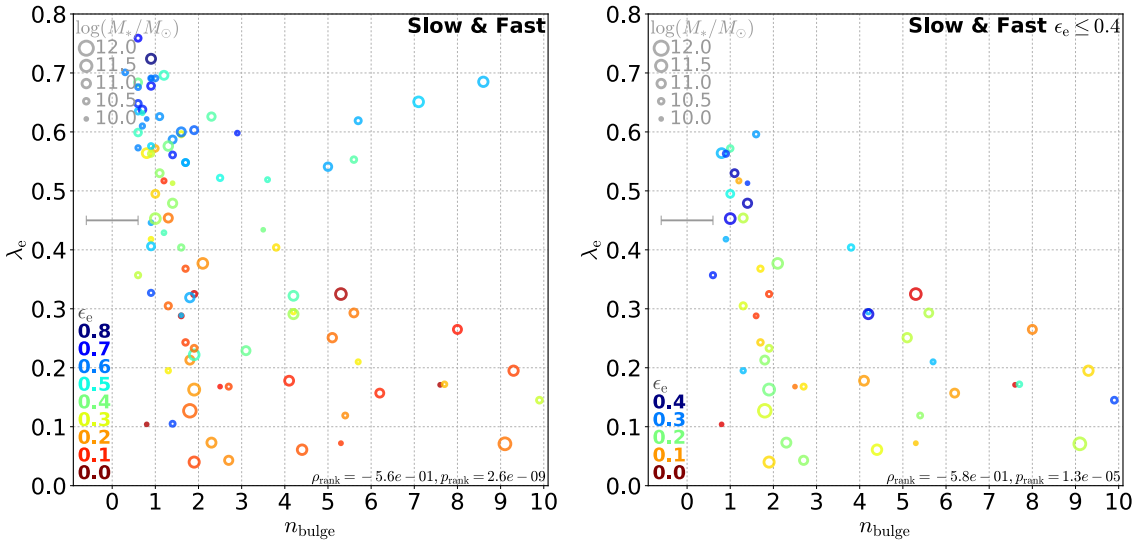

Figure 1.5 Same as Figure 1.4 but for the bulge Sérsic index $n_{\rm bulge}$.

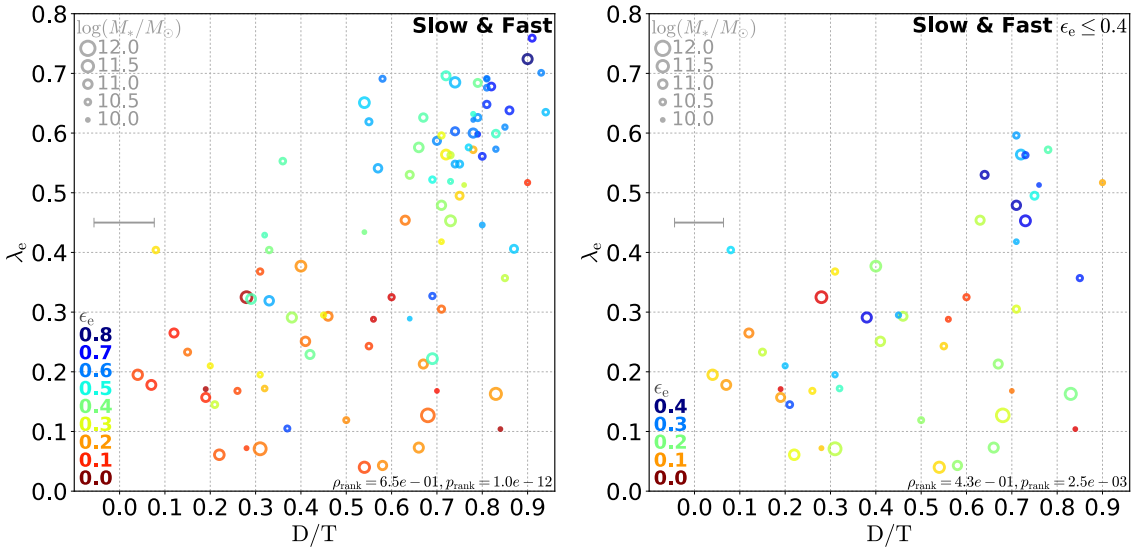

Figure 1.6 Same as Figure 1.4 but for the disk-to-total ratio D/T.

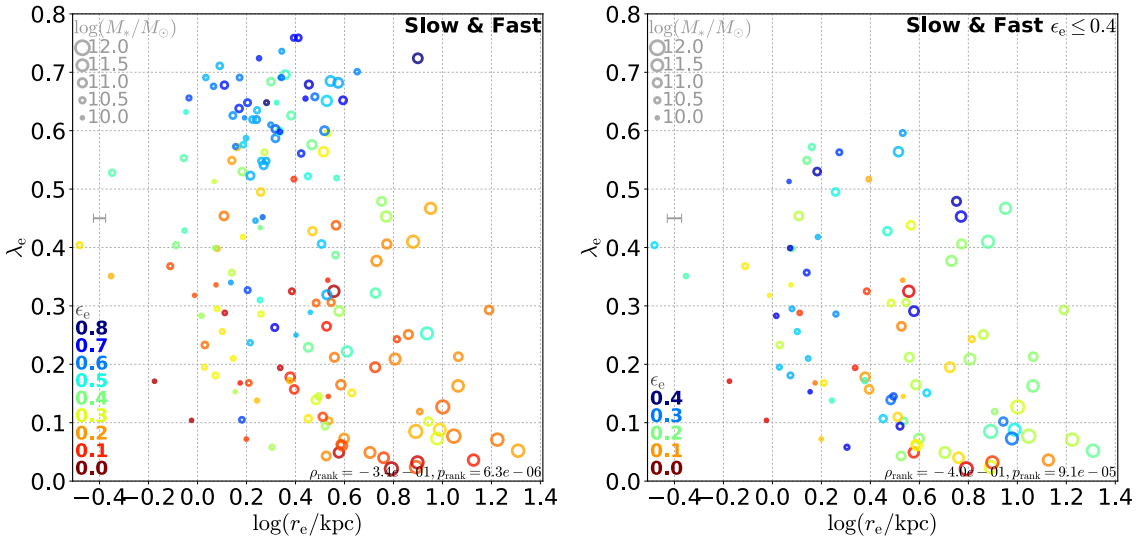

Figure 1.7 Same as Figure 1.4 but for the effective radius r_e.

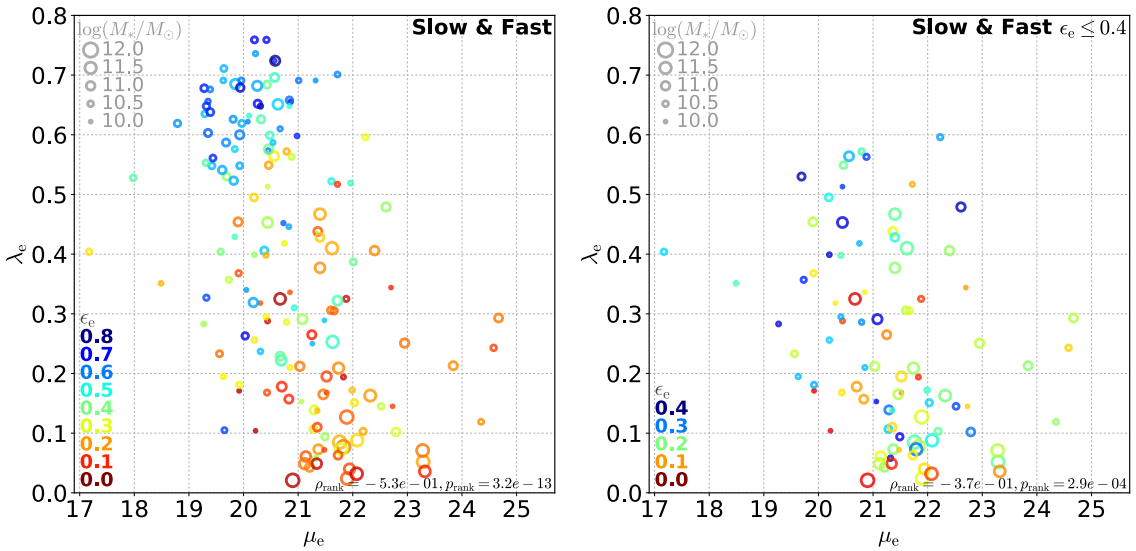

Figure 1.8 Same as Figure 1.4 but for the surface brightness at the effective radius μ_e.

a galaxy significantly deviates from pure Sésic. In such a case, $r_{\rm e}$ and $\mu_{\rm e}$ tend to be affected by n due to parameter correlation, depending on profile fitting method (Morishita et al., 2014). Therefore, we would like to find a better parameter than $r_{\rm e}$ and $\mu_{\rm e}$. We note that the reason why $r_{\rm e}$ and $\mu_{\rm e}$ correlate to λ may not be due to their correlation to n because the Sérsic index n does no longer show correlation to λ for round galaxies. We suspect that the reason may be that while n is sensitive for light concentration (i.e., bulge fraction), $r_{\rm e}$ and $\mu_{\rm e}$ may be affected by light in the outer regions.

On the profiles of ETGs, an interesting result is recently reported. Schombert (2015) has constructed template profiles of local ETGS which describe average profiles of ETGS as a function of luminosity. He has found that local ETGs can be classified into two families by outer light profiles using the templates. One is those having consistent profiles with the templates, and the other is those having distinctly shallower (i.e., extended outer) profiles. He has shown that more massive galaxies tend to have extended light profiles. He has also presented that extended ETGs seem to have lower V/σ than normal ones (Figure 12 in Schombert, 2015). Although the difference of V/σ might come from the difference of the stellar mass taking account of correlation between kinematics and stellar mass, the light profiles (especially, slopes of the light profile in the outer region, i.e., whether it is extended or not) may have some information about kinematics. Therefore, it is important to discriminate whether the difference of the outer light profiles is originated from the stellar mass or from kinematics (or from both).

In this study, we investigate the relation between slopes of radial light profiles and kinematics of ETGs. We carry out surface photometry in order to extract r-band radial light profiles for 166 non-barred ETGs in the ATLAS$^{\rm 3D}$ sample which are covered by imaging data of Sloan Digital Sky Survey (SDSS York et al., 2000) Data Release 12 (DR12, Alam et al., 2015). We measure slopes of the light profiles in inner and outer regions. We also introduce a new parameter $\Delta Slope$ using the inner and outer slopes which roughly indicates the deviation of the light profiles from a pure Sérsic function. We show that almost all slow rotators have extended profiles with negative ΔSlope while the majority of fast rotators are consistent with Sérsic ($\Delta{\rm Slope} \sim 0$) or truncated ($\Delta{\rm Slope} > 0$). We also present that there is a significant correlation between ΔSlope and λ for round objects. This part will be described in Chapter 2.

1.4.2 Surface Photometry of High-Redshift ETGs

In the second part, Chapter 3, we carry out surface photometry for high-redshift quiescent ETGs as well as their low-redshift counterparts. We prepare a large sample of $\gtrsim 600$ ETGs residing in massive clusters both at $z \sim 1$ and 0. We would like to note that advantages of using massive clusters are that we can construct a sample of large number of massive ETGs and that they are unique environment where galaxies evolve within the cluster once they enter into such an environment. The latter advantage help us construct a sample of the low-redshift counterparts which are likely ancestors of the high-redshift ETGs.

We make use of high-quality imaging data taken in i and z bands which we have gathered in the Hubble Space Telescope (HST) Cluster Supernova (SN) Survey (Dawson et al., 2009, Suzuki et al., 2012, PI-Perlmutter: GO-10496). In the program, 25 massive clusters at $0.9 < z < 1.5$ have been targeted. We also use a spectroscopic catalog created in the program through ground-based spectroscopic follow-up observations. As we have co-added many images taken over multiple epoch, the z-band images have a total exposure time of ~ 10 k sec or more. The spatial resolution is also high (PSF FWHM ~ 0.1 arcsec ~ 0.8 kpc at $z \sim 1$) enough for studying light profiles of $z \sim 1$ galaxies. We select quiescent ETGs which are likely to be members of the clusters using color and morphological selection, taking advantage of a large number of spectroscopically confirmed members.

For the low-redshift comparison sample, we use imaging data and photometric and spectroscopic catalogs provided by SDSS DR12 (Alam et al., 2015). We select massive clusters according to their halo mass taking account of the growth of the halo mass (Zhao et al., 2009) so that we could select likely ancestors of the high-redshift clusters. We extract low-redshift ETGs in a consistent manner with the high-redshift sample so that we could select likely ancestors of the high-redshift ETGs assuming passive evolution.

We carry out surface photometry, extract light profiles in the rest-frame optical wavelength, and derive inner and outer slopes as well as $\Delta\mathrm{Slope}$ We also simulate effect of PSF using local ETG samples which we use in Chapter 2, and correct the slopes and $\Delta\mathrm{Slope}$ for the effect. We find the significant difference of $\Delta\mathrm{Slope}$ distribution between the high- and low-redshift samples. This part will be described in Chapter 3.

1.4.3 Structure of the Paper

This paper is organized as follows: In Chapter 2, we present the first part where the relation between $\Delta\mathrm{Slope}$ and λ is shown. In Chapter 3, we carry out surface photometry to obtain $\Delta\mathrm{Slope}$ for high-redshift ETGs as well as for low-redshift comparison sample. In Chapter 4, we discuss formation and evolution mechanisms based on finding in Chapter 2 and 3. Finally, in Chapter 5, we summarize this study with conclusions. Throughout this paper, magnitudes are described in the AB system. We assume a ΛCDM cosmology with parameters of $(\Omega_m, \Omega_\Lambda, H_0)$=$(0.3, 0.7, 70\ \mathrm{km\ s^{-1}\ Mpc^{-1}})$.

2

Relation between Kinematics and Light Profiles of Local Early-Type Galaxies

In this chapter, we present the relation between light profile and kinematic properties of local ETGs. We prepare a sample of local ETGs from a large IFS survey, the ATLAS^{3D}, within the SDSS imaging survey area. We carry out surface photometry on the SDSS images in order to measure radial light profiles and the slopes of the profiles in inner and outer regions. We investigate relation between degree of rotation support and the deviation of the light profile which is parameterized by the slopes.

This chapter is structured as follows. We present sample and data in Section 2.1. We then describe how we carry out surface photometry for the extraction of the radial light profiles and how we derive the inner and outer slopes in Section 2.2. We show the results in Section 2.3.2.1 where we present the slopes of fast and slow rotators as well as the definition of $\Delta\mathrm{Slope}$. Finally in Section 2.4, we provide brief discussions. In this chapter, we use the following rough classification for slow and fast rotators unless otherwise indicated. We regard galaxies with $\lambda_\mathrm{e} \leq 0.3$ as slow rotators and others as fast rotators.

2.1 Data and Sample

We have created a non-barred ATLAS^{3D} ETG sample within the SDSS imaging survey area. We measure radial light profiles of the non-barred ATLAS^{3D} ETG using SDSS images and compare them with kinematical properties investigated by the ATLAS^{3D} Project.

2.1.1 ATLAS^{3D} Data

The ATLAS^{3D} Project (Cappellari et al., 2011a) is a volume-limited, multi-wavelength survey of a complete sample of 260 ETGs within the local volume of radius of $D = 42$ Mpc combined with galaxy formation simulation such as numerical simulations and semi-analytic modeling.

The sample selection of the ATLAS^{3D} Project is detailed in Cappellari et al. (2011a). Here, we briefly describe the ATLAS^{3D} ETG sample. The ATLAS^{3D} ETGs are selected from parent 871 galaxies which lie within $D < 42$ Mpc in the northern hemisphere ($|\delta - 29| < 35$, where δ is the sky declination) and have absolute K-band magnitude brighter than $M_K = -21.5$ mag. The magnitude limit corresponds to the stellar mass of $M_* = 6 \times 10^9 M_\odot$ for ETGs.

The ATLAS^{3D} ETGs are morphologically selected based on the absence of spiral structure. The spiral structure is visually examined using true color red-green-blue images (Lupton et al., 2004) provided by the SDSS DR7 (Abazajian et al., 2009) which is 82 percent of the parent sample as well as B-band DSS2-blue images in the Online Digitized Sky Survey* and images taken by the ATLAS^{3D} team with the Isaac Newton Telescope. Basic properties of the sample such as masses, sizes, and colors are given in the series of ATLAS^{3D} papers (e.g., Cappellari et al., 2011a, 2013a). We note that the ETG selection is solely based on the morphology and no color selection is applied although majority of the selected ETGs have red color consistent with the red sequence.

In this study we make use of publicly available data from the ATLAS^{3D} Project†. The data include the right ascension, declination, distance (Cappellari et al., 2011a), morphological features such as bar, ring, and shell (Krajnović et al., 2011), ellipticity, spin parameters (Emsellem et al., 2011), luminosity and the mass-to-luminosity ratio in r-band (Cappellari et al., 2013b), and Sérsic parameters (Krajnović et al., 2013).

*http://archive.eso.org/dss/dss
†http://www-astro.physics.ox.ac.uk/atlas3d/

2.1.2 SDSS Imaging Data

We prepare mosaic images for the ETG sample from SDSS DR12 because the galaxies are so large that one single frame can not cover entire galaxy images. We collected all frames within $\pm$ 10 arcmin from the center of the galaxies from SDSS DR12 Science Archive Server. We make use of flux-calibrated, sky subtracted images provided by SDSS DR12 which have been processed with the photometric pipeline version `5_6`. The sky subtraction around bright objects is improved in this version in that the over-subtraction of the outer parts of large galaxies are minimal.

We then create a mosaic image for each galaxy using an iraf task `wregister`. First, we prepare a reference image with the size of 4000 pix $\times$ 4000 pix in which WCS parameters are defined so that the central pixel (2001, 2001) has RA and Dec of the target galaxy with the same pixel scale as original SDSS images (0.396 arcsec pix^{-1}) and with the north up. Then, all frames for the target galaxies are transferred to the projection defined in the reference image by `wregister`. Finally, all transferred frames are combined. We created the mosaic images for all SDSS u, g, r, i, z filters, respectively, although the results are derived from r-band images.

We also created mosaic images of variance. We prepared variance image for each single frame from sky image, calibration factor, flat field, gain, and dark variance as described in SDSS website*. We then transfer and combine all frames for the target galaxies, and obtain mosaic images of variance.

2.1.3 Non-barred ETGs Sample

In order to reliably measure the light profiles of the main body of galaxies, we focus on ETGs without bars, rings, and shells based on the inspection by Krajnović et al. (2011). We exclude galaxies noted as either "B" (bar), "R" (ring), "S" (shell), or "U" (unknown) in Table D1 in Krajnović et al. (2013). We have 180 non-barred ETGs at this stage which are exactly the same galaxies whose Sérsic parameters are studied by Krajnović et al. (2013).

We then selected galaxies which are within the SDSS imaging survey area. Among the 180 non-barred ETGs, 14 galaxies lack SDSS coverage. Therefore, in this study, we focus on the remaining 166 galaxies.

*https://data.sdss.org/datamodel/files/BOSS_PHOTOOBJ/frames/RERUN/RUN/CAMCOL/frame.html

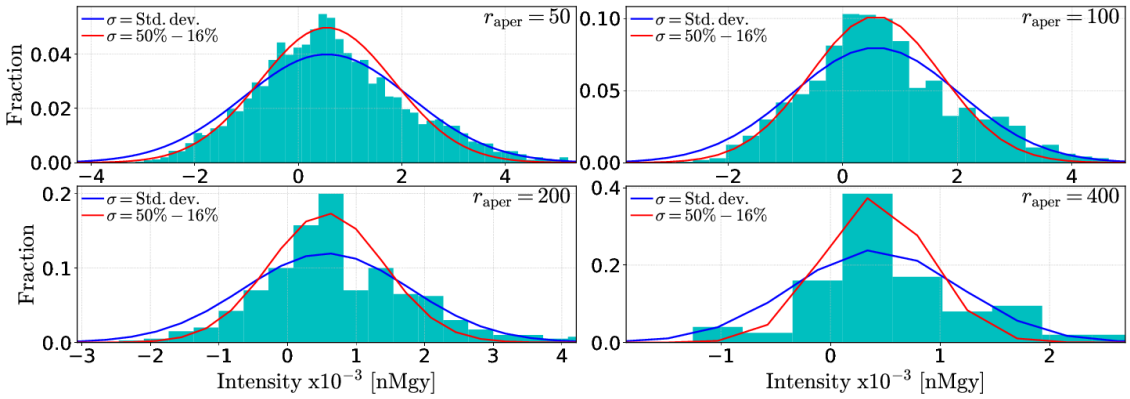

Figure 2.1 Distributions of the median intensity within circular apertures for IC0560. The unit of the intensity is given in nano Maggy per pixel which is the brightness unit of calibrated images in SDSS DR12. From top-left to bottom-right panels, the aperture radius is 50, 100, 200, and 400 pixels as noted in the top-right corner of each panel. For comparison, Gaussian distributions with the width σ equivalent to the standard deviation of the cyan histogram is shown by blue curves. Red curves are also Gaussian distributions but with the width set to the interval between 16 percentile and 50 percentile. Blue ones are too wide because of the extended positive wings in the median intensity distributions, which indicates that the median intensity (i.e., estimated sky residual) is probably affected by undetected objects.

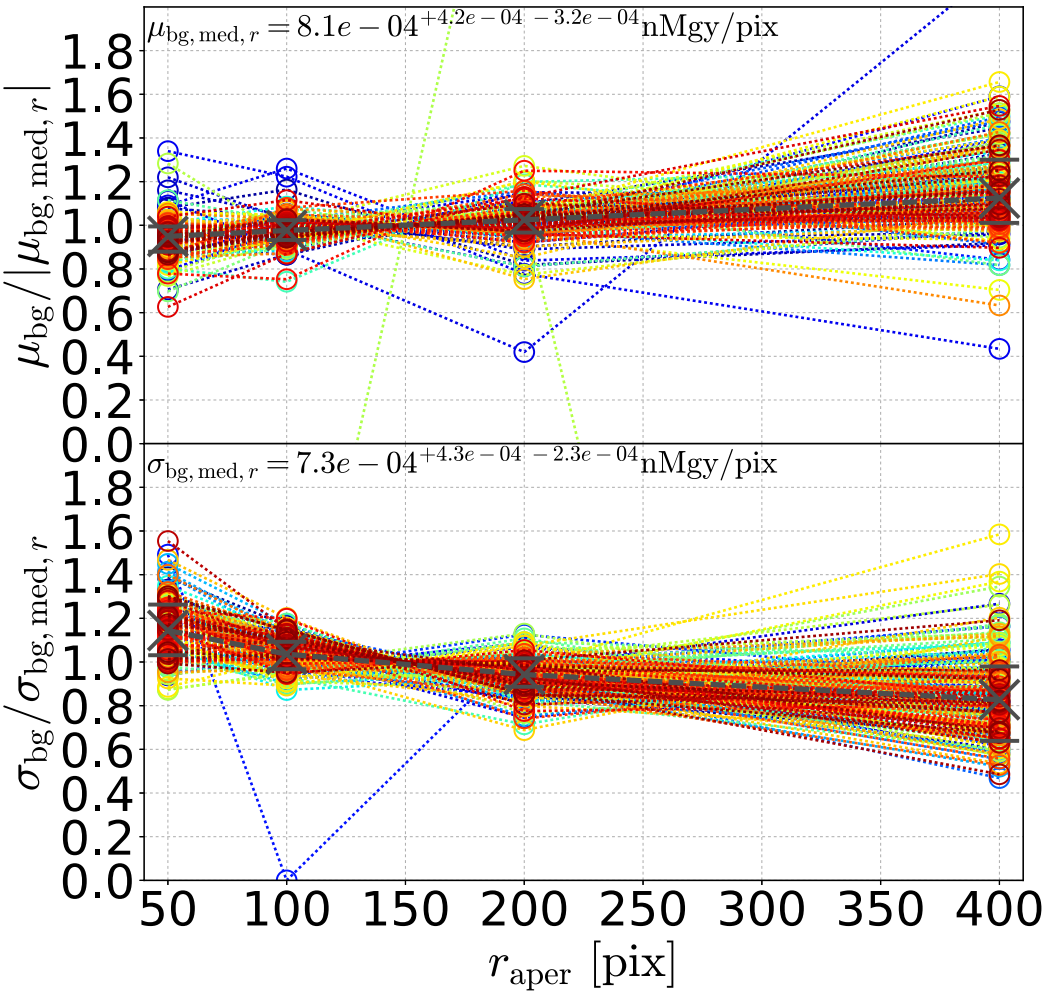

Figure 2.2 μ_{bg} (top) and σ_{bg} as a function of the aperture size for all of the ETG sample (colored circles, same color for one galaxy). The vertical axis is normalized with the median taken along the x-axis ($\mu_{\mathrm{bg,med},r}$ and $\mu_{\mathrm{bg,med},r}$) which are noted in the panels. 16, 50, and 84 percentiles of the data points for each r_{aper} are shown by gray crosses.

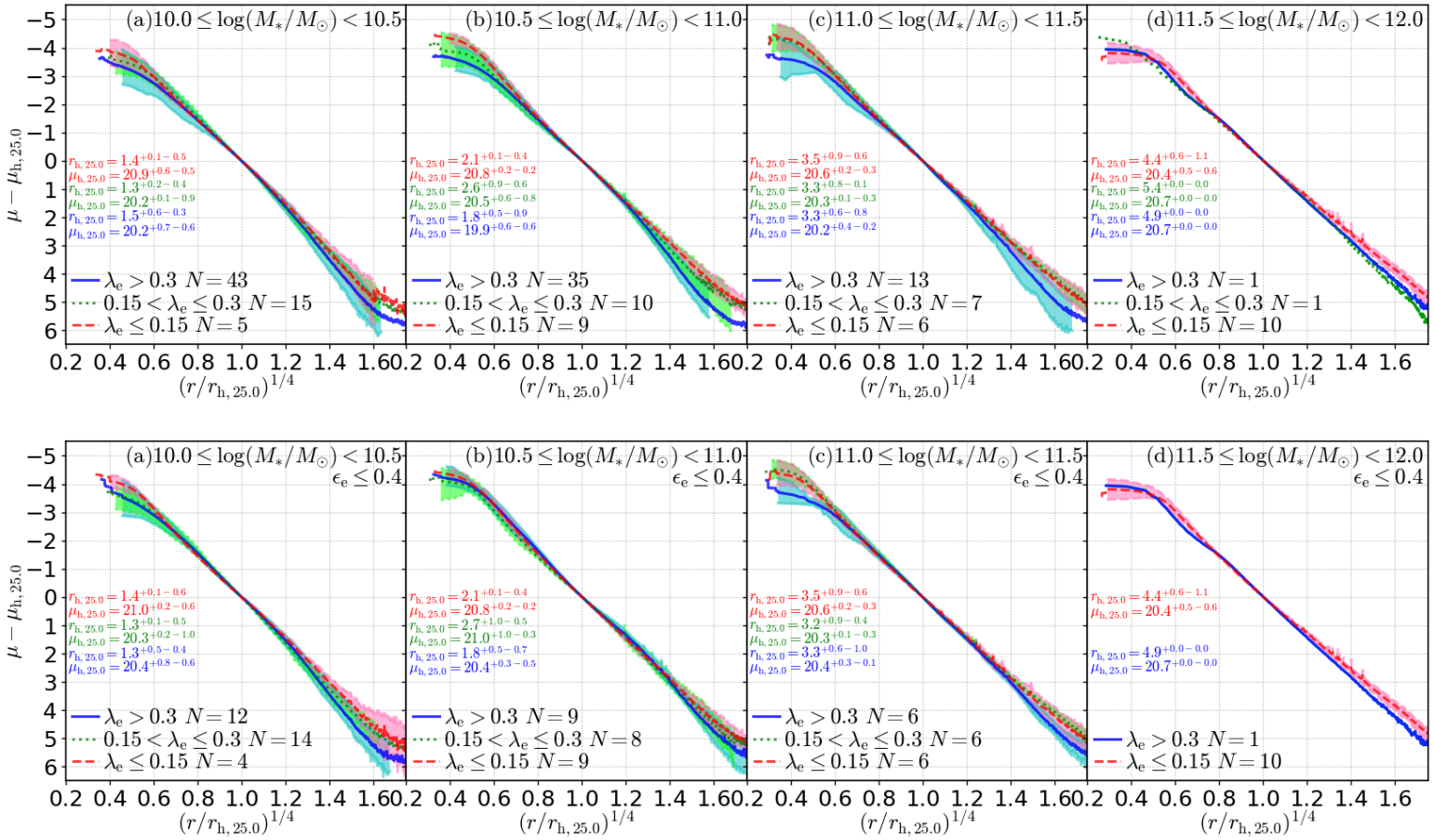

Figure 2.3 Stacked (averaged) light profiles for different spin parameters, $\lambda_e \leq 0.15$ (red dashed lines), $0.15 < \lambda_e \leq 0.3$ (green dotted lines), and $0.3 < \lambda_e$ (blue solid lines) in four stellar mass bins (from panels (a) to (d)). The number of galaxies in each λ_e and stellar mass bin is noted in the legend (N). Panels in the upper row includes all galaxies in our ETG sample while those in the lower row only includes round galaxies with $\epsilon_e \leq 0.4$. Shaded regions indicate 16 to 84 percentile distribution of the light profile in each λ_e and stellar mass bins. The radius is normalized at the half-light radius ($r_{h,25.0}$) while the surface brightness is normalized by the value at $r_{h,25.0}$. The median of the half-light radius and the surface brightness at $r_{h,25.0}$ in each bin (same color as the profile) are shown in each panel with 16 and 84 percentile.

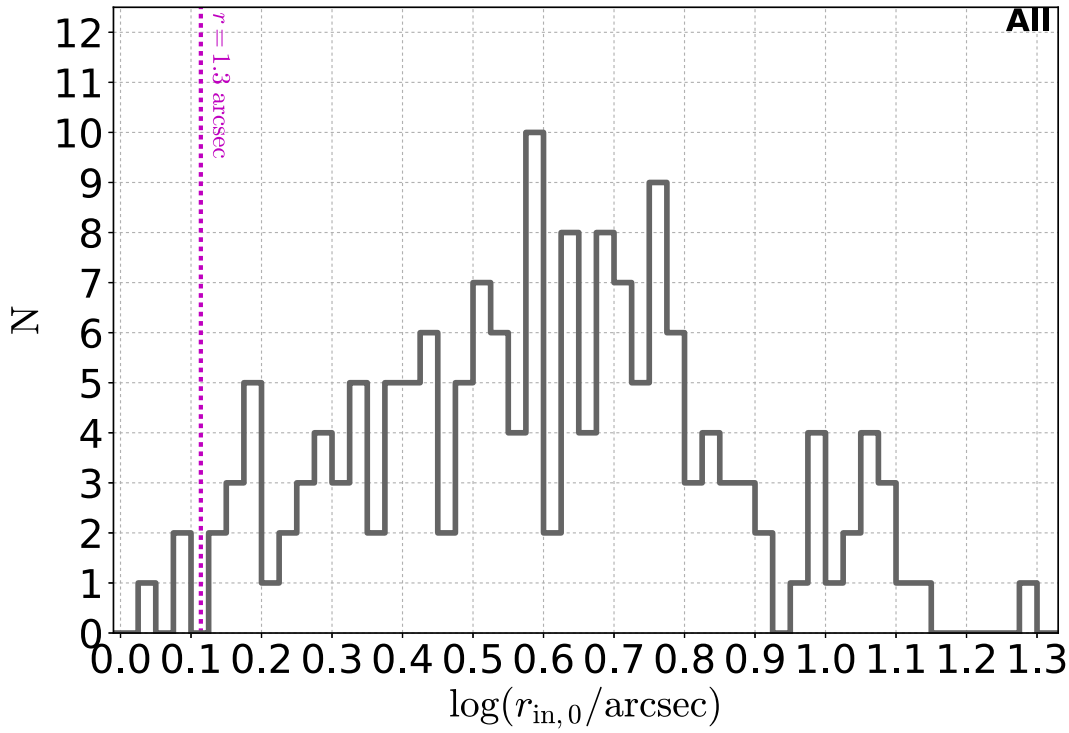

Figure 2.4 Histogram of the inner most radius ($r_{\mathrm{in},0} = 0.7(r/r_{\mathrm{h},25.0})^{1/4}$). Vertical dotted line indicates the typical PSF FWHM in SDSS r-band images.

2.2 Measuring surface brightness profiles and slopes

In this section, we describe how surface brightness profiles are obtained as well as how inner and outer slopes are measure from the profiles.

2.2.1 Measuring light profiles

We obtain radial (semi-major axis) surface brightness profiles from SDSS r-band images. We prepare mask images and measure radial light profiles. We also estimate possible sky residual and subtract it from radial profiles, although automatic sky subtraction has already been applied by SDSS in a sophisticated way. We then compute inner and outer slopes. We take account of local fluctuation of the sky residual into uncertainty of the inner and outer slopes.

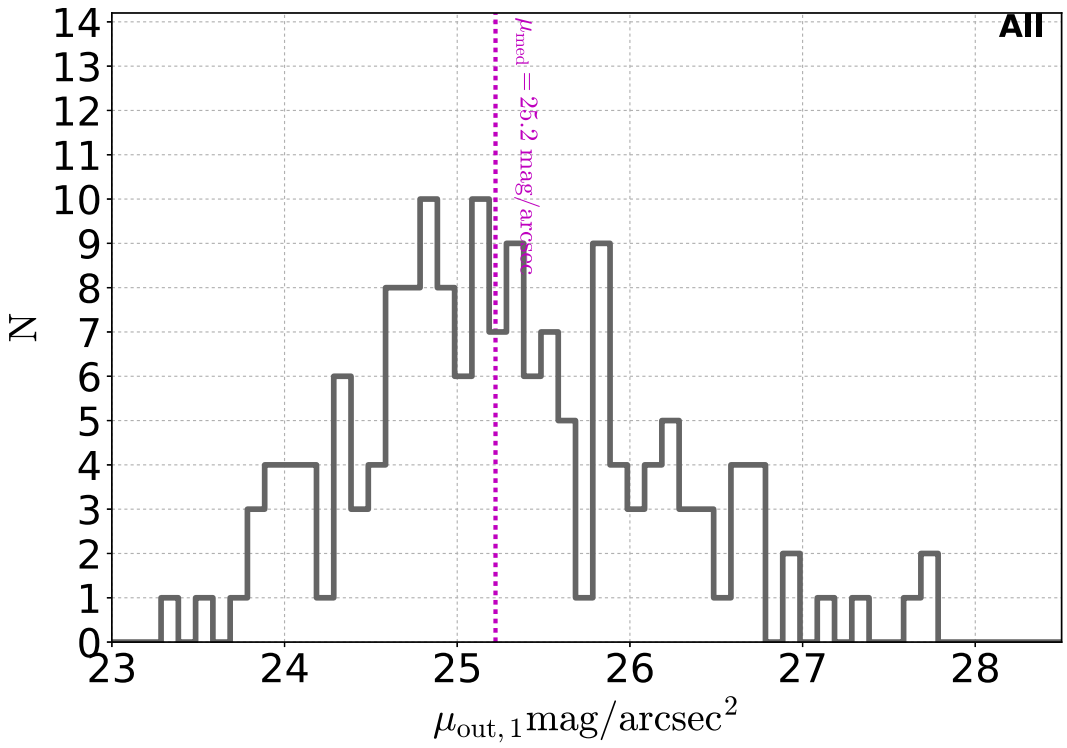

Figure 2.5 Histogram of the surface brightness at the outer most radius ($\mu_{r_{\rm out,1}}$). Vertical dotted line indicates the median of $\mu_{r_{\rm out,1}}$.

2.2.1.1 Creating masks by SExtractor

First, a mask image for objects around each target galaxy is prepared. We run Source Extractor (`SExtractor`, Bertin & Arnouts, 1996) to detect objects within each mosaic image in two-step manner (hot and cold detection; Rix et al., 2004). The detection and deblending parameters are optimized by trial and error judged by the successful detection and segmentation of objects around the target galaxies. We make use of the segmentation image provided by SExtractor to construct the mask image. All the non-zero pixels in the segmentation are masked except for those belonging to the target galaxy.

2.2.1.2 Measuring radial profiles

From the mosaic image and mask, r-band light profile is measured for each galaxy. We measure the average intensity at r_i within an elliptical annulus with the inner semi-major axis of $r_i - 0.5\Delta r$ and outer one of $r_i + 0.5\Delta r$. Here, r_i is taken from 0.5 pixel to 20 times the Petrosian radius (i.e., `PETRO_RADIUS` in SExtractor) with the interval of 1 pixel, and Δr is set to 1 pixel. Near the edge of the annulus, a pixel is divided into 100×100 sub-pixels, and the intensity is integrated using the sub-pixels. Geometry parameters of the ellipse such as the central position, position angle, and ellipticity is fixed to those measured by SExtractor for all annulus. The average intensity is converted into surface brightness after the subtraction of sky residual (see below) using the pixel scale and magnitude-zero point (22.5 for SDSS).

2.2.1.3 Estimating and subtracting sky residual

Although the sky subtraction carried out with the SDSS photometric pipeline version `5_6` is sophisticated, there may be global and/or local under- or over-subtraction within the mosaic images. We first estimate the residuals of the sky subtraction as follows. For all 166 ETGs in our sample, we randomly put circular apertures with various radii on the mosaic images, take median intensity, and estimate the fluctuation of the median. Since the median intensity within an aperture can be regarded as local background level (i.e., sky residual), the fluctuation of the median intensity over apertures reflects the possible variation of the local sky residual plus the random error originated from noise. For this purpose, we aggressively mask object by masking elliptical regions within $r < 4r_{\rm Petro}$ with the el-

lipticity and position angle determined by SExtractor. Here, $r_{\rm Petro}$ is the Petrosian (semi-major axis) radius (Petrosian, 1976) which is also derived by SExtractor. The pixels detected in the segmentation image created by SExtractor are also avoided. We set the aperture radii ($r_{\rm aper}$) to 50, 100, 200, and 400 pixels. We also set the number of apertures put on the mosaic images to 6400, 1600, 400, 200, respectively for the aperture sizes. We discard apertures if the amount of unmasked pixels within an aperture is less than 75 percent in which case a new aperture is taken instead.

Figure 2.1 is an example of the distributions of the median intensity within apertures. We also plot two Gaussian distributions for comparison. One has the width (σ) equivalent to the standard deviation, and the other to the interval between 16 and 50 percentile. Both has the same central value which is set to the median of the original distribution ($\mu_{\rm bg}$). In this example (and most cases), the Gaussians with the standard deviation are too wide while those with the 16 to 50 percentile interval agree well with the original distribution in the area where the intensity (x-axis) less than the median. This is due to extended positive wings in the median intensity distribution which may be caused by undetected objects or fluxes outside the mask. The positive value of $\mu_{\rm bg}$ is indicative of possible global sky residual (i.e., under-subtraction) and negative value is indicative of over-subtraction. Therefore, we apply additional subtraction of the residual from radial profiles. Note that the residual $\mu_{\rm bg} \sim 8 \times 10^{-4}$ nMgy/pix is small (0.1 %) compared to the subtracted sky revel which is $\sim$ 0.7 nMgy/pix for the typical r-band sky brightness of $\sim$ 21 mag arcsec^{-2}. We have checked that the results do not change significantly even if we do not apply the additional subtraction.

We also evaluate the possible variation of the local sky residuals. We also obtain the median variance from mosaic variance image within the same aperture for the median intensity. We quadratically subtract the median of the median variance (background and photon noises) from the 16 to 50 percentile interval of the median intensity and obtain the possible variation of the local sky residuals ($\sigma_{\rm bg}$). For most cases, contribution from the variance is small. In Figure 2.2, $\mu_{\rm bg}$ (top) and $\sigma_{\rm bg}$ for all of the ETG sample are shown as a function of the aperture size. $\mu_{\rm bg}$ tends to increase marginally with increasing aperture sizes. This may be because larger apertures have more chance to contain pixels close to masked regions. We check the dependance of the median fraction of unmasked pixels within an aperture on aperture sizes. The fraction decreases from $\sim$ 97 percent for $r_{\rm aper} = 50$ pix to $\sim$ 93 percent for $r_{\rm aper} = 400$ pix, which indicates that the larger aperture tends to contain pixels close to the edge of the masks likely to be contaminated by light from the masked objects. On the other hand, $\sigma_{\rm bg}$ marginally decreases with increasing aperture sizes. This may be because small scale fluctuations

of the sky residual are smoothed out by taking large apertures. Also, the contribution from the noise could be underestimated because pixel-to-pixel correlation is not taken into account. Therefore, we consider $\sigma_{\rm bg}$ as an upper limit of the fluctuation of local sky residual.

2.2.2 Stacked profiles of ETGs

In Figure 2.3, stacked profiles are shown for different spin parameters ($\lambda_{\rm e} \leq 0.15$, $0.15 < \lambda_{\rm e} \leq 0.3$ and $0.3 < \lambda_{\rm e}$) in four stellar mass bins. The radius is scaled at the half-light radius $r_{\rm h,25.0}$ (see below) and shown in the scale of $(r/r_{\rm h,25.0})^{1/4}$. The surface brightness is normalized at the surface brightness at $r_{\rm h,25.0}$. Faster rotators with larger $\lambda_{\rm e}$ tend to have lower surface brightness in outer regions ($(r/r_{\rm h,25.0})^{1/4} \gtrsim 1.2$). Although the lower surface brightness is also observed in the central regions ($(r/r_{\rm h,25.0})^{1/4} \lesssim 0.6$) in panels (a) to (c) in the upper row, the central region is likely to be affected by the PSF. The difference of the stacked light profile is large in outer regions even for round galaxies or massive galaxies. We quantify the difference using inner and outer slopes of light profiles in this study. We describe how the slopes are measured in the following sections.

2.2.3 Measuring inner and outer slopes

We measure the inner and outer slopes of light profiles as follows. We determine the scale length as the half-light radius $r_{\rm h,25.0}$ in r-band so that one half of the light integrated above the surface brightness of 25.0 mag arcsec^2 is included. Using the half-light radius is better than the effective radius $r_{\rm e}$ derived by fitting a single Sérsic model when the light profile of a galaxy is deviated from the model in which case $r_{\rm e}$ tend to be overestimated (e.g., Bernardi et al., 2014). We have checked that the derived half-light radius $r_{\rm h,25.0}$ agree well with that derived with independent method by Cappellari et al. (2013a).

The slopes are defined as the slope of linear functions which are fitted to radial profiles on the $(r/r_{\rm h,25.0})^{1/4} - \mu$ plane where μ is the surface brightness. The radial ranges in which the fitting is carried out are set to $0.7 \leq (r/r_{\rm h,25.0})^{1/4} \leq 1.0$ for the inner slope and $1.0 \leq (r/r_{\rm h,25.5})^{1/4} \leq 1.6$. We equally weight all of the data point in the intervals regardless of the signal-to-noise ratio during the fitting. As a result, the fitted slopes become close to the gradient of the light profile at the mid point of the intervals, i.e., $0.85 \times (r/r_{\rm h,25.0})^{1/4}$ for the inner and 1.3 for the outer slopes, respectively. We derive uncertainty of the slopes by Monte-Carlo simulations. We randomly resample the surface brightness level at each data point from the noise estimated from variance images, assuming

the Gaussian distribution. The one-sigma uncertainty is estimated by the standard deviation from 1000-time trials.

If the light profile of a galaxy follows pure Sérsic profile with the Sésic index of n, the light profile is expressed as

$$\mu(r) = \mu_{\rm e} + \frac{2.5}{\ln 10} b_n [(\frac{r}{r_{\rm e}})^{1/n} - 1] \quad (2.1)$$

$$= \mu_{\rm e} + \frac{2.5}{\ln 10} b_n [x^{4/n} - 1], \quad (2.2)$$

where $\mu_{\rm e}$ is the surface brightness at the effective radius r_e, b_n is a dimensionless scale factor depending on n (Ciotti & Bertin, 1999), and $x = (r/r_{\rm e})^{1/4}$. Therefore, the slope of the profile evaluated at a radius $x = x_{\rm a}$ is given as

$$\frac{\partial \mu}{\partial x}|_{x_{\rm a}} = \frac{2.5}{\ln 10} b_n \frac{4}{n} x_{\rm a}^{4/n}. \quad (2.3)$$

For example, for de Vaucouleurs ($n = 4$) profiles (de Vaucouleurs, 1948), the slope is always 8.33 regardless of radii. For smaller n than 4, the inner slope becomes shallower while the outer slope becomes steeper, and vice versa. We will use Equation 2.3 in Section 2.3, in order to derive the deviation of the slopes from pure Sérisic profiles for the ETG sample.

Setting the inner most radius to $r_{\rm in,0} = 0.7 \times (r/r_{\rm h,25.0})^{1/4}$ assures that the radial range for determining the inner slope is well outside the very central region where point spread function (PSF) may affect the measurement. In Figure 2.4, we show the histogram of $r_{\rm in,0}$. For most cases (163/166), $r_{\rm in,0}$ is greater than PSF FWHM (1.3 arcsec). Moreover, the mid point of the radial interval, $0.85 \times (r/r_{\rm h,25.0})^{1/4}$, is 2.2-times larger than $r_{\rm in,0}$ in the linear scale. Therefore, we consider that the effect of PSF on the inner slope should be small.

We note that the surface brightness at the outer most radius ($\mu_{r_{\rm out,1}}$) is not very faint. In Figure 2.5, we show the histogram of $\mu_{r_{\rm out,1}}$. The majority of the sample have the surface brightness of $\mu_{r_{\rm out,1}} \lesssim 26$ mag arcsec^{-2}. Only a few galaxies have low surface brightness at $r_{\rm out,1}$ reaching the level of $\sim$27 mag arcsec^{-2} where the sky subtraction uncertainty may affect light profiles. We investigate the effect of the sky subtraction uncertainty on the slopes later in the next section, and the effect is taken into account the uncertainty of the slopes.

2.2.3.1 Uncertainty of the Slopes

We then estimated uncertainty of the slopes in the following way. We subtract or add $\sigma_{\rm bg}$ evaluated with the 200-pixel apertures (see Section 2.2.1.3) from the radial profile, and then derived the inner and outer slopes. This aperture size of 200 pixel is close to the typical outer most radius (median $r_{\rm out,1} = 260$ pixels) of the radial range with which the outer slopes are derived. This chose is reasonable because the outer slopes are more likely to be affected by sky subtraction as they are derived in relatively faint regions. As uncertainty of the slopes, we take the largest value among the difference between those measured with $\sigma_{\rm bg}$-subtracted and original profiles, those with $\sigma_{\rm bg}$-subtracted and original, and uncertainty derived from readout and photon noises. For the inner slopes, the median uncertainty from $\sigma_{\rm bg}$ subtraction or addition is only slightly larger ($\sim$0.08 percent) than that from the noises ($\sim$0.06 percent). On the other hand, the median uncertainty of the outer slopes become $\sim$1 percent from the $\sigma_{\rm bg}$ which is much larger than that from the noises ($\sim$0.2 percent). Still, the uncertainty of the outer slopes derived from $\sigma_{\rm bg}$ subtraction or addition is not very large and the outer slopes are robustly measured. At a surface brightness level of 27.5 mag arcsec^{-2} which is the almost faintest brightness at the outer most radius ($r_{\rm out,1}$) used for evaluating the outer slopes (Figure 2.5), the difference of the surface brightness between $\sigma_{\rm bg}$-subtracted (or added) and original profile becomes as much as $\sim$ 0.5 mag arcsec^{-2} in the case of $\sigma_{\rm bg} = 7.3 \times 10^{-4}$ nMgy arcsec^{-2} (median, see Figure 2.2). Although this difference is not small, as the radial range in which the outer slopes are evaluated lies much closer to the center of a galaxy than the outer most radius ($r_{\rm out,1}$), the outer slope is not very sensitive to the edge of the interval. For example, the radius at the mid point of the interval, $1.3 \times (r/r_{\rm h,25.0})^{1/4}$, is 2.3-times smaller than $r_{\rm out,1}$ in the linear scale.

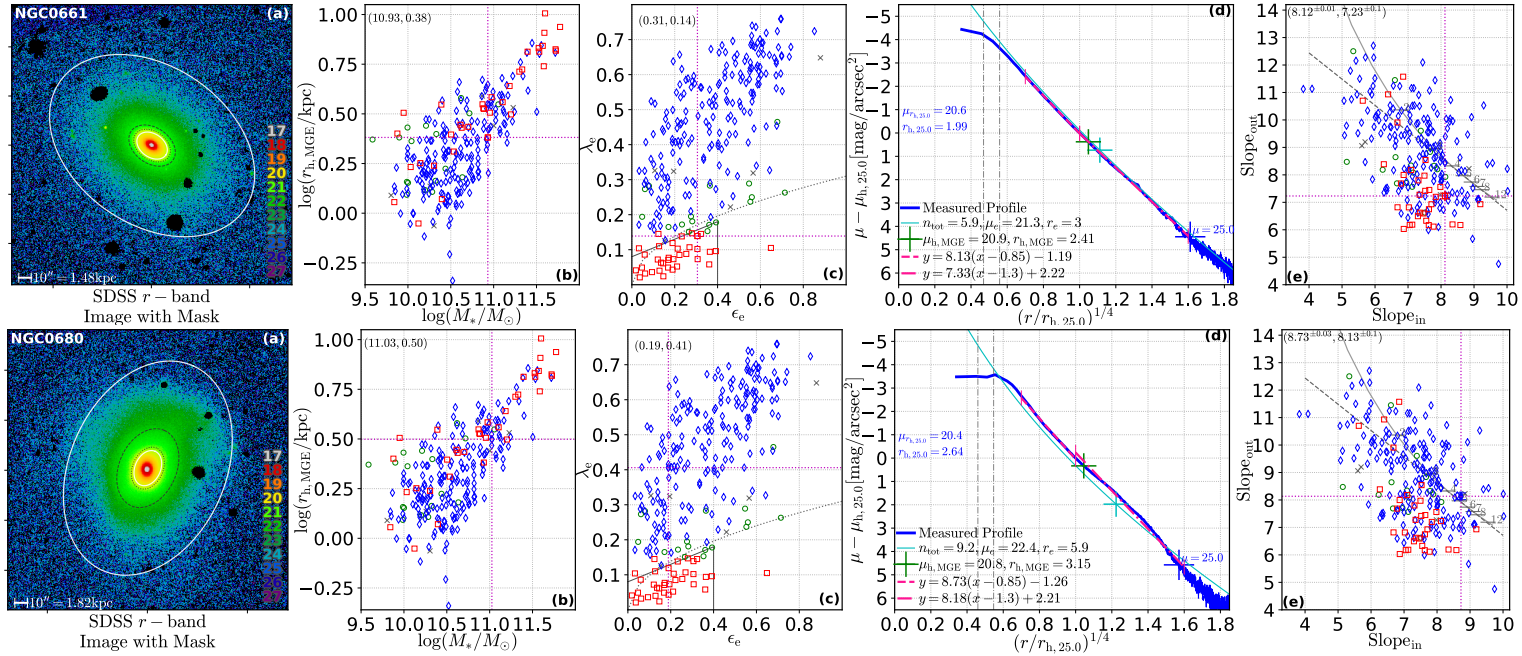

Figure 2.6 Examples of the light profile and inner and outer slopes with other properties. Top: NGC0661 (slow rotator). Bottom: NGC0680 (fast rotator). (a): SDSS r-band image (north-up and east-left). The bar in the lower left indicates 10 arcsec with corresponding physical scale. The brightness (mag arcsec^2) is shown by color noted in the bottom right. The while outer ellipse indicates the radius where the brightness reaches to 25.0 mag arcsec^2 while the inner indicates $r_{\rm h,25.0}$. The gray dashed ellipse indicates the effective radius measured by Sérsic fit in Krajnović et al. (2013) while dotted indicates the half-light radius ($r_{\rm h,MGE}$) measured by Cappellari et al. (2013b) using Multi-Gaussian Expansion (MGE). (b): Sizes ($r_{\rm h,MGE}$) and stellar masses of the sample ETGs. Colors correspond to kinematic properties (see text). Blue: regular rotators. Red: non regular slow rotators. Green: intermediate. Gray crosses: undefined. The locus of the target galaxy is indicated by the crossing point of magenta dotted lines with the values written in the upper left. (c): Ellipticity and $\lambda_{\rm e}$. Symbols are the same as in the panel (b). Gray dotted curve is the separation criteria in Emsellem et al. (2011) while gray solid lines in the bottom right indicates the criteria in (Cappellari, 2016). (d): Radial right profile measured from the SDSS r-band image (blue solid line). $r_{\rm h,25.0}$ (kpc) and surface brightness there (mag arcsec^2) are given in the panel. The blue large cross indicates the radius at which the surface brightness becomes 25.0 mag arcsec^2. Vertical gray dashed lines indicates the PSF radii, 0.65 and 1.3 arcsec. The cyan curve indicates the single Sérsic profile in Krajnović et al. (2013) with its parameters given in the legend. The Sérsic parameters, $r_{\rm e}$ and $\mu_{\rm e}$, are marked by cyan cross. The green cross indicates $r_{\rm h,MGE}$ with the value written in the legend. The fitting linear functions to derive inner and outer slopes are shown by magenta dashed and dash-dotted lines. The slope and intercept of the functions are written in the legend. (e): Inner and outer slopes of the sample ETGs. Symbols are the same as the panel (b). The gray curve indicates expected relation between the slopes for pure Sérsic profiles while the gray dashed line is the fitting linear function between $n = 4$ to 8 (see Section 2.3.2).

2.2.4 Example

In Figure 2.6, we show two examples of the measurement of inner and outer slopes with some other properties. One is a slow rotator, NGC0661 (upper panels) and the other is a fast rotator, NGC0680 (lower panels). Both galaxies have similar stellar mass and half-light radius as shown in panel (b) as well as similar ellipticity. In Krajnović et al. (2013), both of them are judged to be well fitted by a single component Sérsic profile rather than two component (bulge + disk). These galaxies are undistinguishable by usual photometric quantities such as ellipticity and Sérsic parameters. Using inner and outer slopes, the slow rotator is classified as extended, i.e., the shallower outer slope compared to the inner, while the other is classified as slightly truncated (panel (e)). For the panels (b), (c), and (d), other galaxies are also shown. We assign colors according to kinematical properties based on $\lambda_{\rm e}$ and k_5/k_1. The latter parameter indicates deviations in the velocity and velocity dispersion fields from ordered rotation evaluated using the kinemetry method (Krajnović et al., 2006, 2011). We classified the ETGs into three classes in these panels, regular rotators which have $k_5/k_1 < 0.07$, non regular rotators with $k_5/k_1 \geq 0.07$ and $\lambda_{\rm e} \leq 0.15$, and intermediate populations with $k_5/k_1 \geq 0.07$ and $\lambda_{\rm e} > 0.15$. The classification mostly consistent with the classification using ellipticity and $\lambda_{\rm e}$ given in Emsellem et al. (2011) and Cappellari (2016). The non regular rotators are located in the lower left region in the inner and outer slope plot which is panel (e).

2.3 Results

In this section, we present the relation between light profiles and kinematics.

2.3.1 Inner and outer slopes of light profiles

First, we present the inner and outer slopes of the light profile for ATLAS^{3D} slow ($\lambda_e \leq 0.3$) and fast ($\lambda_e > 0.3$) rotators in Figure 2.7. Most of slow rotators have smaller outer slope values compared to pure Sérsic profiles when compared at a fixed inner slope, which means their light profiles are more extended than Sérsic profiles. Among slow rotators, those with smallest λ_e (e.g., $\lambda_e < 0.05$) tend to have the most extended outer profiles. In contrast, fast rotators distribute evenly above (truncated) and below (extended) the pure Sérsic curves (dotted curves).

This trend holds even after we select galaxies with ellipticity $\epsilon_e \leq 0.4$. In Figure 2.8, the inner and outer slopes of ATLAS^{3D} galaxies with $\epsilon_e \leq 0.4$ are shown. While slow rotators occupy the region below the pure Sérsic curve, fast rotators distribute evenly above and below. Thus, the deviation of outer light profiles from Sérsic profiles carries independent information about kinematics from ellipticity. Later, we propose new method to discriminate slow and fast rotators using ellipticity and deviation of light profiles from Sérsic.

2.3.2 Deviation of light profile from Sérsic: ΔSlope

We evaluate the deviation of light profiles from Sérsic profiles in the following manner. First, we fit a linear function $f_{\rm out,Sersic}$ to the pure Sérsic curves (shown in Figures 2.7 and 2.8) for Sérsic index $4 \leq n \leq 8$. We obtain

$$f_{\rm out,Sersic} = -0.955(\mathrm{Slope_{in}} - 8.33) + 8.30. \tag{2.4}$$

The fitting results are shown by the dotted lines in the Figures 2.7 and 2.8. Second, we define the deviation ΔSlope as the difference between an outer slope and the fitting function at a inner slope,

$$\Delta\mathrm{Slope} = \mathrm{Slope_{out}} - f_{\rm out,Sersic}(\mathrm{Slope_{in}}). \tag{2.5}$$

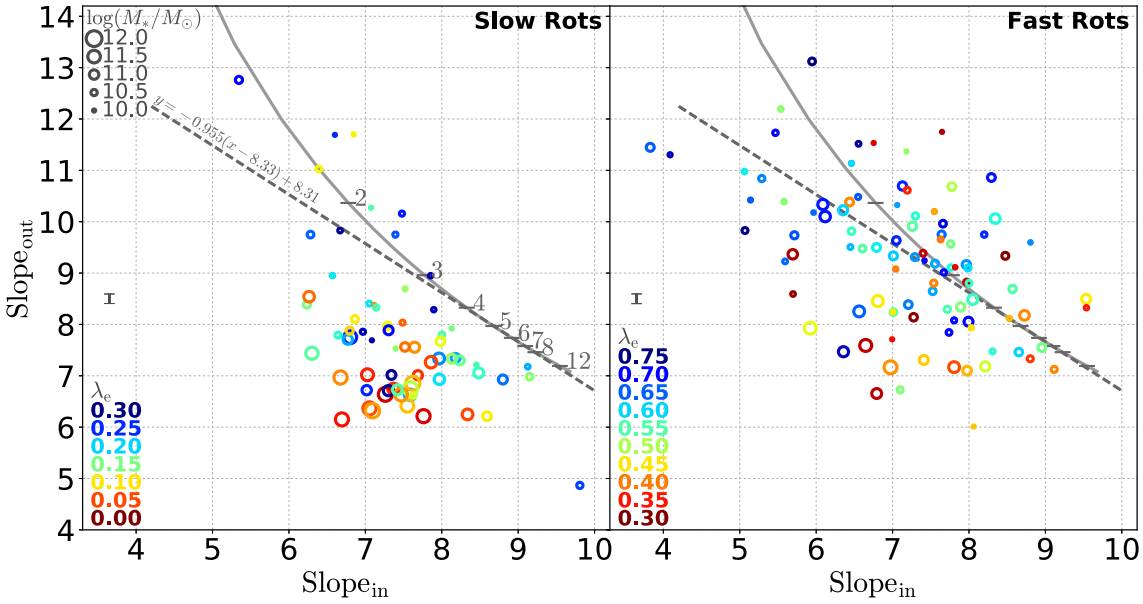

Figure 2.7 Inner and outer slopes of ATLAS^{3D} slow (left) and fast (right) rotators. Marker size corresponds to the stellar mass denoted on the top left of the left panel while color corresponds to the spin parameter λ as shown in the bottom left of each panel. Dotted curves indicate the slopes of pure Sérsic profiles with the Sérsic index n written in the panels while dotted straight lines are fits to the pure Sésic slopes in the range of $4 < n < 8$. Median uncertainties of the slopes are shown by error bars.

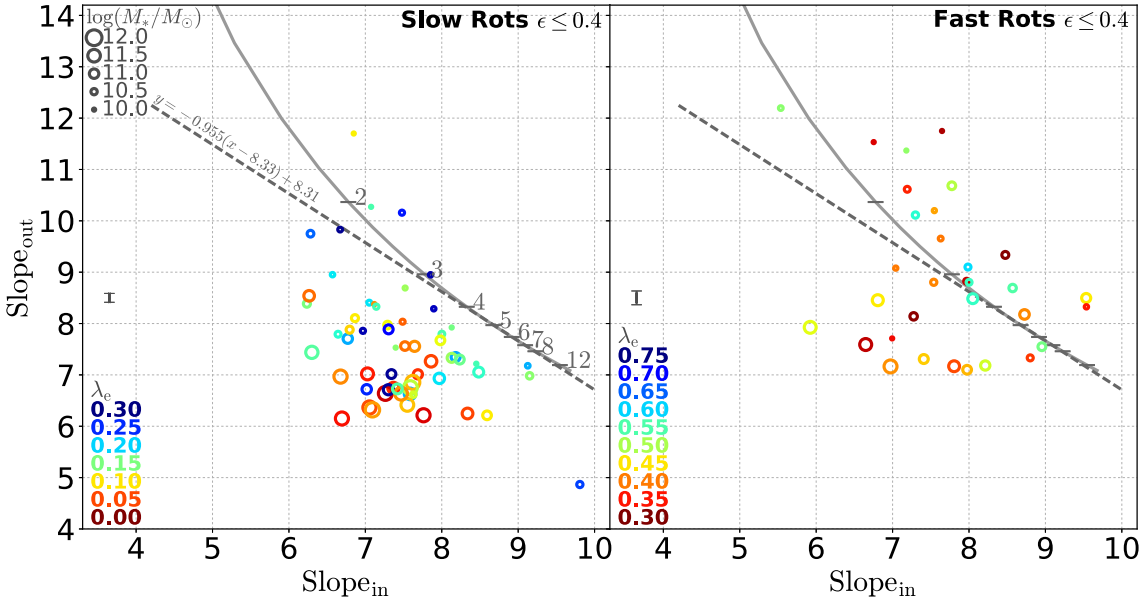

Figure 2.8 Same as Figure 2.7, but for round galaxies with $\epsilon \leq 0.4$.

Although the linear function deviates from the original pure Sérsic curve especially for $n < 2$, most of ETGs have $n > 2$ especially for round galaxies with $\epsilon \geq 0.4$. We will use both ellipticity and deviation of light profiles to isolate slow and fast rotators. Therefore, this definition of the deviation $\Delta\mathrm{Slope}$ is enough for the purpose. Compared at the same inner slope, i.e., the same concentration, ETGs with negative $\Delta\mathrm{Slope}$ have more extended outer profiles than pure Sérsic profile while those with positive $\Delta\mathrm{Slope}$ have more truncated profiles.

2.3.2.1 Relation between $\Delta\mathrm{Slope}$ and λ_e

In Figure 2.9, relation between the deviation $\Delta\mathrm{Slope}$ and spin parameter λ_e is shown. There is a global trend that ETGs with smaller $\Delta\mathrm{Slope}$ has smaller λ_e (slowly rotating). We carry out Spearman's rank correlation tests to investigate the significance because the scatter is large. Although the correlation coefficient $\rho_\mathrm{rank} = 0.49$ is not very large due to the scatter, the p-value, $p_\mathrm{rank} = 3.8 \times 10^{-11}$, is very small, which suggests there is a significant monotonic relation between the two parameters. The significant correlation remains even after we select galaxies with $\epsilon_\mathrm{e} \leq 0.4$. In this case, we get $\rho_\mathrm{rank} = 0.55$ with the p-value of 1.4×10^{-8}.

For round galaxies, the $\Delta\mathrm{Slope}$ parameter gives the smallest p-value (1.4×10^{-8}) among photometric parameters such as the total and bulge Sésic indices (n and n_bulge) and disk-to-total ratios (D/T). In Section 1.4.1, we have shown the relation between these parameters and λ_e in Figures 1.4 to 1.6 in which p-values are also shown. The p-values are 1.5×10^{-2}, 1.3×10^{-5}, and 2.5×10^{-3} for n, n_bulge, and D/T, respectively.

We fit a linear function to the relation between $\Delta\mathrm{Slope}$ and λ_e. We derive the linear function by minimizing the variance perpendicular to the function on the $\Delta\mathrm{Slope}$-λ_e diagram*. The uncertainty of the coefficients of the function is estimated from Monte-Carlo simulations. In the Monte-Carlo simulations, the $\Delta\mathrm{Slope}$ and λ_e values of each galaxy are resampled assuming Gaussian distribution. The Gaussian width for $\Delta\mathrm{Slope}$ is the measured uncertainty of each galaxy while that for λ_e is set to 0.05 for all galaxies. As mentioned in Emsellem et al. (2011), it is difficult to estimate the uncertainty of λ_e because the measurement of λ_e is affected by systematics. Note that the uncertainty of λ_e from noise in the data is smaller than ~ 0.02 (Emsellem et al., 2007). Since the uncertainty is not given in the table in Emsellem et al. (2011), we simply assign 0.05 following Emsellem et al. (2011) who carry

* This is similar to the method of primary component analysis (PCA) with two components.

out Monte-Carlo simulation with this value to derive the fraction of slow rotators classified with λ_e and ϵ_e. As a result, we obtain the linear function for all galaxies in our sample as

$$\lambda_{\rm e} = 0.16^{+0.01-0.02}\Delta{\rm Slope} + 0.48^{+0.01-0.07}, \tag{2.6}$$

where upper and lower limits are 16 and 84 percentile of the distribution of each coefficient in the Monte-Carlo simulation. Equation 2.6 indicates that ETGs whose profiles are consistent with Séric ($\Delta{\rm Slope} = 0$) rotates rapidly with $\lambda_{\rm e} \sim 0.5$. This is not surprising given that majority of ETGs are fast rotators (Emsellem et al., 2011) and that light profiles of ETGs can be largely expressed by Séric. Note that median ΔSlope0 of fast rotators is ~ 0 for majority ($\log(M_*/M_\odot) < 11$). The physical origin of the fact that ETGs with $\Delta{\rm Slope} = 0$ have $\lambda_{\rm e} \sim 0.5$ is not clear (see discussion in Section 4.1 for possible formation mechanisms for light profiles and kinematics).

We also fit a linear function for round galaxies ($\epsilon_{\rm e} \leq 0.4$). We obtain

$$\lambda_{\rm e} = 0.13^{+0.01-0.01}\Delta{\rm Slope} + 0.38^{+0.01-0.01}. \tag{2.7}$$

The round galaxies have shallower slope and smaller intercept. This reflects the fact that highly flattened objects have relatively larger λ_e compared at the same ΔSlope. In fact, galaxies with small ellipticity ($\epsilon \gtrsim 0.6$) tend to have larger ΔSlope than the best-fit relation in Figure 2.7. The measurement of the slopes may be affected edge-on projection.

We also evaluate the intrinsic scatter of the relation between ΔSlope and $\lambda_{\rm e}$. The apparent standard deviation of the offset of $\lambda_{\rm e}$ from the fitted function is 0.26 and 0.16 for all and round galaxies, respectively. We quadratically subtract the uncertainty of $\lambda_{\rm e}$ (i.e., 0.05) and the median uncertainty of ΔSlope. The intrinsic scatter becomes 0.25 and 0.15 for all and round galaxies, respectively, which indicates the intrinsic scatter dominates the apparent standard deviation. Thus, $\lambda_{\rm e}$ could be predicted from ΔSlope with an accuracy 0.16 for ETGs with $\epsilon_{\rm e} \leq 0.4$. The accuracy is not very high but at least ΔSlope can be used as a proxy for the dynamical properties such as λ_e of ETGs.

2.3.2.2 Relation between ΔSlope and V/σ

We also carry out similar analysis using the traditional spin parameter V/σ instead of $\lambda_{\rm e}$. In Figure 2.10, V/σ is plotted as a function of ΔSlope. The similar trend can be found that ETGs with smaller

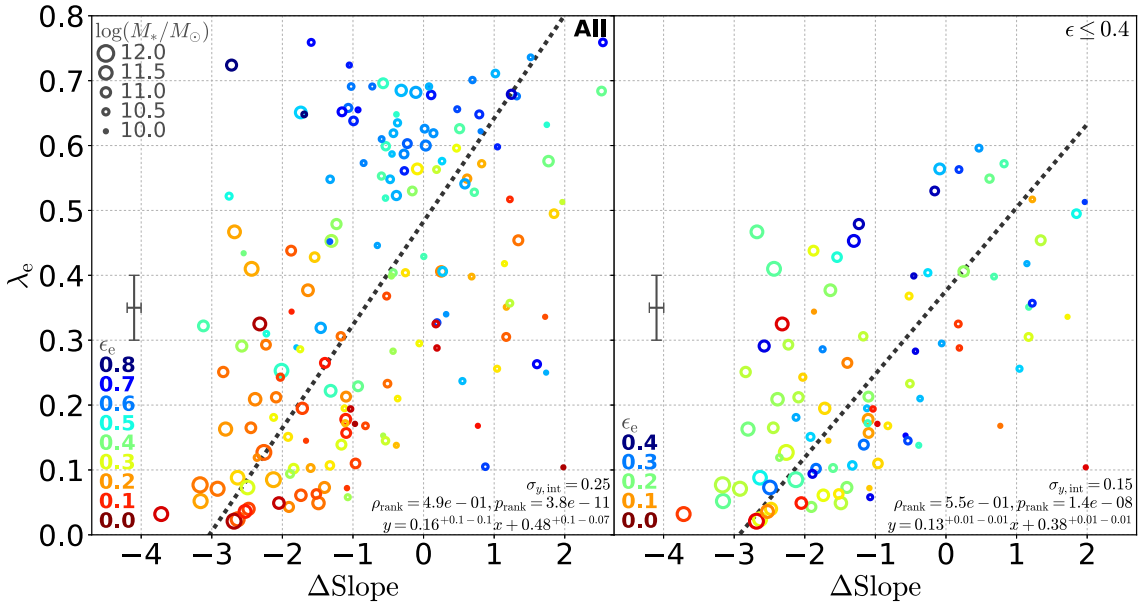

Figure 2.9 Deviation of the slopes (ΔSlope) and spin parameter (λ_e) of ATLAS^{3D} ETGs. Left panel includes all sample galaxies while right is only for round objects with $\epsilon_e \leq 0.4$. Marker size corresponds to the stellar mass while color corresponds to ellipticity ϵ_e. Median uncertainties of ΔSlope and assumed uncertainty of λ_e (see text) are shown by error bars. Spearman's rank correlation efficiency ρ_{rank} and p-value (p_{rank}) are shown in the bottom right of the panels. Dotted line indicates the fitted linear function (see text) whose coefficients are given in the lower right in each panel. Intrinsic scatter from the relation along y-axis is also shown in the lower right in each panel.

ΔSlope have smaller V/σ (slowly rotating). The correlation of the two parameter is significant. The Spearman's rank correlation coefficient is $\rho_{\rm rank} = 0.46$ with the p-value of $p_{\rm rank} = 5.6 \times 10^{-10}$ for all galaxies while it becomes $\rho_{\rm rank} = 0.53$ with the $p_{\rm rank} = 6.1 \times 10^{-8}$.

We fit a linear function to the relation in the same manner as for $\lambda_{\rm e}$. In this case too, we assign 0.05 to the uncertainty of V/σ as it takes the similar value to $\lambda_{\rm e}$ ($\sim$ 0 to 1). We obtain the function for all galaxies

$$\lambda_{\rm e} = 0.18^{+0.2-0.1}\Delta{\rm Slope} + 0.53^{+0.1-0.09}, \tag{2.8}$$

and for round galaxies, we have

$$\lambda_{\rm e} = 0.122^{+0.01-0.009}\Delta{\rm Slope} + 0.39^{+0.01-0.01}. \tag{2.9}$$

The intrinsic scatter is also evaluated. The apparent standard deviation of the offset of V/σ from the fitted function is 0.3 and 0.16 for all and round galaxies, respectively. By quadratically subtracting the contribution of the uncertainty of the two parameters, the intrinsic scatter becomes 0.3 and 0.16 all and round galaxies, respectively.

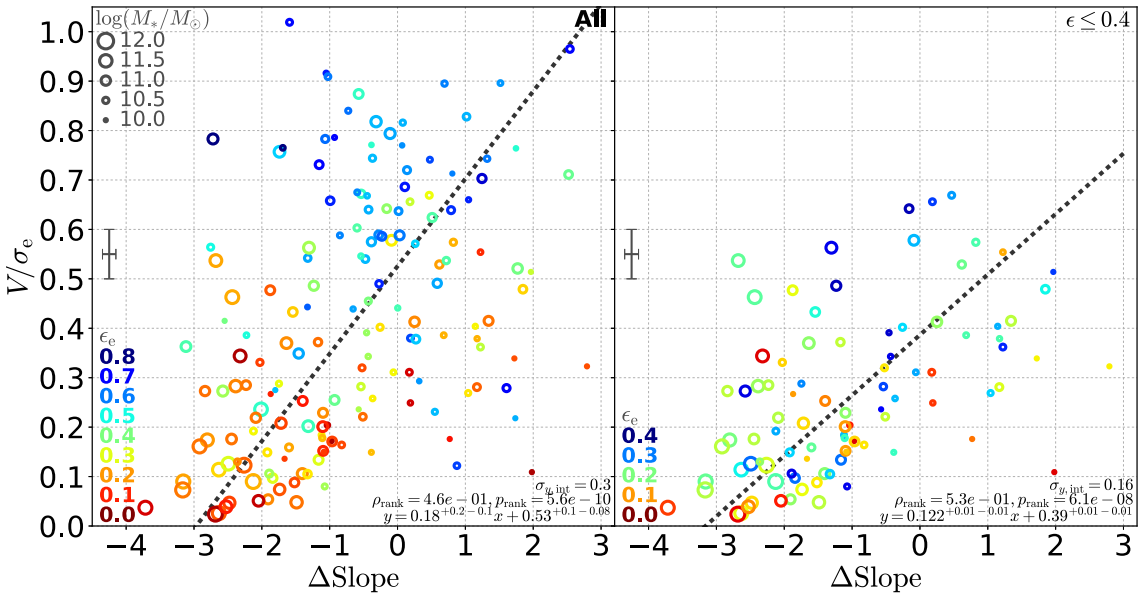

Figure 2.10 Same as Figure 2.9 but for V/σ instead of $\lambda_{\rm e}$.

2.3.3 ΔSlope depending on mass

Many properties of galaxies such as ellipticity, Sérsic index, and spin parameter are correlated with stellar masses of galaxies. The deviation of light profiles ΔSlope also correlates with mass as shown in Figure 2.11. We take running median of ΔSlope with the bin width of ± 0.25. For slow rotators, median ΔSlope monotonically decreases with increasing stellar masses. The Spearman's rank correlation test gives the correlation coefficient $\rho_{\rm rank} = -0.73$ with a small p-value of 1.1×10^{-13}. For fast rotators, median ΔSlope stays zero for $\log(M_*/M_\odot) < 11.0$ and decreases with increasing stellar masses above this stellar mass. The correlation between ΔSlope and stellar mass is not significant. The p-value of the rank correlation test is not small (0.019).

For galaxies with $\log(M_*/M_\odot) < 11.5$, slow rotators tend to have smaller ΔSlope compared than fast rotators at a fixed stellar mass. Thus, correlation between ΔSlope and $\lambda_{\rm e}$ (and V/σ) is not a false correlation via stellar masses. We note that for the most massive galaxies ($\log(M_*/M_\odot) > 11.5$) we do not have enough large number of fast rotator to examine the difference of ΔSlope between slow and fast rotators at a fixed stellar mass. The results above do not significantly change if we select round objects with the ellipticity $\epsilon_{\rm e} \leq 0.4$ as shown in Figure 2.12.

2.3.4 Photometric classification of slow and fast rotators

We propose a new criterion to classify ***photometric*** slow and fast rotators with the ellipticity and ΔSlope. The ellipticity shows strong correlation to the spin parameter. The correlation efficiency and p-value of the rank correlation test is $\rho_{\rm rank} = 0.66$ and $p_{\rm rank} = 3.6 \times 10^{-34}$ (see Figure 1.2). After selecting round objects as candidates of slow rotators as they are basically round with $\epsilon \leq 0.4$, ΔSlope is the most significantly correlated with $\lambda_{\rm e}$ compared to other photometric parameters such as Séric parameters (see right panels in Figures 1.4 through 1.8). Therefore, we define ***photometric*** slow rotators as those satisfy

$$\epsilon_{\rm e} \leq \epsilon_{\rm crit} \text{ and } \Delta\text{Slope} \leq \Delta\text{Slope}_{\rm crit}, \tag{2.10}$$

while ***photometric*** fast rotators are selected as remaining others.

In Figure 2.13, completeness and contamination of the ***photometric*** slow and fast rotators are shown as a function of $\Delta\text{Slope}_{\rm crit}$ with different $\epsilon_{\rm crit}$. Here, the completeness for slow (or fast) rotators

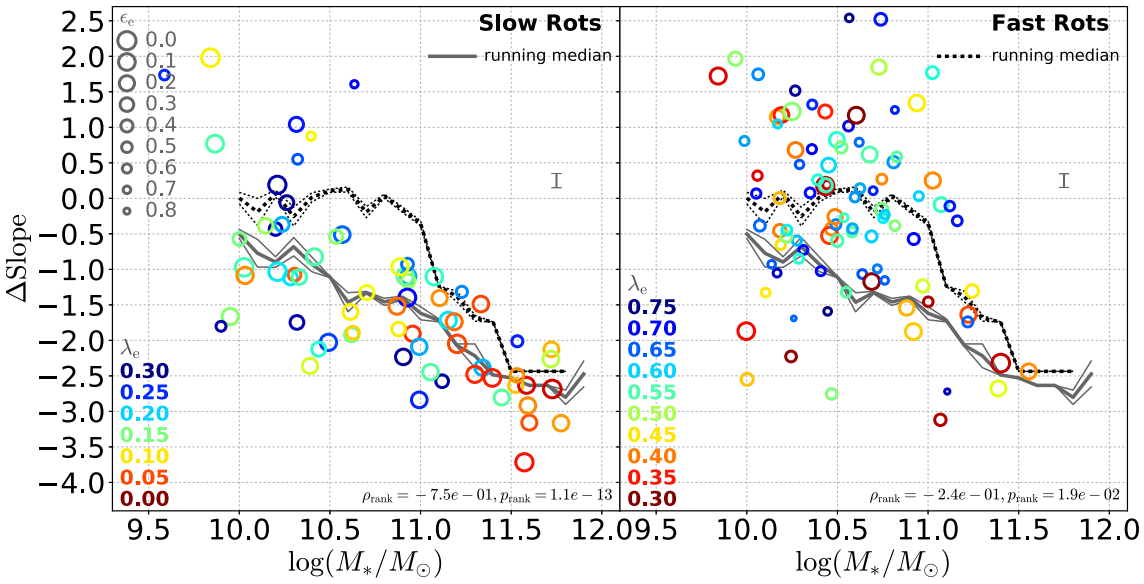

Figure 2.11 ΔSlope as a function of stellar mass. Left panel is for slow rotators ($\lambda_e \leq 0.3$) while right is for fast rotators ($\lambda_e > 0.3$). Maker size corresponds to ellipticity as shown in the top left of the left panel and color corresponds to the spin parameter. We take running median with the bin width of ± 0.25 which is shown by gray solid curves for slow rotators and by black dotted curves for fast rotators. The one-sigma uncertainty of the running median is evaluated by 1000-times bootstrap resampling and shown in the panels.

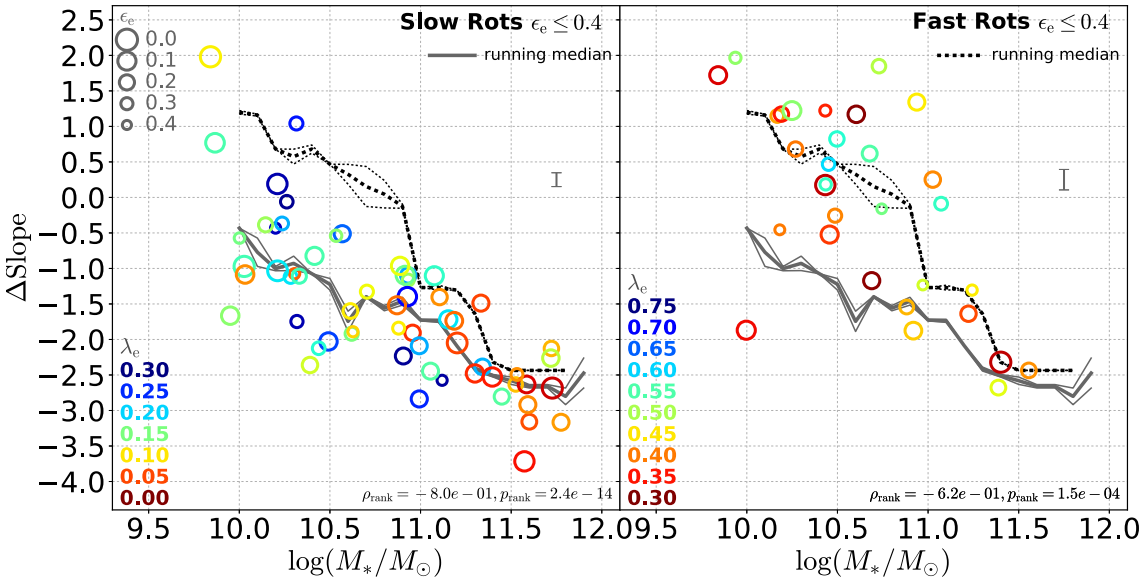

Figure 2.12 Same as Figure 2.11, but for round objects with $\epsilon_e \leq 0.4$.

is given by the fraction of kinematic slow (or fast) rotators included in ***photometric*** slow (or fast) rotators. The contamination is given by the fraction of kinematic fast (or slow) rotators included in ***photometric*** slow (or fast) rotators. From Figure 2.13, $\epsilon_{\rm crit} = 0.4$ can maximize the completeness of both slow and fast rotators with the completeness of ~ 0.83 at $\Delta{\rm Slope}_{\rm crit} \sim 0.1$. $\epsilon_{\rm crit} = 0.4$ can also minimize the contamination with the contamination of ~ 0.18 with $\Delta{\rm Slope}_{\rm crit} \sim -0.8$. The ellipticity limit $\epsilon_{\rm crit} = 0.4$ is consistent with the fact that almost all of slow rotators have $\epsilon_e < 0.4$ (Emsellem et al., 2011, Cappellari, 2016)

The best choice for $\Delta{\rm Slope}_{\rm crit}$ depends on whether one would like to maximize the completeness ($\Delta{\rm Slope}_{\rm crit} \sim 0.1$) or to minimize the contamination ($\Delta{\rm Slope}_{\rm crit} \sim -0.8$). For example, if we simply take $\epsilon_{\rm crit} = 0.4$ and $\Delta{\rm Slope}_{\rm crit} = 0$, the completeness and contamination of the ***photometric*** slow rotators become 0.84 and 0.22, whereas those of the fast rotators become 0.83 and 0.13. Our selection criteria is better than previously proposed ***photometric*** parameter criterion. For example, Krajnović et al. (2013) propose to select fast rotators by disk-to-total light ratio $D/T > 0.5$ and total Sésic index $n < 3$ for $D/T \leq 0.05$, and slow rotators as remaining. Although this selection gives very high completeness for fast rotators (0.89), the contamination for fast rotators is as high as 0.29 and slow-rotator completeness is only 0.4 with the contamination of 0.29. Thus, our selection criteria are better for lower contamination for the fast rotators, higher slow-rotator completeness, and lower slow-rotator contamination. In addition, our criteria use parameters which are relatively easy to measure. $\Delta{\rm Slope}_{\rm crit}$ can be measured from light profiles without applying complicated processes such as Sérisic profile fit and bulge-disk decomposition.

2.3.5 Kinematic Classes of ETGs on the $\epsilon_{\rm e}$-ΔSlope Diagram

We investigate kinematic properties of ***photometric*** slow and fast rotators selected by $\epsilon_{\rm e}$ and $\Delta{\rm Slope}$. In Figure 2.14, we show $\epsilon_{\rm e}$ and $\Delta{\rm Slope}$ of the ETGs. We replace λ by $\Delta{\rm Slope}$ of the ϵ-λ with which slow and fast rotators are classifies based on IFU data. The panel (a) is essentially the same as Figure 2.9 but plotted in different projection. Clearly slowly rotating ETGs are clustering in the bottom-left region ($\Delta{\rm Slope} < 0, \epsilon_{\rm e} < 0$). In the panel (b), the color indicates $k_5\bar{/}k_1$ which represents deviations of velocity fields from ordered rotation (Krajnović et al., 2006, 2011). While non-regular rotators (slow rotators with large deviations) are clustering in the bottom-left region, slowly rotating ETGs but whose velocity fields are consistent with regular rotation are also residing in the region and most of

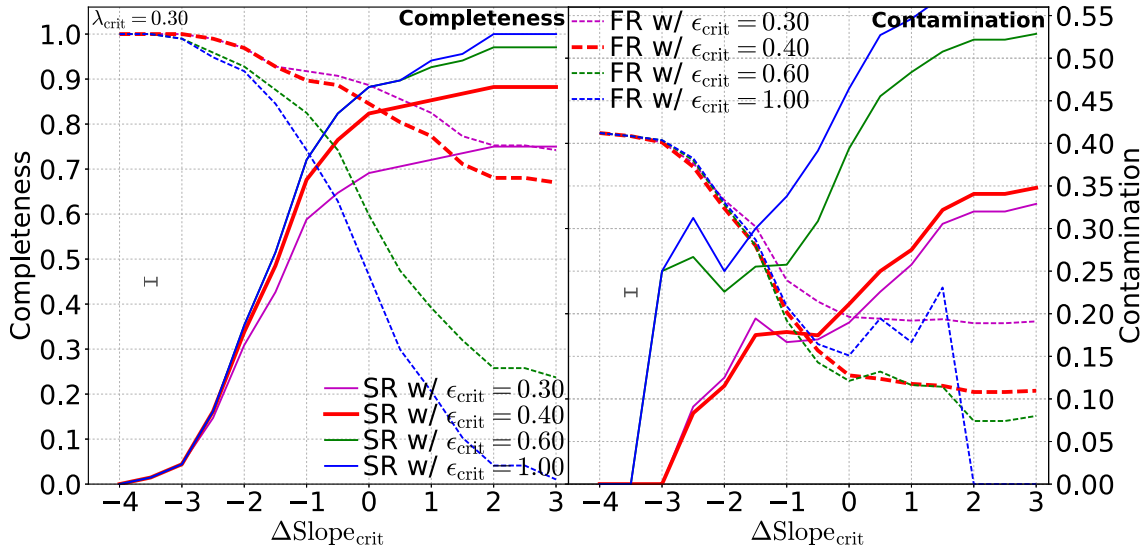

Figure 2.13 Completeness (left) and contamination (right) of slow (slid curves) and fast (dashed curves) rotators as a function of critical ΔSlope ($\Delta{\rm Slope}_{\rm crit}$; x-axis) with different ellipticity threshold ($\epsilon_{\rm crit}$; color-coded). Completeness is given by the fraction of kinematic slow (or fast) rotators included in the ***photometric*** slow (or fast) rotators while contamination is given by the fraction of kinematic fast (or slow) rotators included in the ***photometric*** slow (or fast) rotators. The ***photometric*** slow rotators are selected by the criterion $\epsilon \leq \epsilon_{\rm crit}$ and $\Delta{\rm Slope} \leq \Delta{\rm Slope}_{\rm crit}$ (x-axis), and the fast rotators are remaining. Here, kinematic slow rotators are galaxies with $\lambda_{\rm e} \leq 0.3$ and fast rotators are those having $\lambda_{\rm e} > 0.3$.

them are massive.

The situation may become more clear when we see the kinematic classes in the diagram. Krajnović et al. (2011) classified ATLAS^{3D} ETGs into five groups based on key features in velocity and velocity dispersion fields. Slow rotators are classified into three groups, a, b, and c. Galaxies in the group a are non-rotators with no apparent rotation, those in the group b are non-regular rotators with irregular velocity pattern but without any specific kinematic feature, and those in the group c have kinematically distinct cores (KDC) or counter-rotating cores. These groups are shown in the panel (c) Figure 2.14. While group c galaxies spread in the $\Delta\mathrm{Slope} < 0$ and $\epsilon_\mathrm{e} < 0$, group a galaxies tend to be the most extended and round ($\Delta\mathrm{Slope} \lesssim -2.5$ and $\epsilon_\mathrm{e} \lesssim 0.1$). Galaxies in the group b seem to have moderate values of $\Delta\mathrm{Slope} \sim$ -2.5 to -1.5.

Fast rotators are classified into two groups, d and e. Galaxies in the group d is so-called $2-\sigma$ galaxies whose velocity dispersion field shows apparent double peaks offset from the galaxy center. The feature is interpreted as systems which have two counter-rotating flattened stellar disks. Since they are highly flattened and most of them have $\epsilon > 0.4$, they are rarely classified into ***photometric*** slow rotators, Group e galaxies are regular rotators whose rotation axis is almost aligned to photometric semi-major axis. These groups are shown in the panel (d) in Figure 2.14. Galaxies selected as ***photometric*** slow rotators are groups a, b, c, and e. As group e galaxies are regular rotators, the ***photometric*** slow rotators are contaminated by face-on rotators.

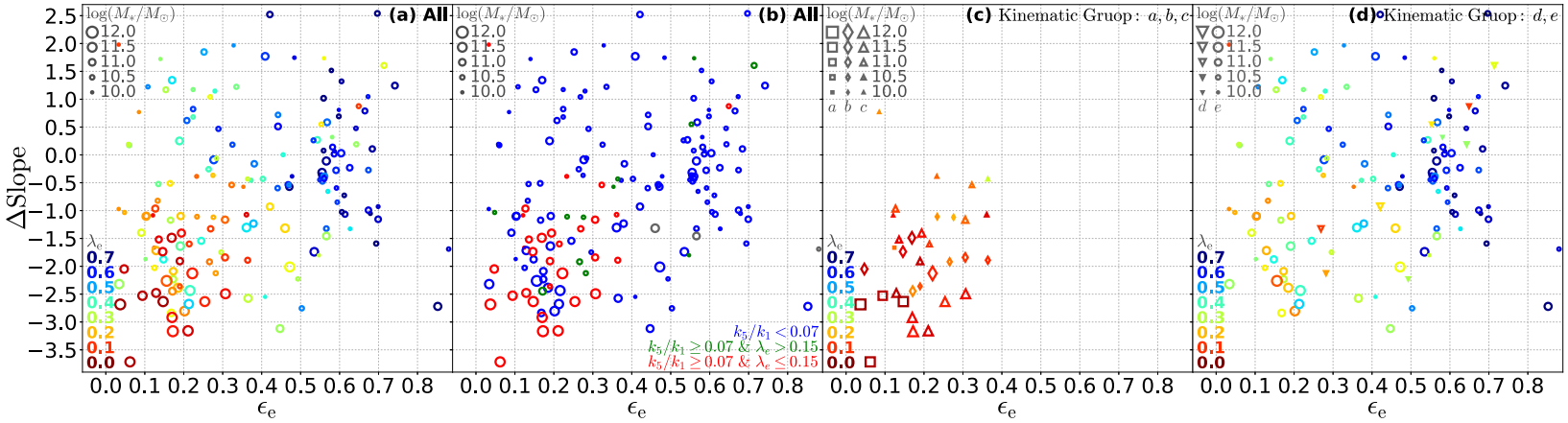

Figure 2.14 ΔSlope and ϵ distribution of the ETG sample. (a): Color code represents for λ_e while maker sizes corresponds to the stellar mass. (b): Colors indicate kinematic properties (Krajnović et al., 2011). Blue is assigned to regular rotators, red to non regular rotators, green to intermediate, and gray to undefined. (c): ETGs included in the kinematic groups (see text) a (squares), b (diamonds), and c (triangles). Color code and marker size are the same as in panel (a). (d): Those included in the groups d, and e with the same color code and marker sizes as panel (a).

2.4 Discussion

In the previous section, we see that kinematic properties of ETGs are correlated with outer light profile. While most of slowly rotating galaxies have more extended envelope than pure Sérsic profile, large fraction of fast rotators have consistent or truncated profile with Sésic.

It is well known that the most massive ($\log(M_*/M_\odot \gtrsim 11)$) ETGs are dispersion dominated while less massive galaxies are supported by rotation. The deviation of outer light profile from Sésic ($\Delta\mathrm{Slope}$) is also correlated with stellar mass (Fig. 2.11). However, slow rotators have smaller $\Delta\mathrm{Slope}$ (i.e., extended outer profiles) than fast rotators compared at a fixed stellar mass. We provide possible interpretation about the correlation between $\Delta\mathrm{Slope}$ and kinematics in this section.

2.4.1 Which slope matters?

First, we investigate which slope, inner or outer, contributes to the correlation between $\Delta\mathrm{Slope}$ and λ_e presented in Figure 2.9. In Figure 2.15, we plot λ_e against the inner and outer slopes. Between the inner slope and λ_e, the Spearman's rank correlation test reveals no significant correlation. Although the p-value is not so large for all galaxies ($p_\mathrm{rank} = 0.04$, panel (a)) and the parameters may be marginally correlated ($\sim 2\sigma$), that for round galaxies is large ($p_\mathrm{rank} = 0.18$, panel (b)).

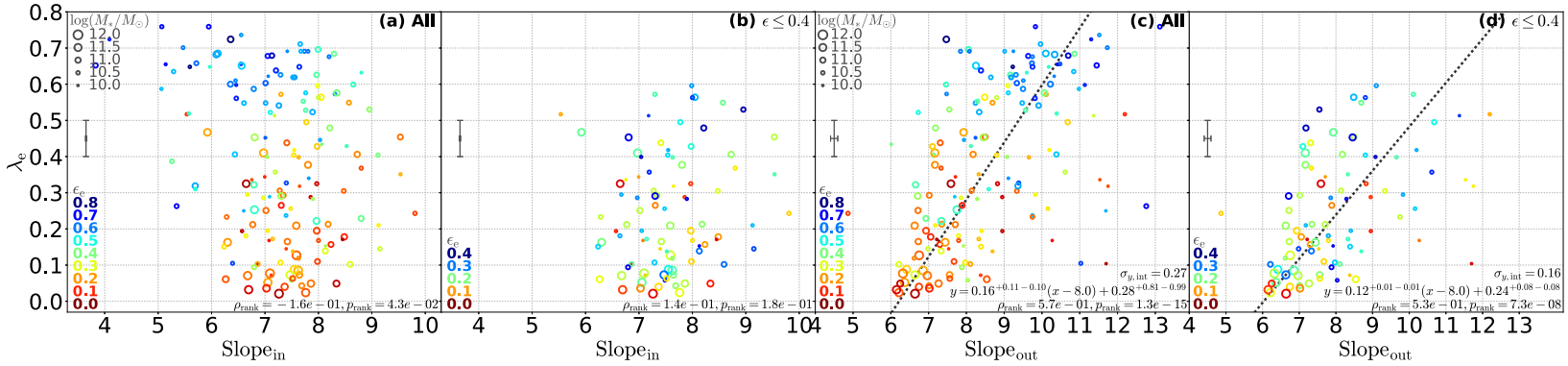

Figure 2.15 λ_e plotted as a function of the inner slope for all (a) and round galaxies (b) as well as plotted as a function of the outer slope for all (c) and round galaxies (d). Symbols are the same as in Figure 2.9. In panels (a) and (b), only median uncertainty of the inner slope is shown by error bars, and linear function fitting is not carried out because there is no significant correlation between the inner slope and λ_e.

On the other hand, the outer slope and $\lambda_{\rm e}$ have significant correlation with the p-value of $p_{\rm rank} = 1.3\times10^{-15}$ for all (panel (c)) and $p_{\rm rank} = 7.3\times10^{-8}$ for round objects (panel (d)). Thus, we conclude that the deviation of light profiles in the outer region is related to galaxy kinematics. We obtain an approximated linear relation between the two parameters as well as the intrinsic scatter in a similar manner done in Section 2.3.2.1. The linear relation becomes

$$\lambda_{\rm e} = 0.15^{+0.01-0.02}({\rm Slope}_{\rm out} - 8.0) + 0.28^{+0.81-0.99}, \tag{2.11}$$

for all galaxies, and

$$\lambda_{\rm e} = 0.12^{+0.01-0.01}({\rm Slope}_{\rm out} - 8.0) + 0.24^{+0.08-0.08}, \tag{2.12}$$

where ${\rm Slope}_{\rm out}$ is the outer slope. The intrinsic scatter becomes 0.27 and 0.16 for all and round objects, respectively.

Although the outer slope is correlated with $\lambda_{\rm e}$, $\Delta{\rm Slope}$ provides better results when we try to isolate slow and fast rotator using the parameter. Figure 2.16 is a completeness-contamination plot similar to Figure 2.13. This time, however, we use the criterion, $\epsilon_{\rm e} \leq \epsilon_{\rm crit}$ and ${\rm Slope}_{\rm out} \leq {\rm Slope}_{\rm out,crit}$, instead of the original one in Equation 2.10. The maximum completeness of ~ 0.79 is achieved at ${\rm Slope}_{\rm out,crit} \sim 8.8$ with $\epsilon_{\rm crit} = 0.4$. This is slightly smaller than that obtained with the original criterion (0.83). On the other hand, the minimum contamination becomes ~ 0.19 at ${\rm Slope}_{\rm out,crit} \sim 8.1$ with $\epsilon_{\rm crit} = 0.4$, which is larger than the original value of 0.13.

2.4.2 ΔSlope and other structural parameters

Next, we investigate relation between $\Delta{\rm Slope}$ and these structural parameters such as Sérsic index. We also compare our criterion for separating ***photometric*** slow and fast rotators and that given in the previous study (Krajnović et al., 2013).

In Figure 2.17, total Sésic index ($n_{\rm tot}$) is shown as a function of $\Delta{\rm Slope}$. There is significant correlation between the two parameters except for the case where only galaxies with small disk-to-total ratio and ellipticity are selected (panel (d)). The Spearman's rank correlation efficiency and p-value are given in the panels. From the panel (a) in Figure 2.17, we confirm that slower rotators have on average greater $n_{\rm tot}$ than faster ones. However, there are large number of fast rotators (e.g.,

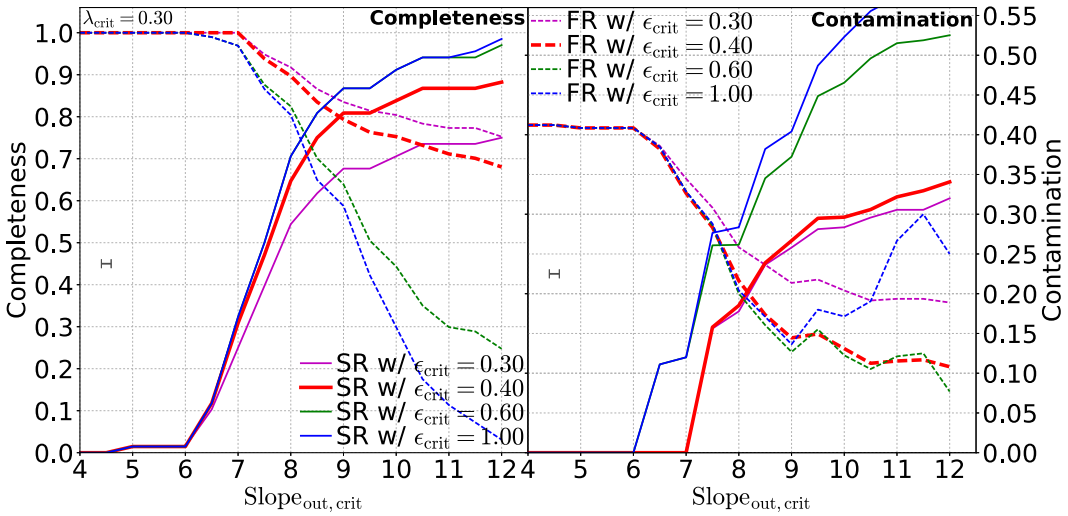

Figure 2.16 Completeness (left) and contamination (right) of slow (slid curves) and fast (dashed curves) rotators as a function of critical outer slope ($\rm Slope_{out,crit}$; x-axis) with different critical ellipticity ($\epsilon_{\rm crit}$; color-coded) similarly to Figure 2.13.

$\lambda_{\rm e} \gtrsim 0.5$) that have $n_{\rm tot} \gtrsim 2-3$. The situation is the same in the panel (b) where round galaxies ($\epsilon \leq 0.4$) are plotted. Basically, the round galaxies have $n_{\rm tot} \gtrsim 2$.

The panel in Figure 2.17 indicates close connection between our classification criterion for ***photometric*** slow/fast rotators and those given in Krajnović et al. (2013). For galaxies with small disk-to-total ratio $D/T < 0.05$, Krajnović et al. (2013) suggest a criterion, $n_{\rm tot} < 3$, for selecting fast rotators. The panel (c) clearly shows their criterion efficiently selects fast rotators. The difference of ours and Krajnović et al. (2013) is that we use $\epsilon_{\rm e}$ instead of $n_{\rm tot}$. However, for round galaxies with $D/T < 0.05$ (panel (d) in Figure 2.17), our criterion $\Delta{\rm Slope} > 0$ can efficiently select fast rotators (e.g., $\lambda_{\rm e} \gtrsim 0.3$) with only small contamination (1/7) from slower rotators. If we select galaxies with $n_{\rm tot} < 3$ in the panel (d), the contamination fraction become larger. This is one reason why our criterion works better than that of Krajnović et al. (2013) in terms of lower contamination for slow and fast rotators and higher completeness for slow rotators.

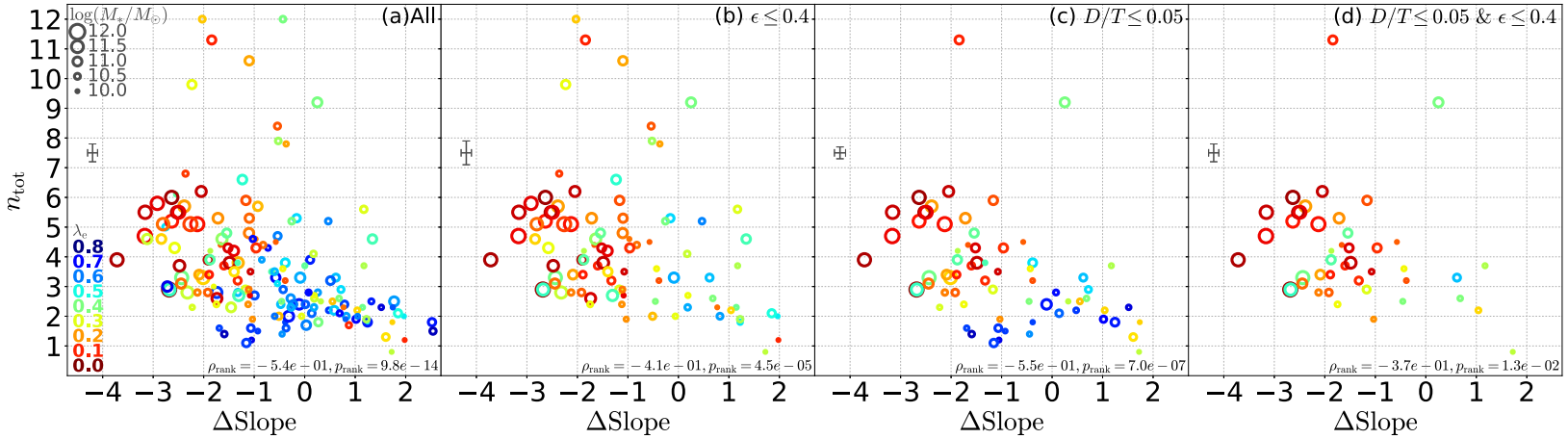

Figure 2.17 Total Sérsic index $n_{\rm tot}$ as a function of ΔSlope for all ETGs (a), ETGs with $\epsilon_e \leq 0.4$ (b), $D/T \leq 0.05$ (c), and $D/T \leq 0.05$ and $\epsilon_e \leq 0.4$ (d). Error bars indicate the median uncertainty. Marker size corresponds to the stellar mass denoted on the top left of the left panel while color corresponds to the spin parameter λ as shown in the bottom left of the left panel. Spearman's rank correlation efficiency $\rho_{\rm rank}$ and p-value ($p_{\rm rank}$) are shown in the bottom right of each panel.

In Figure 2.18, disk-to-total ratio is plotted against ΔSlope for the galaxies requiring bulge-disk decomposition ($D/T > 0$; see Krajnović et al., 2013, for detail). The Spearman's rank correlation test indicates significant correlation between these parameters only if all galaxies are used (left panel). This figure highlights another reason why our selection criterion achieves lower contamination for slow and fast rotators as well as higher completeness for slow rotators than that given in Krajnović et al. (2013). As can be seen in the figure, there are significant amount of slowly rotating galaxies having quite large disk-to-total ratios $D/T \gtrsim 0.5$, although $D/T \gtrsim 0.7$ is dominated by fast rotators. Using ΔSlope gives better solution for separating slow and fast rotators than D/T for galaxies requiring bulge-disk decomposition.

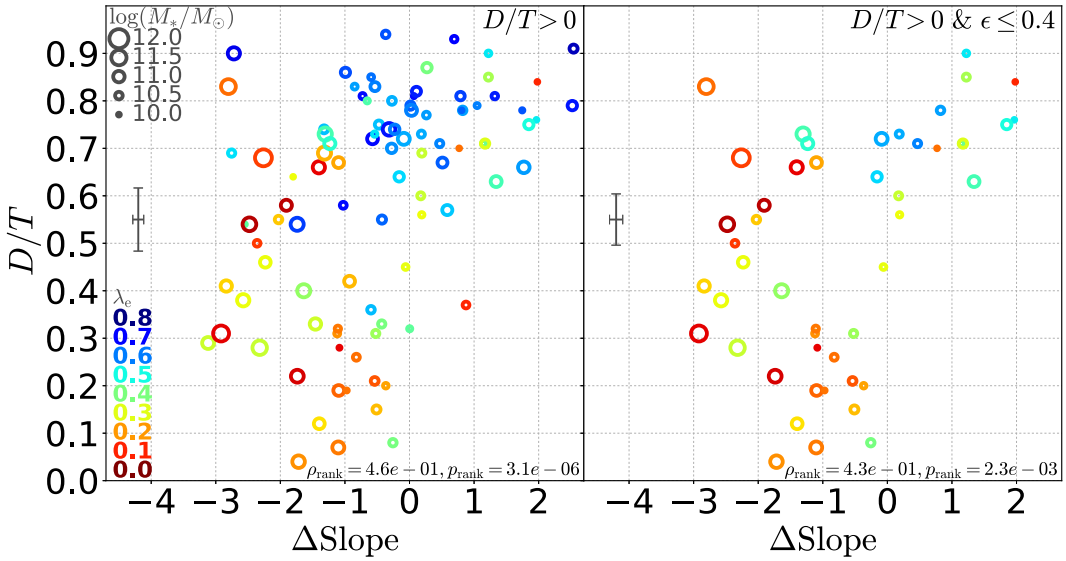

Figure 2.18 Disk-to-total ratio D/T as a function of ΔSlope for the galaxies with $D/T > 0$ (left) and for those with $D/T > 0$ and $\epsilon_e \leq 0.4$. Symbols are the same as Figure 2.17.

Figure 2.19 shows the relation between the bulge Sérsic index ($n_{\rm bulge}$) and ΔSlope for galaxies with $D/T > 0$. Significant correlation is found between the parameters from the Spearman's rank correlation test even after round galaxies are selected. The bulge Sérsic index is highly correlated with λ_e, which is already shown by Krajnović et al. (2013). The correlation remains for round galaxies. Even after applying our selection criterion for slow rotators ($\epsilon_e \leq 0.4$ and ΔSlope < 0), we can ged rid of five fast rotators with $\lambda_e > 0.3$ by excluding galaxies having $n_{\rm bulge} < 1.5$ although one slow rotator is discarded. If we apply this additional selection criterion with $n_{\rm bulge}$, we would get smaller contamination for ***photometric*** slow rotators and higher completeness for fast rotators. The

completeness and contamination of ***photometric*** slow rotators would be 0.81 and 0.15 while those of fast rotators would be 0.89 and 0.13.

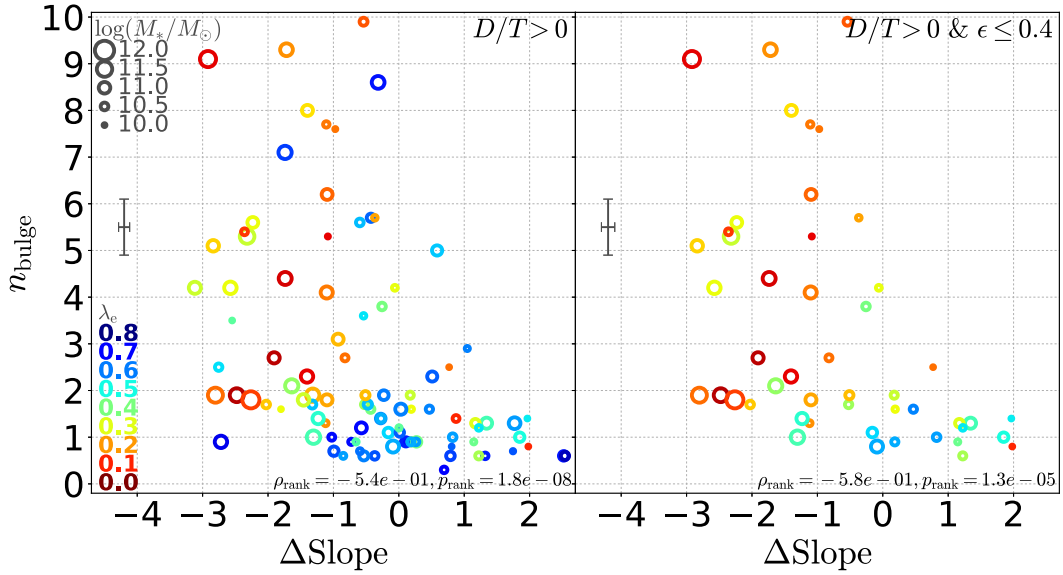

Figure 2.19 Bulge Sérsic index $n_{\rm tot}$ as a function of ΔSlope for galaxies with $D/T > 0$ (left) and for those with $D/T > 0$ and $\epsilon_{\rm e} \leq 0.4$. Symbols are the same as Figure 2.17.

We attempt to use the total and bulge Sérsic indices, $n_{\rm tot}$ and $n_{\rm bulge}$, instead of ϵ. Using four parameters ΔSlope, $n_{\rm tot}$, D/T, and $n_{\rm bulge}$, we now define alternative selection criterion for ***photometric*** slow rotators as

$$\begin{aligned} n_{\rm tot} \geq n_{\rm tot,crit} \text{ and } \Delta\text{Slope} &\leq \Delta\text{Slope}_{\rm crit}\ (D/T \geq 0.05) \\ \text{or} & \\ n_{\rm bulge} \geq n_{\rm bulge,crit} \text{ and } \Delta\text{Slope} &\leq \Delta\text{Slope}_{\rm crit}\ (D/T < 0.05), \end{aligned} \tag{2.13}$$

while others are selected as ***photometric*** fast rotators. In Figure 2.20, the completeness and contamination of ***photometric*** slow/fast rotators are shown as a function of $\Delta\text{Slope}_{\rm crit}$ with different $n_{\rm bulge,crit}$ and with $n_{\rm tot}$ fixed to 2. With this selection criterion, $n_{\rm bulge,crit} = 1.5$ gives the maximum completeness (~ 0.8 at $\Delta\text{Slope}_{\rm crit} \sim -0.5$) and the minimum contamination (~ 0.25 at $\Delta\text{Slope}_{\rm crit} \sim -1.5$) for slow and fast rotators, simultaneously. If we set the parameters as $n_{\rm bulge,crit} = 1.5$ and $\Delta\text{Slope}_{\rm crit} \sim -0.5$, the completeness and contamination of slow rotators become 0.78 and 0.27 while

those of fast rotators become 0.82 and 0.14. Although the completeness and contamination are not as good as when we use the original criterion including ϵ_e and $\Delta\mathrm{Slope}_{\mathrm{crit}}$ given in Section 2.3, this alternative selection criterion works quite well. Of course, the original criterion is much simpler, we can use the alternative to ***photometrically*** isolate slow and fast rotators. We note that taking $n_{\mathrm{tot,crit}} = 2.5$ instead of 2 also gives the similar result while taking $n_{\mathrm{tot,crit}}$ smaller than 2 or greater than 2.5 gives worse results.

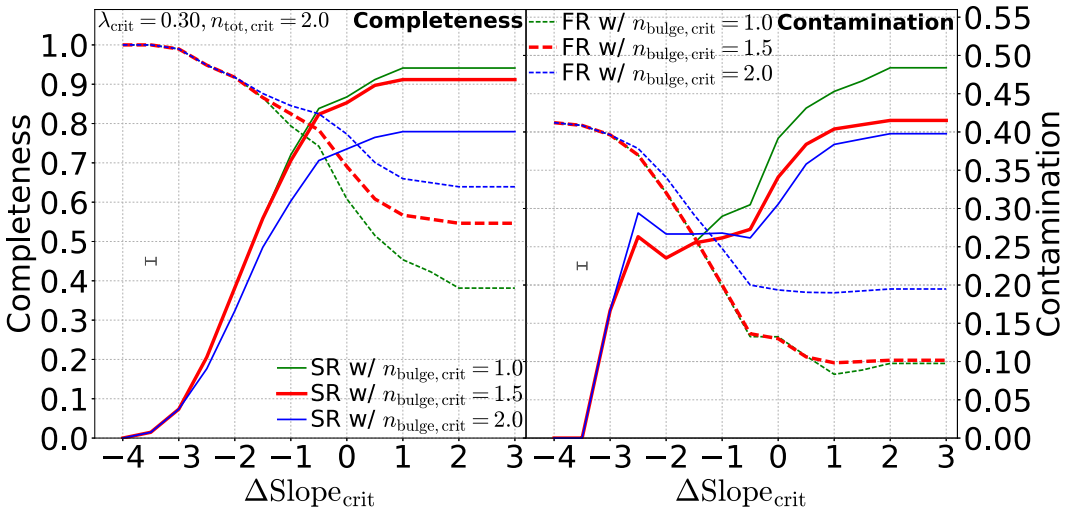

Figure 2.20 Completeness (left) and contamination (right) of slow (slid curves) and fast (dashed curves) rotators as a function of critical ΔSlope ($\Delta\mathrm{Slope}_{\mathrm{crit}}$; x-axis) with different critical bulge Sérsic indices ($n_{\mathrm{bulge,crit}}$; color-coded) similarly to Figure 2.13. The ***photometric*** slow rotators are selected by the criterion defined in Equation 2.13.

2.4.3 Possible Interpretation of the Correlation between ΔSlope and Kinematics

In Section 2.3, we have shown that fast rotators can have positive and negative ΔSlope, while most of slow rotators have $\Delta\mathrm{Slope} < 0$ (Figure 2.11). Therefore, there are largely three main populations, (1) truncated fast rotators ($\Delta\mathrm{Slope} > 0$), (2) extended fast rotators ($\Delta\mathrm{Slope} < 0$), and (3) extended slow rotators ($\Delta\mathrm{Slope} < 0$). For fast rotators, the first population is the majority for low masses ($\log(M_*/M_\odot) \lesssim 11$) while the second one becomes dominant for high masses.

These populations may be explained by the combination of spheroidal component and disks. First, truncated fast rotators may be interpreted as systems consisting of inner spheroidal component (i.e., bulge) and outer disk. The left panel in Figure 2.21 illustrates this situation. The central region is

dominated by the spheroidal component and the inner slope reflects the profile of it. The outer disk would appear as truncation if the inner profile is extrapolated to large radii, because the profile of disks (exponential or Sésic index $n = 1$) declines faster than the extrapolation of inner bulge. NGC0680 is a typical example of this system. The light profile is given in Figure 2.6 (panel (d), bottom row). While the slope of the measured light profile is comparable to the single Sérsic profile in the inner region, the measured one becomes more truncated than the Sérsic in the outer region. The signature of the outer disk can be seen in the image of this galaxy (panel (a), bottom row in Figure 2.6) as an asymmetric component tailing toward upper right.

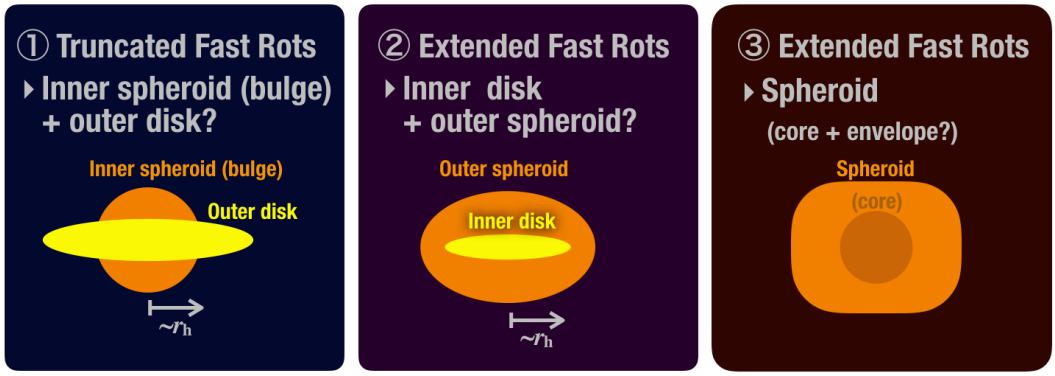

Figure 2.21 Possible interpretations for three main populations of ETGs, truncated fast rotators ($\Delta\mathrm{Slope} > 0$; left panel), extended fast rotators ($\Delta\mathrm{Slope} < 0$; central panel), and extended slow rotators ($\Delta\mathrm{Slope} < 0$; right panel).

Second, extended fast rotators may be interpreted as systems consisting of central disk component and outer spheroid (central panel in Figure 2.21). In this case, the outer profile influenced by the outer spheroid can be more extended than the extrapolation of the inner profile dominated by the central disk. Such systems may be observed as fast rotators because the field of view covered by the ATLAS^{3D} survey is not large and comparable to one half-light radius (Cappellari et al., 2011a), and the central disk will be observed as a rotating component. The existence of disk components in fast rotators has already reported by Krajnović et al. (2013). They have used Sérsic parameters, Sérsic index, disk-to-total ratio, and bulge Sérsic index. We have reached similar conclusion with a much simpler parameter to measure, $\Delta\mathrm{Slope}$.

Finally, slow rotators which usually have negative $\Delta\mathrm{Slope}$ may be interpreted as systems dominated by spheroidal components. The situation is illustrated in the right panel in Figure 2.21. As spheroidal components are dynamically hot, they will be classified as slow rotators. Stars with large

radial velocity dispersion in the spheroid may be the origin of extended profiles although we do not know whether the systems are two-component or not. In Section 4.1, we will further discuss the possible origins of fast and slow rotators.

2.4.4 ΔSlope using different radial ranges

We show the relation between ΔSlope and kinematic properties of ETGs using another chose of the radial ranges in which inner and outer slopes are measured. In the next chapter, we will measure ΔSlope for distant galaxies. In such situations, we have to optimize the radial ranges. For the inner slope, due to small apparent sizes of galaxies, the effect of point spread function (PSF) becomes much more significant while lower surface brightness due to cosmological dimming limits the outer most radius within which the outer slope is measured. For preparation for the next chapter, we measure the slopes using radial ranges which are optimized to distant galaxies. In the next chapter the radial ranges will be set to $0.8 \leq (r/r_{\rm h})^{1/4} \leq 1.0$ for the inner slope and $1.0 \leq (r/r_{\rm h})^{1/4} \leq 1.4$, taking account of the PSF sizes and signal-to-noise ratio in the outer regions.

In Figure 2.22, the inner and outer slopes measured using the new radial ranges defined above. Compared to those measured with the original ranges (Figures 2.7 and 2.8), fast rotators tends to be shifted to smaller $\mathrm{Slope}_{\rm out}$. This may be because, the outer slope becomes less sensitive to the outer truncation of the light profiles due to a narrower range and/or using more inner regions than original. Because of this shift there would be more contamination in the photometrically selected slow rotators using $\epsilon_{\rm e}$ and $\Delta_{\rm Slope}$. We will see the completeness and contamination late in this section.

In Figure 2.23, we show the relation between $\lambda_{\rm e}$ and $\Delta_{\rm Slope}$. The significant correlation still remains with the new ranges. We give the rank correlation efficiency ($\rho_{\rm rank}$) and $p-$value ($p_{\rm rank}$) in the panels in Figure 2.23. We also derive the linear relation as done for the original ranges. The fitted linear relation does not change very much from the original although the scatter becomes larger. The fitting function becomes

$$\begin{aligned} \lambda_{\rm e} &= 0.19^{+0.01-0.01}\Delta\mathrm{Slope} + 0.58^{+0.01-0.01}\ (\text{for all galaxies}),\ \text{and} \\ \lambda_{\rm e} &= 0.15^{+0.01-0.01}\Delta\mathrm{Slope} + 0.44^{+0.02-0.02}\ (\text{for } \epsilon \leq 0.4). \end{aligned} \tag{2.14}$$

The intrinsic scatter becomes larger than original. It becomes 0.24 for all galaxies and 0.19 for round

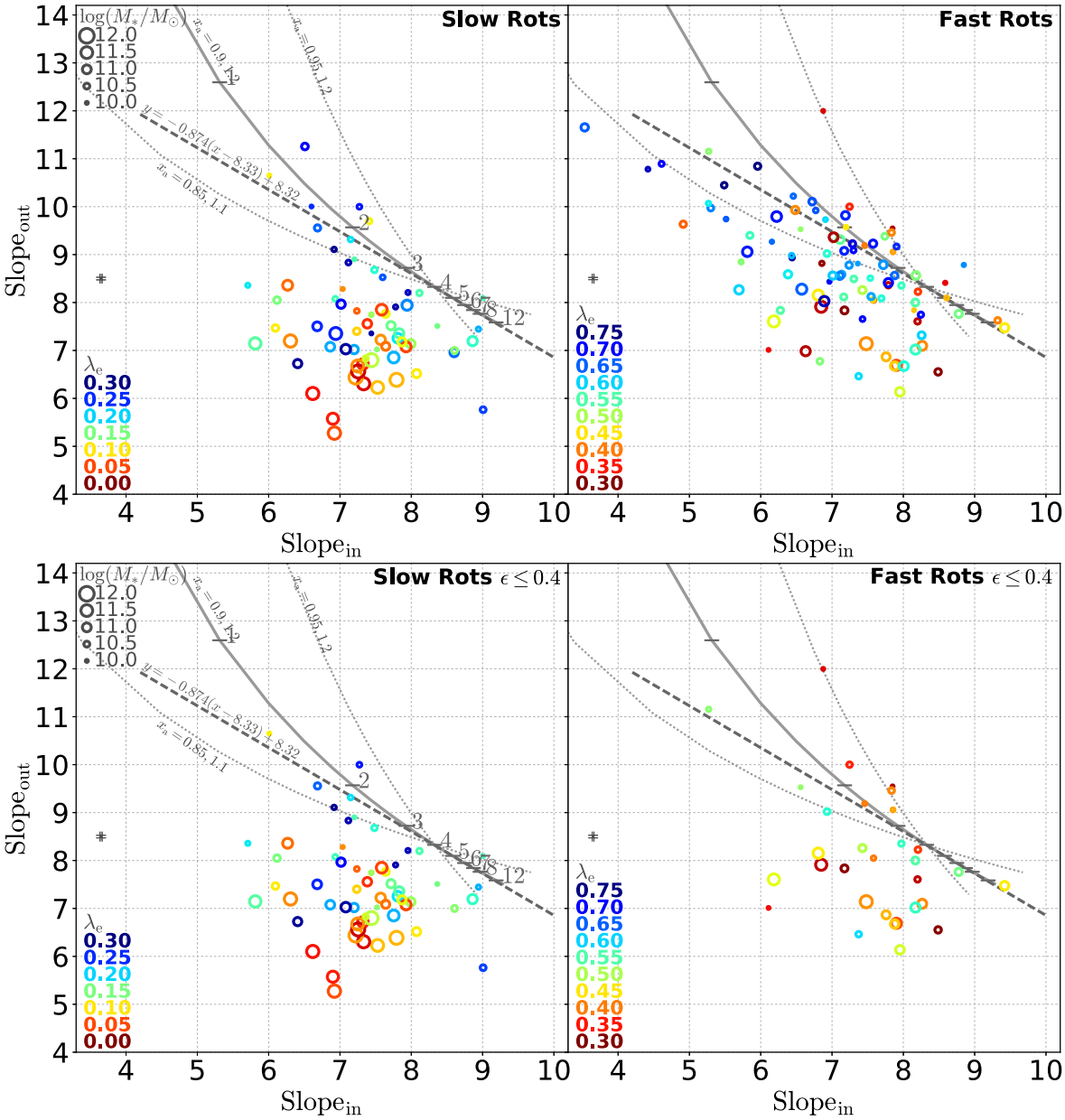

Figure 2.22 Same as Figures 2.7 and 2.8, but the slopes measured with different radial ranges. Top panels are for all galaxies while bottom ones are for round galaxies with $\epsilon_{\rm e} \leq 0.4$.

galaxies. Similarly, the relation between $V/\sigma_{\rm e}$ and $\Delta_{\rm Slope}$ becomes

$$\begin{aligned} V/\sigma_{\rm e} &= 0.22^{+0.01-0.01}\Delta{\rm Slope} + 0.64^{+0.01-0.01}\ ({\rm for\ all\ galaxies}),\ {\rm and} \\ V/\sigma_{\rm e} &= 0.14^{+0.02-0.02}\Delta{\rm Slope} + 0.45^{+0.02-0.02}\ ({\rm for}\ \epsilon \leq 0.4). \end{aligned} \tag{2.15}$$

The intrinsic scatter is 0.28 and 0.19 for all and round galaxies, respectively.

In Figure 2.24, we show $\Delta_{\rm Slope}$ as a function of the stellar mass. As expected from the down shift of the fast rotators seen in Figure 2.22, the difference between fast and slow rotators becomes less prominent than original. Still, fast rotators tend to have larger $\Delta_{\rm Slope}$ especially for round galaxies in lower masses.

In Figure 2.25, we show the completeness and contamination as a function of critical ΔSlope as in Figure 2.13. Similarly to the original case, using $\epsilon_{\rm crit} = 0.4$ gives the best in terms of completeness and contamination. The completeness does not change much from the original. It becomes 0.84 for slow and 0.77 for fast rotators if we set $\Delta{\rm Slope}_{\rm crit} \sim 0$. On the other hand, the contamination to the photometric slow rotator becomes as large as 0.29 from the original value of 0.22. Although the contamination becomes large with the new ranges for distant ETGs, $\Delta_{\rm Slope}$ could be used at least as a proxy for kinematical properties given the significant correlation to $\lambda_{\rm e}$.

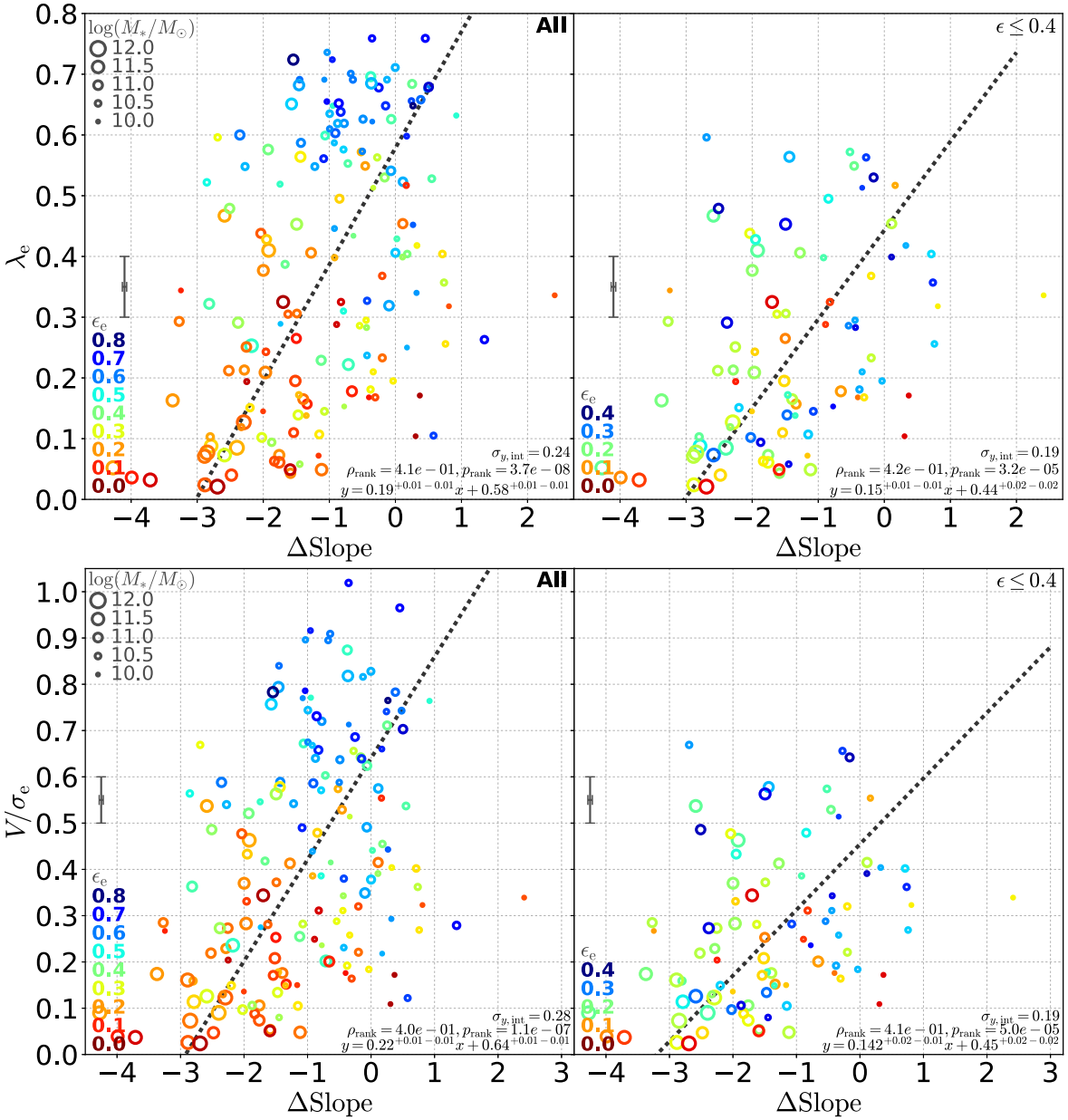

Figure 2.23 Same as Figures 2.9 and 2.10, but ΔSlope measured with different radial ranges.

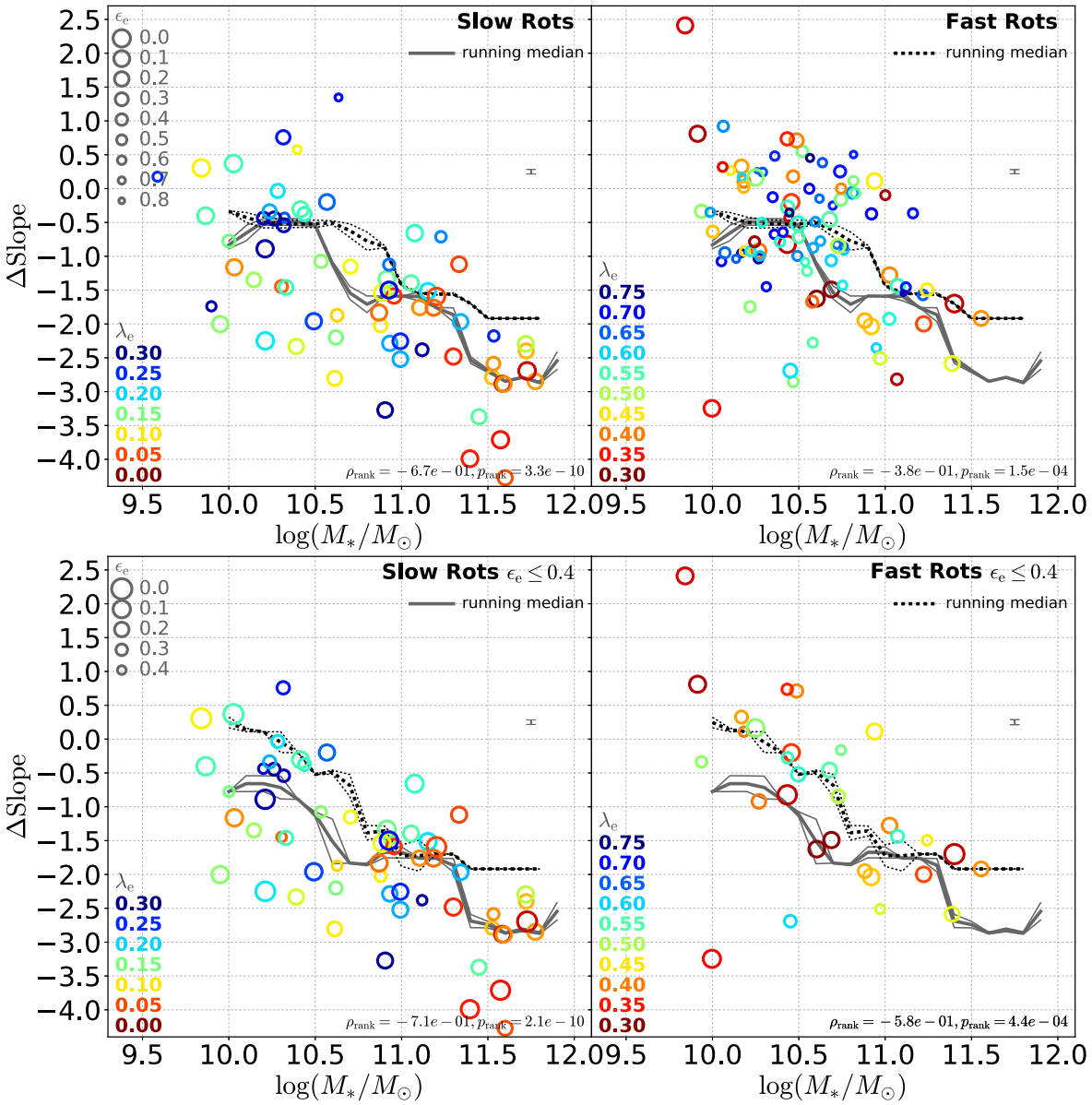

Figure 2.24 Same as Figures 2.11 and 2.12, but ΔSlope measured with different radial ranges. Top panels are for all galaxies while bottom ones are for round galaxies with $\epsilon_e \leq 0.4$.

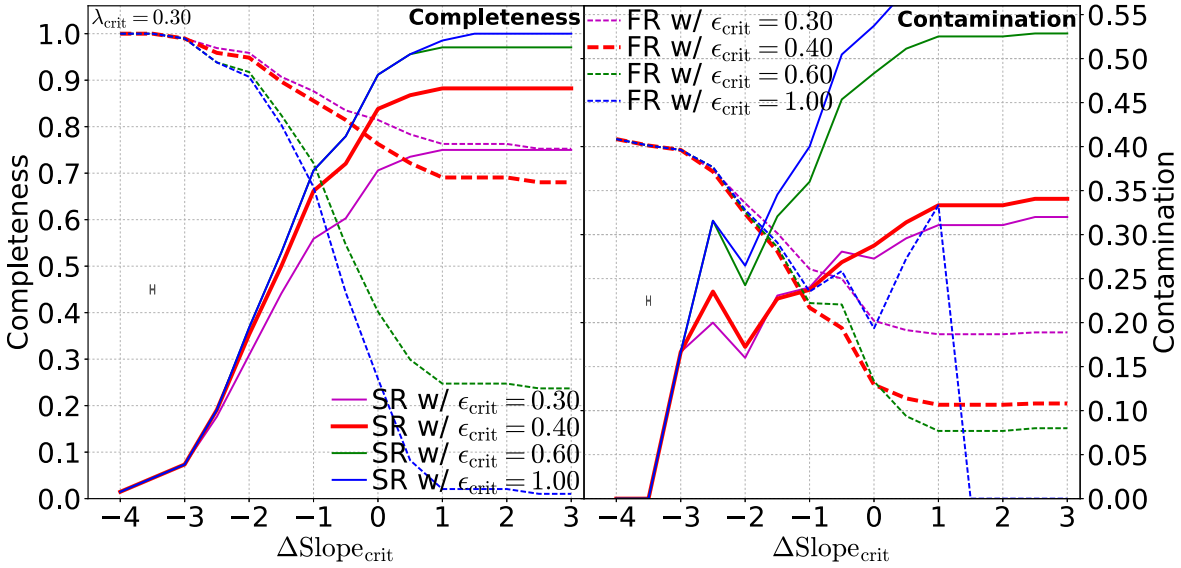

Figure 2.25 Same as Figures 2.13, but ΔSlope measured with different radial ranges.

3

Evolution of Kinematic Properties of ETGs Investigated by Light Profiles

In this chapter, we carry out surface photometry for high-redshift quiescent ETGs at $z \sim 1$ as well as low-redshift counterparts at $z \sim 0$. We prepare a sample of $\gtrsim 600$ ETGs residing in massive clusters at each redshift using color selection and morphological selection. We carry out surface photometry to derive radial light profiles of the ETGs, measure inner and outer slopes with appropriate PSF correction, and obtain the $\Delta\mathrm{Slope}$ parameter.

This chapter is structured as follows. We present the data and sample selection and basic properties of the high- and low-redshift samples in Section 3.1. We describe surface photometry as well as correction for the PSF effect in Section 3.2. We show the results in Section 3.3. We provide brief discussions in Section 3.4.

3.1 The Galaxy Samples and Data

In this section, we describe the sample selection and basic properties of our sample galaxies. We create stellar-mass limited samples of quiescent ETGs at high redshift ($z \sim 1.2$) and low redshift ($z \sim 0.03$).

We make use of a color magnitude diagram and morphological parameters.

3.1.1 High-Redshift Galaxy Sample

For the high-redshift sample, we use imaging data obtained in the ***HST*** Cluster SN Survey (Dawson et al., 2009). In the ***HST*** Cluster SN Survey (Dawson et al., 2009), twenty-five massive high-redshift clusters are selected from X-ray, optical, and IR surveys (Dawson et al., 2009). The properties of the clusters such as redshifts, virial masses, and radii are summarized in Tables 3.1 and 3.2. The total mass of the clusters spans from $\log(M_{200}/M_{\odot}) \sim 14.2$ to 14.9, where M_{200}, adopted from Jee et al. (2011), is the total mass enclosed in the radius, R_{200}, inside of which the mean density is 200 times the critical density of the universe at the cluster redshift. We include all of the twenty-five clusters. The median halo mass is $\log(M_{200}/M_{\odot}) \sim 14.6$ from X-ray observations and ~ 14.7 from lensing analysis.

3.1.1.1 ***HST*** Imaging Data

In the survey program, we have obtained multi-epoch ***HST*** imaging data (PID 10496) and follow-up spectroscopic data of galaxies in the clusters. Imaging data obtained by ***HST*** are detailed in Suzuki et al. (2012) and Meyers et al. (2012). We briefly describe basic properties here.

The twenty-five target clusters were visited by ***HST*** four to nine times between July 2005 and December 2006. Each visit typically consisted of four ∼500 s exposures in the F850LP filter (hereafter z_{850}) of the Advanced Camera for Surveys (ACS) Wide Field Camera (WFC) (Ubeda, 2012) and one ∼500 s exposure in the F775W filter (hereafter i_{775}) of the ACS WFC. The i_{775} filter (central wavelength $\lambda_c = 7692.4$ Å, bandwidth $\Delta\lambda = 434.4$ Å)* roughly matches rest-frame U band for clusters with $0.9 < z < 1.25$, with the best match occurring at $z = 1.1$. The z_{850} filter ($\lambda_c = 9033.1$ Å, $\Delta\lambda = 525.7$ Å) roughly matches the rest-frame B band in this redshift range with its closest match occurring at $z = 1.05$. For more distant clusters with $1.25 < z < 1.46$, the z_{850} filter more closely matches the rest-frame U band, with the largest overlap at $z = 1.45$. For galaxies at $z \sim 1$, these two photometric bands cover the wavelength region around the 4000Å break which is an important spectral feature of quiescent galaxies.

*http://www.stsci.edu/hst/acs/analysis/bandwidths

Table 3.1. Properties of the High-Redshift Clusters

ID [1]	Cluster [1]	RA(J2000) [1] [h:m:s]	Dec(J2000) [1] [d:m:s]	Redshift [1]	Discovery [1]	$N_{\rm spec}$ [2] member	$N_{\rm spec}$ [2] interloper
A	XMMXCS J2215-1738	22:15:58.5	-17:38:01	1.45	X-ray	30	22
B	XMMU J2205.8-0159	22:05:50.7	-01:59:30	1.12	X-ray	3	9
C	XMMU J1229.4+0151	12:29:28.8	+01:51:33	0.98	X-ray	22	21
D	RCS022144-0321.7	02:21:41.9	-03:21:47	1.02	Optical	10	26
E	WARP J1415.1+3612	14:15:11.1	+36:12:02	1.03	X-ray	21	32
F	ISCS J1432.4+3332	14:32:29.1	+33:32:47	1.11	IR-*Spitzer*	17	14
G	ISCS J1429.3+3437	14:29:18.5	+34:37:25	1.26	IR-*Spitzer*	8	0
H	ISCS J1434.5+3427	14:34:28.5	+34:26:22	1.24	IR-*Spitzer*	6	25
I	ISCS J1432.6+3436	14:32:38.3	+34:36:48	1.34	IR-*Spitzer*	6	0
J	ISCS J1434.7+3519	14:34:46.3	+35:19:44	1.37	IR-*Spitzer*	2	0
K	ISCS J1438.1+3414	14:38:09.5	+34:14:18	1.41	IR-*Spitzer*	8	16
L	ISCS J1433.8+3325	14:33:51.1	+33:25:50	1.376	IR-*Spitzer*	1	8
M	Cl J1604+4304	16:04:22.6	+43:04:38	0.90	Optical	15	43
N	RCS022056-0333.4	02:20:55.7	-03:33:10	1.03	Optical	1	6
P	RCS033750-2844.8	03:37:50.4	-28:44:28	1.1[a]	Optical	0	0
Q	RCS043934-2904.7	04:39:38.0	-29:04:54	0.95	Optical	0	0
R	XLSS J0223.0-0436	02:23:03.7	-04:36:18	1.22	X-ray	23	55
S	RCS215641-0448.1	21:56:42.1	-04:48:04	1.07	Optical	0	0
T	RCS2-151104+0903.3	15:11:03.8	+09:03:15	0.97	Optical	9	11
U	RCS234526-3632.6	23:45:27.3	-36:32:49	1.04	Optical	27	28
V	RCS231953+0038.0	23:19:53.3	+00:38:12	0.91	Optical	9	14
W	RX J0848.9+4452	08:48:56.2	+44:52:00	1.26	X-ray	6	2
X	RDCS J0910+5422	09:10:44.9	+54:22:07	1.11	X-ray	21	15
Y	RDCS J1252.9-2927	12:52:54.4	-29:27:16	1.23	X-ray	37	168
Z	XMMU J2235.3-2557	22:35:20.6	-25:57:41	1.39	X-ray	23	70

[1]Dawson et al. (2009).

[2]The number of spectroscopically confirmed member and interloper (Meyers et al., 2012).

[a]Photometric redshift.

References. — Dawson et al. (2009) and references therein; (A) Stanford et al. (2006), Hilton et al. (2007); (B and C) Böhringer et al. (2005); (D) Andreon et al. (2008a,b); (E) Perlman et al. (2002); (F) Elston et al. (2006); (G, I, J, and L) Eisenhardt et al. (2008); (H) Brodwin et al. (2006); (K) Stanford et al. (2005); (L) Brodwin et al. (2013), Wagner et al. (2015), Zeimann et al. (2013); (M) Postman et al. (2001); (N, U) Gilbank et al. (2008); (Q) Cain et al. (2008); (R) Andreon et al. (2005), Bremer et al. (2006); (S) Gladders et al. (2003); (V) Hicks et al. (2008); (W) Rosati et al. (1999); (X) Stanford et al. (2002); (Y) Rosati et al. (2004); (Z) Mullis et al. (2005);

Table 3.2. Properties of the High-Redshift Clusters ‖

ID [1]	$\sigma_V^S[\mathrm{km\ s^{-1}}]^2$	$M_{200}^X[10^{14}M_\odot]^3$	$M_{200}^L[10^{14}M_\odot]^4$	$R_{200}[\mathrm{Mpc}]$
A	$720_{\pm 110}$	$2.0^{+0.5}_{-0.6}$	$4.3^{+3.0}_{-1.7}$	$0.9^{0.2}_{-0.1}$
B	···	···	$3.0^{+1.6}_{-1.0}$	$0.9^{0.1}_{-0.1}$
C	$683_{\pm 62}$	$5.7^{+1.0}_{-0.8}$	$5.3^{+1.7}_{-1.2}$	$1.1^{0.1}_{-0.1}$
D	$710_{\pm 150}$	···	$1.8^{+1.3}_{-0.7}$	$0.8^{0.2}_{-0.1}$
E	$807_{\pm 185}$	$4.6^{+1.5}_{-0.8}$	$4.7^{+2.0}_{-1.4}$	$1.1^{0.1}_{-0.1}$
F	$734_{\pm 115}$	···	$4.9^{+1.6}_{-1.2}$	$1.1^{0.1}_{-0.1}$
G	$767_{\pm 295}$	···	$5.4^{+2.4}_{-1.6}$	$1.0^{0.1}_{-0.1}$
H	$863_{\pm 170}$	···	$2.5^{+2.2}_{-1.1}$	$0.8^{0.2}_{-0.1}$
I	$807_{\pm 340}$	···	$5.3^{+2.6}_{-1.7}$	$1.0^{0.1}_{-0.1}$
J	···	···	$2.8^{+2.9}_{-1.4}$	$0.8^{0.2}_{-0.2}$
K	757^{+247}_{-208}	$3.2^{+3.9}_{-1.4}$	$3.1^{+2.6}_{-1.4}$	$0.8^{0.2}_{-0.1}$
L	···	···	···	···
M	$1226^{+245\mathrm{a}}_{-154}$	···	$1.5^{+1.5\mathrm{b}}_{-1.5}$	···
N	···	···	$4.8^{+1.8}_{-1.3}$	$1.1^{0.1}_{-0.1}$
P	···	···	$4.9^{+2.8}_{-1.7}$	$1.1^{0.2}_{-0.1}$
Q	$1080_{\pm 320}$	$0.46^{+6.0}_{-1.7}$	$4.3^{+1.7}_{-1.2}$	$1.1^{0.1}_{-0.1}$
R	$799_{\pm 129}$	$2.4^{+1.5}_{-1.5}$	$7.4^{+2.5}_{-1.8}$	$1.2^{0.1}_{-0.1}$
S	···	···	$1.8^{+2.5}_{-1.0}$	$0.8^{0.3}_{-0.2}$
T	$717_{\pm 208}$	···	$1.9^{+1.4}_{-0.8}$	$0.8^{0.2}_{-0.1}$
U	$670_{\pm 190}$	···	$2.4^{+1.1}_{-0.7}$	$0.9^{0.1}_{-0.1}$
V	$990_{\pm 240}$	$5.4^{+1.2}_{-1.0}$	$5.8^{+2.3}_{-1.6}$	$1.2^{0.1}_{-0.1}$
W	$720_{\pm 140}$	$3.8^{+1.5}_{-1.4}$	$4.4^{+1.1}_{-0.9}$	$1.0^{0.8}_{-0.1}$
X	$675_{\pm 190}$	$7.4^{+2.6}_{-2.3}$	$5.0^{+1.2}_{-1.0}$	$1.1^{0.1}_{-0.1}$
Y	747^{+74}_{-84}	$4.4^{+1.1}_{-1.0}$	$6.8^{+1.2}_{-1.0}$	$1.1^{0.1}_{-0.1}$
Z	802^{+77}_{-48}	$6.1^{+1.4}_{-1.2}$	$7.3^{+1.7}_{-1.4}$	$1.1^{0.1}_{-0.1}$

[1]Dawson et al. (2009).

[2]Velocity dispersion from optical spectroscopy (Jee et al., 2011, Table2, and references therein).

[3]Cluster mass derived from X-ray observation (Jee et al., 2011, Table2, and references therein).

[4]Cluster mass derived from lensing analysis (Jee et al., 2011, Table2).

[a]Postman et al. (1998).

[b]Sereno & Covone (2013).

References. — Dawson et al. (2009); Jee et al. (2011, Table2, and references therein);

Table 3.3. Properties of SDSS Imaging Survey I

SDSS imaging observation	
Effective Aperture	2.5 m
Median PSF FWHM in r-band	1.3 arcsec
Pixel scale	0.396 arcsec
Exposure time per band	53.9 arcsec

References. — http://www.sdss3.org/dr10/scope.php

Table 3.4. Properties of SDSS Imaging Survey II

SDSS imaging filters					
Band pass filter	u	g	r	i	z
Effective wavelength [Å]	3551	4686	6165	7481	8931
(95% completeness for point sources)	22.0	22.2	22.2	21.3	20.5

References. — http://www.sdss3.org/dr12/scope/

Table 3.5. Properties of SDSS Spectroscopic Survey

SDSS Spectroscopic Observation	
Wavelength coverage	3800 to 9200 [Å]
Resolution R	1800 to 2000
Typical redshift accuracy	30 $\mathrm{km\ s^{-1}}$ rms
Approximate magnitude limits	r (Petrosian) < 17.7

Note. — The quantities are those for the SDSS spectrograph and for the main sample galaxies.

References. — http://www.sdss3.org/dr10/scope.php

In this study, we use the deep co-additions of exposures from all observation epochs. Four clusters, RDCS J0910+54 (Mei et al., 2006), RDCS J0848+44 (Postman et al., 2005), RDCS J1252-29 (Blakeslee et al., 2003), and XMMU 2235.3-2557 (Jee et al., 2009), had been previously targeted by ACS in i_{775} and z_{850} (PID9290 and PID9919), and these exposures are also included in our co-added images. We use both i_{775} and z_{850} images in order to select quiescent galaxies which are promising candidates of cluster members while we only use z_{850} images for the morphological classification and for obtaining radial light profiles because the co-added images in z_{850} is much deeper (the effective exposure time is $\sim$10 k sec or more depending on clusters) than in i_{775}.

We prepare PSF images for each cluster field by stacking images of stars as we have done in Mitsuda et al. (2017). We select $\sim$ 30 unsaturated stars, cutout 101 $\times$ 101 pixel around them, and normalize them with the central value. We then oversample the cutouts by 51 times, align the center in the subpixel scale, and take an average. We measure PSF FWHM in z_{850} using IRAF task imexam. The median FWHM for all cluster fields is 0.112 arcsec with the Moffat profile and the standard deviation is 0.003 arcsec.

3.1.1.2 Spectroscopic Redshifts

We will photometrically select quiescent galaxies in clusters based on photometry in two bands of i_{775} and z_{850} using color-magnitude diagrams. In order to determine the loci of cluster members on the diagrams, we make use of spectroscopically confirmed members. The redshifts of the spectroscopic members are taken from a spectroscopic catalog created in the ***HST*** Cluster SN Survey (Meyers et al., 2012). The catalog information is described in Meyers et al. (2012). Briefly, as the ***HST*** Cluster SN Survey produced SN candidates, galaxies were spectroscopically targeted with multi-object slits using prescheduled observing time on DEIMOS on Keck II (Faber et al., 2003), and FOCAS on Subaru (Kashikawa et al., 2002), and with Target of Opportunity (ToO) requests on FORS1 and FORS2 on Kueyen and Antu at the Very Large Telescope (Appenzeller et al., 1998). The FORS1, FORS2, and DEIMOS observations are described in Lidman et al. (2005) and Dawson et al. (2009); the FOCAS observations are described in Morokuma et al. (2010). Galaxy redshifts are measured through cross-correlation with template eigenspectra derived from SDSS spectra (Aihara et al., 2011). The important spectroscopic features are the 4000Å break, the absorption of Ca H, K, and the emission lines of [O II] 3727Å doublet. The spectroscopic catalog includes these redshifts and additional ones from literature (Andreon et al., 2008b, Bremer et al., 2006, Brodwin et al., 2006, Demarco et al., 2007, Eisenhardt et al., 2008, Hilton et al., 2007, 2009, Postman et al., 1998, Rosati et al., 1999, Stanford et al., 2002, 2005). The equivalent width (EW) of the [O II] is also provided for some galaxies (about a half of $z \sim 1$ cluster galaxies). Although typical high-redshift spectroscopic surveys tend to target star-forming blue galaxies with strong emission lines such as $H\alpha$ and [O II], quiescent galaxies on the red-sequence are mainly targeted in the program and our spectroscopic members are rich in quiescent galaxies. Note that, however, the completeness of the spectroscopic sample is not high and varies with cluster to cluster, since many galaxies are additional targets in ***HST*** Cluster SN Survey whose main targets are SNe and their hosts.

We provide basic information about the spectroscopic members. We have 301 $z \sim 1$ cluster galaxies with the spectroscopic redshift. The redshift of the selected galaxies spans from 0.90 to 1.48 with the median redshift of $z \sim 1.2$. Of these galaxies, 286 lie within one R_{200} from the cluster center, and other 15 galaxies within 1.5 R_{200}, where R_{200} is adopted from Jee et al. (2011). The redshifts of 279 galaxies are within ± 0.01 from the cluster redshift, and those of other 22 are within ± 0.02.

3.1.1.3 Reference red sequence from spectroscopic ETGs

We first select quiescent galaxies residing in the 25 clusters (i.e., quiescent member galaxies) using i_{775} and z_{850} color magnitude diagram. For this, we derive the $i_{775} - z_{850}$ color and z_{850} magnitude which quiescent member galaxies in each cluster should have, using spectroscopically confirmed member galaxies. We make use of the stellar mass limited, quiescent ETG sample created in Mitsuda et al. (2017). Here, we briefly describe how the sample are created. In the study, we first select 224 red galaxies from the 301 members whose i_{775} - z_{850} is consistent with passively evolving galaxies. We then apply the stellar mass limit of $\log(M_*/M_\odot) \geq 10.5$ and obtain 158 galaxies. Finally, ETGs are selected based on the concentration parameter and mean surface brightness (Doi et al., 1993, and see below), and 130 quiescent ETGs are included in the sample. In addition to the sample of Mitsuda et al. (2017), we include lower mass ETGs than $\log(M_*/M_\odot) = 10.5$. In total, we use 180 galaxies in total.

We compute the ***composite red sequence*** following Meyers et al. (2012). We first derive Petrosian magnitude (Petrosian, 1976) in i_{775} and z_{850} bands measured from the co-added images of each cluster using the Source Extractor (`SExtractor`, Bertin & Arnouts, 1996). Since magnitude are measured in cut out images in Mitsuda et al. (2017), we derived the magnitude again so that photometric quiescent ETGs can be selected using i_{775} and z_{850} magnitude measured exactly in the same way. Petrosian magnitude (`MAG_PETRO` in `SExtractor`) is measured within 2.5-times the Petrosian radius ($r_{\rm P}$, Petrosian, 1976) aperture, where $r_{\rm P}$ is the radius at which the ratio of the local surface brightness to the mean surface brightness within the radius comes the "Petrosian Ratio", $\nu_{\rm P}$, as described by Blanton et al. (2001) and Yasuda et al. (2001):

$$\nu_{\rm P}(r) \equiv \frac{\int_{0.8r}^{1.25r} {\rm d}r' 2\pi r' I(r') / [\pi(1.25^2 - 0.8^2) r'^{\,2}]}{\int_0^r {\rm d}r' 2\pi r' I(r') / [\pi r'^{\,2}]}, \tag{3.1}$$

where $I(r)$ is the azimuthally averaged surface brightness profile. In `SExtractor`, $\nu_{\rm P}$ is set to 0.2. We run `SExtractor` in two-step mode (Cold/Hot method, Rix et al., 2004) on z_{850} images for object detection and photometry in the band. In the two-step mode, the first run (cold mode) is carried out with a high threshold of the signal-to-noise ratio in order to detect relatively bright galaxies, aggressively segmenting galaxies near cluster cores. After detecting bright galaxies, the second run (hot mode) is carried out with a lower threshold and less aggressive parameter settings for deblending in order

not to segment features within galaxies such as spiral arms and clumps. Newly detected objects in the second run are compiled with those detected in the first run to create a combined catalog. The detection parameters in the two steps are optimized by trial and error judged by the successful identification and segmentation of galaxies near cluster cores. We then run `SExtractor` again on i_{775} images in double image mode in which object detection is done in z_{850} images but photometry in i_{775} images. Finally, we obtain i_{775} and z_{850} Petrosian magnitude by matching the position of detected objects and the spectroscopic ETGs in Mitsuda et al. (2017).

From the measured i_{775} and z_{850} magnitude of the spectroscopically confirmed quiescent ETGs, the magnitude of them at a redshift of every cluster is simulated using stellar population synthesis models. First, we derive a stellar mass and metallicity of each spectroscopic ETGs by fitting simple stellar population (SSP) models using Bruzual & Charlot (2003, hereafter BC03) with Salpeter initial mass function (IMF). We fit synthetic spectral energy distribution (SED) to the i_{775} and z_{850} magnitude. Since we have photometry only in two bands, two parameters can be determined from the fitting. We fix the formation redshift of the single population to $z_{\rm form} = 3$ following Meyers et al. (2012), and the fitting parameters are the stellar mass and metallicity. In the next step, we derive i_{775} and z_{850} magnitude at redshifts of all 25 clusters by computing SEDs with the stellar mass and metallicity using BC03 SSP models and convolving the synthetic spectra with system throughputs in the filters [*].

Then, color-magnitude relation of red sequence at redshifts of all of the clusters (***composite red sequence***) are computed from the simulated i_{775} and z_{850} magnitude. The color-magnitude relation is derived by fitting a linear function to the i_{775}-z_{850} colors and z_{850} magnitude. The simulation procedure is not perfect in many aspects such as the assumption of fixed $z_{\rm form}$, SSP, and of no dust. As a result, when the i_{775}-z_{850} color is computed at a very different redshift from the original, the simulated color become inconsistent with observed colors of quiescent galaxies at the redshift. Therefore, in the fitting, we assign a Gaussian weight $w = \exp(-(z_{\rm galaxy} - z_{\rm cluster})^2/(2 \cdot 0.15^2))$ for each galaxy following Meyers et al. (2012), where $z_{\rm galaxy}$ is the original redshift of the galaxy and $z_{\rm cluster}$ is the redshift of a target cluster. In Figure 3.1, we show an example of the computation of the ***composite red sequence*** at a redshift of the cluster E ($z_{\rm cluster}$=1.026). Although the computed i_{775}-z_{850} colors of galaxies with original redshift less and larger than $\sim$ 1.1 are not consistent, the fitting function (***composite red sequence***) is consistent with the colors of $z \sim 1.0$ galaxies thanks to assigning the weights. In the next section, we use the ***composite red sequence*** to select photometric quiescent

[*] http://www.stsci.edu/hst/acs/analysis/throughputs

members of each cluster.

3.1.1.4 Selecting photometric quiescent members of each cluster

Quiescent galaxies which are likely cluster members are selected based on the ***composite red sequence*** for each cluster. We first select objects whose z_{850} magnitude brighter than 25.5 mag and fainter than $min(z_{850})_{\rm comp-redseq}-0.2$. Here, $min(z_{850})_{\rm comp-redseq}$ is the minimum magnitude of the ***composite red sequence*** (i.e., the brightest spectroscopic member). The fainter magnitude limit is set to 25.5 which is faint enough for quiescent galaxies with the stellar mass greater than $10^{10}M_{\odot}$ to be selected but brighter than the detection limit which is $z_{850} \sim 27.6$ for point sources to be detected in $\sim 7\sigma$. Second, objects whose $i_{775} - z_{850}$ color is consistent with the ***composite red sequence*** within ± 0.3 mag is selected. Third, objects lie within $0.5 \times R_{200}$ from the cluster center are selected. Finally, we exclude point sources by selecting objects with FWHM in z_{850} larger than 0.13 arcsec. Hereafter, we refer to the galaxies selected in this procedure as the photometric quiescent galaxy sample.

In Figure3.2, we present an example of the selection procedure for the cluster E. We consider that we could select likely members by applying these criteria. Although significant amount of spectroscopically confirmed interloper lie inside the $i_{775}-z_{850}$ color criterion, by applying the cluster-centric distance, most of them (6/8) are excluded. Also the FWHM limit would be reasonable to separate stars and galaxies. Note that spectroscopic members can be excluded from the sample if they are too blue (or red) or too far from the cluster center.

For the selected quiescent galaxies, we create cutouts of i_{775} and z_{850} images with the size of 400×400 pixels from the co-added images. We run `SExtractor` again on the cutouts similarly as previous in order to obtain photometry such as Petrosian magnitude, position angles, and axis ratios of the galaxies. Hereafter, photometric quantities derived by `SExtractor` refer to those measured in this step.

3.1.1.5 Contamination in the photometric quiescent members

We estimate a contamination fraction of spectroscopic interlopers included in the photometric quiescent galaxy sample. When the completeness of the spectroscopic member is given by $f_{\rm comp,men}$, the

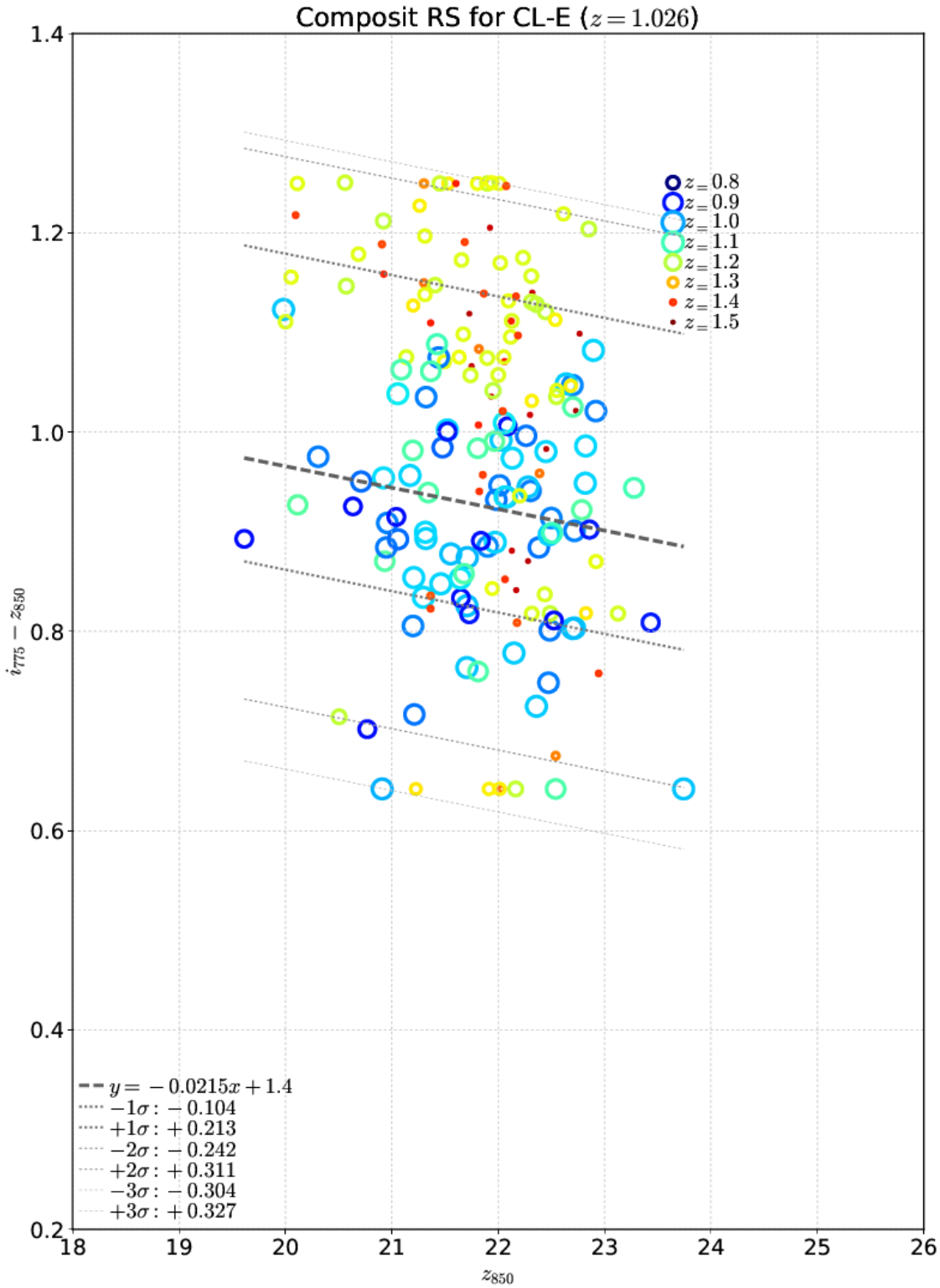

Figure 3.1 Example of the simulated i_{775}-z_{850} colors and z_{850} magnitude of the spectroscopically confirmed ETGs computed at a redshift of the cluster E ($z_{\rm cluster} = 1.026$). Colors correspond to the original redshift of each galaxy shown in as shown in the figure while marker sizes is proportional to the weight assigned for each galaxy. The fitting function, i.e., ***composite red sequence***, is shown with the thick dashed line with $1, 2$, and 3σ scatters shown with dotted lines.

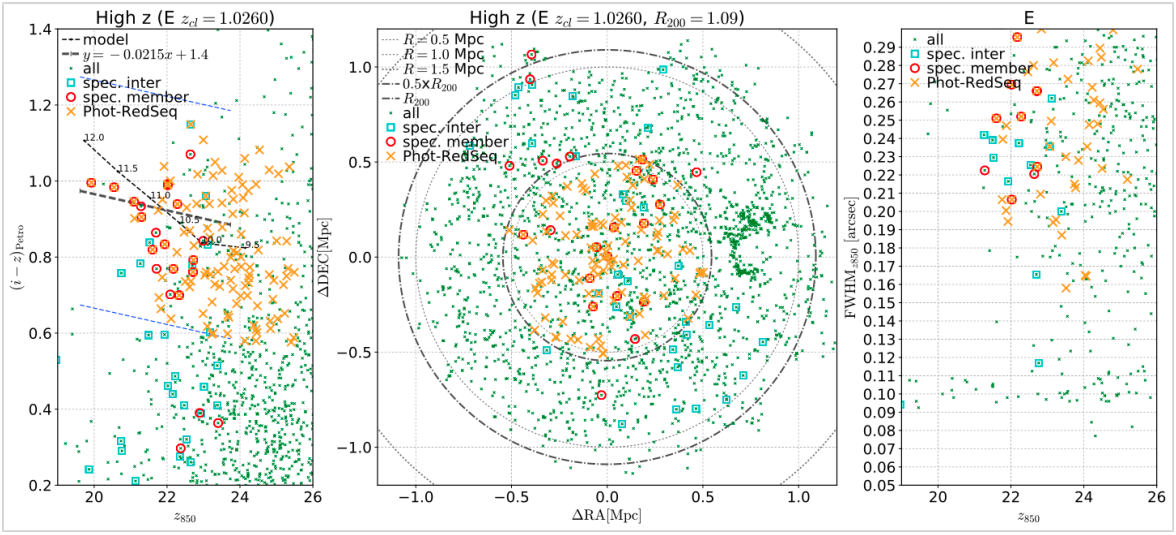

Figure 3.2 Example of the selection of photometric quiescent members for the cluster E ($z_{\rm cluster} = 1.026$). i_{775} and $z850$ color-magnitude diagram (left), position (center), and FWHM and magnitude of all detected objects by SExtractor (green small crosses), spectroscopically confirmed interloper (cyan boxes), spectroscopic member (red circles), and selected photometric quiescent members (orange crosses). In the left panel ***composite red sequence*** is shown by thick dashed line with a ± 0.3 mag window (blue dashed lines) for selecting photometric members. We also show SSP model (thin dashed curve) with different stellar masses denoted in the panel. In the central panel, circles with the radius of $0.5\times$ and $1 \times R_{200}$ are shown by dash-dot lines as well as those with the radius of 0.5, 1.0, and 1.5 Mpc are shown by dotted lines.

number of spectroscopic member $N_{\rm spec,mem}$ is

$$N_{\rm spec,mem} = f_{\rm comp,men}\, N_{\rm mem}, \tag{3.2}$$

where $N_{\rm mem}$ is the total number of member galaxies. Likewise, the number of spectroscopic interloper $N_{\rm spec,intr}$ is

$$N_{\rm spec,intr} = f_{\rm comp,intr}\, N_{\rm intr}, \tag{3.3}$$

where $f_{\rm comp,intr}$ is the completeness for interlopers, and $N_{\rm intr}$ is the total number of interlopers. The number of the spectroscopic members and interlopers included in the photometric quiescent galaxy sample can also be computed using the equations above by replacing $N_{\rm mem}$ and $N_{\rm intr}$ by the number of interlopers and members included in the sample, respectively. In the following, we consider $N_{\rm mem}$ and $N_{\rm intr}$ as the number of interlopers and members in the photometric quiescent galaxy sample. Assuming the same spectroscopic completeness for members and interlopers, $f_{\rm comp,men} = f_{\rm comp,intr}$, we have the contamination fraction,

$$\begin{aligned} f_{\rm cont} &= \frac{N_{\rm intr}}{N_{\rm mem} + N_{\rm intr}} \\ &= \frac{\dfrac{N_{\rm spec,intr}}{f_{\rm comp,intr}}}{\dfrac{N_{\rm spec,mem}}{f_{\rm comp,men}} + \dfrac{N_{\rm spec,intr}}{f_{\rm comp,intr}}} \\ &= \frac{N_{\rm spec,intr}}{N_{\rm spec,mem} + N_{\rm spec,intr}}. \end{aligned} \tag{3.4}$$

We note that the completeness can be different for members and interlopers. The interlopers can be star-forming galaxies reddened by, e.g., dust attenuation, whose redshifts are mainly determined by emission lines, such as $H\alpha$, $H\beta$, [O III] for foreground objects, accompanied with their strong star-forming activity. On the other hand, the members are passive galaxies whose spectroscopic redshifts often determined by absorption features when the [O II] emission line is weak. Since it is more difficult to determine redshifts from absorption than emission, the completeness of the members may be lower than that of the interlopers, and the contamination fraction estimated by Equation 3.4 may

be an upper limit.

We compute the number of the spectroscopic members and interlopers ($N_{\rm spec,intr}$ and $N_{\rm spec,mem}$) for all clusters that have at least 5 spectroscopic members and interlopers cataloged (see Table 3.1). We use 15 clusters A, C, D, E, F, H, K, M, R, T, U, V, X, Y, Z. In Figure 3.3, we show the contamination fraction as a function of the z_{850} magnitude as well as the stellar mass. We only include galaxies with the stellar mass $\log(M_*/M_\odot \geq 10)$ which is the mass limit of our final sample (see below). The contamination fraction is $\sim$ 20 percent for the whole photometric sample. The fraction is a strong function of the stellar mass as well as z_{850} magnitude. The fraction becomes the largest in the smallest mass bin $\log(M_*/M_\odot) < 10.5$ reaching $\sim$ 28 percent. It decreases to $\sim$ 15 percent in $10.5 < \log(M_*/M_\odot) < 11.0$ and $\sim$ 10 percent in $11.0 < \log(M_*/M_\odot) < 11.5$, and then it drops to $\sim$ 0 in the highest mass bin.

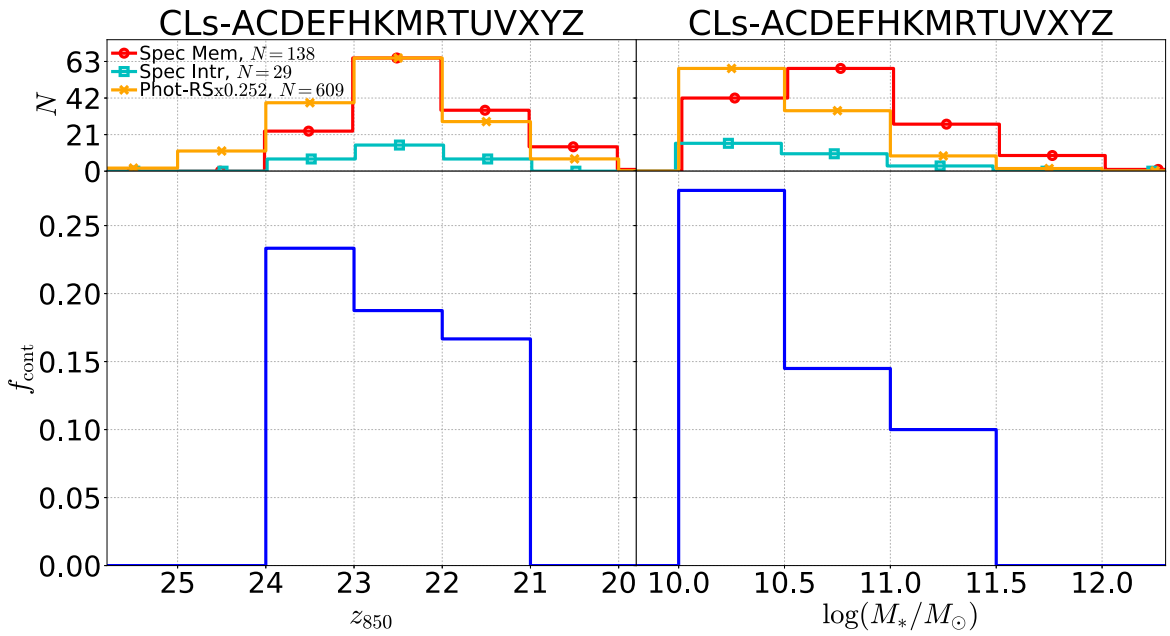

Figure 3.3 Contamination fraction $f_{\rm cont}$ (bottom panels) as a function of the z_{850} magnitude (left) and stellar mass (right). We use clusters A, C, D, E, F, H, K, M, R, T, U, V, X, Y, Z, which have at least 5 spectroscopic members and interlopers cataloged (Table 3.1). Only galaxies with $\log(M_*/M_\odot \geq 10)$, the stellar mass limit of our final sample, are included in both panels. In top panels we present histograms of the members (red), interlopers (cyan), and all photometric quiescent members scaled by 0.29 (orange). Histograms are slightly offset horizontally for visibility.

3.1.1.6 Stellar mass limit

A stellar mass limit is imposed on the photometric quiescent galaxy sample. We select galaxies with the stellar mass $\log(M_*/M_\odot) \geq 10$, using the mass estimated in the following way. We estimate a stellar mass by fitting SSP models of BC03 with Salpeter IMF using i_{775} and z_{850} magnitude. As we have shown in Section 3.1.1.3, we only have photometry in two bands. Hence, only two parameters can be determined by the fitting. This time, following Mitsuda et al. (2017), we use the relation between stellar mass and age established in quiescent galaxies in the local universe (Thomas et al., 2005) because the quiescent galaxy sample is likely evolving passively. During the fitting, the SSP age is connected to the stellar mass by Equation (3) in Thomas et al. (2005). Then, independent fitting parameters are the stellar mass and metallicity with the metallicity ranging from 1×10^4 to 0.07. We fit synthetic SSP SED to the i_{775} and z_{850} Petrosian magnitude.

We also estimate the stellar mass with different assumptions and check consistency. One assumption is to connect stellar masses and metallicity also using Equation (3) in Thomas et al. (2005). The stellar mass estimated this way is highly consistent with the original. The median difference is only 0.0042 dex with slightly larger value for masses estimated with the stellar mass-to-metallicity relation, and the standard deviation of the difference is 0.26 dex. We have also done similar test of the stellar mass estimated with the fixed formation epoch ($z_{\rm form}$) as well as fixed metallicity ($Z_{\rm form}$). The median difference between the mass estimated with $z_{\rm form} = 3.0$ and the original is 0.27 with a larger value for former, and the standard deviation is 0.21. The mass estimated with $Z_{\rm form} = 0.02$ (solar metallicity) is on average slightly smaller than the original by 0.014 dex, and the standard deviation is 0.45. As done in Mitsuda et al. (2017), as an uncertainty of a stellar mass, we take the difference between that estimated with the mass-age and mass-metallicity relation. In Figure 3.4, an example of the stellar mass estimation is presented.

The possible systematics in the stellar mass estimated with the mass-age relation is discussed in Mitsuda et al. (2017). We have found that stellar masses estimated by our method with two-band photometry are on average under estimated by ~ 0.2 dex than those estimated with four-band photometry presented in Delaye et al. (2014). Therefore, we would remind readers that the estimated stellar mass may have systematic uncertainty of ~ 0.2 dex, which is comparable to the standard of the difference between masses estimated with the different assumptions.

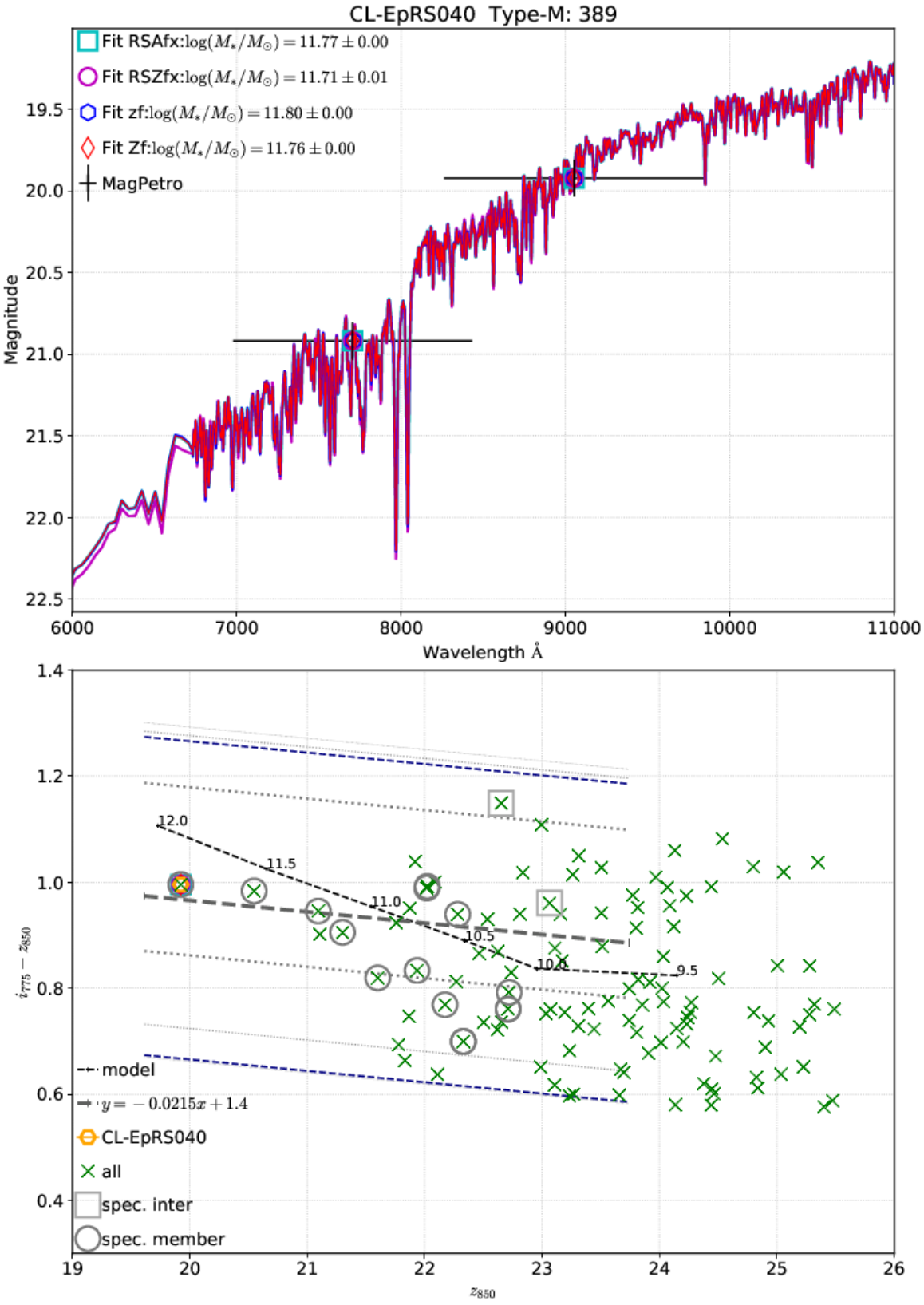

Figure 3.4 Example of the stellar mass estimation done for a galaxy in the cluster E.

3.1.1.7 Selecting ETGs by morphological parameters

In the next step, we select ETGs using morphological parameters, and create a mass-limited sample of quiescent ETGs. There are many ways to classify galaxy morphology. Visual classification which has a long history in morphological classification (e.g, Sandage, 1961, Dressler, 1980, Sandage & Tammann, 1981; recent studies by Fukugita et al., 2007 and Postman et al., 2005). There have also been classification using the light concentration (Morgan, 1958), and parameter combination of the concentration and mean surface brightness (Doi et al., 1993, Abraham et al., 1994), asymmetry (Abraham et al., 1996), or smoothness (Conselice, 2003, Yamauchi et al., 2005). The Gini coefficient is also adopted instead of the concentration parameter (Abraham et al., 2003) for its simplicity. Recently, machine learning scheme is introduced by Huertas-Company et al. (2011).

In Mitsuda et al. (2017), we have compared the parameters, Gini coefficient, asymmetry, concentration index, and mean surface brightness, to find the parameter sets which are the most insensitive to signal-to-noise ratio. We have investigated the reproducibility of the parameters by measuring the parameters in simulated noise-less and noise-added galaxy images. We have shown that the concentration parameter $C_{\rm in}$ and the mean surface brightness SB are less likely to be affected by signal-to-noise ratios. Thus, in this study, we make use of these parameters to select ETGs from the quiescent galaxy sample following Mitsuda et al. (2017).

The concentration index and mean surface brightness are measured in the similar manner as described in Mitsuda et al. (2017) and Doi et al. (1993, for further description). Here, we briefly introduce how the parameters are measured. We first determine an isophote aperture by collecting pixels above the certain limiting surface brightness $\mu_{\rm lim}$. We use the smoothed images with a Gaussian kernel of $\sigma = 2$ pixel to determine the isophote. The mean surface brightness SB is computed as the total flux within the aperture divided by the total area $A_{\rm aper}$. We derive the equivalent outer radius as $r_{\rm out} = \sqrt{A_{\rm aper}/\pi}$ and inner radius $r_{\rm in} = \alpha\, r_{\rm out}$, where α is set to 0.3 in this paper. The concentration index C_{in} is defined as the ratio between the fluxes within a circular aperture with $r_{\rm in}$ and that with $r_{\rm out}$.

We prepare interloper-subtracted images using `GALFIT` (Peng et al., 2002) on the z_{850} cut-out image as done in Mitsuda et al. (2017). The target galaxies are modeled by a single Sésic profile with its index n constrained between 0.2 and 16. Objects detected by `SExtractor` are fitted simultaneously or masked depending on the degree of overlap with the target galaxy. The PSF image of the

cluster field (Section 3.1.1.1) is convolved with the model before fitting with the actual galaxy image. We create interloper-subtracted images by subtracting nearby objects with the best-fit Sésic model convolved with the PSF. The interloper-subtracted images are used for measuring C_{in} and SB while other unsubtracted objects are masked.

In this study, $\mu_{\rm lim}$ is set to 24.0 $\rm mag\ arcsec^{-2}$ in the rest-frame g band. When we measure $C_{\rm in}$ and SB, we make the limiting brightness fainter taking account of the cosmological surface brightness dimming in which apparent brightness decreases as a function of redshift as $(1+z)^{-4}$. In addition to the cosmological dimming, we take account of the difference between the wavelength of the the rest frame g and z_{850} at $z\sim1.2$ We also taking account of the luminosity evolution of the galaxies. We set the limiting brightness so that it corresponds to the same stellar surface density between the high-redshift ETG sample and the low-redshift comparison sample (see below). For this purpose, we need some assumptions on the luminosity evolution because star formation and assembly history of galaxies are complicated. Here, we just adopt the difference of average luminosity between low- and high- redshift samples compared at the same stellar mass as the luminosity evolution. The difference of the wavelength between rest-frame g and z_{850} at $z\sim1.2$ is also included here.

In Figure 3.5, magnitude in z_{850} of the quiescent sample is shown as a function of the stellar mass. Also shown is the g-band magnitude of quiescent galaxies from the low-redshift comparison sample galaxies. We will describe the comparison sample later in Section 3.1.2. Magnitude and stellar masses are tightly correlated with a scatter of $\sim\pm0.5$ mag. We obtain the difference of running medians of the magnitude between the high- and low-redshift samples. The difference is almost constant at $\sim2.0-2.3$ mag with slight mass dependence in that the difference tends to be larger ($\sim2.2-2.3$ mag) for massive galaxies ($\log(M_*/M_\odot)>11$). We adopt the median, 2.1 mag, as the difference of average luminosity between low- and high- redshift samples. This is largely consistent with the luminosity evolution of $\sim2-3$ mag (in z_850 at $z\sim1.2$ to g at $z=0$) for galaxies with $\log(M_*/M_\odot)=11-12$ predicted by BC03 SSP models assuming passive evolution with no merger. For example, when we measure C_{in} and SB of a galaxy at $z\sim2$ where the cosmological surface brightness dimming becomes $\mu_{\rm dim}=-2.5\log(1+z)^4\sim3.4\rm mag\ arcsec^{-2}$, the limiting brightness is set to $\mu_{\rm lim}=24.0-2.1$ (luminosity evolution) $+3.4$ (surface brightness dimming) $=25.3\ \rm mag\ arcsec^{-2}$.

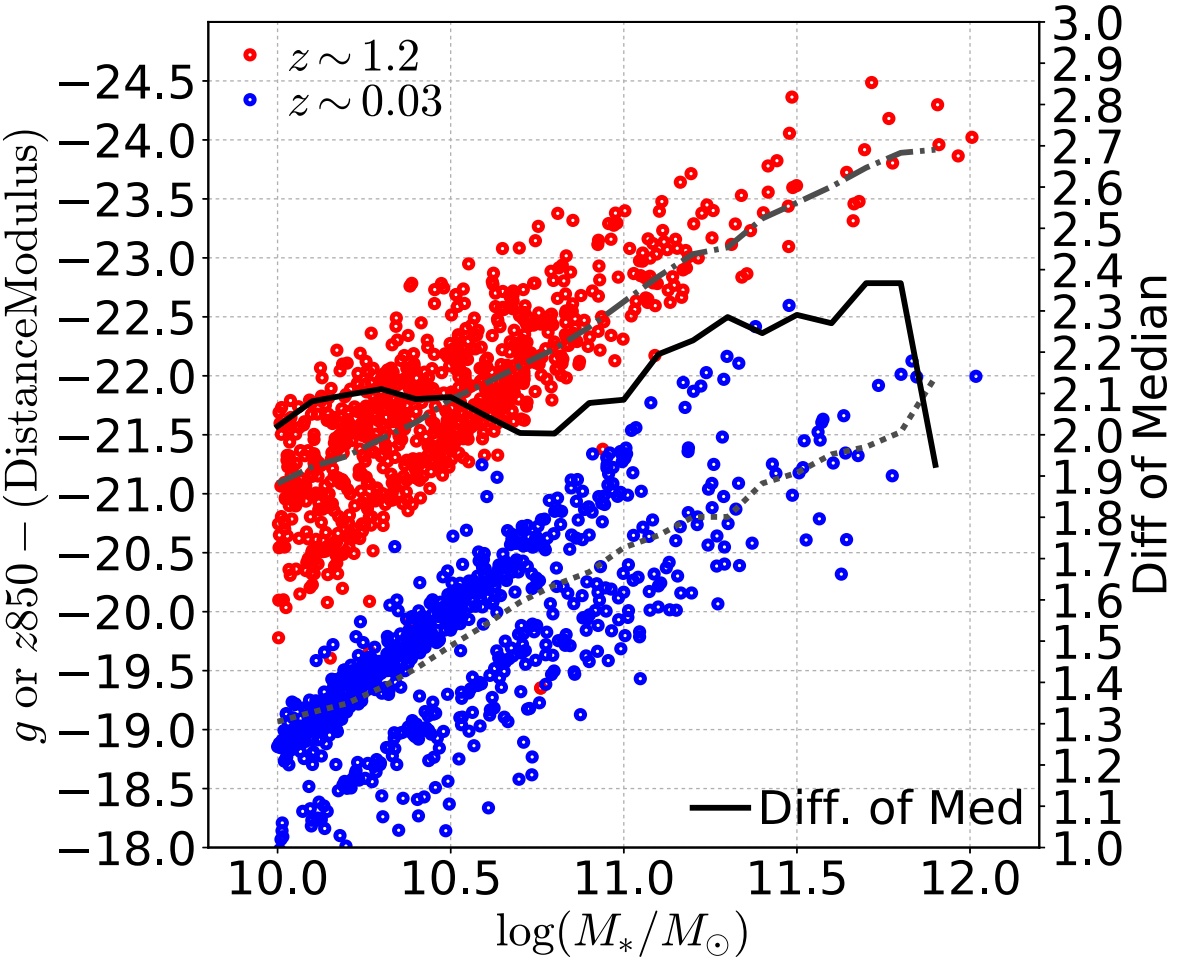

Figure 3.5 Magnitude (apparent magnitude - distance modulus) as a function of the stellar mass for the high- (z_{850}, red) and low-redshift (g, blue) quiescent galaxy samples. Gray dash-dotted and dotted lines indicate the running median of the magnitude for the high- and low-redshift samples, respectively. Black solid line indicates the difference of the running median with its scale given on the right-hand side.

We set the classification criteria for selecting ETGs from the quiescent sample as

$$\begin{aligned} C_{\rm in} &\geq -0.250(SB - 22.5) + 0.330 \ (M_{z_{850}} \leq -23), \ \text{or} \\ C_{\rm in} &\geq -0.133(SB - 22.5) + 0.392 \ (M_{z_{850}} > -23). \end{aligned} \tag{3.5}$$

The reason why the different criterion is adopted for luminous and less luminous galaxies is detailed in Mitsuda et al. (2017). Briefly, our target include massive elliptical galaxies with low surface brightness (Kormendy, 1977). As described in Doi et al. (1993), ETGs with low surface brightness ($\mu_e \gtrsim 23 - 24 \mathrm{mag\ arcsec^{-2}}$) and LTG with the brightness of $\mu_{\rm e} \gtrsim 23 \mathrm{mag\ arcsec^{-2}}$ overlap on the $C_{\rm in} - SB$ plane depending on the PSF size (see Figures 1 and 2 in Doi et al., 1993). As a result, massive ellipticals drop out from ETG selection if we simply adopt the criterion described in Doi et al. (1993). Therefore, we introduce the additional criterion for massive (luminous), low surface brightness galaxies.

In Figure 3.6, the concentration index and mean surface brightness ($C_{\rm in}$-SB diagram) is shown for the mass-limited quiescent sample. While majority of the galaxies are consistent with de Vaucouleurs (Sésic index $n = 4$) profiles, there is a fraction of galaxies which are consistent with exponential disks. By the separation line defined by Equation 3.6, galaxies with $n \lesssim 2$ are excluded.

3.1.1.8 Interlopers in the quiescent ETG sample

We estimate the contamination fraction of the interlopers for the quiescent ETG sample as we have done in Section 3.1.1.5. As shown in Figure 3.7, the fraction only slightly improved by the morphological selection. The fraction is $\sim$ 10 percent for $10.5 < \log(M_*/M_\odot < 11.5)$ and $\sim$ 25 percent for the lowest stellar mass bin. From the selected quiescent ETGs, we exclude known spectroscopic interlopers in the following analysis.

3.1.2 Low-redshift comparison sample

For comparison, we make a low-redshift sample of quiescent ETGs residing in massive clusters. The sample selection is almost the as in Mitsuda et al. (2017). The difference between the sample in this study and Mitsuda et al. (2017) is the stellar mass limit and selection criterion in the ETG selection. We briefly describe our sample selection. We make use of SDSS public DR12 (Alam et al., 2015). We extract target galaxies from the spectroscopic and imaging catalogs provided by SDSS, and we

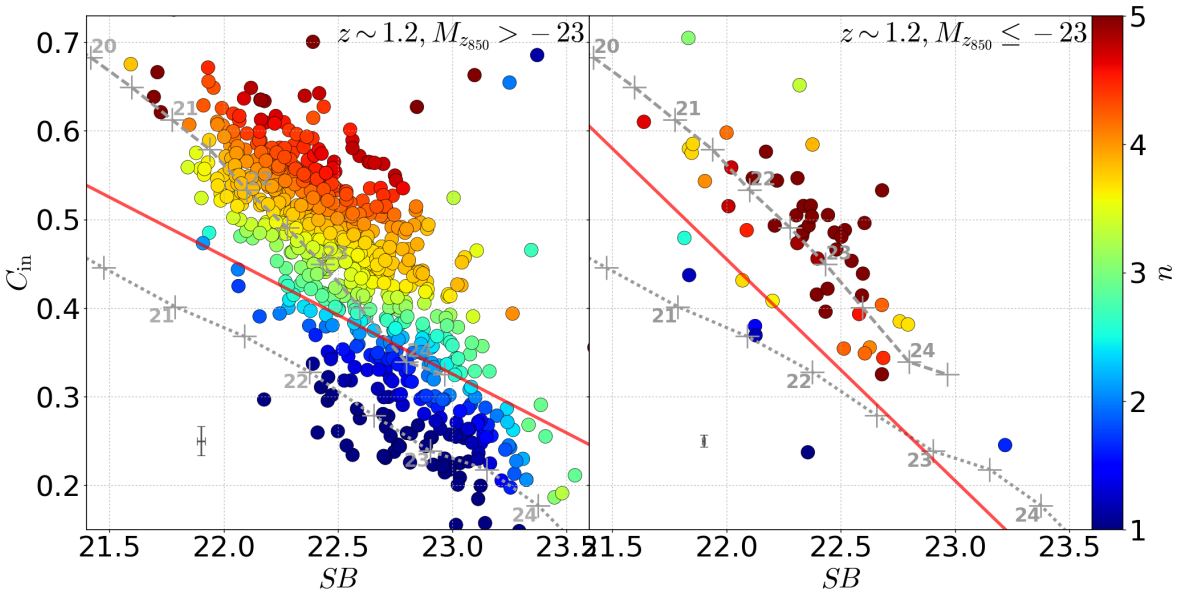

Figure 3.6 $C_{\rm in}$-SB diagram of the mass-limited quiescent galaxy sample for fainter ($M_{z_{850}} > -23$, left) and brighter ($M_{z_{850}} \leq -23$, right) galaxies. The Sérsic index n locally averaged (i.e., smoothed) around each point on the $C_{\rm in}$-SB plane is color coded. Gray dashed line indicates expected loci for galaxies with $n = 4$ Sérsic (de Vaucleur) profile with the surface brightness at the effective radius (mag arcsec^{-2}) noted in the figures while gray dotted line below indicates those for exponential disks with $n = 1$. Red solid line is the separation line defined in Equation 3.6 above which galaxies are selected as ETGs.

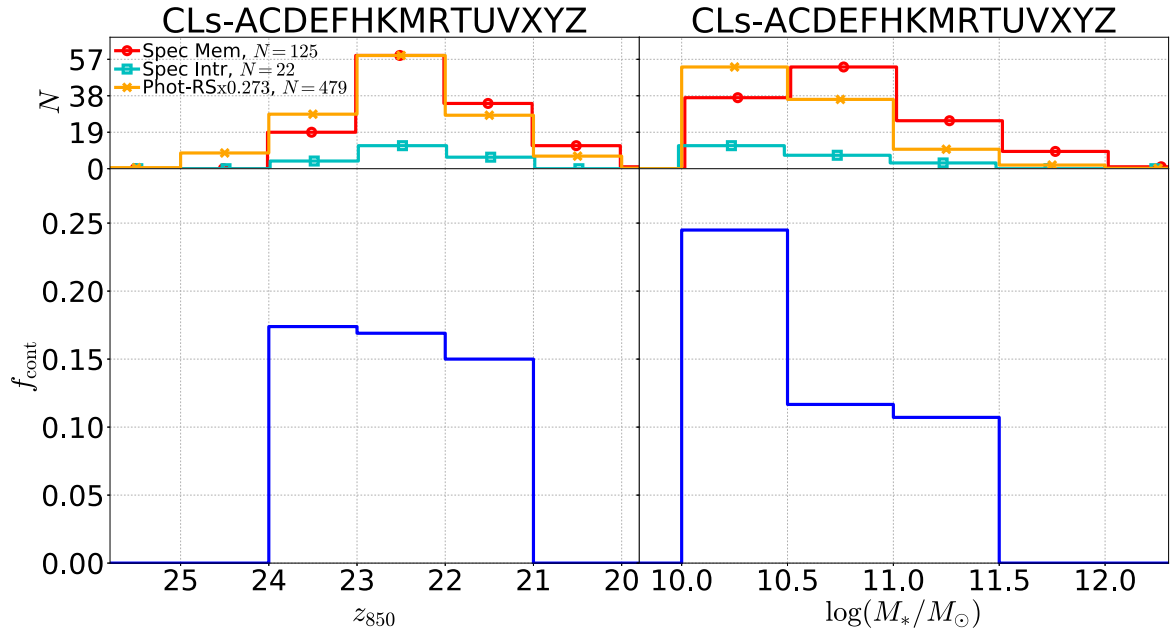

Figure 3.7 Same as Figure 3.3 but for ETGs selected by morphological parameters.

Table 3.6. Properties of the Low-Redshift Clusters

Cluster	RA(J2000) [h:m:s]	Dec(J2000) [d:m:s]	Redshift z	M_{200} $[10^{14} M_{\odot}]$	R_{200} [Mpc]
A0119	00:56:15.6	-01:14:56	0.0440	$15.1^{+2.1}_{-1.9}$	$3.7^{+0.2}_{-0.2}$
A1367	11:44:45.7	+19:42:11	0.0216	$8.0^{+0.9}_{-0.8}$	$3.0^{+0.1}_{-0.1}$
COMA	12:59:47.2	+27:56:19	0.0232	$27.1^{+2.9}_{-2.8}$	$4.5^{+0.2}_{-0.2}$
MKW8	14:40:38.3	+03:28:18	0.0270	$4.7^{+2.0}_{-1.2}$	$2.5^{+0.3}_{-0.2}$
A2052	15:16:44.3	+07:01:16	0.0348	$4.3^{+0.1}_{-0.2}$	$2.5^{+0.0}_{-0.0}$
MKW3S	15:21:51.4	+07:42:21	0.0450	$6.8^{+0.7}_{-0.7}$	$2.8^{+0.1}_{-0.1}$
A2063	15:23:05.6	+08:36:40	0.0354	$6.4^{+0.5}_{-0.4}$	$2.8^{+0.1}_{-0.1}$
A2147	16:02:15.1	+15:57:31	0.0351	$6.8^{+2.3}_{-1.4}$	$2.8^{+0.3}_{-0.2}$
A2199	16:28:38.1	+39:32:52	0.0302	$9.4^{+0.7}_{-0.7}$	$3.2^{+0.1}_{-0.1}$

References. — Reiprich & Böhringer (2002)

use g-band images for the morphological classification as well as surface photometry. The central wavelength of SDSS g-band for galaxies at $z \sim 0.03$ is the similar, in terms of rest-frame wavelength, to z_{850} for galaxies at $z \sim 1$.

Low-redshift galaxies are selected from those residing in massive clusters. We selected nine low-redshift massive clusters which are likely descendants of the high-redshift ones based on halo masses (M_{200}) and redshifts. We make use of a galaxy cluster catalog by Reiprich & Böhringer (2002) who study basic properties of low-redshift clusters such as mass and radius based on X-ray observations. The clusters are selected if they (i) lie in the redshift range $0.02 < z_{\rm CL} < 0.05$, (ii) lie within the SDSS imaging and spectroscopic surveys, and (iii) more massive than $\log(M_{200}/M_{\odot}) \sim 14.5$. They are A0119, A1367, COMA, MKW8, A2052, MKW3S, A2063, A2147, and A2199. The median halo mass is $\log(M_{*}/M_{\odot}) \sim 14.8$. We summarize properties of the clusters in Table 3.6. The redshift range is determined so that the PSF size of SDSS images for $z \sim 0$ galaxies become comparable to that of ***HST*** ACS z_{850} images for $z \sim 1$ galaxies in physical scales. By doing so, we try to make effects of PSF on surface photometry comparable between high- and low-redshift samples. The median PSF size of SDSS images is 1.3 arcsec FWHM which corresponds to $0.53 - 1.3$ kpc at $z = 0.02 - 0.05$ while that of ***HST*** ACS z_{850} images (0.11 arcsec) corresponds to $0.87 - 0.95$ kpc at $z = 0.9 - 1.5$.

The halo mass of the low-redshift clusters spans from $\log(M_{200}/M_{\odot}) \sim 14.6$ to 15.2, which are slightly larger than the high-redshift clusters. Considering halo mass growth from z$\sim$1 to 0 (e.g., Zhao et al., 2009), the high-redshift clusters with the halo mass of $\sim 10^{14.5} M_{\odot}$ will evolve to as massive as $\sim 10^{15} M_{\odot}$ at $z \sim 0$. Therefore, the selected low-redshift clusters are the likely descendants of the high-redshift ones.

3.1.2.1 Selection of the Low-Redshift Galaxies

Then, member galaxies of each cluster are selected based on SDSS spectroscopic catalog. From the catalog, all galaxies within $0.5 \times R_{200}$ radius from the cluster center and within a redshift range of $z_{\rm CL} - \Delta z \leq z \leq z_{\rm CL} + \Delta z$ are selected, where we set $\Delta z = 0.0067$ which corresponds to 2000 $\mathrm{km \cdot s^{-1}}$. In total, 3278 galaxies with SDSS spectroscopy ($r < 17.77$ mag) are selected at this point. The median redshift is $z \sim 0.029$

3.1.2.2 Quiescent galaxy selection for the low redshift

In the next step, quiescent galaxies are selected based on the $u - g$ color and g magnitude diagram. This is done in the same manner in Mitsuda et al. (2017). Briefly, we compare the $u - g$ color and g magnitude to the synthetic color magnitude relation which is derived from the stellar mass-age and stellar mass-metallicity relation of nearby quiescent ETGs (Thomas et al., 2005) using BC03 SSP models with Salpeter IMF.

We select likely descendants of the high-redshift quiescent galaxies as the low-redshift counterpart but it is not a simple task because we need to assume luminosity and color evolution. Here, we assume passive evolution with no mergers. We obtain the color magnitude relation for the SSP that have a smaller metallicity by three times the intrinsic scatter ($\sigma_{[Z/H]} \sim 0.08$dex, see Thomas et al., 2005) from the mean stellar mass-metallicity relation and a fixed age of 7 Gyr which corresponds to the look-back time to $z \sim 0.9$, the lowest redshift of the high-redshift galaxies. We consider the color magnitude relation obtained this way as the bluest limit for passively evolving galaxies from $z \sim 1$, and select galaxies with redder $u - g$ colors than the limit. The color magnitude diagram of the low-redshift galaxies and the synthetic color-magnitude relation is shown in Figure 2 in Mitsuda et al. (2017)

3.1.2.3 Stellar mass limit for the low redshift

We set a stellar mass limit of $\log(M_*/M_\odot) \geq 10.0$ in this study in order to match the limit to the high-redshift samples. The limit is slightly different from that in Mitsuda et al. (2017). We describe possible concerns arising from setting the new stellar mass limit below. In Mitsuda et al. (2017), as we have selected galaxies with the mass limit of $\log(M_*/M_\odot) \geq 10.5$, all galaxies in the sample are brighter than $r = 17.77$, the magnitude limit of the SDSS spectroscopic survey, taking account of their mass-to-luminosity ratio (M/L). However, in our new sample, some of low mass galaxies ($10 \leq \log(M_*/M_\odot) < 10.5$) with large M/L (i.e., the reddest galaxies) could be fainter than $r = 17.77$. As the low-redshift quiescent galaxies have the median $g - r$ color of 0.77, the magnitude limit for the SDSS spectroscopy corresponds to $g \sim 18.54$ which is -18.19 in absolute magnitude at $z = 0.05$. This magnitude corresponds to $\log(M_*/M_\odot) \sim 10.5$ for galaxies with the largest M/L (e.g., Figure 3.5). The critical redshift below which all galaxies with $\log(M_*/M_\odot) \geq 10.0$ can be included in the SDSS spectroscopic catalog ($r < 17.77$) is $z \sim 0.04$. Since redshifts of the majority of the clusters (7/9) are less than 0.04, the fraction of galaxies more massive than $\log(M_*/M_\odot) = 10.0$ but excluded by the magnitude limit may be small. Therefore, we consider that setting the stellar mass limit to $\log(M_*/M_\odot) \geq 10.0$ does not significantly change the results.

3.1.2.4 Morphological ETG selection for the low redshift

We select ETGs from the quiescent sample as for the high-redshift sample using $C_{\rm in}$ and SB. We use the surface brightness limit for measuring SB to rest-frame 24.0 mag arcsec^2. The cosmological surface brightness dimming is taken into account. The selection criterion of the low-redshift ETGs is given as

$$\begin{aligned} C_{\rm in} &\geq -0.250(SB - 22.5) + 0.330 \ (M_g \leq -20.5), \text{ or} \\ C_{\rm in} &\geq -0.133(SB - 22.5) + 0.392 \ (M_g > -20.5). \end{aligned} \tag{3.6}$$

This criterion is slightly different from that in Mitsuda et al. (2017) as the surface brightness limit has been set to 24.5 mag arcsec^2 in that paper. In Figure 3.8, $C_{\rm in}$ and SB of the mass limited low-redshift quiescent sample. Similarly to the high-redshift sample, on average, galaxies with the Sésic index greater than 2 are selected as ETGs.

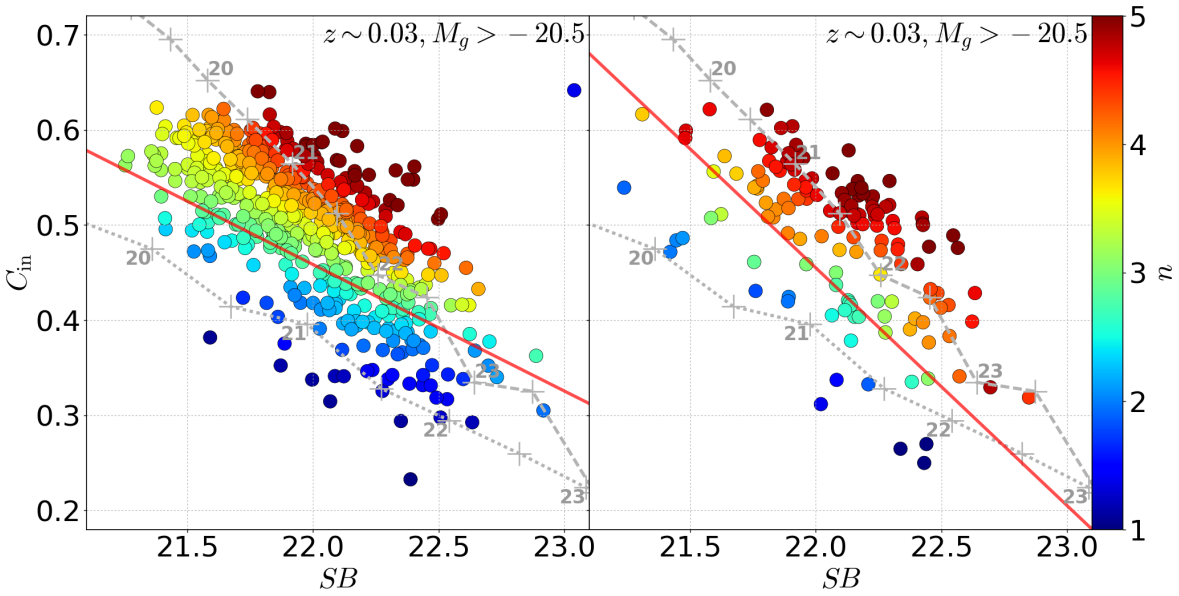

Figure 3.8 $C_{\rm in}$-SB diagram of the mass-limited quiescent galaxy sample for fainter ($M_g > -20.5$, left) and brighter ($M_g \leq -20.5$, right) galaxies. Color coding and symbols are the same as in Figure 3.8.

3.1.3 Properties of the samples

In the end of this section, we summarize basic properties of the high- and low-redshift samples.

3.1.3.1 Stellar mass distribution

In Figure 3.9, we show the stellar mass distribution of the high- and low-redshift ETG samples (left panels) as well as parent quiescent samples from which ETGs are selected (right panels). Top panels show the number of galaxies within $0.5 \times R_{200}$ per galaxy cluster per stellar mass bin, whereas bottom panels show the normalized version of the top panels. From the normalized histograms of the ETG samples, the shape of the stellar mass distribution is similar between the high and low redshifts. The Kolmogorov-Smirnov (KS) test indicates that the two samples are statistically indistinguishable with the large p-value of 0.11. Many previous cluster studies have shown that the shape of luminosity function of ETGs has not changed from $z \sim 1$, assuming passive evolution (e.g., de Propris et al., 1998, 1999, Lin et al., 2006, De Propris et al., 2007, Cerulo et al., 2016). Our samples are in line with these studies.

For the parent quiescent sample, the fraction of low mass ($\log(M_*/M_\odot) < 10.5$) is larger than

the ETG samples both for the high- and low-redshift samples. The shape of the distribution is still similar between low- and high-redshift samples, although the KS test indicates $> 2\sigma$ difference (but less than 3σ) with the p-value of 0.029. Also, looking at the high-redshift spectroscopic member ETGs (magenta histograms in Figure 3.9), the decline of the number of lower mass galaxies than $\log(M_*/M_\odot) \sim 10.5$ indicates that the stellar mass limit for the spectroscopic members is around there.

The stellar mass distribution without normalization, i.e., the number of galaxies per cluster in each stellar mass bin, carries information about evolution of the distribution of galaxies in a halo (halo occupation) which can be inferred from a scaling relation between the number of galaxies in a cluster (i.e., richness $N_{\rm gal}$) and cluster halo mass (e.g., Lin et al., 2003). For our samples, the average cluster halo mass M_{200} increases from $\log(M_{200}/M_\odot) \sim 14.6$ at $z \sim 1.2$ to $\log(M_{200}/M_\odot) \sim 14.8$ at $z \sim 0.03$. On the other hand, the total number of ETGs with $log(M_*/M_\odot) \geq 10$ per cluster increases from 28 ($= 692/25$) to 69 ($= 621/9$) from $z \sim 1.2$ to $z \sim 0.03$. Taking account of the scaling relation between richness and cluster halo mass $N_{\rm gal} \propto (1+z)^\gamma M_{200}^s$* (Lin et al., 2006, Andreon et al., 2008a), where $s \sim 0.8$ (Lin et al., 2004, 2006). We input $N_{\rm gal}$, z, and M_{200} of the high- and low-redshift ETG samples, and compare the scaling relation. Then, we obtain the redshift evolution factor $\gamma \sim -0.4$, which is in agreement with previous studies (Lin et al., 2006, Andreon et al., 2008a). The slightly negative value of γ indicates that the evolution of the richness can be mostly explained by passive evolution of ETGs with mild increase of newly emerging ETG probably due to quenching of star-forming galaxies (i.e., the progenitor bias).

The mild increase of newly quenched galaxies in the low-redshift sample is naturally expected. At redshift ~ 1, although the core of massive clusters (< 0.5 Mpc) are dominated by quiescent galaxies, the outer part is well populated by star-forming galaxies (Muzzin et al., 2012). Therefore, as the high-redshift clusters grown in the virial mass and radius, those star-forming galaxies are included in the low-redshift sample if they quench star-forming activity. Thus, there is a possibility that the newly quenched galaxies below $z < 1$ are included in the low-redshift sample. Note that, however, we have not applied any correction for completeness and contamination when we derive the stellar mass distribution, and the derived γ parameter is only a rough estimate.

* The original formula has a normalization constant. But as it depends on the lower mass limit of the sample and the choice of the virial mass such as M_{200} or M_{500}, we do not take account of the normalization, and only consider the proportionality.

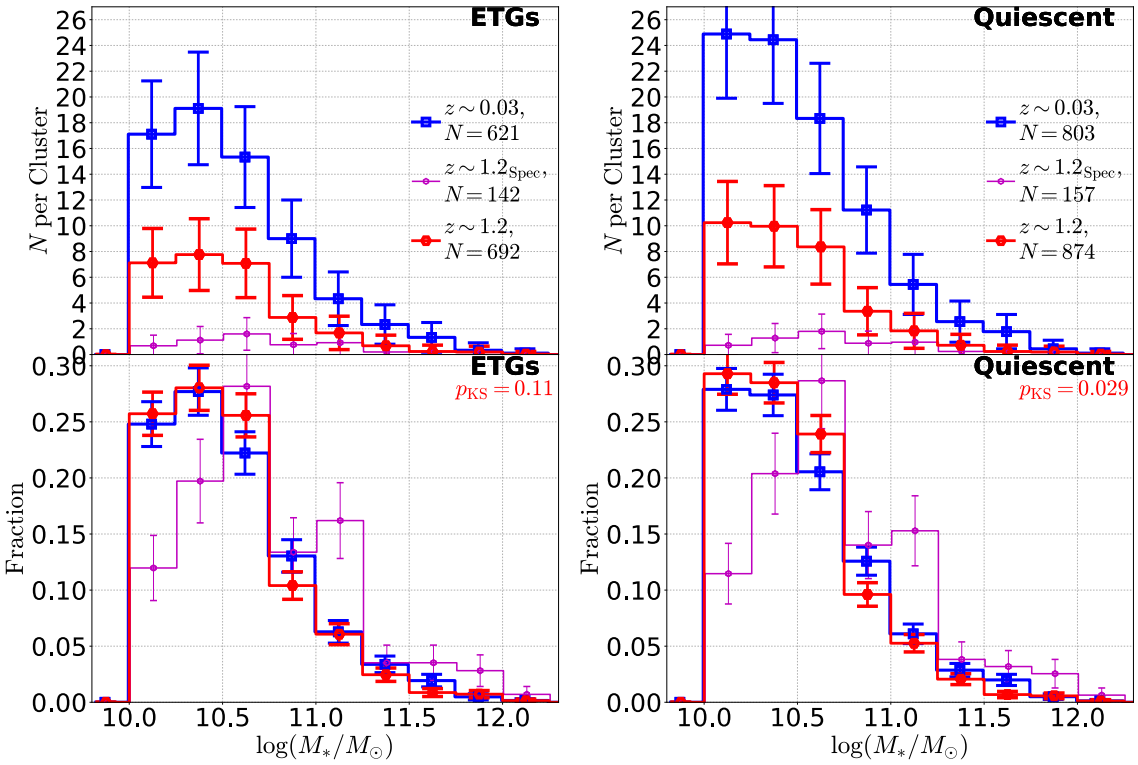

Figure 3.9 Left: Stellar mass distribution of the ETG samples The high-redshift sample is shown by red while the low-redshift by blue. Also shown by magenta is the stellar mass distribution for spectroscopic members in the high-redshift sample. Top: Number of galaxies per bin per cluster (i.e., within $0.5 \times R_{200}$). The total number of galaxies used in the plot is presented in the legend. Bottom: Normalized version of the top panel. The total number is normalized to unity. Error bars are given assuming the Poisson noise. Right: Same as left but for the quiescent samples.

3.1.3.2 Ellipticity distribution

In Figure 3.10, we show the ellipticity ϵ distribution of the high- and low-redshift ETG samples. The ellipticity is converted from axis ratio $q = b/a$ as $\epsilon = 1 - q$ where a and b are semi-major and minor axes. The axis ratio is measured by GALFIT. We note that for one galaxy in the high-redshift sample, GALFIT failed to fit a model, which is the reason why the sample size here is $N = 691$ instead of 692. In our previous study, the evolution of ellipticity is only marginal (Mitsuda et al., 2017). In this study, however, by increasing the sample size using photometric quiescent ETG members, we detect significant evolution in the ellipticity distribution. The Kolmogorov-Smirnov test indicates the high- and low-redshift samples are different with the p-value of 0.01 for the whole sample (panel (a) in Figure 3.10). The median ellipticity is 0.36 ± 0.03 for the high-redshift sample and 0.31 ± 0.03 for the low-redshift, where the uncertainty is derived from 10000 times bootstrapping. If we divide the samples in stellar mass bins, the difference of the ellipticity distribution is significant only for the $10.5 \leq \log(M_*/M_\odot) < 11$ bin although the ellipticity is marginally larger (i.e., flattened) for the high-redshift ETGs in other bins. The fact that high-redshift ETGs have larger ellipticity is consistent with other studies on ETGs in clusters (e.g., De Propris et al., 2015, 2016) as well as in fields (e.g., Chang et al., 2013b,a).

3.1.3.3 Size distribution

In Figure 3.11, we show the effective radius distribution of the high- and low-redshift ETG samples. The effective radius $r_{\rm e}$ is measured by GALFIT. In the histograms in the figure, $r_{\rm e}$ is normalized with the stellar mass at $\log(M_*/M_\odot) = 11$ in order to remove the correlation between $r_{\rm e}$ and M_* (Newman et al., 2012, Cimatti et al., 2012). The mass-normalized effective radius $r_{{\rm e},M_{11}}$ is given as

$$\log(r_{{\rm e},M_{11}}) = (\log(M_*/M_\odot) - 11) - \beta. \tag{3.7}$$

The parameter β corresponds to the slope of a linear mass-size relation, $\log(r_{\rm e}) = \beta(\log(M_*/M_\odot) - 11) + \alpha$, which is indicated in the panels (b) and (d) by cyan and orange lines. In this study β is fixed to 0.57 following Delaye et al. (2014). Similarly to previous studies (Delaye et al., 2014, Mitsuda et al., 2017), a significant size evolution is found for the whole samples (see KS p-value in Figure 3.11). The KS tests indicates statistically significant difference for galaxies less massive than $\log(M_*/M_\odot) = 11$

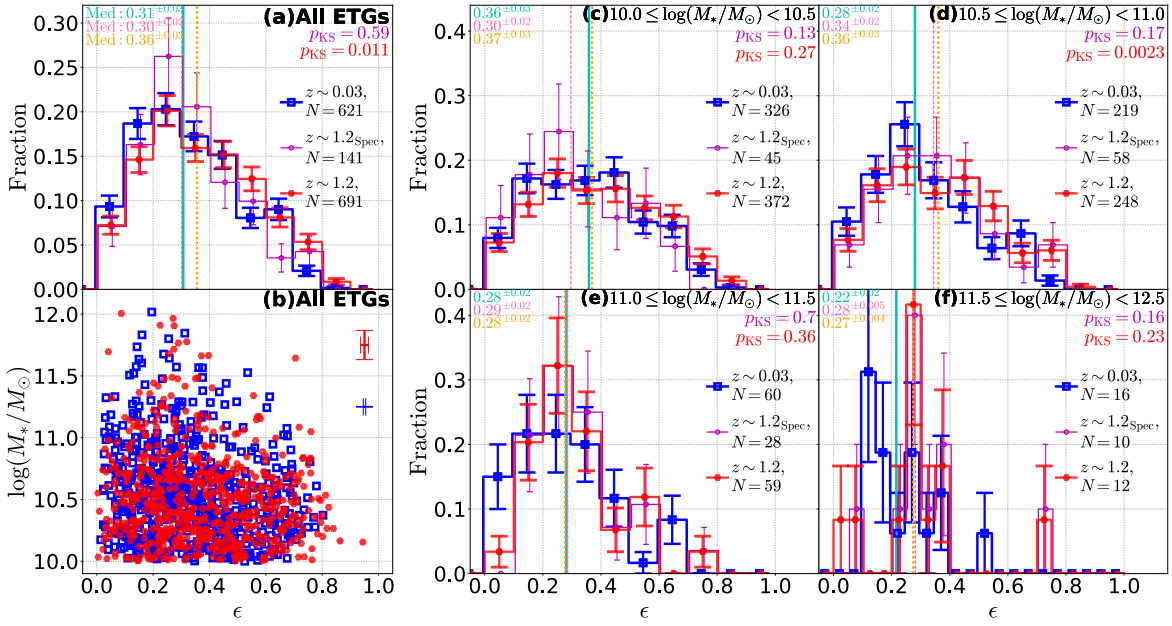

Figure 3.10 Ellipticity of the ETG samples. (a): Ellipticity distribution of the high- (red histogram) and low-redshift (blue histogram) ETGs. Magenta histograms is that of spectroscopic members in the high-redshift sample. Median values for high-, low-redshift sample, and spectroscopic members are written in the panel with orange, cyan, and pink, respectively. The total number of galaxies used in the plot is presented in the legend. (b): Ellipticity and stellar mass distribution of the high- (red) and low-redshift (blue) ETGs. Median uncertainty is shown by error bars. (c)-(f): Same as (a) but for different stellar masses noted in the panels.

($p_{\rm KS} < 0.004$), In higher mass bins, although the KS p-value is not small, median $r_{{\rm e},M_{11}}$ is smaller for the high-redshift sample. The statistically significant size difference is also observed for round galaxies. Even if we divide the samples into mass bins, the significant difference can be observed in the stellar mass bin, $10.5 < \log(M_*/M_\odot) < 11$ ($p_{\rm KS} = 3 \times 10^{-5}$).

3.1.3.4 Sérsic index distribution

In Figure 3.12, we show the Sésic index n distribution of the high- and low-redshift ETG samples. The distribution is significantly different for the whole samples as well as for those with $\log(M_*/M_\odot) < 11$, and the high-redshift ETGs tend to have smaller n. The similar trend is also found for the round galaxies. In spite of the morphological selection with which galaxies $n \gtrsim 2$ are selected, the high-redshift galaxy contains significant fraction of $n < 2$ galaxies especially in the low mass regime ($\log(M_*/M_\odot) < 11$). We have checked the Sésic index distribution for the parent quiescent samples, and we have found that the high-redshift quiescent sample has larger fraction of galaxies with $n < 2$. Later, we will discuss the influence of the morphological selection on the results which will be presented in the next section.

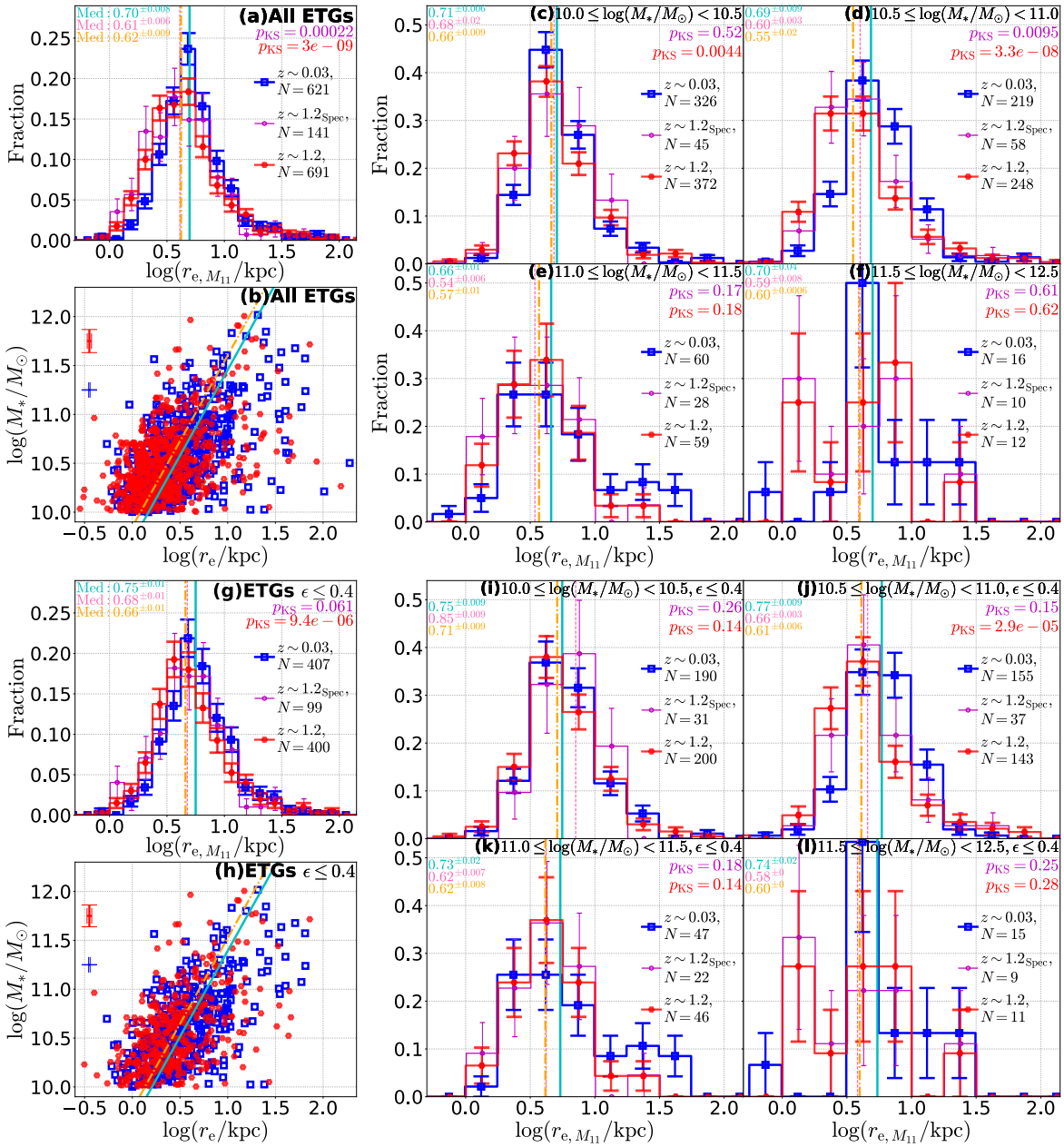

Figure 3.11 (a)-(f): Same as Figure 3.10, but for the effective radius $r_{\rm e}$. (a): Mass-normalized effective radius $r_{\rm e,M_{11}}$, see text) distribution of the high- (red histogram) and low-redshift (blue histogram) ETGs. We also present the p-values of KS tests ($p_{\rm KS}$) between the low- and high-redshift sample by red text while those between the low and spectroscopic high-redshift sample are shown by magenta. Also shown in cyan, pink, and orange in the upper left corner are median values of $r_{\rm e,M_{11}}$ for the low-, the spectroscopic high- and the high-redshift samples with their uncertainty derived from bootstrap resampling. (b): Effective radius $r_{\rm e}$ and stellar masses of the high- (red hexagons) and low-redshift (blue squares) ETGs. The median uncertainty is shown by the error bars. The linear mass-size relations with a fixed slope of 0.57 is fitted to the $r_{\rm e}$ and M_* distribution for the high- and low-redshift samples are presented by orange dash-dotted and cyan solid lines. (c)-(f): Same as (a) but for different stellar masses noted in the panels. (g)-(l): Same as (a)-(f) but for round galaxies with $\epsilon \leq 0.4$.

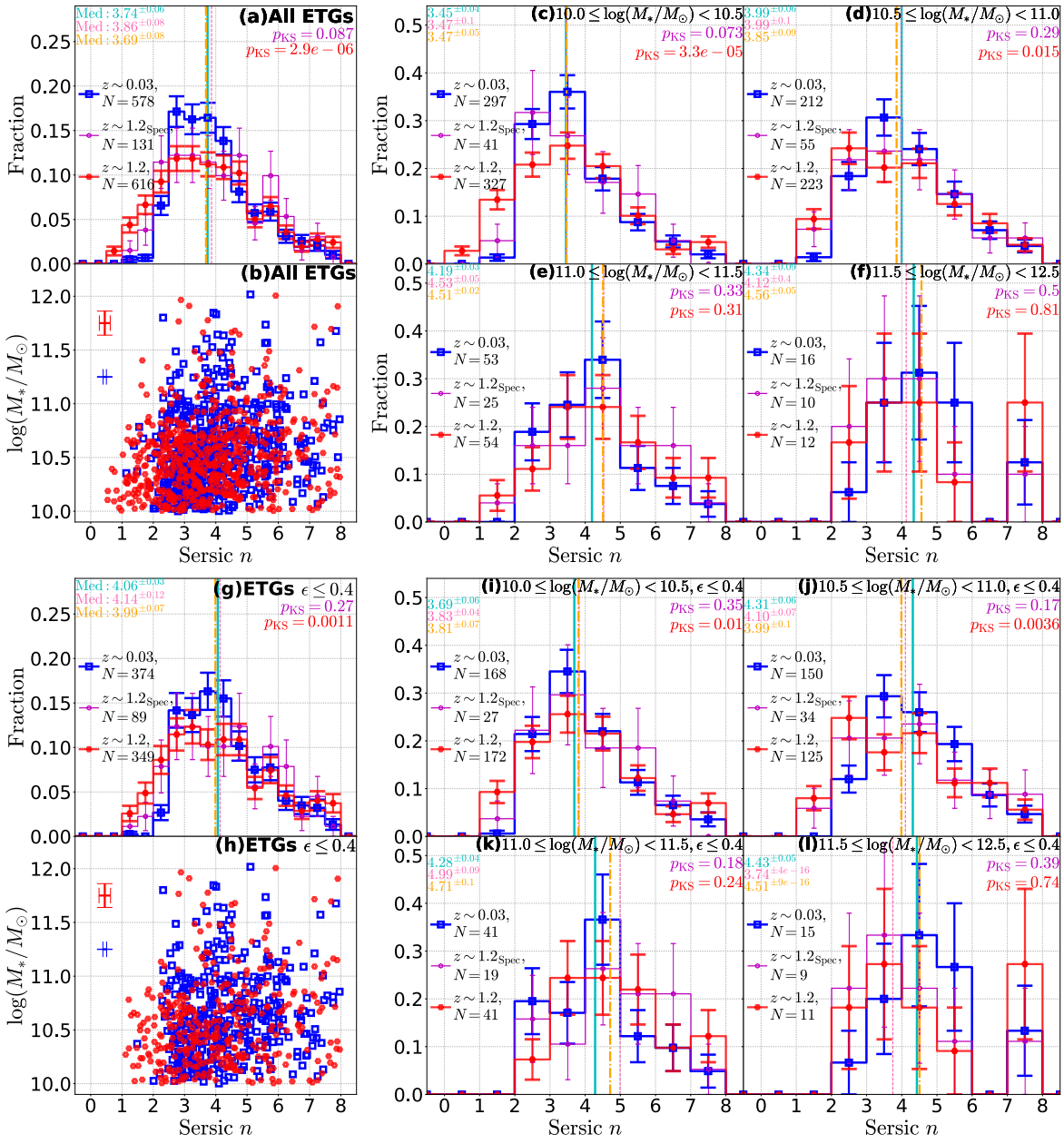

Figure 3.12 (a)-(f): Same as Figure 3.11, but for the Sérsic index n. (a): Sérsic index distribution of the high- (red histogram) and low-redshift (blue histogram) ETGs. (b): Sérsic index and stellar masses. (c)-(f): Same as (a) but for different stellar masses noted in the panels. (g)-(l): Same as (a)-(f) but for round galaxies with $\epsilon \leq 0.4$.

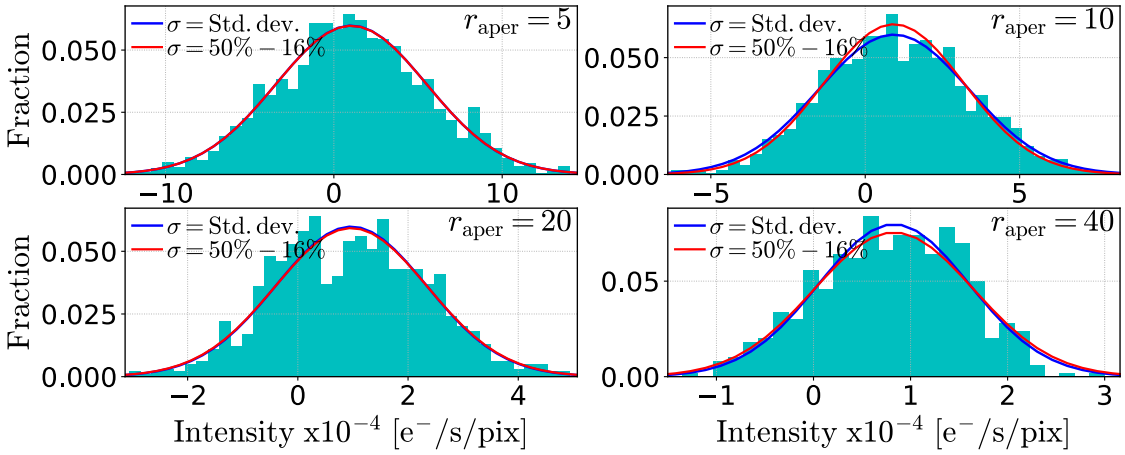

Figure 3.13 Example of background residual analysis done for a high-redshift galaxy in the cluster A. Cyan histogram is distribution of the median intensity within randomly placed apertures with the size noted on the top right of each panel. Blue curves represent for Gaussian distribution with the median and standard deviation derived from the intensity distribution. Red curves are also Gaussian but with its width (σ) set to the interval between 16 and 50 percentiles.

3.2 Measuring the Slopes of Light Profiles of Distant Galaxies

In this section, we describe how we obtain radial light profiles of the high- and low-redshift ETGs and measure the inner and outer profiles. We use the z_{850} cutout images for the high-redshift galaxies while we use g cutouts for the low redshifts.

3.2.1 Measuring light profiles

We take the same procedure as in Section 2.2 in the previous chapter. First, we generate a mask for each galaxy. All objects detected by `SExtractor` (see Section 3.1.1.3) are masked with the segmentation map created by the program. We use the interloper-subtracted images created in Section 3.1.1.7 with pixels belonging to the subtracted objects masked. We use elliptical aperture with fixed central position, position angle, and ellipticity to those measured by `SExtractor`. With the images and masks, we obtain radial (semi-major axis) surface brightness profile.

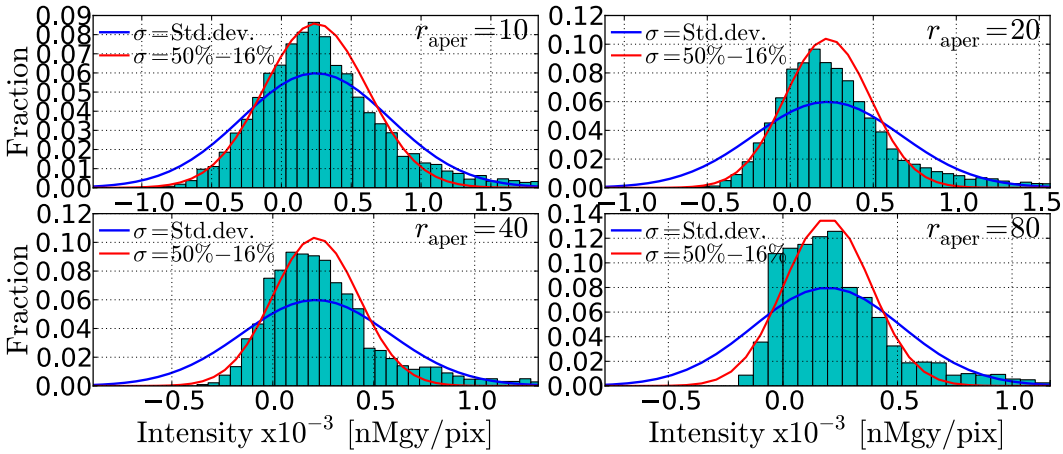

Figure 3.14 Same as Figure 3.13 but for a low-redshift galaxy.

3.2.1.1 Background residual subtraction

The background of the SDSS and HST images has already been subtracted. There could be, however, residual of the global background level as well as local one due to the fluctuation of the background level in an image, although the background is subtracted taking account of spatial variation both for SDSS and HST images. We estimate the global and local background residual in the same manner as described in Section 2.2.1.3. We randomly put circular apertures with various radii on the mosaic images, take median intensity, and estimate the median ($\sim$ global residual, $\mu_{\rm bg}$) and standard deviation ($\sim$ spatial fluctuation of residual, $\sigma_{\rm bg}$) of the median intensity within the apertures. We prepare an aggressive mask by which all objects detected by `SExtractor` are masked out either by ellipses with the semi-major radius of $4 \times r_{\rm Petro}$ or the segmentation map. The size of the circular apertures are determined taking account of apparent sizes of the galaxies. For high-redshift galaxies, we set the aperture radii to $r_{\rm aper} = 5, 10, 20, 40$ pixels and the number of aperture put on an image to $N_{\rm aper} = 2000, 1500, 1000, 500$, respectively for the aperture sizes. For low-redshift galaxies, these value are $r_{\rm aper} = 10, 20, 40, 80$ and $N_{\rm aper} = 2000, 1500, 1000, 500$. We exclude apertures which have smaller fraction of unmasked pixels than 75 percent.

Figure 3.13 is an example of the background analysis for a high-redshift galaxy in the cluster A. Figure 3.14 is the same figure but for a low-redshift galaxy. While the distribution of the median intensity can be well described by Gaussian (blue curves) for the high-redshift galaxy, that for the low-redshift deviates from Gaussian when its width σ is set to the standard deviation of the distribution.

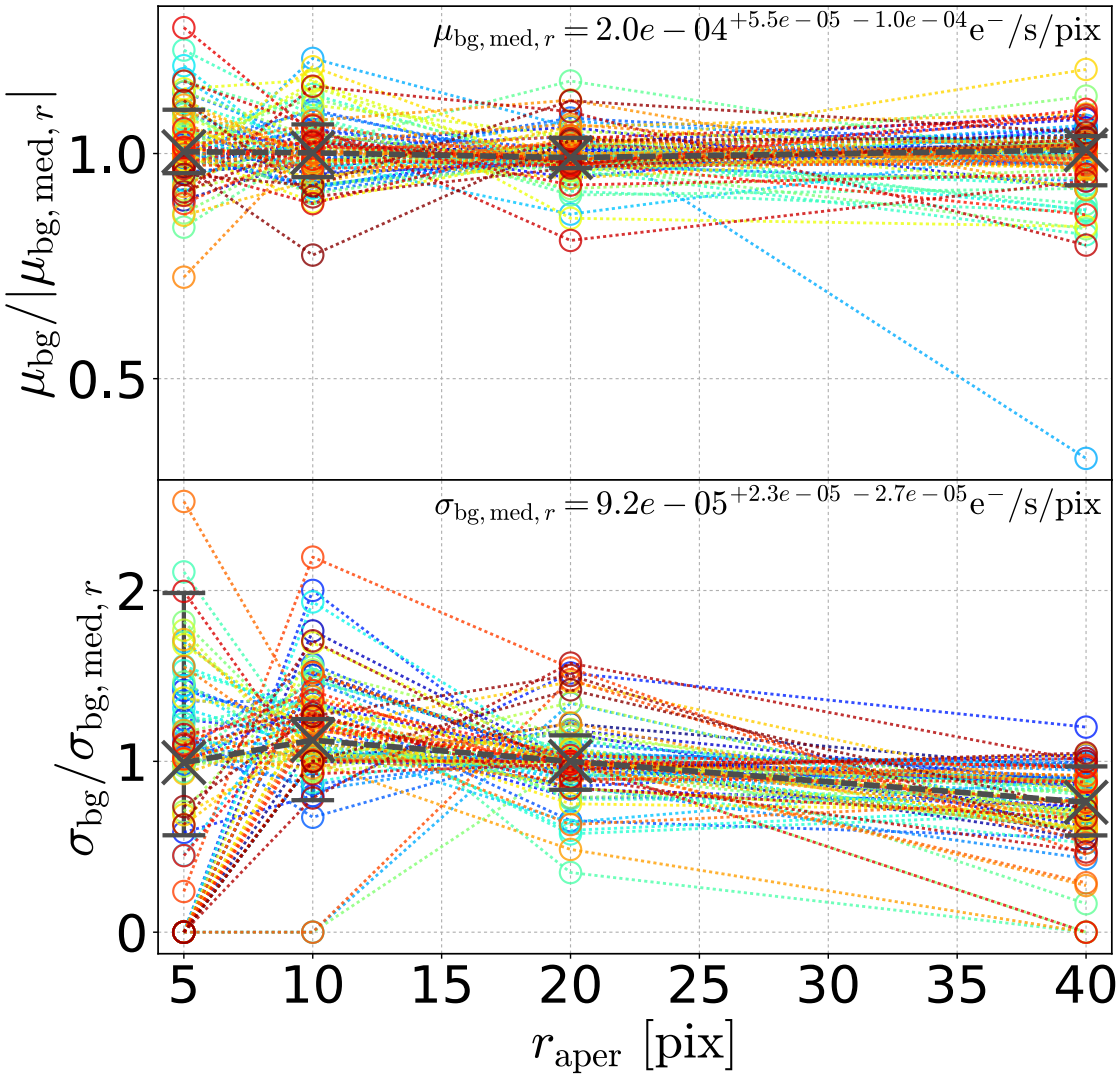

Figure 3.15 μ_{bg} (top) and σ_{bg} as a function of the aperture size for all ETGs in the cluster A. The vertical axis is normalized with the median taken along the x-axis ($\mu_{\mathrm{bg,med},r}$ and $\mu_{\mathrm{bg,med},r}$) which are noted in the panels. 16, 50, and 84 percentiles for each aperture are shown by gray crosses.

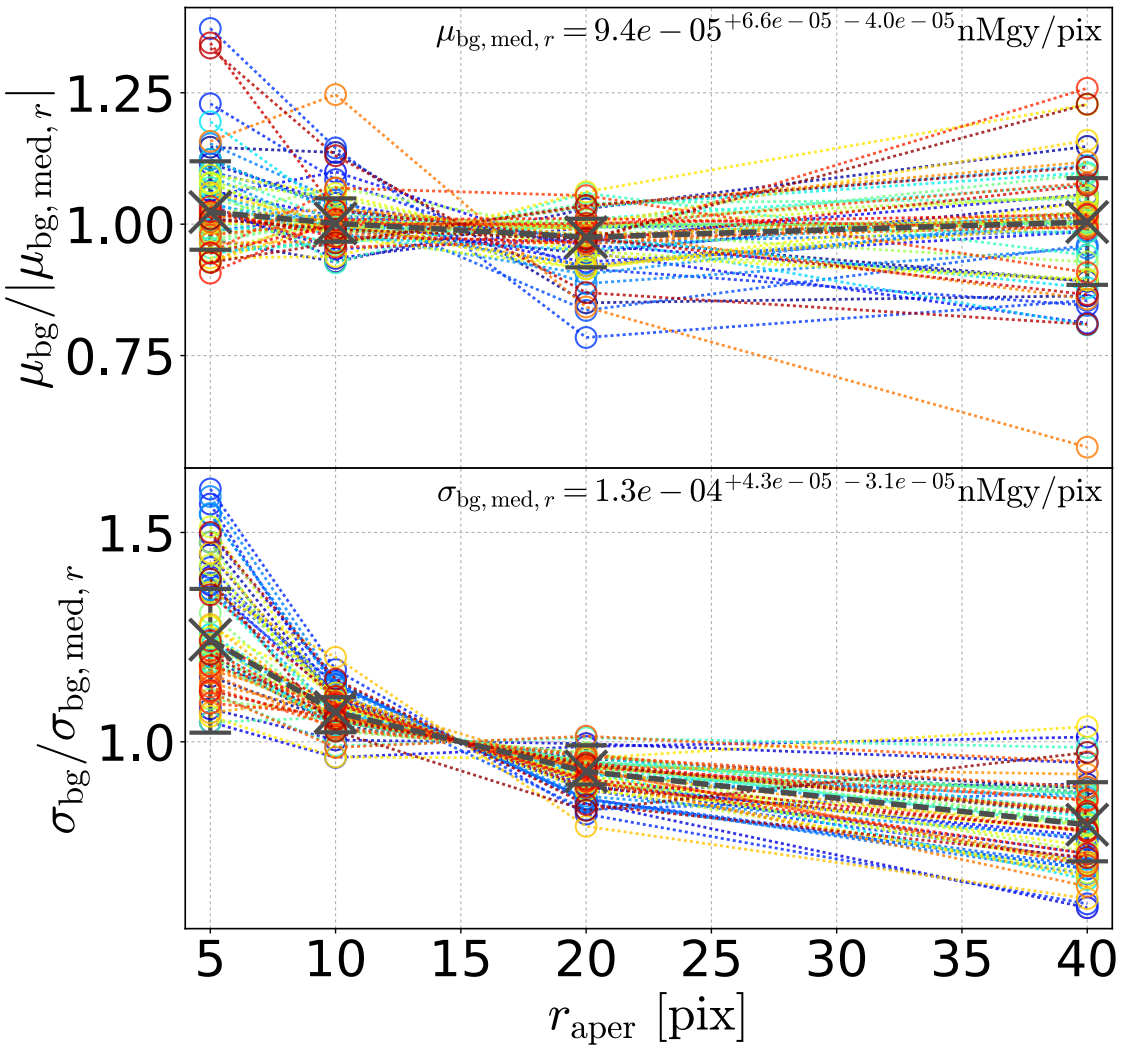

Figure 3.16 Same as Figure 3.15 but for a low-redshift cluster A0119.

As we have seen in Section 2.2.1.3, the deviation is due to the extended positive wing arising from insufficient masking of undetected objects. The situation is similar for other low-redshift galaxies. On the other hand, the median intensity distribution for the high-redshift galaxy has no extended wing implying that faint objects are detected thanks to high sensitivity of HST and very long exposure.

In Figures 3.15 and 3.16, the median of the median intensity ($\mu_{\rm bg}$) and fluctuation of it are shown as a function of the aperture size $r_{\rm aper}$. Here, $\mu_{\rm bg}$ is derived by quadratically subtract contribution of noise from the interval between 16 and 50 percentile. For the high-redshift cluster A, there is no dependence of $\mu_{\rm bg}$ and $\mu_{\rm bg}$ on $r_{\rm aper}$. For this cluster, there is significant global residual $\mu_{\rm bg} \sim 2.0^{-4}$ e$^-$/s which corresponds to $\sim$ 28 mag arcsec^2, which means background is under-subtracted. The global background residual for high-redshift galaxies varies for different cluster fields. For the low-redshift galaxy, situation is almost the same in Section 2.2.1.3. From radial light profiles, we subtract $\mu_{\rm bg}$ measured with apertures of $r_{\rm aper} = 20$ pixels (for high-redshift) and 40 pixels (for low-redshift) before we measure the inner and outer profiles. The aperture sizes are comparable with the outer most radius within which the slopes are measured (see below).

3.2.2 Measuring inner and outer slopes

Similarly to the previous chapter, we measure the inner and outer slopes. We carry out the same procedure as described in Section 2.2.3 but with slightly different parameter settings in order to optimize them for the image quality of the high- and low-redshift samples. The parameters we optimized are the surface brightness threshold for determining half-light radius ($r_{\rm h}$*) and radial ranges in which the slopes are measured.

We set the surface brightness threshold for determining $r_{\rm h}$ to rest-frame† 25.5 mag arcsec^{-2} in g-band. Therefore the half-light radius $r_{\rm h}$ is defined so that one half the total light integrated above the surface brightness of 25.5 mag arcsec^2 is included. We select 25.5 mag arcsec^{-2} so that the surface brightness threshold becomes comparable with the threshold we have used in Chapter 2 (25.0 mag arcsec^{-2} in r-band). As the median color of the low-redshift quiescent galaxies is $g - r \sim 0.8$, the threshold used in the chapter corresponds to $\sim$ 24.7 mag arcsec^{-2}. When we measure $r_{\rm h}$ for the low-

* As the surface brightness threshold depends on redshifts in observed-frame, we do not write suffix for the half-light radius in this chapter.

† Although we take account of the surface brightness dimming, we do not take account of the wavelength difference in g-band for the low-redshift galaxies at $z \sim 0.03$, which is practically not a problem as the relative wavelength difference between the high- and low-redshift samples is included.

redshift galaxies, taking account for the surface brightness dimming, we use the surface brightness threshold of $\mu_{\rm lim}(z_{\rm gal}) = 25.5 + \mu_{\rm dim}(z_{\rm gal})$ mag arcsec^{-2}, where $\mu_{\rm dim}(z_{\rm gal}) = -2.5\log(1+z_{\rm gal})^{-4}$ is the surface brightness dimming at the redshift of a galaxy $z_{\rm gal}$. For high-redshift galaxies, we also take account of the passive evolution of galaxy luminosity and difference of the wavelength. Following Section 3.1.1.7, we adopt 2.1 mag for the correction. Therefore, the surface brightness threshold for the high-redshift galaxies is $\mu_{\rm lim}(z_{\rm gal}) = 25.5 - 2.1 + \mu_{\rm dim}(z_{\rm gal})$ mag arcsec^{-2}.

We also optimize the radial ranges in which the slopes are measured. We use $0.8 \leq (r/r_{\rm h})^{1/4} \leq 1.0$ for measuring inner slopes, and $1.0 \leq (r/r_{\rm h})^{1/4} \leq 1.4$ for outer slopes. The inner most radius (0.8 $(r/r_{\rm h})^{1/4}$) is determined so that it becomes larger than the PSF radius, i.e., one half the PSF FWHM, for majority of the samples, while the outer most radius (1.4 $(r/r_{\rm h})^{1/4}$) is determined so that the outer slopes can be meaningfully measured.

3.2.2.1 Uncertainty of the Slopes

We estimate uncertainty of the slopes originated from possible background residual fluctuation as done in Section 2.2.3.1. We subtract or add $\sigma_{\rm bg}$ evaluated with apertures of $r_{\rm aper} = 20$ pixels (for high-redshift) and 40 pixels (for low-redshift). As uncertainty of the slopes, we take the largest value among the difference between the slope measured with $\sigma_{\rm bg}$-subtracted and original profiles, those with $\sigma_{\rm bg}$-subtracted and original, and uncertainty derived from readout and photon noise.

3.2.3 Effects of the PSF on the measured slopes

We evaluate effects of the PSF on the measured slopes and derive appropriate correction for the effect because both for high- and low-redshift galaxies, the relative PSF size to galaxy sizes is not as small as local galaxies which we have dealt with in the previous chapter.

We evaluate the effect using the SDSS g-band images of the non-barred ATLAS^{3D} ETG sample which we have created in Chapter 2. We carry out simulations for the high-redshift sample (high-redshift simulation) and for the low-redshift sample (low-redshift simulation). We create simulated galaxy images for the high- and low-redshift simulations as follows. We first prepare 8 binned images with a different binning factor for each of the the non-barred ATLAS^{3D} ETGs. The binning factors are $5 \times 5, 7 \times 7, ...,$ and 19×19.

Then the images are convolved with PSF images for the high- and low-redshift samples. For the

high-redshift simulation, we use the PSF images of arbitrarily selected 12 clusters. Therefore, at this point, 8×12 images are created for each non-barred ATLAS^{3D} ETG. For the low-redshift simulation, we use the PSF images of all 9 clusters, and there are 8×9 images at this point.

Then random noise is added to the convolved images assuming Gaussian noise. Gaussian sigma is set to the typical noise level for the high- and low-redshift samples. We create 5 independent noise-added images for each convolution. Therefore, we have $8 \times 12 \times (1 + 5)$ and $8 \times 9 \times (1 + 5)$ images including noise-free and noise-added images for the high- and low-redshift simulations, respectively.

Then, we measure the inner and outer slopes for the simulated images as well as for the original SDSS g-band image, and compare the simulated values and the original value. We present the results in what follows.

3.2.3.1 The PSF Effect on the Inner Slope

In Figure 3.17, how the measurement of the inner slope is affected by the PSF is described. The ratio of the simulated inner slope to the original value (inner slope correction, hereafter) is plotted as a function of the half-right radius $r_{\rm h}$ measured from the simulated image. Smearing due to the PSF affects the measurement of inner slope of light profiles for the high- and the low-redshift simulations. The inner slope correction clearly depends on the galaxy size. The PSF effect is larger for galaxies with smaller $r_{\rm h}$. The effect is similar between the high- and the low-redshift simulations probably because the relative PSF size to the galaxy size is comparable. The scatter of the inner slope correction is much larger than uncertainty arising from the added Gaussian noise. Rather, the scatter is mostly originated from different shapes of galaxies as well as difference of the PSFs convolved.

We correct inner slopes of the high- and low-redshift ETG samples using the $r_{\rm h}$-dependent inner slope correction. The solid curves in Figure 3.17 indicate the running median of the inner slope correction while dashed curves are 16 and 84 percentiles. We apply the PSF correction using the running median. The measured inner slope of a galaxy having the half-light radius $r_{\rm h}$ is divided by the running median at $r_{\rm h}$. After we corrected the simulated inner slope for the $r_{\rm h}$ dependence, we could not find other parameters which are significantly correlated with residual inner slope correction. There remains a scatter of ~ 10 percent (comparable to the 16 to 84 percentile intervals at a fixed $r_{\rm h}$ in Figure 3.17).

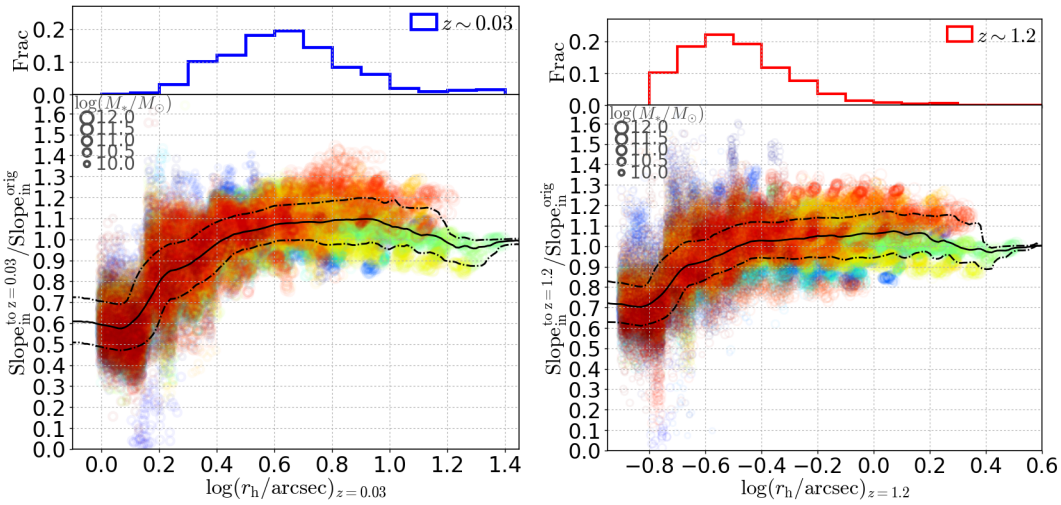

Figure 3.17 Inner slope correction (the ratio of the simulated inner slope to the original value) is show as a function of r_h. Different color indicates different galaxy in the non-barred ATLAS^{3D} ETG sample used in the previous chapter. Size of simbols corresponds to the stellar mass as noted in the panels. Left: The low-redshift simulation. Right: The high-redshift simulation. Histograms shown above are the r_h distribution of the low- and high-redshift quiescent ETG samples. The solid curve indicates the running median while dashed curves indicate 16 and 84 percentiles.

3.2.3.2 The PSF Effect on the Outer Slope

Similarly to the inner slopes, we also evaluate the PSF effect on the outer slope measurement. In Figure 3.18, the ratio of the simulated outer slope to the original value (outer slope correction) is plotted as a function of the half-right radius measured from the simulated image. Unlike the inner slope, the outer slopes are less affected by the PSF as they are measured in the outer region of a galaxy. Still there can be seen the r_h dependence in the outer slope correction. Therefore, we correct outer slopes taking account of the r_h dependence. Similarly to inner slope, the measured outer slope of a galaxy having r_h is divided by the median outer slope correction at r_h.

After the simulated outer slopes are corrected for the r_h dependence, we find correlation between the residual of outer slope correction and the Sérsic index n. In Figure 3.19, the residual of outer slope correction after applying r_h dependent outer slope correction as a function of n. The residual of outer slope correction on average monotonically increases with increasing n. We take running median of the residual outer slope correction between $1 < n < 6$, and use the running median to correct the measured outer slope of the high- and low-redshift galaxies. Since regions with $n < 1$ and $n > 6$

are not well populated by the non-barred ATLAS^{3D} ETGs, we use the edge values for actual galaxies having $n < 1$ or $n > 6$. After we apply the n-dependent correction in addition to the $r_{\rm h}$-dependent correction, the scatter of the residual outer slope correction becomes < 10 percent.

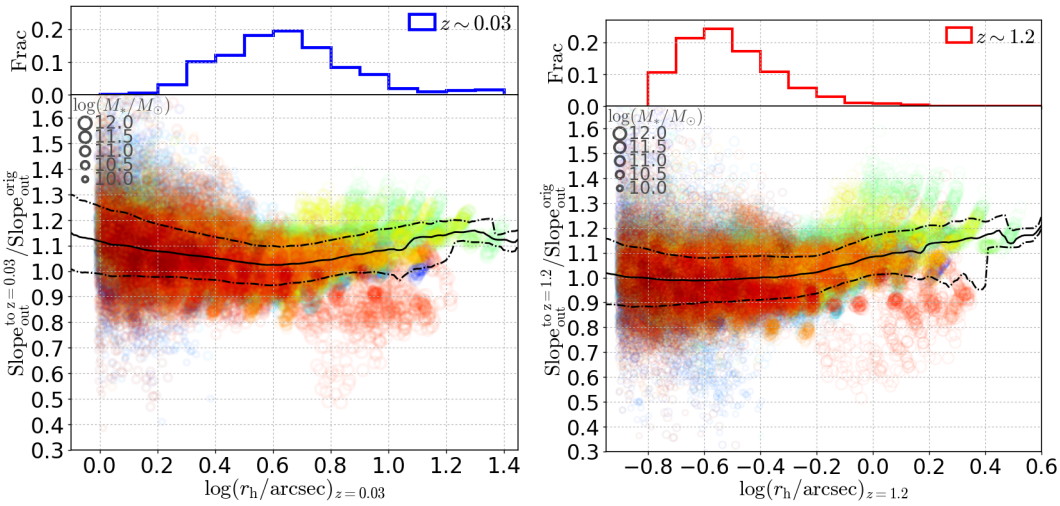

Figure 3.18 Same as Figure 3.17, but for the outer slope correction.

3.2.3.3 Amount of the Correction Applied In Practice

We present the amount of the applied correction for the inner and outer slopes for the high- and low-redshift ETG samples. In Figure 3.20, the ratio of the corrected slope to originally measured one is shown as a function of the stellar mass. For the inner slope, there is a fraction of high-redshift galaxies whose inner slope correction is quite large ($\mathrm{Slope}_{\rm in,corr}/\mathrm{Slope}_{\rm in,orig} > 1.3$). For the outer slope, the average amount of correction is similar between the high- and low-redshift samples with the difference less than a few percent.

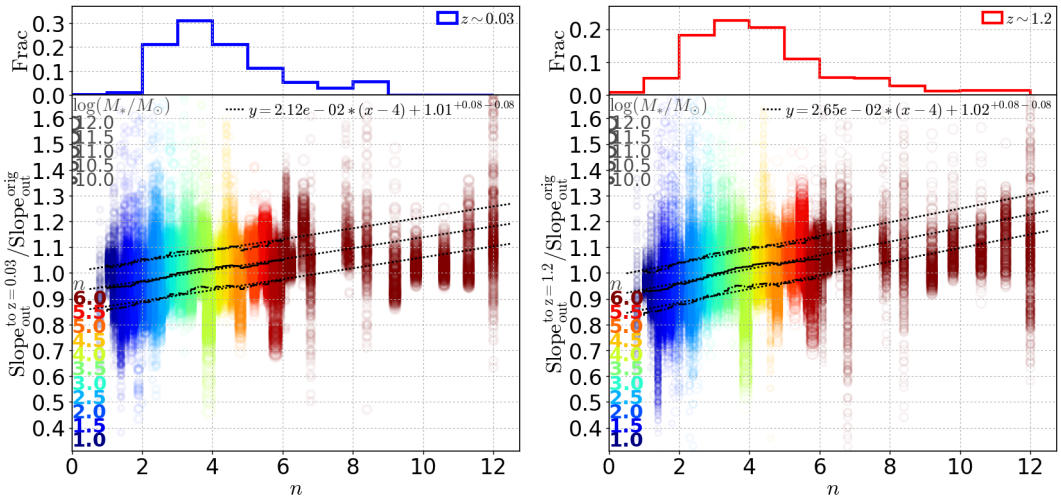

Figure 3.19 Residual outer slope correction which is the residual after the simulated outer slopes are corrected for the $r_{\rm h}$ dependence. Color code indicates Sérsic index as noted in the panels. Other symbols are the same as Figure 3.17. Dotted lines are the linear function fit to the running median (solid curve), and 16 and 18 percentile (dashed curves), although we do not use the linear function for correcting the slope.

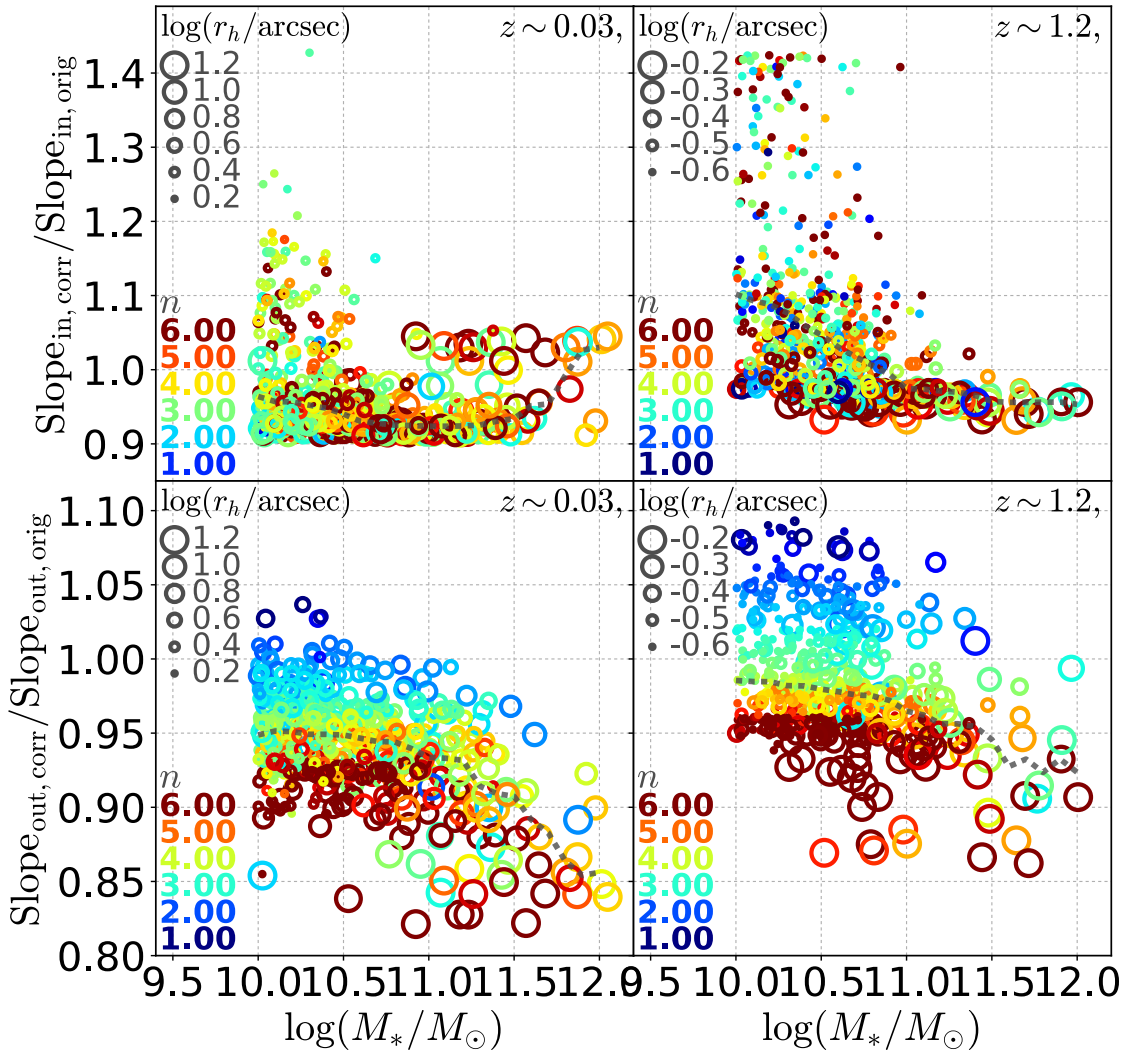

Figure 3.20 Amount of applied correction (the ratio of the corrected slope to originally measured one) as a function of the stellar mass for the high- (right) and low-redshift (left) samples. Top: Inner slope. Bottom: Outer slope. Marker size corresponds to the half-light radius as noted in the upper-left in panels, while color corresponds to the Séric index.

3.3 Results

In this section, we compare the inner and outer slopes of the high- and low-redshift ETG samples.

3.3.1 Inner and outer slopes of light profiles

In Figure 3.21, inner and outer slopes are shown for the high- and low-redshift ETGs. We also show the slopes for pure Séric profiles for different n using Equation 2.3 in the figure (gray curve). The distribution of the samples in the figure is similar in that they are clustering around $\mathrm{Slope_{in}} \sim 7.5$ and $\mathrm{Slope_{out}} \sim 8.0$. This indicates that the light profiles are on average close to Sésic profiles with $n \sim 3-4$, roughly consistent with the Sérsic index distribution shown in Section 3.1.3.4. The high-redshift sample contains significant amount of galaxies having the outer slope greater than ~ 11 while such galaxies are very rare in the low-redshift sample. This trend remains if we select round ($\epsilon \leq 0.4$) galaxies (lower panels in Figure 3.21).

In the upper panels in Figure 3.21, round galaxies with smaller ϵ (redder symbols) tend to be located in the lower right regions than flatter galaxies with larger ϵ (bluer symbols), which is more prominent for the low-redshift sample. This trend is naturally expected from the relation between galaxy rotation and ellipticity and that between galaxy rotation and Sésic index. More round galaxies with slower rotation tend to have larger Sérsic indices, which results in smaller outer slopes and larger inner slopes. The trend vanishes if we select round galaxies (lower panels in Figure 3.21). This is also expected from the fact that the relation between galaxy rotation and Sérsic index becomes insignificant for round objects.

3.3.2 Deviation of light profile from Sérsic: $\Delta\mathrm{Slope}$

As we have done in Section 2.3.2, we quantify the deviation of light profiles from Sérsic in the following manner just as described in Section 2.3.2. First, we fit a linear function $f_{\mathrm{out,Sersic}}$ to the pure Sérsic curves for Sérsic index $4 \leq n \leq 8$. We obtain

$$f_{\mathrm{out,Sersic}} = -0.874(\mathrm{Slope_{in}} - 8.33) + 8.303\ . \tag{3.8}$$

The difference of the slope in this equation and that in Equation 2.4 in Section 2.3.2 (-0.955) reflects the difference of the radial ranges in which the inner and outer slopes are measured. The fitting function

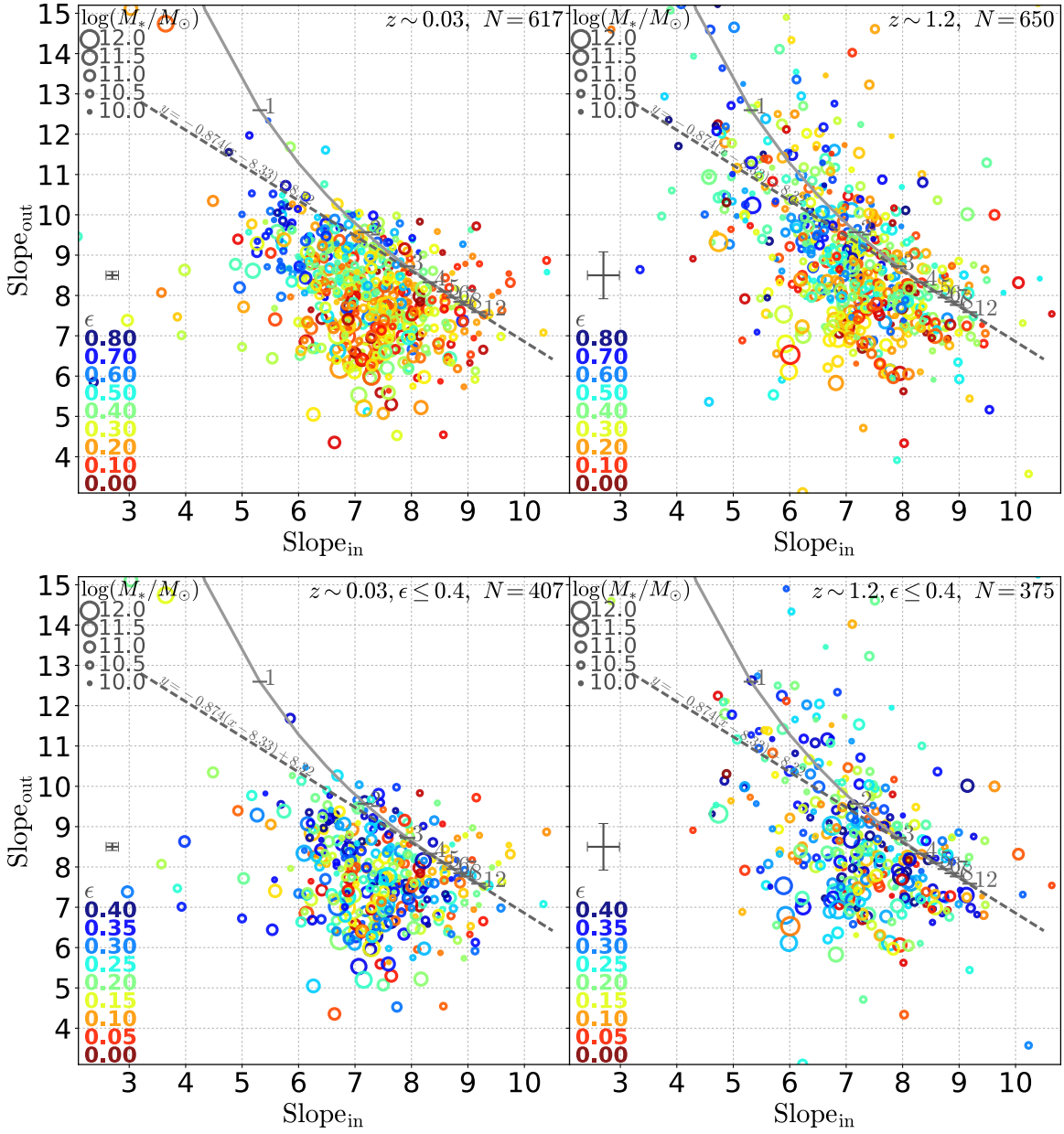

Figure 3.21 Inner and outer slopes of the low-redshift (left) and high-redshift (right) samples. Top two panels include all ETGs for which the slopes could be measured while bottom two panels include only round objects with $\epsilon \leq 0.4$. The symbol size corresponds to the stellar mass denoted on the top left of the left panel while color corresponds to the ellipticity as shown in the bottom left of each panel. Dotted curves indicate the slopes of pure Sérsic profiles with the Sérsic index n written in the panels while dotted straight lines are fits to the pure Sésic slopes in the range of $4 < n < 8$. Median uncertainties of the slopes are shown by error bars.

is shown by the dotted lines in Figure 3.21. Using the function, we define the deviation $\Delta\mathrm{Slope}$ as the difference between an outer slope and the fitting function at a inner slope,

$$\Delta\mathrm{Slope} = \mathrm{Slope}_{\mathrm{out}} - f_{\mathrm{out,Sersic}}(\mathrm{Slope}_{\mathrm{in}}) \ . \tag{3.9}$$

The uncertainty of $\Delta\mathrm{Slope}$ is calculated from that of the inner and outer slopes. In the following sections, we compare $\Delta\mathrm{Slope}$ between the high- and low-redshift ETGs.

3.3.3 Mass dependence of $\Delta\mathrm{Slope}$

In Figure 3.22, $\Delta\mathrm{Slope}$ of the high- and low-redshift samples are shown as a function of the stellar mass. For both samples, significant correlation is detected between $\Delta\mathrm{Slope}$ and the stellar mass by the Spearman's rank correlation test with the p-value less than $\sim 1 \times 10^{-6}$. Although the distribution of $\Delta\mathrm{Slope}$ overlaps between the two samples, median $\Delta\mathrm{Slope}$ (running median) is larger for the high-redshift sample compared at the same stellar mass in all stellar mass ranges.

While median $\Delta\mathrm{Slope}$ monotonically decreases with an increasing stellar mass for the low-redshift sample, that for high-redshift sample is nearly constant at $\Delta\mathrm{Slope} \sim -0.4$ in the lower stellar mass range ($\log(M_*/M_\odot) \lesssim 10.8$) and decreases in the higher mass range. The difference of median $\Delta\mathrm{Slope}$ between high- and low-redshift samples becomes the largest (~ 0.9) in $10.5 \lesssim \log(M_*/M_\odot) \lesssim 11.0$. This trend is the same for round objects with $\epsilon_{\mathrm{e}} \leq 0.4$ (lower panels in Figure 3.22).

3.3.4 Statistical Significance of the $\Delta\mathrm{Slope}$ difference

We investigate the significance of the difference of $\Delta\mathrm{Slope}$ between the high- and low-redshift samples. In Figure 3.23, the distribution of $\Delta\mathrm{Slope}$ of the high- and low-redshift samples are compared for the whole sample as well as for different stellar masses. We also plot the $\Delta\mathrm{Slope}$ distribution of the spectroscopic members in the high-redshift sample for reference. As expected from what we have seen in the previous section, the low-redshift sample tends to have smaller $\Delta\mathrm{Slope}$. $\Delta\mathrm{Slope}$ distribution of the high- and low-redshift samples are significantly different when they are compared with the whole sample. We carried out Kolmogorov-Smirnov (KS) test, and the p-value becomes 3.8×10^{-15} between the high- and low-redshift samples which suggest the two samples are statistically different. The median $\Delta\mathrm{Slope}$ for the high- and low-redshift samples are -0.6 ± 0.1 and -1.2 ± 0.1, respec-

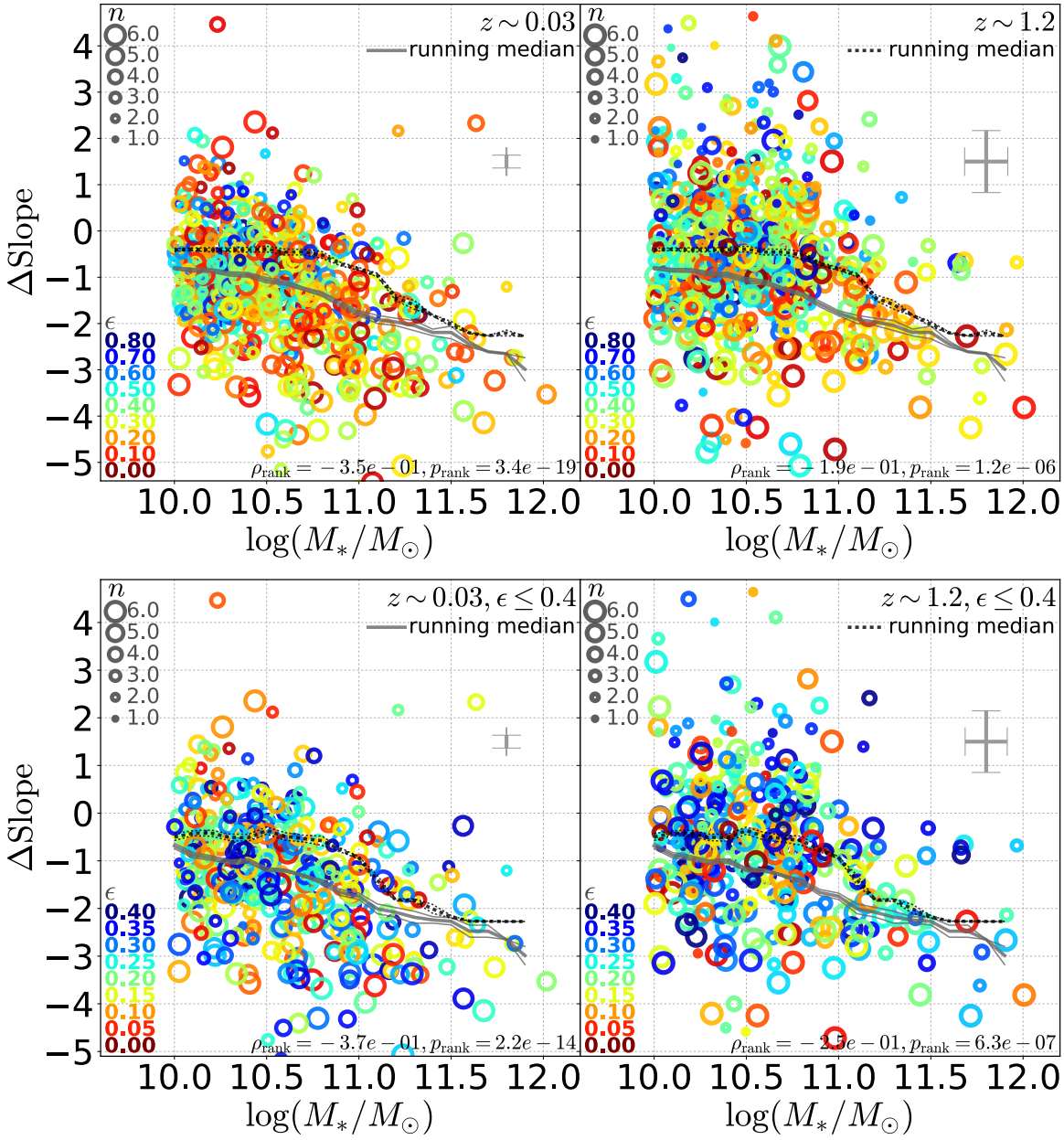

Figure 3.22 Deviation of the light profile from pure Sérisic (ΔSlope) as a function of the stellar mass for the low-redshift (left) and high-redshift (right) samples. Top two panels include all ETGs for which the slopes could be measured while bottom two panels include only round objects with $\epsilon \leq 0.4$. The symbol size corresponds to the Sérisic index denoted on the top left of the left panel while color corresponds to the ellipticity as shown in the bottom left of each panel. We take running median with the bin width of ± 0.25 which is shown by gray solid curves for the low-redshift sample and by black dotted curves for the high-redshift. The one-sigma uncertainty of the running median is evaluated by 1000-times bootstrap resampling and shown in the panels. Results of the Spearman's rank correlation test, the correlation efficiency ($\rho_{\rm rank}$) and p-value ($p_{\rm rank}$), are presented in bottom left of each panel.

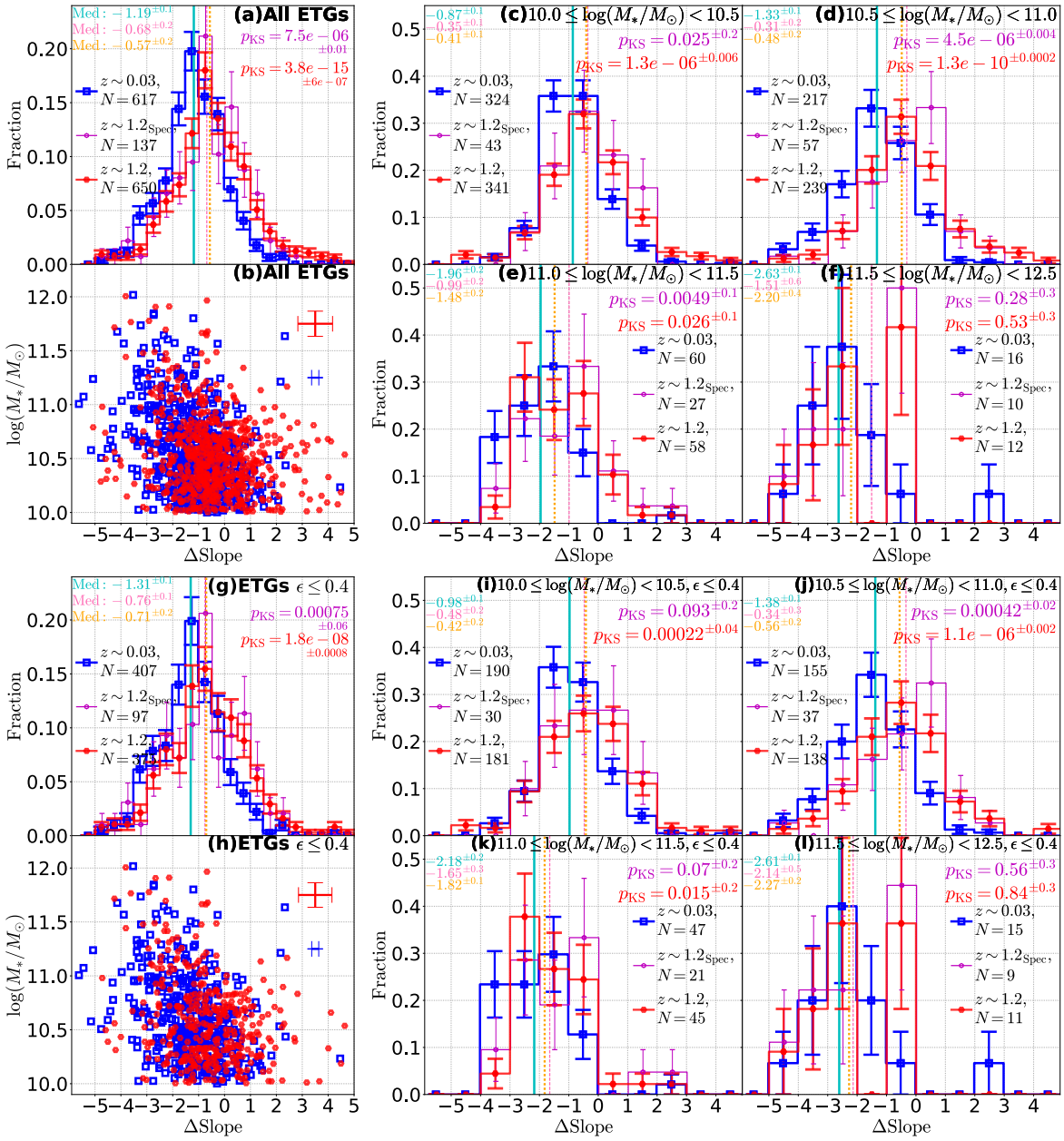

Figure 3.23 Histograms of ΔSlope for the low-redshift (blue) and high-redshift (red) samples. Spectroscopically confirmed galaxies in the high-redshift sample is also shown by magenta histograms. Panel (a): Histograms for all galaxies in the sample. Panels (b) to (e): Histograms for galaxies in the stellar mass bin presented in each panel. Panel (f): Histograms for round ($\epsilon < 0.4$) galaxies of all stellar masses. Panels (g) to (j) Histograms for round ($\epsilon < 0.4$) galaxies in the stellar mass bin presented in each panel. The number of galaxies included in the histogram is shown in the legends in each panel. We also present the p-values of KS tests ($p_{\rm KS}$) between the low- and high-redshift sample by red text while those between the low and spectroscopic high-redshift sample are shown by magenta. Also shown in cyan, pink, and orange in the upper left corner are median values of ΔSlope for the low-, the spectroscopic high- and the high-redshift samples with their uncertainty derived from bootstrap resampling.

tively. Here, the uncertainty of the median is estimated from bootstrap resampling. The difference of the distribution is also significant if we choose spectroscopic members from the high-redshift sample.

The low-redshift sample has larger deviation if the samples are separated into stellar mass bins. For galaxies with $\log(M_*/M_\odot) < 11.5$, $\Delta\mathrm{Slope}$ is significantly smaller for the low-redshift sample. The difference of the median $\Delta\mathrm{Slope}$ is the largest in the $10.5 \leq \log(M_*/M_\odot) < 11.0$ bin, just as expected from Figure 3.22. For the lower mass galaxies with $\log(M_*/M_\odot) < 11.0$, the difference has already been seen in the distribution of other structural parameters such as ellipticity, effective radius, and Sérsic index. In the intermediate mass bin of $11 \leq \log(M_*/M_\odot) < 11.5$ where the Séric parameter distributions are not significantly different, there is more than 2σ (but less than 3σ) significance in the difference of the $\Delta\mathrm{Slope}$ distribution. Only for the largest mass bin ($\log(M_*/M_\odot) \geq 11.5$), there is no statistically significant difference. The difference is also significant for round objects (lower panels in Figure 3.23).

3.3.5 Which slope matters?

We have seen that $\Delta\mathrm{Slope}$ is significantly different between the high- and low-redshift samples. Now, we investigate which slope of inner, outer, or both significantly changes between the two samples. In Figure 3.24, distribution of the inner profile is shown instead of $\Delta\mathrm{Slope}$ in Figure 3.23. For the whole samples, the KS test indicates the distribution is significantly different between the high- and low-redshift samples. The median inner slope is marginally smaller for the high-redshift sample. The difference mostly comes from the lowest stellar mass bin. Only in this stellar mass bin, the distribution and the median inner slope have significant difference between the low- and high-redshift samples. In other stellar mass bins, the difference is not significant. The situation does not change for round galaxies.

The distribution of the outer profile is shown in Figure 3.25. The KS test indicate that the distribution is significantly different for the whole samples. The median value is significantly larger for the high-redshift sample. The smaller inner slope and larger inner slope in the high-redshift sample than in the low-redshift are consistent with the smaller Sésic index presented in Figure 3.12. Unlike the inner slope, the distribution of the outer slope is significantly different in all stellar mass bins except for the massive end. The situation is the same for the round galaxies. Thus, we conclude that the significant difference in $\Delta\mathrm{Slope}$ between the high- and low-redshift samples would be driven by the

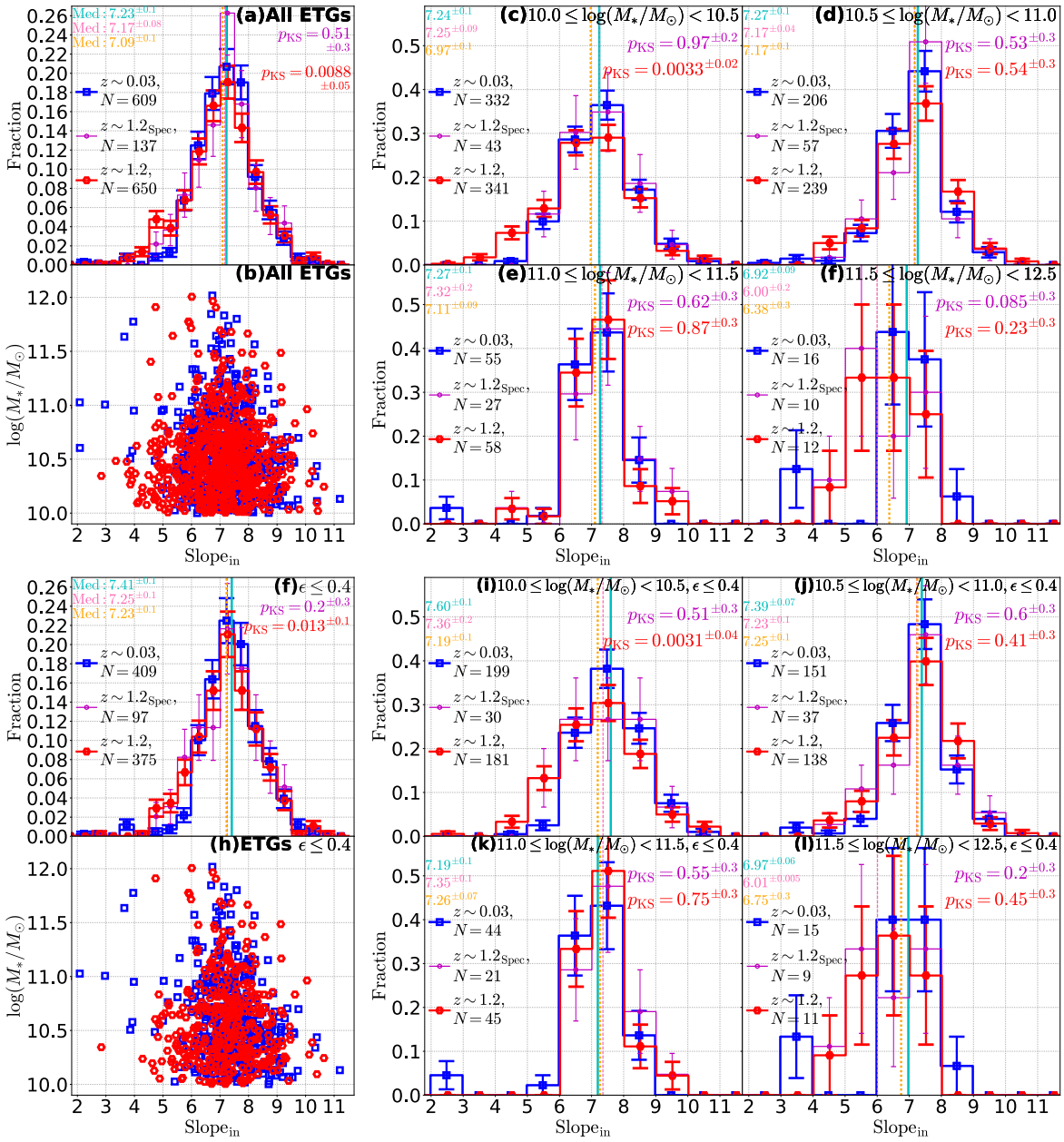

Figure 3.24 Same as Figure 3.23 but for the inner slope ($\mathrm{Slope_{in}}$) instead of $\Delta\mathrm{Slope}$.

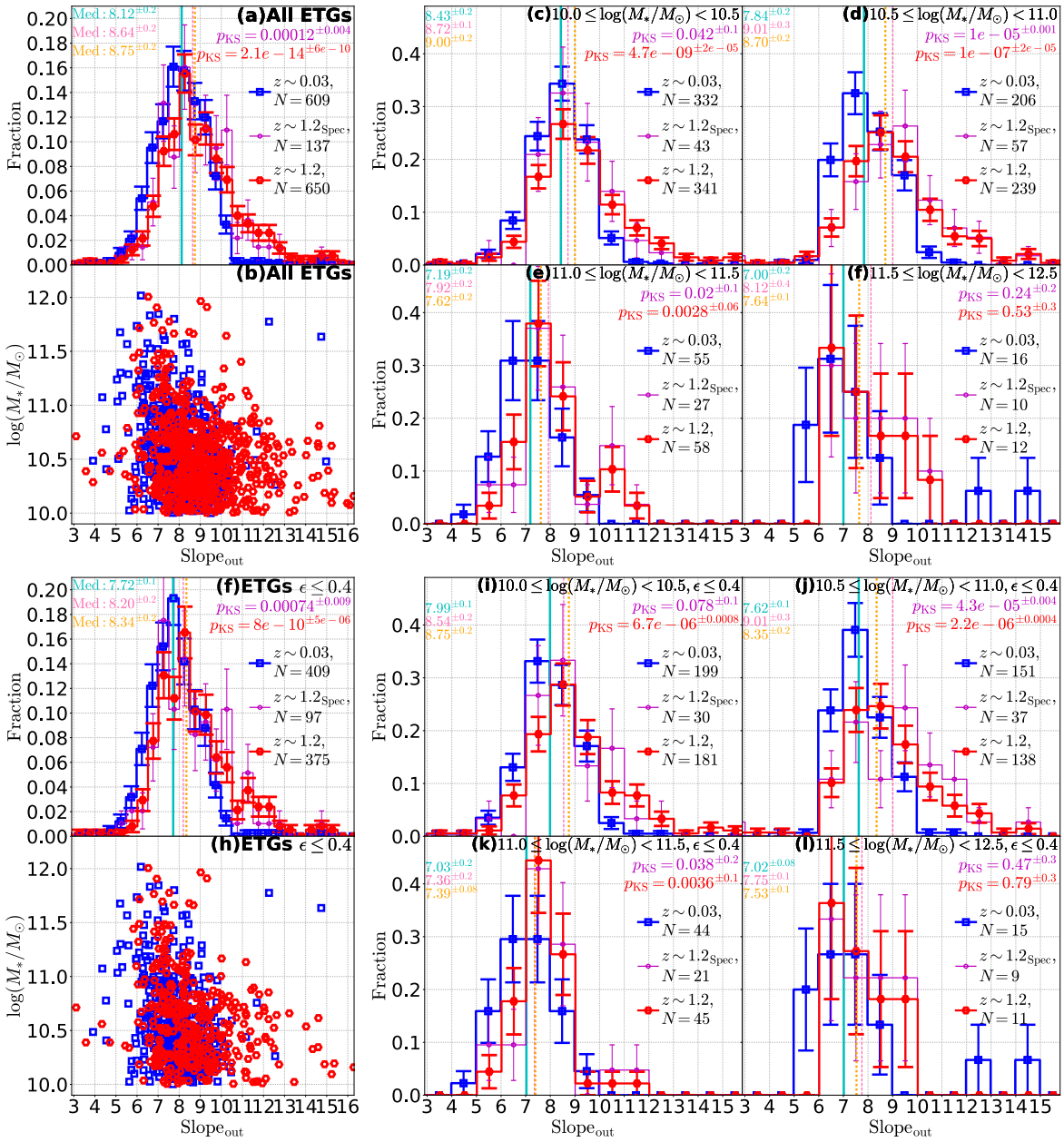

Figure 3.25 Same as Figure 3.23 but for the outer slope $\text{Slope}_{\text{out}}$ instead of ΔSlope.

outer slope for $10.5 \leq \log(M_*/M_\odot) < 11.5$ whereas the difference is originated from both slopes for the lowest stellar mass bin.

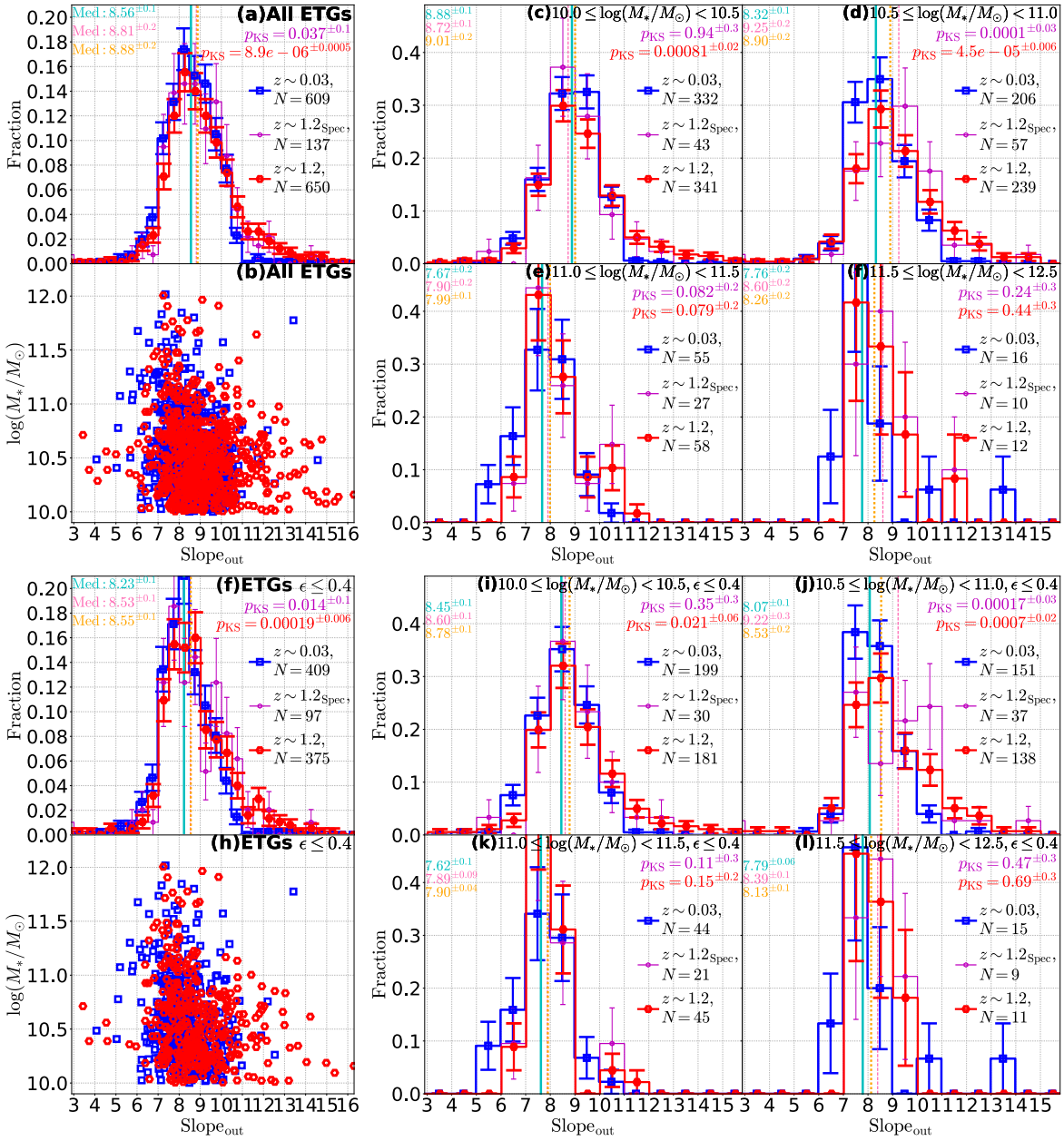

Figure 3.26 Same as Figure 3.25 but without the PSF correction.

3.3.6 Uncertainty arising from the PSF correction

The inner and outer slopes are corrected for the PSF effects. There is, however, significant uncertainty in the correction. From the simulation using the ATLAS^{3D} ETGs, we have shown that there remains

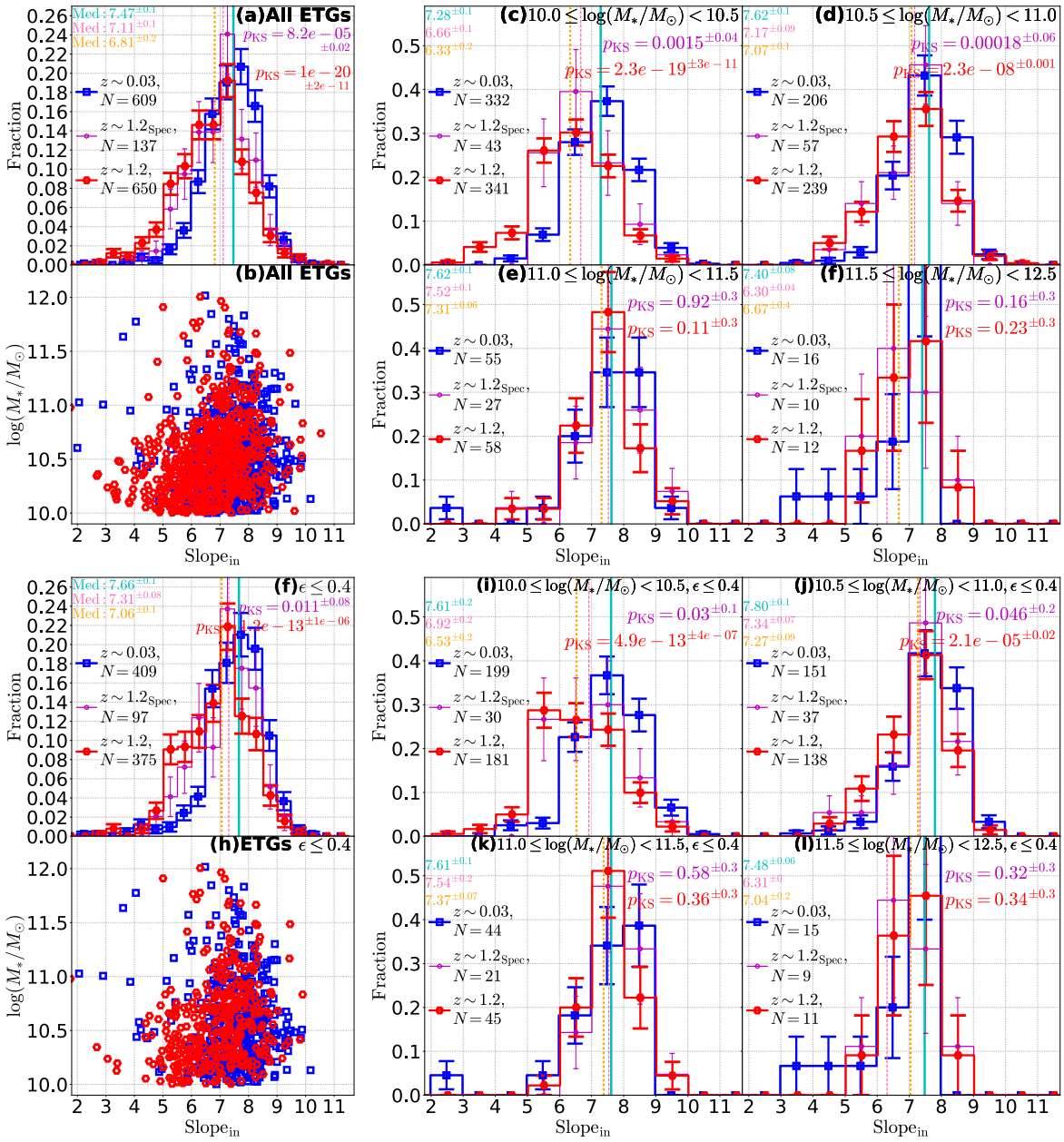

Figure 3.27 Same as Figure 3.24 but without the PSF correction.

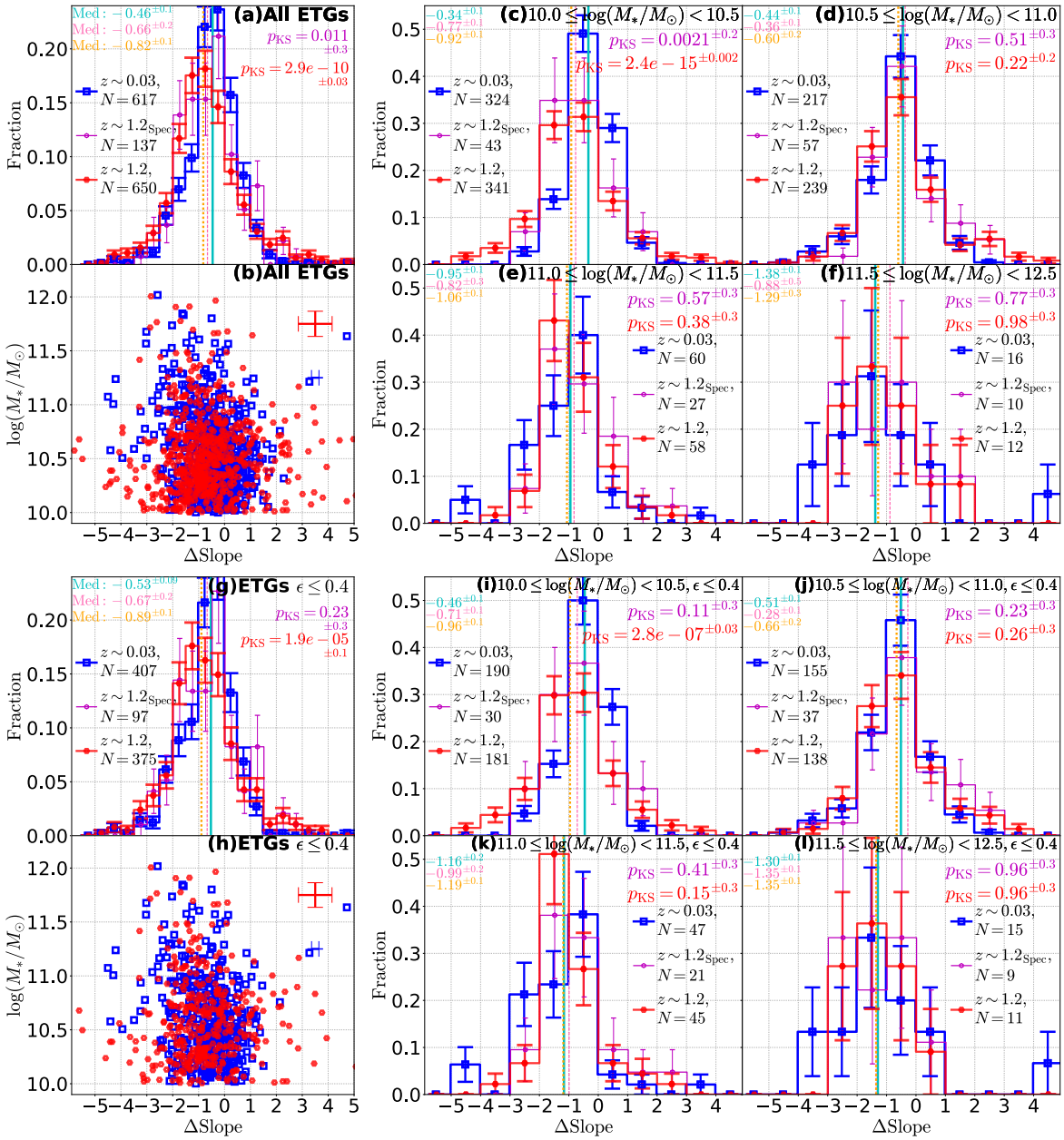

Figure 3.28 Same as Figure 3.23 but without the PSF correction. The figure is only for reference because ΔSlope becomes meaning less unless the significant PSF effect on the inner slope is corrected.

the scatter of an order of $\sim$ 10 % after the PSF effects are corrected. Here, we test the significance of the difference of the ΔSlope distribution between the high- and low-redshift samples including the uncertainty arising from the correction.

We estimate uncertainty of the p-value by carrying out Monte-Carlo Simulations in which uncertainty of ΔSlope arising from the correction for inner slope ($\mathrm{Slope_{in}}$) and outer slope ($Slope_out$) is taken into account as random errors. As the uncertainty is an order of $\sim$ 10 % for $\mathrm{Slope_{in}}$ and less than that for $\mathrm{Slope_{out}}$, the absolute values is ~ 0.7 for $\mathrm{Slope_{in}}$ and ~ 0.8 (or less) for $\mathrm{Slope_{out}}$. This amount of uncertainty in the slopes results in ~ 1 for ΔSlope. Therefore, we resample the high- and low-redshift sample galaxies assuming Gaussian distribution with the mean of the original ΔSlope value and the width of $\sigma = 1$ for 1000 times. At each resampling, the KS p-value is computed and the standard deviation from the 1000-times trial is considered as the uncertainty arising from the correction of the slopes. We give this uncertainty in panels in Figure 3.23. Even if the correction uncertainty is taken into account, the p-value is small for the whole sample and lower mass galaxies with $\log(M_*/M_\odot) < 11.0$. For the intermediate mass bin ($11.0 \leq \log(M_*/M_\odot) < 11.5$), the uncertainty of the p-value is as large as 0.2, and the $> 2\sigma$ difference is marginal if the correction uncertainty is taken into account. Therefore, we conclude that the different ΔSlope is not caused by the correction for the PSF effects but by the intrinsic difference of the shape of light profiles although there is caveat that there can be systematics which is not taken account into in the simulations carried out in Section 3.2.3 such as intrinsic difference of luminosity profiles of the high- and low-redshift galaxies.

We also check the difference of the slopes without the PSF correction. In Figure 3.26, we show the distribution of the outer slope similarly to Figure 3.25 but without the PSF correction. Although the difference between the high- and low-redshift sample becomes slightly smaller, there is still significant difference in the distribution as indicated by KS tests. This is because the applied correction of the outer slope is not large ($\sim$ 10 % at most). Only for the stellar mass bin of $11.0 \leq \log(M)/M_\odot < 11.5$, the significant difference disappears (less than 2σ) according to the KS test. We confirm that the significant difference of the outer slope seen in Figure 3.25 is real and not due to the correction.

Figure 3.27, the distribution of the inner slope without the PSF correction in shown. In this case, the distribution of the high-redshift sample shifts toward the smaller inner slope. The difference between this figure and Figure 3.24 illustrates how PSF affect the inner slope. For lower mass galaxies ($\log(M_*/M_\odot) < 11$), taking the PSF effect into account is crucial, otherwise we would overestimate the evolution of the inner slope. We also show the distribution of ΔSlope without the PSF correc-

tion in Figure 3.28. This figure is only for reference because the inner slope and therefore $\Delta\mathrm{Slope}$ is meaning less unless the PSF effect is corrected.

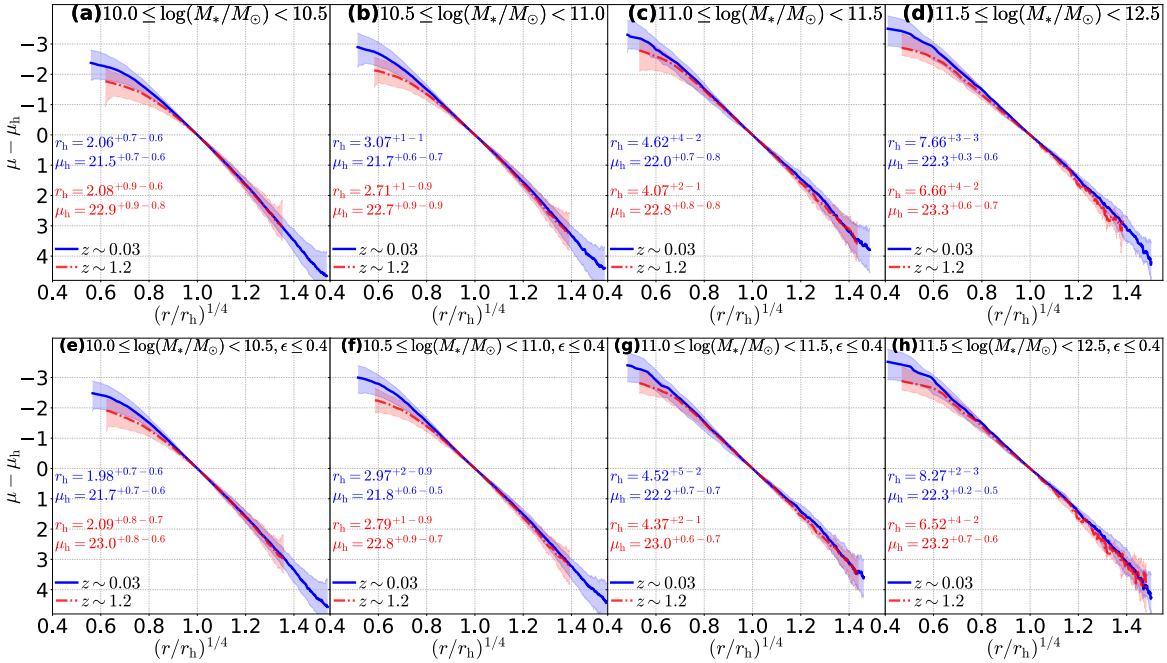

Figure 3.29 Stacked radial light profiles of the high- (red) and low-redshift (blue) samples in different stellar mass bins. In each bin, the median surface brightness a radius is indicated by dash-dotted line for the high-redshift sample and solid line for the low-redshift while shaded area includes 16 to 84 percentile of the surface brightness. The top panels show the profiles for all galaxies while bottom panels for round galaxies. The radius is scaled by the half-light radius r_h while the surface brightness is also normalized by the surface brightness at the half-light radius μ_h. The median r_h and μ_h with 16 and 84 percentiles are presented in the panels with the same color as the profiles. r_h is given in kpc and μ_h mag arcsec^2. Note that μ_h is in the observed frame and that for the high-redshift sample shown here is not corrected for luminosity evolution, difference of the wavelength, and surface brightness dimming.

3.3.7 Stacked light profiles

Finally, we present stacked light profiles of the high- and low-redshift samples in Figure 3.29. Here, the radius is scaled with the half-light radius r_h, and the surface brightness is also normalized with that at r_h. We do not correct the profiles for PSF effects. Therefore, the apparent light deficit in the high-redshift sample in $(r/r_\mathrm{h})^{1/4} \lesssim 0.6 - 0.8$ is probably due to PSF smearing. On the other hand, in outer regions, the low-redshift sample tend to have slight light excess. Although the difference of the profiles is more evident in higher mass bins ($\log(M_*/M_\odot) > 11$), the light excess could be seen the

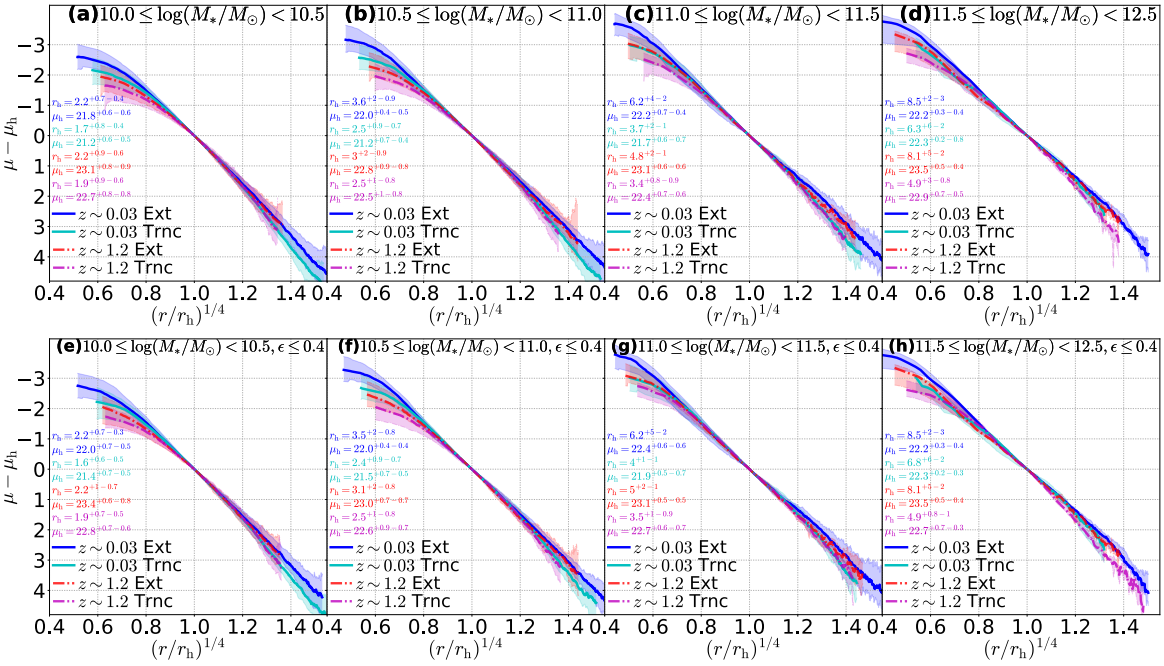

Figure 3.30 Same as Figure 3.29 but the samples are separated into those with $\Delta\mathrm{Slope} \leq \Delta\mathrm{Slope}_{\mathrm{median}}$ (extended) and $\Delta\mathrm{Slope} > \Delta\mathrm{Slope}_{\mathrm{median}}$ (truncated), where $\Delta\mathrm{Slope}_{\mathrm{median}}$ is the median $\Delta\mathrm{Slope}$ of each sample in each bin. The low-redshift sample is shown by blue (extended) or cyan (truncated) while the high-redshift sample is shown by red (extended) or magenta (truncated).

lower mass bins. This is consistent with the fact that the low-redshift sample have larger median outer slope values without the PSF correction (Figure 3.26). The results are the same for round galaxies. Thus, we consider that the difference of the outer slope and $\Delta\mathrm{Slope}_{\mathrm{median}}$ between the high- and low-redshift samples is originated from the evolution of outer light profiles.

In Figure 3.29, we also present the median half-light radius with 16 and 84 percentile intervals. For galaxies with $\log(M_{*(}/M_{\odot}) > 10.5$, the high-redshift sample has smaller r_h than the low-redshift sample. This is consistent with what we have seen for the effective radius r_{e} measured with galfit. For the lowest mass bin, taking account of the small apparent size ($\sim$ 2 kpc corresponds to 0.24 arcsec at $z \sim 1.2$ and 3.3 arcsec at $z \sim 0.03$), the half-light radius would be affected by the PSF.

We also present stacked light profiles separately for those with $\Delta\mathrm{Slope} \leq \Delta\mathrm{Slope}_{\mathrm{median}}$ (extended) and $\Delta\mathrm{Slope} > \Delta\mathrm{Slope}_{\mathrm{median}}$ (truncated), where $\Delta\mathrm{Slope}_{\mathrm{median}}$ is the median $\Delta\mathrm{Slope}$ of each sample in each stellar mass bin. Clearly, extended galaxies tend to have shallower profile at large radii than truncated ones. This also supports that the difference of $\Delta\mathrm{Slope}$ between the high- and low-redshift sample is originate from the outer light profile.

In inner regions, it seems that extended galaxies tend to have higher surface brightness, but it is highly unclear again due to the PSF effect. The central region of truncated galaxies should be more affected by the PSF because the scale length, the half-light radius r_{h} is smaller for the truncated than the extended. Therefore, we consider the profile evolution in the inner region is highly unknown while the evolution of the outer profile would be real.

3.4 Discussion

In this section, we discuss the effect of the ETG sample selection on the results presented in the previous section. For the ETG sample selection we have made use of the structural parameters which are the concentration index $C_{\rm in}$ and mean surface brightness SB. With these parameters, galaxies that have early-type morphology with de Vaucouleurs profiles ($n \sim 4$) and those that have late-type morphology with exponential profiles ($n = 1$) could be separated. Our results, however, as they are derived from light profiles, are likely to be affected by the ETG selection method. Therefore, we carry our additional analysis using different sample selection method.

We also estimate the effect from interloper contamination. As we use photometrically selected member galaxies in clusters at $z \sim 1$, the high-redshift sample contains foreground or background galaxy outside the clusters. If there is a significant contamination from disk galaxies into the high-redshift sample, we may observe evolution in the $\Delta{\rm Slope}$ distribution as shown in the previous section. Although we applied ETG selection and the selection reduces the contamination fraction, the amount of the reduction is small, and interlopers could be included in the ETG sample. Actually, we still have as large as $\sim$ 20 % contamination for the low mass ($\log(M_*/M_\odot) < 10.5$) galaxies. If the outer regions of the interlopers are dominated by disk their, $\Delta{\rm Slope}$ would be positive. We will discuss such effects in what follows.

3.4.1 Effects of ETG selection on the evolution of light profiles

We present the distribution of $\Delta{\rm Slope}$ of the high- and low-redshift galaxies with different sample selection criteria. First, we use the quiescent sample from which the ETGs samples are selected. In Figure 3.31 the $\Delta{\rm Slope}$ distribution is shown for the quiescent sample. The results do not change significantly both for all galaxies and round galaxies. The high-redshift sample have significantly larger $\Delta{\rm Slope}$ for the galaxies with $\log(M_*/M_\odot) < 11$, and marginally ($< 2-3\sigma$) larger $\Delta{\rm Slope}$ for those in $11 \leq \log(M_*/M_\odot) < 11.5$.

We also check the results with the ETG samples selected by Séric indices. Here, we select ETGs from the quiescent sample with a criterion of $n \geq 2$. The $\Delta{\rm Slope}$ distribution in this case is shown in Figure 3.32. Again, there is no significant impact on the difference of the $\Delta{\rm Slope}$ distribution between the high- and low-redshift samples.

We note that, however, the median value of $\Delta{\rm Slope}$ changes depending on the sample selection.

In the original case, the median $\Delta\mathrm{Slope}$ values for the whole samples is -0.57 and -1.19 for the high- and low-redshift samples, respectively. They become -0.46 and -1.05 for the quiescent samples while they are -0.68 and -1.13 for ETGs selected with Sésic indices. For the cause of the difference, we consider that the ETG sample selected with Sésic indices ($n \lesssim 2$) would contain the smallest fraction of disky galaxies which would have truncated outer profiles while the quiescent sample would have largest fraction of such galaxies and the original may be the intermediate.

3.4.2 Effects of interloper galaxy contamination on the results

We discuss the contamination of the foreground and background interlopers included in the samples. Thanks to the HST Cluster SN Survey (Dawson et al., 2009), we can select spectroscopically confirmed members from the photometric ETG samples. In Figures 3.23 to 3.25, we have shown the distribution of $\Delta\mathrm{Slope}$, $\mathrm{Slope_{in}}$, and $\mathrm{Slope_{out}}$ for the spectroscopic members. The trend in $\Delta\mathrm{Slope}$, the high-redshift ETGs have larger $\Delta\mathrm{Slope}$ (i.e., more truncated), is also seen in the spectroscopic members. The median values of $\Delta\mathrm{Slope}$ are consistent within uncertainty between the photometric and spectroscopic samples. The situation is the same for the outer slope.

The difference between the photometric and spectroscopic sample can be seen in the $\mathrm{Slope_{in}}$ distribution of the lowest mass galaxies (panel (c) in Figure 3.24). The distribution of the photometric sample (red) has a tail in the smaller $\mathrm{Slope_{in}}$ direction while the distribution is cut off at $\mathrm{Slope_{in}} \sim 5$ for the spectroscopic members. We check the distribution of the spectroscopic interlopers. In Figure 3.33, we compare the $\mathrm{Slope_{in}}$ distribution between the high-redshift spectroscopic interlopers and members as well as the photometric ETG sample. The interlopers have flatter distribution compared to other samples. Especially in the lowest mass bin, $\mathrm{Slope_{in}}$ distribution of the interlopers is uniformly extends from ~ 3 to ~ 11.

We subtract the distribution of the interlopers from that of the photometric ETG sample, assuming interloper fraction presented in Section 3.1.1.8. We find that the tail in the $\mathrm{Slope_{in}}$ distribution of the photometric ETG sample become less pronounced. Therefore difference of the $\mathrm{Slope_{in}}$ distribution in the lowest mass bin between the high-redshift (photometric) and low-redshift ETG samples may be due to contamination from interlopers. This result does not affect our main conclusions which are drawn from $\Delta\mathrm{Slope}$ and $\mathrm{Slope_{out}}$ because the differences in the $\Delta\mathrm{Slope}$ and $\mathrm{Slope_{out}}$ distribution between the high-redshift and low-redshift samples are also significant for the spectroscopic sample.

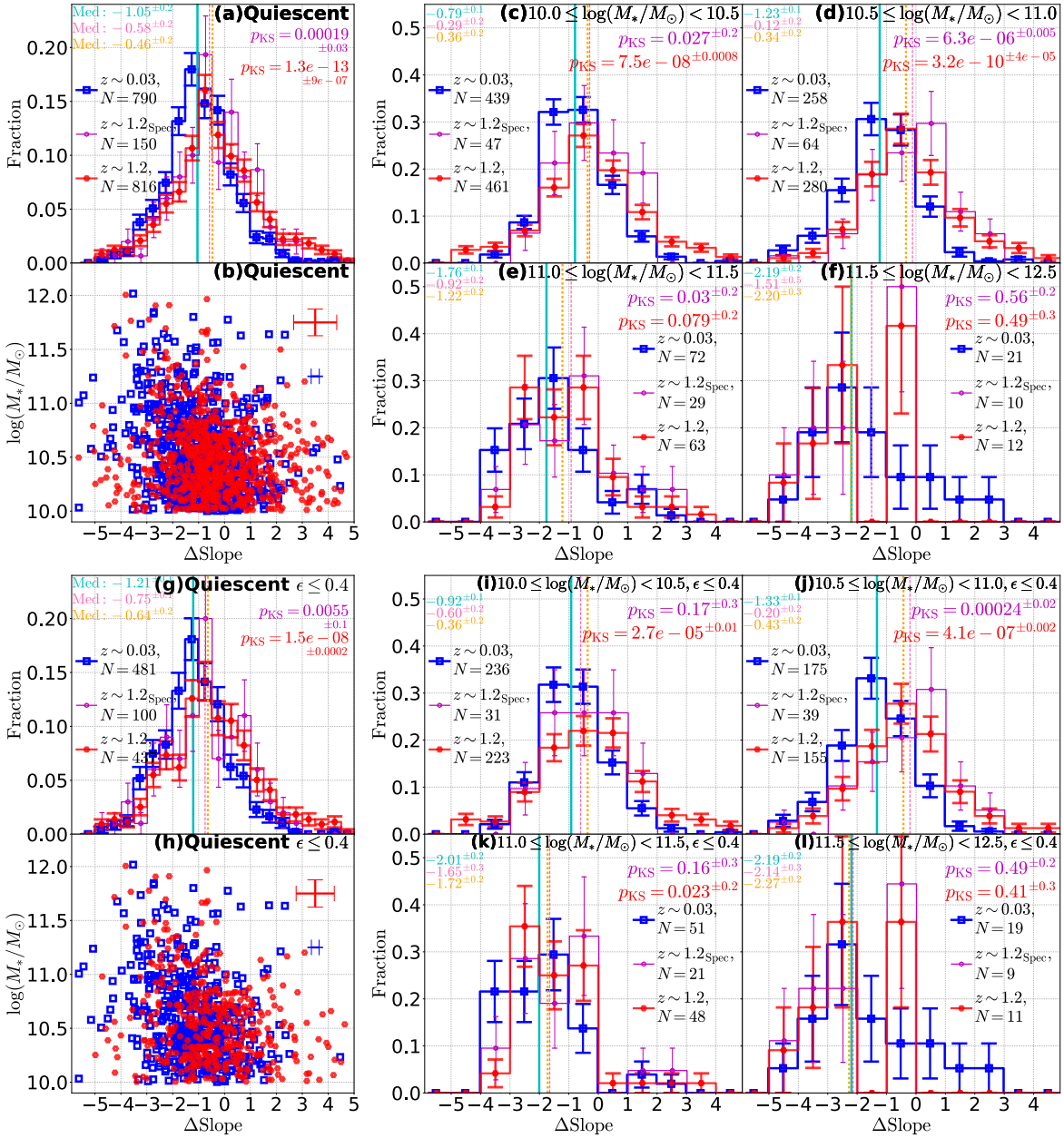

Figure 3.31 Same as Figure 3.23 but for the quiescent galaxy samples before the ETG selection.

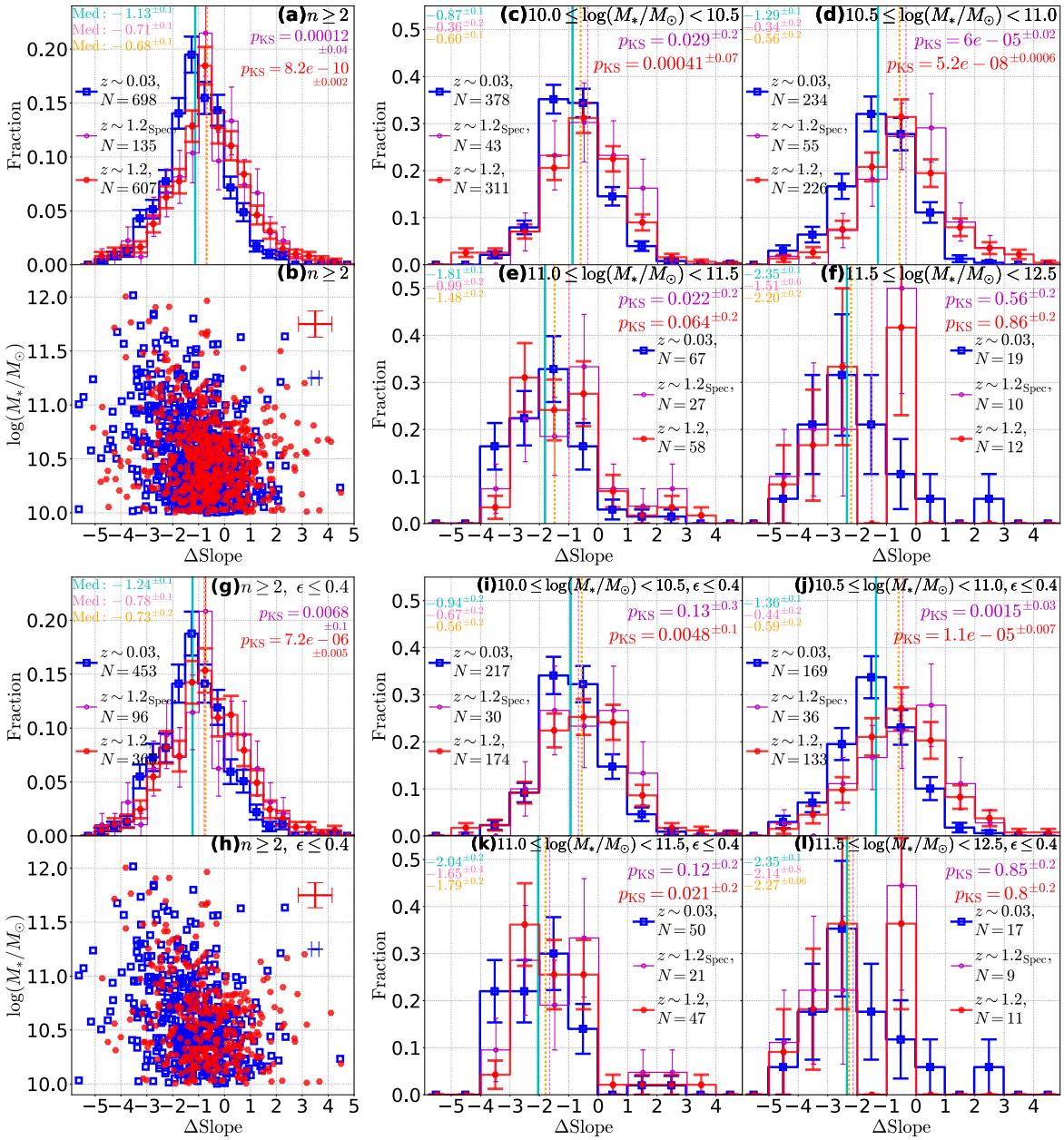

Figure 3.32 Same as Figure 3.23 but for the ETGs selected bySésic index $n \geq 2$ from the quiescent samples.

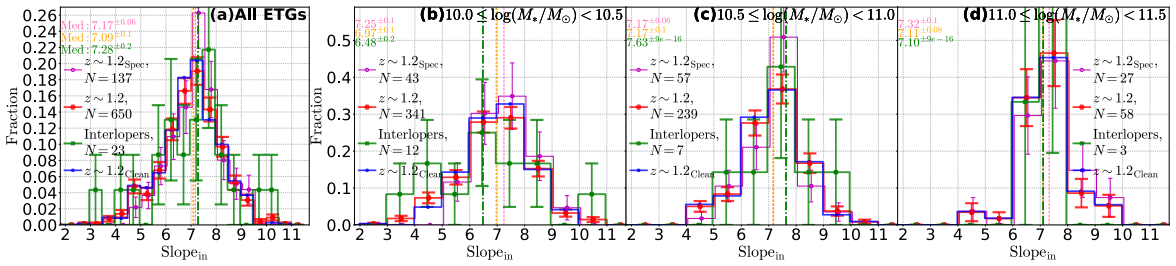

Figure 3.33 Inner slope distribution of the high-z spectroscopic interlopers (green) and members (magenta), and the photometric ETG sample (red). Blue histogram is the interloper subtracted version of that of the photometric ETG sample assuming the contamination fraction presented in Section 3.1.1.8.

4

Discussion on the Evolution of ETGs

In this Chapter we discuss the evolution processes of ETGs based on the findings in the previous chapters. In Section 4.1, we present possible mechanisms for the formation and evolution of ETGs based on the correlation between the outer profiles and kinematic properties that we have shown in Chapter 2. In Section 4.2, we discuss favorable mechanisms which can explain the evolution of the size and the outer profile of the ETGs based on the findings in Chapter 3. Finally, in Section 4.3, by combining the results shown in Chapter 2 and 3, we discuss the evolution of kinematics of ETGs in $z < 1$.

4.1 Possible Formation Mechanisms of Outer Light Profiles and Kinematic Properties of ETGs

In Chapter 2, we have shown that kinematic properties of ETGs are correlated with outer light profile. While most of slowly rotating galaxies have more extended envelop than pure Sérsic profile, large fraction of fast rotators have consistent profiles with Sésic or more truncated than Sésic. Schombert (2015) has already pointed out that there are two families of ETGs, one with extended (or ***diffuse*** in their paper) light profiles than a template profile and the other consistent with the template. He

has reported the mass dependence of the profile which is in accordance with our findings, and he has also mentioned the relation between kinematics and outer profiles. In this study, we have shown that slow rotators have extended profiles compared at a fixed stellar mass. Here, we discuss possible mechanisms behind the correlation.

4.1.1 Formation scenarios for fast rotators

We first discuss formation scenarios for the origin of fast rotators. In this study, we have shown that the deviation of a light profile from Sésic in the outer part of a galaxy, $\Delta\mathrm{Slope}$. is correlated with the spin parameter λ_e. We discuss possible formation scenarios of fast rotators from the results combined with previous studies of local and high-redshift galaxies.

We consider that the truncation detected by positive $\Delta\mathrm{Slope}$ may be originated from outer disk components because the outer truncation is observed for majority of disk-dominated galaxies (van der Kruit, 1979, Pohlen et al., 2004). We have shown that we can select ***photometric*** fast rotators with a high completeness by large ellipticity or by truncation in light profiles ($\Delta\mathrm{Slope} > 0$). We consider that this may be because majority of fast rotators contain significant fraction of a stellar disk, and that the disk component could be detected by ellipticity for edge-on objects or by $\Delta\mathrm{Slope}$ for face-on objects, using the selection criterion (Equation 2.10). The possible disk component in fast rotators has been reported by Krajnović et al. (2013) who detect stellar disks by independent parameters.

4.1.1.1 Truncated fast rotators with $\Delta\mathrm{Slope} > 0$

Our result that the majority of fast rotators show truncated profile at large radii ($\Delta\mathrm{Slope} > 0$) even for those with relatively large Sérsic indices ($n_\mathrm{tot} \gtrsim 2$, see, e.g., panel (a) in Figure 2.17) imply the dominance of disk with a smaller Sérsic index (i.e., more exponential-like) in the outer part. Outer disk would appear as outer truncation if the inner profile dominated by bulge ($n_\mathrm{tot} \gtrsim 2$) is extrapolated to large radii. This suggests that disks do not have to be destroyed when they morphologically transformed from (star-forming) spiral galaxies as long as bulges are formed in the center. Hence, truncated fast rotators which are the majority of local ETGs could be formed in more secular processes than major mergers.

Recent high-redshift studies show some cases in which progenitors of local ETGs at $z \gtrsim 2$ are forming bulges within disks by intense dusty starburst (e.g. Tadaki et al., 2017a,b). Tadaki et al.

(2017a) have shown that two Hα-selected star-forming galaxies at $z = 2.2$ and 2.5 have extremely compact dust emission ($R_{h,870\mu\mathrm{m}} < 1.5$ kpc) by high-resolution imaging of dust continuum using Atacama Large Millimeter/submillimeter Array (ALMA) while the galaxies have disks detected in rest-frame optical emission ($R_{h,1.6\mu\mathrm{m}} \sim 3.2$kpc). Considering their high central star formation rate surface density, a central bulge would be formed by $z \sim 2$. The extremely concentrated star-forming activity is thought to be originated from rapid cold gas accretion which causes the formation of massive gas clumps due to instability in disks (Dekel & Birnboim, 2006, 2008, Dekel & Burkert, 2014). Then, the clumps are rapidly sinking into the center by dynamical friction between the clumps and disk stars (Elmegreen et al., 2008, Burkert et al., 2016). Once such starburst galaxies form a massive central bulge, they may experience quenching of star formation in outer disks due to suppression of disk instability as the gravitational potential becomes deeper as a result of the central mass concentration (Martig et al., 2009). Thus, internal extremely gas-rich processes which are likely to be at work only at high redshifts could be an important channel for the formation of majority of ETGs (i.e., fast rotators). Further discussions about this issue will be given later in Section 4.3.3.

4.1.1.2 Extended fast rotators with $\Delta\mathrm{Slope} < 0$

We also find a fraction of extended fast rotators (e.g., Figure 2.8) although they are relatively minor population. Their outer region is probably dominated by spheroidal components with larger Sésic indices than central components. This could be explained by gas-rich major mergers.

The disk component of merger progenitors may be destroyed as stars originally embedded in the disks are spread out to large radii by obtaining radial velocity dispersion during violent relaxation (e.g., Binney & Tremaine, 2008), which would result in extended profiles in outer regions. If mergers are gas-rich, the remaining gas accretes onto the merger remnant and a rotating disk could be re-created from the gas (Kormendy et al., 2009). As a result, the remnant would be observed as a fast rotator in central regions (e.g.,$r < r_{\mathrm{e}}$) while their light profiles can be observed as extended. We note that there are other possible mechanisms than mergers that are responsible for outer extended profiles. We discuss such mechanisms later in the following sections. Extended fast rotators have relatively small λ ($\sim 0.3 - 0.4$, e.g., Figures 2.11 and 2.12), which may be because their disk has once been destroyed. The mergers may take place at high-redshifts $z > 1$ considering old stellar ages of our ETGs (McDermid et al., 2015). This scenario may be supported by the result that more massive fast

rotators are more likely to have extended profiles because higher major merger rate in more massive galaxies is seen in observations (Xu et al., 2012) as well as in simulations (Rodriguez-Gomez et al., 2015).

4.1.2 Formation scenarios for slow rotators

We have found that almost all of slow rotators have extended outer profiles ($\Delta\mathrm{Slope} < 0$). Gas-poor major mergers are one of the most plausible mechanism to form their extended profiles as well as their slow rotation. If gas is absent from the merger remnant, a new disk could not be formed. As a result, the remnant may only have spheroidal component dominated by dispersion rather than rotation and observed as a slow rotator (Kormendy et al., 2009). However, there are other plausible mechanisms which may be able to explain slow rotation and extended profiles which we discuss in the next section.

4.1.2.1 Possible contribution from major mergers

Major mergers can play a role in shaping dynamical properties as well as outer light profile of ETGs. Binary merger simulations show that slow rotators can be formed in mergers between similar mass disk galaxies with mass ratios smaller than $\sim 2:1$ (Naab & Burkert, 2003, Jesseit et al., 2009, Bois et al., 2011). In such cases, the dynamical property of the remnant depends on the orbit of the more bulge-dominated progenitor (Bois et al., 2011). When the orbit is retrograde where the spin of the galaxy rotation and the spin of the orbital angular momentum are anti-parallel, the remnant almost always results in a slow rotator. On the other hand, if the orbit is prograde, i.e., the spin of the galaxy rotation and orbital angular momentum are parallel, the remnant exclusively becomes a fast rotator. State-of-art cosmological simulations also suggest that merger mergers occurring in $z < 2$ are the main contributor to the spin down of slowly rotating ETGs (Penoyre et al., 2017).

Gas fraction of merger progenitors may also play a role. Some studies show that gas-poor major mergers can be a channel for forming slow rotators (Khochfar & Burkert, 2005, Naab et al., 2006), but others report that gas-rich major mergers can result in spin down of remnants (Naab et al., 2014, Penoyre et al., 2017) and modest gas fraction may be important for slow rotators to achieve round shapes consistent with observations (Jesseit et al., 2009, Naab et al., 2014). Smethurst et al. (2017) compare the quenching timescale of star formation activity between slow and fast rotators using mass-matched ETG samples from SDSS Mapping nearby Galaxies at Apache Point Observatory (MaNGA,

Bundy et al., 2015). They find that slow rotators quench star formation in a shorter timescale ($\lesssim$ 1 Gyr), which favors quick processes such as major mergers than less quick processes such as minor mergers and other secure processes as formation mechanisms of slow rotators (Smethurst et al., 2017).

Major mergers are also relevant to the outer light profile of ETGs. Borlaff et al. (2014) have analyzed dissipative N-body simulations of major mergers in order to investigate the origin of anti-truncated S0 galaxies with stellar masses of $1-3\times10^{11}M_{\odot}$. They show that 70 % of S0-like remnants of major mergers have anti-truncated (i.e., extended) outer light profiles against simple exponential disks. Although their simulations are for S0 galaxies which are the latest-type galaxies among ETGs and our sample is simply ETGs including S0s and ellipticals, the simulation may provide us some hints about the origin of the extended outer profiles of ETGs. The rotational velocity of the S0-like remnants wide spreads from $\sim$ 15 km/s (slow rotators) to 200 km/s (fast rotators). Therefore, if major mergers in certain merging orbits are the main channel of the origin of slow rotators, the fact that almost all slow rotators have extended outer light profiles but a fraction of extended ETGs are fast rotators could be explained. In addition, as pointed out by Schombert (2015), the small fraction of extended galaxies compared to normal or truncated galaxies may be originated from the rareness of major mergers. Major mergers is one promising channel to form slow rotators although other processes may not be ruled out.

4.1.2.2 Possible contribution from minor mergers

Not only major mergers but also multiple minor mergers with the mass ratios greater than $\sim 6:1$ may also be an origin of extended slow rotators. Importance of multiple minor mergers are emphasized in order to explain strong size evolution of ETGs from z $\sim$ 2 to 0 (van Dokkum et al., 2008, Bezanson et al., 2009) as they grow the effective radius more efficiently ($r_{\rm e}\propto M_{\odot}^{2}$) than major mergers ($r_{\rm e}\propto M_{\odot}$, Bezanson et al., 2009). High-resolution hydrodynamical simulations show that ETGs are formed by early ($z>2-3$) dissipation with intensive in-situ star formation in which the central component is formed followed by later ($z<2-3$) accretion of ex-situ stars by minor mergers which is responsible for the origin of outer envelops of ETGs and therefore rapid size growth (Naab et al., 2009, Hopkins et al., 2010). During minor mergers, stellar material in smaller galaxies is stripped by at large radii and accretes onto the outskirt of the larger central galaxy (Naab et al., 2009). The accreting component has a more extended radial profile than the in-situ component, and can be the origin of the extended

outer profiles of slow rotators. Although minor mergers can grow the outer component with the central part almost unchanged (Hopkins et al., 2010), the surviving cores of the accreting galaxies from tidal stripping can heat up the central in-situ component by dynamical friction (El-Zant et al., 2001) and reduce the central stellar density (Naab et al., 2009).

Considering dynamical properties, multiple gas-poor minor mergers is one prevailing mechanism to form slow rotators in addition to major mergers. Naab et al. (2014) analyze kinematic properties of 44 central galaxies from cosmological hydrodynamical simulations and show that remnants of multiple gas-poor minor mergers are round slow rotators with consistent ellipticity and spin parameter with observations. Also using cosmological simulations, Penoyre et al. (2017) have shown that for low mass ETGs with $\log(M_*/M_\odot) < 11$, minor mergers tend to spin up the remnant when they are gas-rich while more massive ETGs are usually spun down by minor mergers regardless of gas fraction.

4.1.2.3 Possible contribution from other mechanisms

Although many cosmological simulations show that properties of ETGs such as light profiles and dynamical properties achieved by assembly history in $z < 2 - 3$, we mention other possible mechanisms. Some theoretical studies try to explain the shape of outer light profiles by initial condition of dark matter haloes. Herpich et al. (2015) carry out hydrodynamical simulations and investigate relation between outer profiles of disk galaxies including S0s and the initial spin of dark matter halos. Galaxies residing in haloes with a spin parameter lower than $\lambda_{\rm halo} \lesssim 0.03$ have up-bending (extended) outer profiles than exponential disk while galaxies in haloes with larger spin parameter have a down-bending (truncated) profiles. Although the simulations mainly deal with late-type, disk galaxies, the relation between outer profiles and initial halo spin might be relevant the relation between light profiles and dynamical properties of ETGs.

Another studies presents possibility of internal processes for explaining kinematics. Martizzi et al. (2014) investigate the effect of feedback from active galactic nuclei (AGN) on masses, sizes, star formation rates and dynamical properties of brightest cluster galaxies (BCGs) by using cosmological hydrodynamical zoom-in simulations. They show that the ellipticity and spin parameter of the simulated BCGs become consistent with observations when AGN feedback is included whereas BCGs become more flattened and rotating faster when the feedback is not included. Taking account that BCGs are the most massive cases of ETGs (e.g., Bai et al., 2014) the results indicate that internal

processes such as AGN feedback can be relevant to the dynamical properties of ETGs. We note that, however, the feedback processes could be both direct and indirect effect for the angular momentum loss (Penoyre et al., 2017). A galaxy can spin down by strong outflows by blowing out large amount of gas which have an angular momentum. Also they can be kept gas-poor by AGN feedback, as the cold gas is blown out or heated up. As a result, they can experience minor mergers in gas-poor conditions. This could be a formation path for slow rotators (Naab et al., 2014, Penoyre et al., 2017).

AGN feedback also influences the light profile by adiabatic expansion (Fan et al., 2008, 2010). By blowing out a large amount of gas from the center by AGN feedback when a galaxy is very gas-rich (e.g., at high redshifts), stars and dark matter could be puffed up as the central potential becomes less deep, which would decrease the stellar density in the central region and increase in the outer region.

At this moment, we can not draw a firm conclusion about formation mechanisms and evolution paths of slowly rotating ETGs. In order to discriminate the contribution from possible mechanisms such as major and minor mergers and others, it is necessary in the future to compare observational results with simulations using many parameters including light profiles (e.g., inner and outer slopes), shapes (e.g., ellipticity), dynamical parameters (e.g., spin parameter), and stellar population parameters (e.g., quenching time scales).

4.2 Evolution of Outer Light Profiles and Sizes of ETGs

In this section, we address the likely mechanisms of the size evolution of ETGs in clusters in $z < 1$ based on the findings in the Chapter 3. In Chapter 3, we have presented that the shape of light profiles of ETGs in massive clusters evolve from $z \sim 1$ to 0. The ΔSlope parameter is larger for the high-redshift ETGs (Figure 3.23), which is due to the change of outer regions (Figures 3.25 and 3.29). The largest amount of the median ΔSlope evolution (~ 0.8) is observed at a stellar mass of $\log(M_*/M_\odot) \sim 10.5 - 11.0$. The amount of the median ΔSlope evolution for whole samples is $\sim 0.6 \pm 0.2$. While lower mass galaxies ($\log(M_*/M_\odot) < 11.5$) show statistically significant evolution in the ΔSlope, the ΔSlope evolution in the largest stellar mass bin ($11.5 \leq \log(M_*/M_\odot)$) is marginal possibly due to small sample size. More light excess in the outer region ($r > r_{\rm h}$) can be seen in the low-redshift ETGs than than in high-redshift, which is also confirmed by the difference of the outer slope distribution.

Previous observations of high-redshift ETGs spanning from redshifts $z \sim 0$ to 2 have revealed that ETGs are by a factor of $\sim 4 - 5$ more compact in the early epoch (Trujillo et al., 2007, van Dokkum et al., 2008). In the field environment, ETGs show strong size evolution from $z \sim 0$ to 1 (Damjanov et al., 2011, Newman et al., 2012, Cimatti et al., 2012) and beyond (van der Wel et al., 2014). On the other hand, in massive clusters, the size evolution is mild up to $z \sim 1$ (Delaye et al., 2014) as well as up to $z = 1.8$ (Andreon et al., 2016). The size of ETGs in dense environments may depend on the halo mass of host clusters at high redshifts. At $z \sim 1$, while ETGs are larger in massive clusters (Delaye et al., 2014), those in groups ($\log(M_{\rm halo}/M_\odot) \lesssim 14$) have similar sizes to field counter parts (Huertas-Company et al., 2013a). The different sizes of ETGs in different environments have been seen only at $z \sim 1$. The size of quiescent galaxies in dense environment becomes comparable to those in fields at $z \sim 0$ (Huertas-Company et al., 2013b, Weinmann et al., 2009, Maltby et al., 2010) as well as $z \sim 2$ (Allen et al., 2015, Wang et al., 2016).

In this study, we have observed the size evolution for the cluster quiescent ETGs between $z \sim 1$ and 0 (Figure 3.11) similarly to previous studies (Delaye et al., 2014, Mitsuda et al., 2017). We have found that the largest evolution occurs in the stellar mass range of $10.5 \leq \log(M_*/M_\odot) < 11$. The difference of the median effective radius is 0.14 ± 0.02 dex between the high- and low-redshift ETGs. In this stellar mass bin, the ΔSlope evolution is also most pronounced with the difference of the median values $\sim 0.9 \pm 0.2$ (Figure 3.23). The evolution of ΔSlope is driven mainly by the outer

slope with the inner slope unchanged (Figures 3.24 and 3.25). In addition, ellipticity and Sérsic index also evolve. The observed mean size evolution can be explained by several mechanisms (Hopkins et al., 2010). First, the evolution of the mean size can be originated from the evolution of individual galaxies or change of the fraction of different galaxy population in the sample. The former include external processes such as gas-poor major and minor mergers (Naab et al., 2009, Hopkins et al., 2010) and secular processes such as AGN feedback (Hopkins et al., 2010). The latter include the progenitor bias (van der Wel et al., 2009, Newman et al., 2012, Carollo et al., 2013) and different morphological mixing (e.g., Bernardi et al., 2014, Huertas-Company et al., 2013a) We discuss these mechanisms in what follows.

Likely mechanisms responsible for the size evolution of individual ETGs is external processes such as gas-poor major and minor mergers We have already shown that major and minor mergers can grow the outer light profile of a galaxy in Sections 4.1.2.1 and 4.1.2.2. The evolution of the outer profile, ellipticity, and Sérsic index observed in this study do not rule out mergers. Rather, such signatures are consistent with merger scenarios because of gas-poor merger remnants tend to be more dispersion-supported (Khochfar & Burkert, 2005, Naab et al., 2006).

Minor mergers are often favored to explain the size evolution of ETGs because ETGs can grow in size more efficiently with little amount of growth in mass($r_{\rm e} \propto M_*^2$) than major mergers (Bezanson et al., 2009, $r_{\rm e} \propto M_*$). In addition minor mergers can occur much more frequently than major mergers. The timescale during of minor mergers, i.e., in which low mass surrounding galaxies sink toward the more massive galaxy by dynamical friction is only a few Gyr (Binney & Tremaine, 2008). Therefore, galaxies would experience many minor mergers from $z \sim 1$ to 0. Thus, minor mergers could be a main contributor for the size evolution of ETGs below $z \sim 1$.

Major mergers, on the other hand, may be rare in massive clusters because the large velocity dispersion prevents galaxies from slowly merging (Binney & Tremaine, 2008). Instead, galaxies would experience high-speed encounters or fly-by with which structure of the galaxies do not change very much except for dwarf galaxies (Moore et al., 1998, 1999) due to too short time scales of the encounter, although not all interactions are done in the high-speed regime (Gnedin, 2003). Therefore, rather than in $z < 1$, structural evolution due to major mergers is likely to be important at higher redshifts where the progenitors of the $z \sim 1$ massive clusters have smaller velocity dispersion. Delaye et al. (2014) propose major mergers as origin of the larger size of ETGs in clusters than in fields at $z \sim 1$. Considering these situation, minor mergers are more likely mechanisms than major mergers to explain the

size evolution of the cluster ETGs in $z < 1$.

Internal processes such as stellar winds and AGN feedback can make galaxy size large by adiabatic manner (Fan et al., 2008, 2010). As the depth of central potential become less deep when significant amount of gas is blown out from the center by AGN or stellar outflows, dark matter particles as well as stars originally concentrated in the central region are redistributed in the outer region. Our observational results alone do not rule out this mechanism because the outer light profile could be changed by these mechanisms (Section 4.1.2.3). Based on the different size evolution between clusters and fields (Delaye et al., 2014, Andreon et al., 2016), Andreon et al. (2016) propose that the internal processes may have only minor contribution because AGN stellar feedback or stellar winds would not dependent on environments. In addition, the quiescent ETGs have only small amount of gas and they are inactive. Therefore, internal processes may not be likely mechanisms for the size evolution of cluster ETGs in $z < 1$.

In stead of the size growth of individual ETGs, the size evolution can be explained by emergence of new galaxy populations in the sample if the new population have larger sizes. This mechanism is called the progenitor bias. If the progenitor bias is at work, newly quenched galaxies at $z < 1$, which have been blue star-forming at $z \sim 1$ and excluded from the high-redshift sample, would enter into the low-redshift sample. As star-forming galaxies have larger size compared at a fixed mass than quiescent galaxies, newly quenched galaxies can make the average size of ETGs larger (Newman et al., 2012, Carollo et al., 2013). The large sizes in the star-forming galaxies is originated from disk morphology with lower stellar density supported by large rotational velocity. Therefore, if the progenitor bias significantly contribute to the size growth, the newly quenched galaxy should keep their disky morphology and rotational support, and the outer profile of the low-redshift ETGs would be more ***truncated*** than the high-redshift sample. This is not consistent with what we have observed in the previous chapter. The low-redshift ETGs have more extended outer profiles indicative of more dispersion support. Moreover, larger Sérsic index (probably driven by the outer profile evolution) and smaller ellipticity in the low-redshift ETGs than in the high-redshift also indicate that they are more likely to be dispersion dominated. We note that ETGs in our samples reside in very center of massive galaxy clusters where most of galaxies are quenched at early epoch, e.g., at redshifts greater than ~ 1.4 (Hayashi et al., 2010, Brodwin et al., 2013) where we have only two clusters. Therefore, the fraction of newly quenched population in $z < 1$ should not be large, and the progenitor bias may not be a main contributor for the ETG size growth in clusters at $z < 1$. Still, we do not completely

rule out the progenitor bias because there seems to be some contribution of newly quenched for the evolution of richness-halo mass relation (Section 3.1.3.1).

The evolution of mean size of ETGs can also be explained by different morphological mixing in the samples. This mechanism is similar to the progenitor bias in that it explains the difference of the mean size by the different fraction of galaxy population. In the progenitor bias, the fraction between recently quenched disk-like and old spheroidal galaxies matters. In this case, we consider the fraction of S0s and Es. S0 galaxies with larger apparent ellipticity tend to be measured as more compact when the size is measured by the circularized radius (Huertas-Company et al., 2013a, Bernardi et al., 2014). Therefore, if a sample contains larger fraction of S0 galaxies, the average size of the sample could appear to be smaller. For the whole samples, this mechanism can explain the size evolution for our samples because the ellipticity is larger in the high-redshift sample. The size evolution as well as the outer slope evolution, however, are also observed for the round galaxies, and the different morphological mixing alone is insufficient for the size and profile evolution.

We have shown several mechanisms which may explain the observed size evolution of cluster ETGs in $z < 1$. Among them, based on the discussion above with the outer profile evolution, structural parameters such as Sérsic index and ellipticity, and other environmental arguments, minor mergers may be the most favored mechanism to explain the size evolution, although the progenitor bias could not completely be ruled out.

4.3 Evolution of Kinematic Properties of ETGs inferred from Outer Light Profiles

We discuss the possible evolution of kinematic properties of ETGs from the evolution of $\Delta\mathrm{Slope}$. We apply the relation between $\Delta\mathrm{Slope}$ and the spin parameter λ or V/σ which we have shown in Chapter 2. Using Equations 2.14 and 2.15, we convert $\Delta\mathrm{Slope}$ into λ and V/σ. The uncertainty in λ and V/σ are derived from that in the median $\Delta\mathrm{Slope}$ and in the intercept of linear relation defined in Equations 2.14 and 2.15.

We present an example here. For, the whole sample. i.e., stellar mass limited ($\log(M_*/M_\odot) > 10$) quiescent ETGs, the median $\Delta\mathrm{Slope}$ is -0.57 ± 0.2 and -1.2 ± 0.1 for the high- and low-redshift samples, respectively (Figure 3.23). If we convert $\Delta\mathrm{Slope}$ into λ, the median λ would be 0.47 ± 0.1 and 0.35 ± 0.02 for the high- and low-redshift samples, respectively. Similarly, if we convert $\Delta\mathrm{Slope}$ into V/σ, V/σ would be 0.51 ± 0.05 and 0.38 ± 0.02 for the high- and low-redshift samples, respectively.

We summarized median λ and V/σ converted from the median $\Delta\mathrm{Slope}$ for different stellar mass bins in Table 4.1 for all galaxies and Figure 4.1. Similarly, we calculate median λ for round galaxies

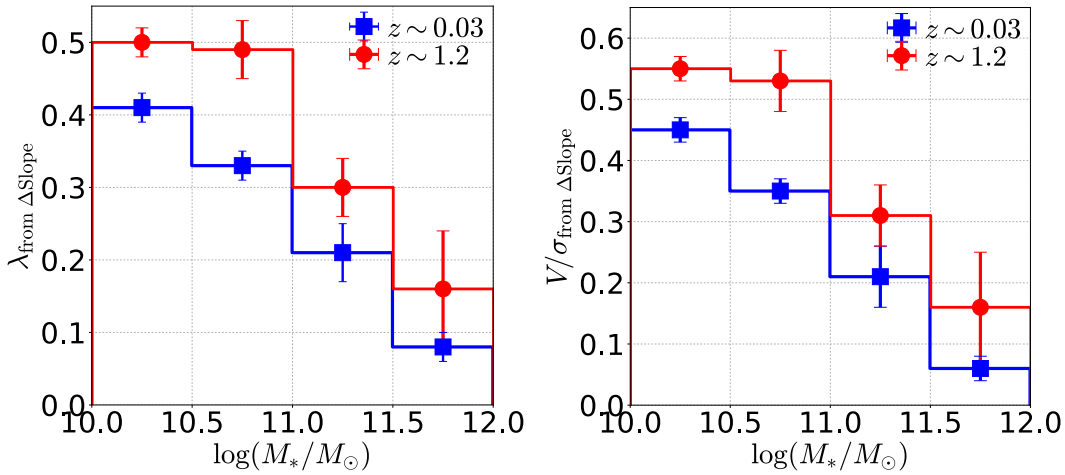

Figure 4.1 Median λ (left) and V/σ (right) converted from median $\Delta\mathrm{Slope}$ as a function of the stellar mass using the relation between λ and $\Delta\mathrm{Slope}$ derived in Chapter 2. The figure is created with the data listed in Table 4.1.

($\epsilon \leq 0.4$) from median $\Delta\mathrm{Slope}$. The converted values are summarized in Table 4.2 and Figure 4.2. Note that we apply oversimplified linear relation between $\Delta\mathrm{Slope}$ and λ or V/σ. Also, we assume that the relation does not change with redshifts and environment. Therefore there would be larger uncertainty in the converted λ and V/σ than presented in here.

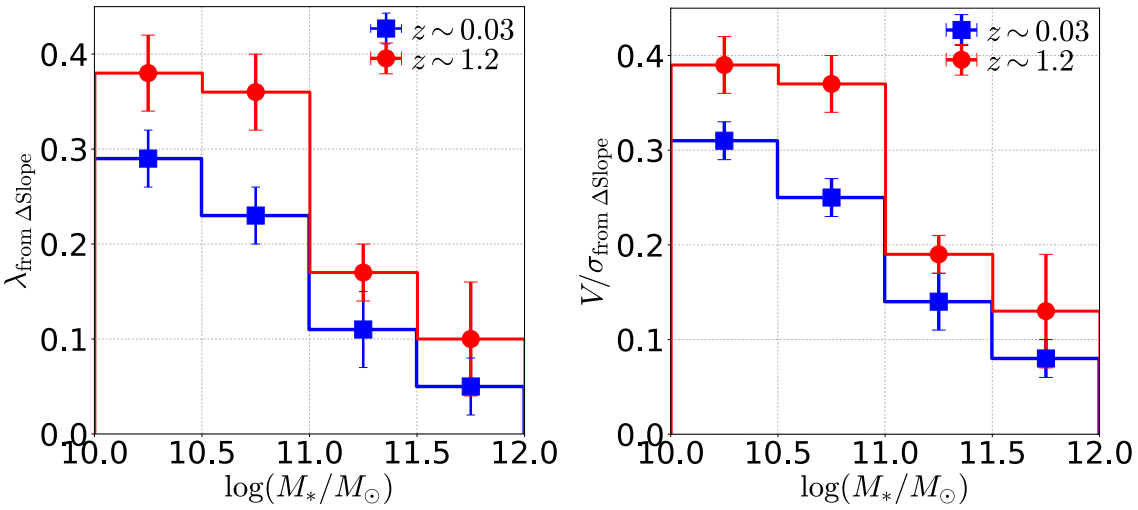

Figure 4.2 Same as Figure 4.1 but for round galaxies ($\epsilon \leq 0.4$). The figure is created with the data listed in Table 4.2.

Table 4.1. Median ΔSlope and converted λ and V/σ for the high- and low-redshift ETG samples.

	High-Redshift			Low-Redshift		
$\log(M_*/M_\odot)$	ΔSlope	λ	V/σ	ΔSlope	λ	V/σ
$10.0 <$	$-0.57^{\pm 0.2}$	$0.47^{\pm 0.04}$	$0.51^{\pm 0.05}$	$-1.19^{\pm 0.1}$	$0.35^{\pm 0.02}$	$0.38^{\pm 0.02}$
$10.0 - 10.5$	$-0.41^{\pm 0.1}$	$0.50^{\pm 0.02}$	$0.55^{\pm 0.02}$	$-0.87^{\pm 0.1}$	$0.41^{\pm 0.02}$	$0.45^{\pm 0.02}$
$10.5 - 11.0$	$-0.48^{\pm 0.2}$	$0.49^{\pm 0.04}$	$0.53^{\pm 0.05}$	$-1.33^{\pm 0.1}$	$0.33^{\pm 0.02}$	$0.35^{\pm 0.02}$
$11.0 - 11.5$	$-1.48^{\pm 0.2}$	$0.30^{\pm 0.04}$	$0.31^{\pm 0.05}$	$-1.96^{\pm 0.2}$	$0.21^{\pm 0.04}$	$0.21^{\pm 0.05}$
$11.5 <$	$-2.20^{\pm 0.4}$	$0.16^{\pm 0.08}$	$0.16^{\pm 0.09}$	$-2.63^{\pm 0.1}$	$0.08^{\pm 0.02}$	$0.06^{\pm 0.02}$

Table 4.2. Same as Table 4.1 but for round galaxies with $\epsilon \leq 0.4$.

	High-Redshift ($\epsilon \leq 0.4$)			Low-Redshift ($\epsilon \leq 0.4$)		
$\log(M_*/M_\odot)$	ΔSlope	λ	V/σ	ΔSlope	λ	V/σ
$10.0 <$	$-0.71^{\pm 0.2}$	$0.33^{\pm 0.04}$	$0.35^{\pm 0.03}$	$-1.31^{\pm 0.1}$	$0.24^{\pm 0.03}$	$0.26^{\pm 0.02}$
$10.0 - 10.5$	$-0.42^{\pm 0.2}$	$0.38^{\pm 0.04}$	$0.39^{\pm 0.03}$	$-0.98^{\pm 0.1}$	$0.29^{\pm 0.03}$	$0.31^{\pm 0.02}$
$10.5 - 11.0$	$-0.56^{\pm 0.2}$	$0.36^{\pm 0.04}$	$0.37^{\pm 0.03}$	$-1.38^{\pm 0.1}$	$0.23^{\pm 0.03}$	$0.25^{\pm 0.02}$
$11.0 - 11.5$	$-1.82^{\pm 0.1}$	$0.17^{\pm 0.03}$	$0.19^{\pm 0.02}$	$-2.18^{\pm 0.2}$	$0.11^{\pm 0.04}$	$0.14^{\pm 0.03}$
$11.5 <$	$-2.27^{\pm 0.4}$	$0.10^{\pm 0.06}$	$0.13^{\pm 0.06}$	$-2.61^{\pm 0.1}$	$0.05^{\pm 0.03}$	$0.08^{\pm 0.02}$

4.3.1 Comparison to simulations of ETG kinematics

We compare our findings to state-of-art cosmological simulations investigating the spin-down history of ETGs. Although the simulations are still not perfect and limited by resolution, some of them provide us the amount of spin down in $z \sim 1$ which should be compared with observations. Now, we have obtained kinematic parameters, λ and V/σ, from observations although they are indirect estimates converted from ΔSlope. Therefore, we are able to compare the amount of spin down statistically.

From cosmological hydrodynamical zoom-in simulations, Naab et al. (2014) have presented three major paths for the spin down of ETGs. One is gas-rich major mergers, another is gas-poor major mergers, and the other is gas-poor multiple minor mergers. While major mergers cause a rapid drop of the angular momentum of the remnant galaxy, minor mergers have cumulative effect, which results in gradual spin down.

We compare evolution of the spin parameter λ quantitatively with simulations done by Penoyre et al. (2017). Penoyre et al. (2017) have investigated the amount of spin down caused by several processes seen in their cosmological hydrodynamical simulations. They suggest that major mergers are the main contributor for the spin down of ETGs. They have presented that major mergers lead to spin down of $\Delta\lambda \sim -0.05$ to -0.2 below $z \sim 1$ (see the top panel in Figure 4.3) for progenitors which originally have $\lambda \sim 0.2$ ($\log(M_*/M_\odot) > 11$) to ~ 0.5 ($\log(M_*/M_\odot) < 11$). They have also shown that minor mergers cause smaller amount of spin down by $\Delta\lambda \sim 0$ to -0.1 below $z \sim 1$ (see the bottom panel in Figure 4.3). The measured amount of the median spin down of our ETGs ($\Delta\lambda \sim 0.08 - 0.16$ depending on the stellar mass) is consistent with the prediction for both major

and minor mergers. Focusing on the massive cluster environment in $z \lesssim 1$ where velocity dispersion is too large for major mergers to take place, continuous gas poor minor mergers may be more likely process.

We note that the simulations in Penoyre et al. (2017) and our observational results do not reach perfect agreement, although the λ evolution is roughly consistent as shown above. While the simulations show that slow rotators have obtain their dispersion-dominated kinematics at $z < 1$, the massive end of our high-redshift ETGs have significantly negative $\Delta\mathrm{Slope}$ implying that they are already slowly rotating. Our results suggest the important epoch for the spin down of the most massive ETGs would be $z > 1$. However, as the evolution of λ inferred from $\Delta\mathrm{Slope}$ in this study would have large uncertainty, it is important to directly and statistically observe kinematics of high-redshift ETGs in the future with next generation telescopes such as JWST and TMT.

The results of situations may be different in different environments. A cosmological hydrodynamical zoom-in simulation focusing on massive clusters has been carried out by Choi & Yi (2017). They have analyzed the spin down mechanisms of ETGs in cluster environments. They have found that while major and minor mergers significantly contribute to the spin down, the dominant driver is not mergers but others whose details are yet unclear. Choi & Yi (2017) propose environmental effects such as fly-by as the unclear contributor to the spin down in their simulation. This looks opposite to the results presented in Penoyre et al. (2017) who suggest major mergers as a main contributor. The discrepancy may arise from the fact that while Choi & Yi (2017) focus on cluster environment with massive haloes ($13.5 < \log(M_{200}/M_{\odot}) < 15$). Penoyre et al. (2017) deal with various environment from fields to clusters up to the halo mass of $\log(M_{200}/M_{\odot}) = 14.7$ (Vogelsberger et al., 2014), and the average environment would be less dense than clusters. Still, Penoyre et al. (2017) do not find significant difference in their simulations between central and satellite galaxies in terms of ellipticity and λ distributions, which implies the environmental effect may not important.

We note that observations of local ETGs have not detected significant dependence of kinematics on environments. Very recent large IFU surveys of nearby ETGs have been revealing that kinematical properties of ETGs do not depend on environments once mass dependence is taken account (Oliva-Altamirano et al., 2017, Brough et al., 2017, Greene et al., 2017b,a), which contradicts with a previous result from a small sample (Scott et al., 2014). Thus, the environmental effect on the kinematics of ETGs has not been observationally confirmed.

To summarize, at the current stage, the most likely mechanism acting on the spin down of the

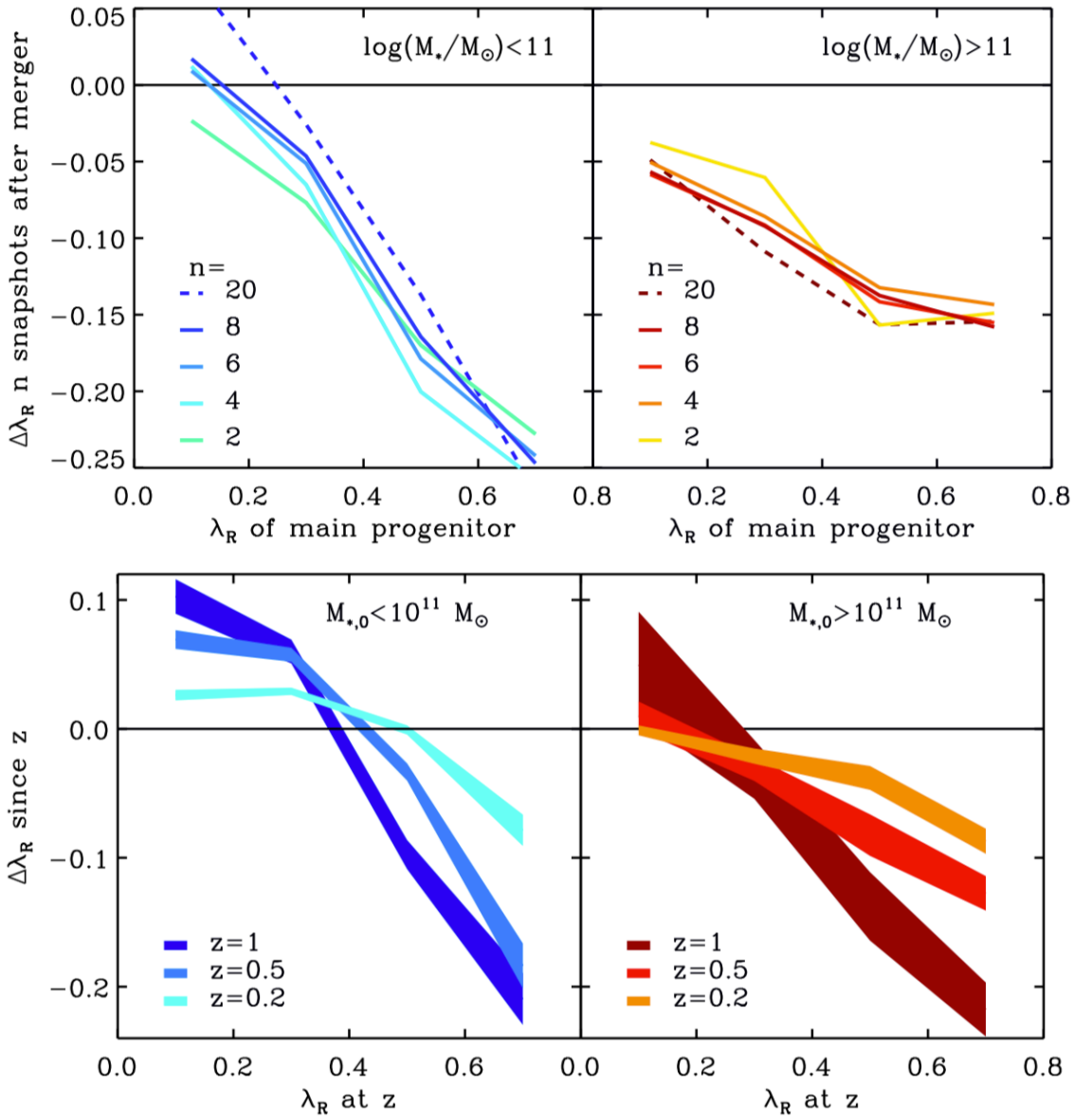

Figure 4.3 Adopted from Figures 14 (top) and 16 (bottom) in Penoyre et al. (2017). Top: Average evolution of λ due to major mergers $\Delta\lambda$ below $z = 1$ shown in the simulation (Penoyre et al., 2017) as a function of λ of the main progenitor at $z = 1$. The left panel is for lower mass galaxies ($\log(M_*/M_\odot) < 11$) while the right panes is for higher mass galaxies ($\log(M_*/M_\odot) < 11$). Color indicate the number of snap show after the merger, i.e., time steps after the merger from 0.25 Gyr (n=2) to 2.5 Gyr (n=20). Considering that our high-redshift ($z \sim 1$) ETG sample have $\lambda \sim 0.5$ for $\log(M_*/M_\odot) < 11$ and $\lambda \sim 0.2$ for $\log(M_*/M_\odot) > 11$ the expected change in λ due to major mergers is $\Delta\lambda \sim -0.2$ for $\log(M_*/M_\odot) < 11$ and $\Delta\lambda \sim -0.05$ for $\log(M_*/M_\odot) > 11$. Bottom: Average evolution of λ due to minor mergers $\Delta\lambda$ below $z = 1$ shown in the simulation (Penoyre et al., 2017) as a function of λ of the main progenitor at a some redshift indicated by color. The left panel is for lower mass galaxies ($\log(M_*/M_\odot) < 11$) while the right panes is for higher mass galaxies ($\log(M_*/M_\odot) < 11$). Similarly to the case of major mergers, the expected change in λ due to minor mergers for our ETG sample is $\Delta\lambda \sim -0.15$ for $\log(M_*/M_\odot) < 11$ and $\Delta\lambda \sim 0$ for $\log(M_*/M_\odot) > 11$.

cluster ETGs in $z < 1$ may be minor mergers, if the environmental effect is not important. We note that, however, environmental effects may be a function of redshifts. As mentioned in the previous section, the size of ETGs does not depend on environment in the local universe but do at $z \sim 1$. If major mergers are the main contributor of the size evolution of cluster ETGs at $z \gtrsim 1$, and if they also contribute to the spin down, we might observe environmental dependence of galaxy rotation at $z \sim 1$. In the future, $\Delta\mathrm{Slope}$ evolution should be compared between clusters and fields.

4.3.2 Comparison to Observations of Kinematics of Distant ETGs

We compare our results with previous observational studies of kinematics of distant ETGs. It is a hard task to investigate stellar kinematics of distant ETGs because absorption lines are very faint and PSF effects on the observed velocity fields is obvious. However, van der Wel & van der Marel (2008) have carried out ultra-deep optical slit spectroscopy (van der Wel et al., 2005), and derived V/σ for 25 field ETGs in the redshift range $0.6 < z < 1.2$. They also apply dynamical modeling to take account of the PSF effects. V/σ of the 25 ETGs widely spreads from ~ 0 to 1.5. The median V/σ of the filed ETGs is ~ 0.5 (see also Wuyts et al., 2010). As stellar masses of the their sample is $\log(M_*/M_\odot) \sim 11$, the median V/σ agree well between the field ETGs and our cluster ETGs. This implies that the environmental effect on ETG kinematics at $z \sim 1$ may not be significant. Note that we have assumed that the relation between V/σ and $\Delta\mathrm{Slope}$ is independent of environments and redshifts, and conversion from $\Delta\mathrm{Slope}$ to V/σ should be taken with caution. Still, it is curious why we have observed the environmental effect on the size of ETGs at $z \sim 1$ (Delaye et al., 2014) which may be originated from more frequent major merger in clusters in the past while we do not detect significant difference in the median V/σ. In the future work, it is important to measure $\Delta\mathrm{Slope}$ for field ETGs at $z \sim 1$ in order to investigate possible environmental effects.

Next, we compare our findings to another result on the ETG kinematics at a high redshift. Taking advantage of strong gravitational lensing caused by a intermediate redshift cluster, Newman et al. (2015) have obtained high-quality near-infrared spectra of a massive ($\log(M_*/M_\odot) = 11.24$) ETG at $z = 2.6$. They analyzed dynamical properties from slit spectroscopic data. They detect rotation in the stellar absorption features, and obtain the spin parameter $V/\sigma = 0.70 \pm 0.21$ using dynamical modeling with observational effects taken into account. The galaxy has very large V/σ compared to the local counter part because it is massive ($\log(M_*/M_\odot) = 11.24$), round ($\epsilon = 0.12 \pm 0.06$), and also

have a large Sérsic index ($n = 3.5 \pm 0.9$). A simple comparison of V/σ between the galaxy and local counter part with a similar mass and ellipticity ($V/\sigma \sim 0.14$) yields the evolution of $\Delta V/\sigma \sim -0.56$ by $z = 0$. Moreover, even by $z \sim 1.2$, the galaxy need to reduce a large amount of V/σ from 0.70 at $z = 2.6$ to ~ 0.19 at $z \sim 1.2$, if we assume that the galaxy is a typical ETG at the redshift. If this is the case, strong evolution of V/σ should take place in a short time scale ($\sim$2.6 Gyr). In addition, the inferred amount of the evolution may be an upper limit because we assume no evolution in the stellar mass. In reality, the galaxy may grow in the stellar mass if major or minor mergers take place.

Minor mergers alone may not be sufficient to reduce the large amount of angular momentum in such a short time scale. Penoyre et al. (2017) have shown that minor mergers decrease λ only by ~ -0.1 per 8Gyr from $z \sim 1$ to 0. If we extrapolate this decreasing rate into $z > 1$, λ ($\sim V/\sigma$) would decrease at most by $\sim 0.2 - 0.3$ even with one order of magnitude higher minor merger rates at $z \sim 2$ than $z \sim 0$ (Rodriguez-Gomez et al., 2015). Even if we take the lower limit for V/σ of the galaxy ($V/\sigma = 0.5$ at $z = 2.6$), the amount of V/σ to be reduced by $z \sim 1.2$ is ~ 0.3. This is still large compared to the predicted amount in minor mergers, although they are marginally consistent.

On the other hand, major mergers may be responsible for the kinematic evolution of the galaxy between $z = 2.6$ to ~ 1. Taking account of rapidly increasing merger rates with increasing redshift, $\sim$ 1 major merger with mass ratio $\gtrsim$ 1:4 can occur between the redshift range (e.g., Figure 7 in Rodriguez-Gomez et al., 2015). Therefore, the galaxy may be able to reduce V/σ sufficiently by $z \sim 1$. Note that merger rates considered here are derived from simulations in various environments (Vogelsberger et al., 2014, Rodriguez-Gomez et al., 2015) and the simulations do not focus on cluster environments.

Based on the discussion above, we propose that the most important epoch for kinematic evolution (i.e., spin down) of massive ETGs, which tend to be slow rotators in the local universe, may be $z \sim 2 - 3$ to 1. We have found that massive ETGs (e.g., $\log(M_*/M_\odot) > 11$) have already had extended profiles at $z \sim 1$ at least in cluster environments. In addition, a possible progenitor of such massive galaxies at $z = 2.6$ has large V/σ. Therefore, large amount of spin down is required for the galaxy if it is a typical ETG at $z = 2.6$.

The possible large spin down in $1 \lesssim z \lesssim 2$ is also supported by another observational study (Belli et al., 2017). Belli et al. (2017) have investigated average V/σ of $z \sim 2$ ETGs, using ellipticity and (spatially-unresolved) line-of-sight velocity dispersion with a simple kinematical model. They have shown that quiescent galaxies at $z \sim 2$ have a factor of two larger V/σ than $z \sim 0$. As the V/σ

evolution inferred from $\Delta\mathrm{Slope}$ is a factor of ~ 1.3 (from 0.38 to 0.51), larger amount of evolution in V/σ would take place at $1 \lesssim z \lesssim 2$. Thus, further studies of ETG kinematics in the redshift range of $z \sim 1$ to 2 (or $\sim$3) would provide critical constraints on the evolution history and its mechanisms of ETGs.

4.3.3 Possible Link between Truncated Fast Rotators and High-Redshift Star-Forming Galaxies

Finally, we discuss the possible link between truncated ($\Delta\mathrm{Slope} > 0$) fast rotators and star-forming galaxies at high redshifts. We have discussed the possibility that majority of intermediate mass ETGs (i.e., truncated fast rotators) may have formed from star-forming galaxies at $z \gtrsim 2$ in secular processes in Section 4.1.1.1. At $z \sim 0$, fast rotators have small V/σ and normal star-forming galaxies have very large V/σ (> 5, e.g., Epinat et al., 2010, Green et al., 2014). However, as there is significant evolution of $\Delta\mathrm{Slope}$ from $z \sim 1$ to 0, progenitors of the local fast rotators may have larger V/σ at high redshifts, assuming passive evolution. We discuss the expected difference of V/σ of the passive progenitors and star-forming galaxies observed at high redshifts

Recent advance of IFS in near-infrared wavelength range has provided us kinematic properties of large samples of star-forming galaxies for which gas kinematics can be obtained from strong $H\alpha$ line emission. Several studies have revealed that high-redshift galaxies are rotating disks but with smaller V/σ compared to local galaxies (e.g., Genzel et al., 2008, Kassin et al., 2012, Wisnioski et al., 2015). In the local universe, V/σ of star-forming galaxies is ~ 10, it becomes $\sim 3-5$ at $z \sim 1$, and then ~ 2 at $z \sim 2-3$ (Wisnioski et al., 2015). Although the gradual decline of V/σ is due to increasing velocity dispersion σ, it does not mean the galaxies are dynamically hot (dispersion dominated) like ETGs or bulges. Rather, the large σ is interpreted as an integration of local non-ordered motion of gas, i.e., turbulence due to large gas fraction in disks at high-redshifts (e.g., Genzel et al., 2011, Tacconi et al., 2010).

On the other hand, the expected amount of evolution in V/σ of ETGs is not large. The average V/σ of ETGs at $z \sim 1$ is ~ 0.5 which is converted from $\Delta\mathrm{Slope}$. This is much smaller than V/σ of star-forming galaxies at $z \sim 2-3$. Therefore, on average, there is a large gap between V/σ of high-redshift star-forming galaxies ($V/\sigma \gtrsim 2$) and $z \sim 1$ ETGs. We note that there should be a fraction of ETGs which would achieve larger V/σ than the average. This fraction may be explained by secular

transformation from the star-forming galaxies into ETGs followed by passive evolution.

If high-redshift star-forming galaxies are transformed into average ETGs, V/σ need to be reduced from $V/\sigma \gtrsim 2$ ($z \sim 2$ star-forming galaxies) to $V/\sigma \lesssim 0.5$ ($z \sim 1$ ETGs). Small V/σ of ETGs (not only slow rotators but also fast rotators) is originated from a dynamically hot bulge. Therefore, bulge formation is a key for the morphological evolution from star-forming disks to ETGs. As we have mentioned in Section 4.1.1.1, at high redshifts ($z \gtrsim 2$), large gas fractions in disks leads to formation of massive clumps which would shrink into the center a galaxy to form a bulge component with small V/σ (~ 1 Elmegreen et al., 2008). Soon after that, star formation may be quenched by morphological quenching (Martig et al., 2009).

Once such a bulge is formed, V/σ become quite close to the expected value of the $z \sim 1$ ETGs ($V/\sigma \sim 0.5$). Still, $V/\sigma \sim 1$ at $z \sim 2$ may be too large for such a galaxy to be an average population of $z \sim 1$ ETGs ($V/\sigma \sim 0.5$). If ETGs formed in the secular process are the main population of fast rotating ETGs with truncated profiles (Section 4.1.1.1), they need to reduce $\Delta V/\sigma \sim 0.5$ by $z \sim 1$. This amount seems to be too large if we assume the evolution is dominated by minor mergers in which case V/σ would decrease only by $\sim 0.2-0.3$ between $z \sim 2$ to 1 as discussed in the previous section. Therefore, it may be difficult to form majority of fast rotators from the high-redshift star-forming galaxies by secular processes which we have proposed in Section 4.1.1.1. However, we have relied on too many assumptions such as the $\Delta\mathrm{Slope}$-V/σ relation and results from the improving yet still imperfect simulations. Therefore, we would like to emphasize again the importance of investigating the spin down history of ETGs or quiescent galaxies at $z \sim 1$ to 2 in order to understand galaxy formation history from star-forming disks to quiescent ETGs.

5

Conclusions

In Chapter 1, we have reviewed up-to-date results of kinematics of ETG from observations and simulations. Recent IFS observations of local ETGs, have established a view that they can be classified into fast rotators and slow rotators. At the same time, observational studies at high redshifts have found that there is a dramatic size growth of massive ETGs from $z \sim 2$ to 0. Cosmological simulations show a that two-phase formation scenario could explain these observational results. However, the dominant processes are not clear mainly because of complexity in the formation and evolution processes. Observations of kinematic properties of high-redshift ETGs is inevitably important to observationally constrain the processes. In spite of the importance, crucial difficulty of absorption line spectroscopy at high redshifts prevents us from studying kinematics. Surface photometry measurement which is a less observationally expensive tool is important with which kinematics of high-redshift ETGs could be indirectly investigated. In this study, in order to observationally investigate the evolution of kinematic properties of ETGs, first, we find a photometric parameter which can be used as a good proxy for kinematics of ETGs. Then, we measure the parameters for high-redshift and low-redshift ETGs.

In Chapter 2, we have analyzed radial light profiles of 166 non-barred ETGs in the local universe. Since the ETGs have been observed by the large IFS survey ATLAS^{3D}, spatially resolved kinematics

is available for the sample. By comparing the r-band light profiles, slowly rotating ETGs tend to have extended profile in outer regions than fast rotators. We have defined a parameter $\Delta\mathrm{Slope}$ using the inner and outer slopes of the light profiles. With the parameter, the deviation of the light profiles from a pure Sérsic profile can be evaluated. As a result, almost all slow rotators with the spin parameter $\lambda_\mathrm{e} \leq 0.3$ have negative values of $\Delta\mathrm{Slope}$ indicative of more extended profile than a Sérsic profile. On the other hand, fast rotators can have various $\Delta\mathrm{Slope}$ values from negative to positive, but a large fraction of them have signature of disks characterized by large ellipticity ($\epsilon > 0.4$) or positive $\Delta\mathrm{Slope}$ (i.e., truncated outer profiles). We have found a significant correlation between $\Delta\mathrm{Slope}$ and λ_e by carrying out KS tests. The correlation is also found for round ETGs for which other structural parameters do not show significant correlations to λ_e. We obtain an approximated linear relation between $\Delta\mathrm{Slope}$ and λ_e although the intrinsic scatter is large.

In Chapter 3, we have analyzed and compared radial light profiles of ETGs residing in massive galaxy clusters at $z \sim 1$ and 0, focusing on the $\Delta\mathrm{Slope}$ parameter. We construct a sample of ~ 600 quiescent ETGs at each redshift using color-magnitude selection and parametric morphological selection. For the high-redshift sample, we have made use of high-quality imaging data taken by HST as well as spectroscopic data obtained the HST Cluster Supernovae Survey. For the low-redshift counterpart, we have utilized publicly available imaging and spectroscopic data provided by SDSS. We have measured the inner and outer slopes of light profiles in the rest-frame optical wavelength ($\lambda \sim 4000$ Å) and applied appropriate corrections for the effect of PSF. Our findings in this chapter is summarized as follows: The high-redshift ETGs have significantly larger $\Delta\mathrm{Slope}$ than the low-redshift, with the largest difference at $\log(M_*/M_\odot) \sim 10.5 - 11$. The difference of $\Delta\mathrm{Slope}$ is originated mostly from the outer slope of the light profile, and the contribution from the inner slope is not significant. The difference of the outer slope could also be seen in the staked light profiles of ETGs revealing that the high-redshift ETGs tend to have more truncated outer profiles than the low-redshift ETGs. The mass dependence of $\Delta\mathrm{Slope}$ is observed both in the high- and low-redshift samples with the massive end dominated by extended ($\Delta\mathrm{Slope}<0$) galaxies. The results do not significantly change even if we do not apply correction for the PSF effect or if we use different selection criteria of ETGs.

In Chapter 4, we discuss evolution of ETGs based on the findings above. In Section 4.1, we first discuss possible formation and evolution mechanisms of fast rotating and slowly rotating ETG based on the relation between $\Delta\mathrm{Slope}$ and λ in Chapter 2. The fact that a large fraction of fast rotators have signatures of the dominance of disks at large radii implies the possible contribution of secure processes

for the formation mechanisms of rotating ETGs with which outer disks would not be destroyed. Major mergers may be important for fast rotators with extended outer profiles which tend to be massive. We consider that the formation and evolution processes forming slow rotators may also be responsible for the extended outer profiles because most of them have negative $\Delta\mathrm{Slope}$. At this moment, we have not yet reached a firm conclusion about which processes is the dominant, but they include external processes such as major or minor mergers, internal ones such as AGN feedback. In the future, quantitative comparisons of parameters including λ, $\Delta\mathrm{Slope}$, and others between observations and simulations will help us understand the mechanisms.

In Section 4.2, we address the possible mechanisms of the structural evolution of quiescent ETGs in massive clusters, focusing the size evolution based on findings in Chapter 3. We have found the size evolution for the ETG samples, which is consistent with previous studies (Delaye et al., 2014, Andreon et al., 2016, Mitsuda et al., 2017). Taking account of the outer slope evolution from truncated at $z \sim 1$ to extended at $z \sim 0$ combined with other structural parameters such as Sérsic index and ellipticity, we consider that the size evolution of the cluster ETG samples is more likely to be originated from evolution of individual galaxies, although we do not completely rule out the progenitor bias. Together with previous studies showing environmental dependence of the size evolution of ETGs (Delaye et al., 2014, Andreon et al., 2016) as well as inactive nature of the ETGs and large velocity dispersion of the clusters, minor mergers may be the most likely processes of the size evolution of individual ETGs in clusters at $z \sim 1$.

Finally, in Section 4.3, we have discussed kinematical evolution of ETGs, adopting the relation between $\Delta\mathrm{Slope}$ and λ found in Chapter 2. We simply convert $\Delta\mathrm{Slope}$ of the high- and low-redshift ETGs into λ or V/σ, assuming that the relation between $\Delta\mathrm{Slope}$ and λ does not change with redshifts and environments. The median value of V/σ of the high-redshift ETG sample becomes ~ 0.5. This value is roughly consistent with that of 25 field ETGs ($V/\sigma \sim 0.5$) at $z \sim 1$ which is directly measured with ultra-deep slit spectroscopy (van der Wel & van der Marel, 2008). The average amount of decrease of λ from $z \sim 1$ to 0 (~ 0.1) is comparable with the amount of spin down due to minor mergers in cosmological simulation (Penoyre et al., 2017). Although we have found significant evolution of $\Delta\mathrm{Slope}$ between $z \sim 1$ to 0, massive ETGs with $\log(M_*/M_\odot) > 11$ have extended outer profile even at $z \sim 1$, which suggests that the dominant processes for forming massive slow rotators would work efficiently at $z > 1$.

As presented above, we have investigated evolution of kinematic properties of ETG in $z < 1$ with

large samples of ~ 600 ETGs at $z \sim 1$ and 0, using the relation between $\Delta\mathrm{Slope}$ and λ found in the local Universe. As a result, we have found significant evolution in $\Delta\mathrm{Slope}$ which may be related to kinematical evolution. Our approach is an indirect method, and therefore there would be uncertainty in the interpretation from $\Delta\mathrm{Slope}$ into kinematics. In a future work, two approaches is important. One is to test whether the relation $\Delta\mathrm{Slope}$ and λ holds in another environment using upcoming large IFU surveys such as MaNGA (Bundy et al., 2015) and HECTOR (Bland-Hawthorn, 2015). Also, direct observations of stellar kinematics of distant ETG, especially at $z \sim 1$ to 2 (or 3), using next generation space-based and 30-m class ground-based telescopes such as JWST, GMT, ELT, and TMT, which will provide critical constraints on the formation and evolution mechanisms of ETGs.

References

Abazajian, K. N., Adelman-McCarthy, J. K., Agüeros, M. A., Allam, S. S., Allende Prieto, C., An, D., Anderson, K. S. J., Anderson, S. F., Annis, J., Bahcall, N. A., & et al. (2009). The Seventh Data Release of the Sloan Digital Sky Survey. ***ApJS***, 182, 543–558.

Abraham, R. G., Valdes, F., Yee, H. K. C., & van den Bergh, S. (1994). The morphologies of distant galaxies. 1: an automated classification system. ***ApJ***, 432, 75–90.

Abraham, R. G., van den Bergh, S., Glazebrook, K., Ellis, R. S., Santiago, B. X., Surma, P., & Griffiths, R. E. (1996). The Morphologies of Distant Galaxies. II. Classifications from the Hubble Space Telescope Medium Deep Survey. ***ApJS***, 107, 1.

Abraham, R. G., van den Bergh, S., & Nair, P. (2003). A New Approach to Galaxy Morphology. I. Analysis of the Sloan Digital Sky Survey Early Data Release. ***ApJ***, 588, 218–229.

Aihara, H., Allende Prieto, C., An, D., Anderson, S. F., Aubourg, É., Balbinot, E., Beers, T. C., Berlind, A. A., Bickerton, S. J., Bizyaev, D., Blanton, M. R., Bochanski, J. J., Bolton, A. S., Bovy, J., Brandt, W. N., Brinkmann, J., Brown, P. J., Brownstein, J. R., Busca, N. G., Campbell, H., Carr, M. A., Chen, Y., Chiappini, C., Comparat, J., Connolly, N., Cortes, M., Croft, R. A. C., Cuesta, A. J., da Costa, L. N., Davenport, J. R. A., Dawson, K., Dhital, S., Ealet, A., Ebelke, G. L., Edmondson, E. M., Eisenstein, D. J., Escoffier, S., Esposito, M., Evans, M. L., Fan, X., Femenía Castellá, B., Font-Ribera, A., Frinchaboy, P. M., Ge, J., Gillespie, B. A., Gilmore, G., González Hernández, J. I., Gott, J. R., Gould, A., Grebel, E. K., Gunn, J. E., Hamilton, J.-C., Harding, P., Harris, D. W., Hawley, S. L., Hearty, F. R., Ho, S., Hogg, D. W., Holtzman, J. A., Honscheid, K., Inada, N., Ivans, I. I., Jiang, L., Johnson, J. A., Jordan, C., Jordan, W. P., Kazin, E. A., Kirkby, D., Klaene, M. A., Knapp, G. R., Kneib, J.-P., Kochanek, C. S., Koesterke, L., Kollmeier, J. A., Kron, R. G., Lampeitl, H., Lang, D., Le Goff, J.-M., Lee, Y. S., Lin, Y.-T., Long, D. C., Loomis, C. P., Lucatello, S., Lundgren, B., Lupton, R. H., Ma, Z., MacDonald, N., Mahadevan, S., Maia, M. A. G., Makler, M., Malanushenko, E., Malanushenko, V., Mandelbaum, R., Maraston, C., Margala, D., Masters, K. L., McBride, C. K., McGehee, P. M., McGreer, I. D., Ménard, B., Miralda-Escudé, J., Morrison, H. L., Mullally, F., Muna, D., Munn, J. A., Murayama, H., Myers, A. D., Naugle, T., Neto, A. F., Nguyen, D. C., Nichol, R. C., O'Connell, R. W., Ogando, R. L. C., Olmstead, M. D., Oravetz, D. J., Padmanabhan, N., Palanque-Delabrouille, N., Pan, K., Pandey, P., Pâris, I., Percival, W. J., Petitjean, P., Pfaffenberger, R., Pforr, J., Phleps, S., Pichon, C., Pieri, M. M., Prada, F., Price-Whelan, A. M., Raddick, M. J., Ramos, B. H. F., Reylé, C., Rich, J., Richards, G. T., Rix, H.-W., Robin, A. C., Rocha-Pinto, H. J., Rockosi, C. M., Roe, N. A., Rollinde, E., Ross, A. J., Ross, N. P., Rossetto, B. M., Sánchez, A. G.,

Sayres, C., Schlegel, D. J., Schlesinger, K. J., Schmidt, S. J., Schneider, D. P., Sheldon, E., Shu, Y., Simmerer, J., Simmons, A. E., Sivarani, T., Snedden, S. A., Sobeck, J. S., Steinmetz, M., Strauss, M. A., Szalay, A. S., Tanaka, M., Thakar, A. R., Thomas, D., Tinker, J. L., Tofflemire, B. M., Tojeiro, R., Tremonti, C. A., Vandenberg, J., Vargas Magaña, M., Verde, L., Vogt, N. P., Wake, D. A., Wang, J., Weaver, B. A., Weinberg, D. H., White, M., White, S. D. M., Yanny, B., Yasuda, N., Yeche, C., & Zehavi, I. (2011). The Eighth Data Release of the Sloan Digital Sky Survey: First Data from SDSS-III. ***ApJS***, 193, 29.

Alam, S., Albareti, F. D., Allende Prieto, C., Anders, F., Anderson, S. F., Anderton, T., Andrews, B. H., Armengaud, E., Aubourg, É., Bailey, S., & et al. (2015). The Eleventh and Twelfth Data Releases of the Sloan Digital Sky Survey: Final Data from SDSS-III. ***ApJS***, 219, 12.

Allen, R. J., Kacprzak, G. G., Spitler, L. R., Glazebrook, K., Labbé, I., Tran, K.-V. H., Straatman, C. M. S., Nanayakkara, T., Brammer, G. B., Quadri, R. F., Cowley, M., Monson, A., Papovich, C., Persson, S. E., Rees, G., Tilvi, V., & Tomczak, A. R. (2015). The Differential Size Growth of Field and Cluster Galaxies at z = 2.1 Using the ZFOURGE Survey. ***ApJ***, 806, 3.

Andredakis, Y. C., Peletier, R. F., & Balcells, M. (1995). The Shape of the Luminosity Profiles of Bulges of Spiral Galaxies. ***MNRAS***, 275, 874.

Andredakis, Y. C. & Sanders, R. H. (1994). Exponential bulges in late-type spirals: an improved description of the light distribution. ***MNRAS***, 267, 283–296.

Andreon, S., de Propris, R., Puddu, E., Giordano, L., & Quintana, H. (2008a). Scaling relations of the colour-detected cluster RzCS 052 at z = 1.016 and some other high-redshift clusters. ***MNRAS***, 383, 102–112.

Andreon, S., Dong, H., & Raichoor, A. (2016). Size growth of red-sequence early-type galaxies in clusters in the last 10 Gyr. ***A&A***, 593, A2.

Andreon, S., Puddu, E., de Propris, R., & Cuillandre, J.-C. (2008b). Galaxy evolution in the high-redshift, colour-selected cluster RzCS 052 at z = 1.02. ***MNRAS***, 385, 979–985.

Andreon, S., Valtchanov, I., Jones, L. R., Altieri, B., Bremer, M., Willis, J., Pierre, M., & Quintana, H. (2005). Batch discovery of nine z∼ 1 clusters using X-ray and K or R, z' images. ***MNRAS***, 359, 1250–1260.

Appenzeller, I., Fricke, K., Fürtig, W., Gässler, W., Häfner, R., Harke, R., Hess, H.-J., Hummel, W., Jürgens, P., Kudritzki, R.-P., Mantel, K.-H., Meisl, W., Muschielok, B., Nicklas, H., Rupprecht, G., Seifert, W., Stahl, O., Szeifert, T., & Tarantik, K. (1998). Successful commissioning of FORS1 - the first optical instrument on the VLT. ***The Messenger***, 94, 1–6.

Bacon, R., Copin, Y., Monnet, G., Miller, B. W., Allington-Smith, J. R., Bureau, M., Carollo, C. M., Davies, R. L., Emsellem, E., Kuntschner, H., Peletier, R. F., Verolme, E. K., & de Zeeuw, P. T. (2001). The SAURON project - I. The panoramic integral-field spectrograph. ***MNRAS***, 326, 23–35.

Bai, L., Yee, H. K. C., Yan, R., Lee, E., Gilbank, D. G., Ellingson, E., Barrientos, L. F., Gladders, M. D., Hsieh, B. C., & Li, I. H. (2014). The Inside-out Growth of the Most Massive Galaxies at 0.3 $<$ z $<$ 0.9. ***ApJ***, 789, 134.

Baldry, I. K., Balogh, M. L., Bower, R. G., Glazebrook, K., Nichol, R. C., Bamford, S. P., & Budavari, T. (2006). Galaxy bimodality versus stellar mass and environment. ***MNRAS***, 373, 469–483.

Baldry, I. K., Glazebrook, K., Brinkmann, J., Ivezić, Ž., Lupton, R. H., Nichol, R. C., & Szalay, A. S. (2004). Quantifying the Bimodal Color-Magnitude Distribution of Galaxies. ***ApJ***, 600, 681–694.

Baum, W. A. (1959). Population Inferences from Star Counts, Surface Brightness and Colors. ***PASP***, 71, 106–117.

Bekki, K. (1998). Unequal-Mass Galaxy Mergers and the Creation of Cluster S0 Galaxies. ***ApJ***, 502, L133–L137.

Bekki, K. & Shioya, Y. (1997). Formation of Boxy and Disky Elliptical Galaxies in Early Dissipative Mergers. ***ApJ***, 478, L17–L20.

Belli, S., Newman, A. B., & Ellis, R. S. (2015). Stellar Populations from Spectroscopy of a Large Sample of Quiescent Galaxies at Z $>$ 1: Measuring the Contribution of Progenitor Bias to Early Size Growth. ***ApJ***, 799, 206.

Belli, S., Newman, A. B., & Ellis, R. S. (2017). MOSFIRE Spectroscopy of Quiescent Galaxies at 1.5 $<$ z $<$ 2.5. I. Evolution of Structural and Dynamical Properties. ***ApJ***, 834, 18.

Bender, R., Doebereiner, S., & Möllenhoff, C. (1988). Isophote shapes of elliptical galaxies. I - The data. ***A&AS***, 74, 385–426.

Bender, R. & Möllenhoff, C. (1987). Morphological analysis of massive early-type galaxies in the Virgo cluster. ***A&A***, 177, 71–83.

Bender, R., Surma, P., Doebereiner, S., Möllenhoff, C., & Madejsky, R. (1989). Isophote shapes of elliptical galaxies. II - Correlations with global optical, radio and X-ray properties. ***A&A***, 217, 35–43.

Bernardi, M., Meert, A., Vikram, V., Huertas-Company, M., Mei, S., Shankar, F., & Sheth, R. K. (2014). Systematic effects on the size-luminosity relations of early- and late-type galaxies: dependence on model fitting and morphology. ***MNRAS***, 443, 874–897.

Bertin, E. & Arnouts, S. (1996). SExtractor: Software for source extraction. ***A&AS***, 117, 393–404.

Bezanson, R., van Dokkum, P. G., Tal, T., Marchesini, D., Kriek, M., Franx, M., & Coppi, P. (2009). The Relation Between Compact, Quiescent High-redshift Galaxies and Massive Nearby Elliptical Galaxies: Evidence for Hierarchical, Inside-Out Growth. ***ApJ***, 697, 1290–1298.

Binney, J. (1978). On the rotation of elliptical galaxies. ***MNRAS***, 183, 501–514.

Binney, J. (2005). Rotation and anisotropy of galaxies revisited. ***MNRAS***, 363, 937–942.

Binney, J. & Tremaine, S. (2008). ***Galactic Dynamics: Second Edition***. Princeton University Press.

Blakeslee, J. P., Franx, M., Postman, M., Rosati, P., Holden, B. P., Illingworth, G. D., Ford, H. C., Cross, N. J. G., Gronwall, C., Benítez, N., Bouwens, R. J., Broadhurst, T. J., Clampin, M., Demarco, R., Golimowski, D. A., Hartig, G. F., Infante, L., Martel, A. R., Miley, G. K., Menanteau, F., Meurer, G. R., Sirianni, M., & White, R. L. (2003). Advanced Camera for Surveys Photometry of the Cluster RDCS 1252.9-2927: The Color-Magnitude Relation at z = 1.24. ***ApJ***, 596, L143–L146.

Bland-Hawthorn, J. (2015). The Hector Survey: integral field spectroscopy of 100,000 galaxies. In B. L. Ziegler, F. Combes, H. Dannerbauer, & M. Verdugo (Eds.), ***Galaxies in 3D across the Universe***, volume 309 of ***IAU Symposium*** (pp. 21–28).

Blanton, M. R., Dalcanton, J., Eisenstein, D., Loveday, J., Strauss, M. A., SubbaRao, M., Weinberg, D. H., Anderson, Jr., J. E., Annis, J., Bahcall, N. A., Bernardi, M., Brinkmann, J., Brunner, R. J., Burles, S., Carey, L., Castander, F. J., Connolly, A. J., Csabai, I., Doi, M., Finkbeiner, D., Friedman, S., Frieman, J. A., Fukugita, M., Gunn, J. E., Hennessy, G. S., Hindsley, R. B., Hogg, D. W., Ichikawa, T., Ivezić, Ž., Kent, S., Knapp, G. R., Lamb, D. Q., Leger, R. F., Long, D. C., Lupton, R. H., McKay, T. A., Meiksin, A., Merelli, A., Munn, J. A., Narayanan, V., Newcomb, M., Nichol, R. C., Okamura, S., Owen, R., Pier, J. R., Pope, A., Postman, M., Quinn, T., Rockosi, C. M., Schlegel, D. J., Schneider, D. P., Shimasaku, K., Siegmund, W. A., Smee, S., Snir, Y., Stoughton, C., Stubbs, C., Szalay, A. S., Szokoly, G. P., Thakar, A. R., Tremonti, C., Tucker, D. L., Uomoto, A., Vanden Berk, D., Vogeley, M. S., Waddell, P., Yanny, B., Yasuda, N., & York, D. G. (2001). The Luminosity Function of Galaxies in SDSS Commissioning Data. ***AJ***, 121, 2358–2380.

Böhringer, H., Mullis, C., Rosati, P., Lamer, G., Fassbender, R., Schwope, A., & Schuecker, P. (2005). Galaxy Cluster Archaeology. ***The Messenger***, 120, 33–36.

Bois, M., Emsellem, E., Bournaud, F., Alatalo, K., Blitz, L., Bureau, M., Cappellari, M., Davies, R. L., Davis, T. A., de Zeeuw, P. T., Duc, P.-A., Khochfar, S., Krajnović, D., Kuntschner, H., Lablanche, P.-Y., McDermid, R. M., Morganti, R., Naab, T., Oosterloo, T., Sarzi, M., Scott, N., Serra, P., Weijmans, A.-M., & Young, L. M. (2011). The ATLAS^{3D} project - VI. Simulations of binary galaxy mergers and the link with fast rotators, slow rotators and kinematically distinct cores. ***MNRAS***, 416, 1654–1679.

Borlaff, A., Eliche-Moral, M. C., Rodríguez-Pérez, C., Querejeta, M., Tapia, T., Pérez-González, P. G., Zamorano, J., Gallego, J., & Beckman, J. (2014). Formation of S0 galaxies through mergers. Antitruncated stellar discs resulting from major mergers . ***A&A***, 570, A103.

Bower, R. G., Lucey, J. R., & Ellis, R. S. (1992). Precision Photometry of Early Type Galaxies in the Coma and Virgo Clusters - a Test of the Universality of the Colour / Magnitude Relation - Part Two - Analysis. ***MNRAS***, 254, 601.

Bremer, M. N., Valtchanov, I., Willis, J., Altieri, B., Andreon, S., Duc, P. A., Fang, F., Jean, C., Lonsdale, C., Pacaud, F., Pierre, M., Shupe, D. L., Surace, J. A., & Waddington, I. (2006). XMM-LSS discovery of a z = 1.22 galaxy cluster. ***MNRAS***, 371, 1427–1434.

Brodwin, M., Brown, M. J. I., Ashby, M. L. N., Bian, C., Brand, K., Dey, A., Eisenhardt, P. R., Eisenstein, D. J., Gonzalez, A. H., Huang, J.-S., Jannuzi, B. T., Kochanek, C. S., McKenzie, E., Murray, S. S., Pahre, M. A., Smith, H. A., Soifer, B. T., Stanford, S. A., Stern, D., & Elston, R. J. (2006). Photometric Redshifts in the IRAC Shallow Survey. ***ApJ***, 651, 791–803.

Brodwin, M., Stanford, S. A., Gonzalez, A. H., Zeimann, G. R., Snyder, G. F., Mancone, C. L., Pope, A., Eisenhardt, P. R., Stern, D., Alberts, S., Ashby, M. L. N., Brown, M. J. I., Chary, R.-R., Dey, A., Galametz, A., Gettings, D. P., Jannuzi, B. T., Miller, E. D., Moustakas, J., & Moustakas, L. A. (2013). The Era of Star Formation in Galaxy Clusters. ***ApJ***, 779, 138.

Brough, S., van de Sande, J., Owers, M. S., d'Eugenio, F., Sharp, R., Cortese, L., Scott, N., Croom, S. M., Bassett, R., Bekki, K., Bland-Hawthorn, J., Bryant, J. J., Davies, R., Drinkwater, M. J., Driver, S. P., Foster, C., Goldstein, G., López-Sánchez, Á. R., Medling, A. M., Sweet, S. M., Taranu, D. S., Tonini, C., Yi, S. K., Goodwin, M., Lawrence, J. S., & Richards, S. N. (2017). The SAMI Galaxy Survey: Mass as the Driver of the Kinematic Morphology-Density Relation in Clusters. ***ApJ***, 844, 59.

Bruzual, G. & Charlot, S. (2003). Stellar population synthesis at the resolution of 2003. ***MNRAS***, 344, 1000–1028.

Bryant, J. J., Owers, M. S., Robotham, A. S. G., Croom, S. M., Driver, S. P., Drinkwater, M. J., Lorente, N. P. F., Cortese, L., Scott, N., Colless, M., Schaefer, A., Taylor, E. N., Konstantopoulos, I. S., Allen, J. T., Baldry, I., Barnes, L., Bauer, A. E., Bland-Hawthorn, J., Bloom, J. V., Brooks, A. M., Brough, S., Cecil, G., Couch, W., Croton, D., Davies, R., Ellis, S., Fogarty, L. M. R., Foster, C., Glazebrook, K., Goodwin, M., Green, A., Gunawardhana, M. L., Hampton, E., Ho, I.-T., Hopkins, A. M., Kewley, L., Lawrence, J. S., Leon-Saval, S. G., Leslie, S., McElroy, R., Lewis, G., Liske, J., López-Sánchez, Á. R., Mahajan, S., Medling, A. M., Metcalfe, N., Meyer, M., Mould, J., Obreschkow, D., O'Toole, S., Pracy, M., Richards, S. N., Shanks, T., Sharp, R., Sweet, S. M., Thomas, A. D., Tonini, C., & Walcher, C. J. (2015). The SAMI Galaxy Survey: instrument specification and target selection. ***MNRAS***, 447, 2857–2879.

Bundy, K., Bershady, M. A., Law, D. R., Yan, R., Drory, N., MacDonald, N., Wake, D. A., Cherinka, B., Sánchez-Gallego, J. R., Weijmans, A.-M., Thomas, D., Tremonti, C., Masters, K., Coccato, L., Diamond-Stanic, A. M., Aragón-Salamanca, A., Avila-Reese, V., Badenes, C., Falcón-Barroso, J., Belfiore, F., Bizyaev, D., Blanc, G. A., Bland-Hawthorn, J., Blanton, M. R., Brownstein, J. R., Byler, N., Cappellari, M., Conroy, C., Dutton, A. A., Emsellem, E., Etherington, J., Frinchaboy, P. M., Fu, H., Gunn, J. E., Harding, P., Johnston, E. J., Kauffmann, G., Kinemuchi, K., Klaene, M. A., Knapen, J. H., Leauthaud, A., Li, C., Lin, L., Maiolino, R., Malanushenko, V., Malanushenko, E., Mao, S., Maraston, C., McDermid, R. M., Merrifield, M. R., Nichol, R. C., Oravetz, D., Pan, K., Parejko, J. K., Sanchez, S. F., Schlegel, D., Simmons, A., Steele, O., Steinmetz, M., Thanjavur, K., Thompson, B. A., Tinker, J. L., van den Bosch, R. C. E., Westfall, K. B., Wilkinson, D., Wright, S., Xiao, T., & Zhang, K. (2015). Overview of the SDSS-IV MaNGA Survey: Mapping nearby Galaxies at Apache Point Observatory. ***ApJ***, 798, 7.

Burkert, A., Förster Schreiber, N. M., Genzel, R., Lang, P., Tacconi, L. J., Wisnioski, E., Wuyts, S., Bandara, K., Beifiori, A., Bender, R., Brammer, G., Chan, J., Davies, R., Dekel, A., Fabricius, M., Fossati, M., Kulkarni, S., Lutz, D., Mendel, J. T., Momcheva, I., Nelson, E. J., Naab, T., Renzini, A., Saglia, R., Sharples, R. M., Sternberg, A., Wilman, D., & Wuyts, E. (2016). The Angular Momentum Distribution and Baryon Content of Star-forming Galaxies at z $\sim$ 1-3. ***ApJ***, 826, 214.

Cain, B., Gilbank, D. G., Bautz, M. W., Hicks, A., Yee, H. K. C., Gladders, M., Ellingson, E., Barrientos, L. F., & Garmire, G. P. (2008). Evidence for Line-of-Sight Structure in a Comparison of X-Ray and Optical Observations of the High-Redshift Cluster RCS 043938-2904.7. ***ApJ***, 679, 293–300.

Caon, N., Capaccioli, M., & D'Onofrio, M. (1993). On the Shape of the Light Profiles of Early Type Galaxies. ***MNRAS***, 265, 1013.

Cappellari, M. (2015). Dynamical Mass Determinations and Scaling Relations of Early-Type Galaxies. In M. Cappellari & S. Courteau (Eds.), ***IAU Symposium***, volume 311 of ***IAU Symposium*** (pp. 20–30).

Cappellari, M. (2016). Structure and Kinematics of Early-Type Galaxies from Integral Field Spectroscopy. ***ARA&A***, 54, 597–665.

Cappellari, M., Emsellem, E., Bacon, R., Bureau, M., Davies, R. L., de Zeeuw, P. T., Falcón-Barroso, J., Krajnović, D., Kuntschner, H., McDermid, R. M., Peletier, R. F., Sarzi, M., van den Bosch, R. C. E., & van de Ven, G. (2007). The SAURON project - X. The orbital anisotropy of elliptical and lenticular galaxies: revisiting the (V/σ, ϵ) diagram with integral-field stellar kinematics. ***MNRAS***, 379, 418–444.

Cappellari, M., Emsellem, E., Krajnović, D., McDermid, R. M., Scott, N., Verdoes Kleijn, G. A., Young, L. M., Alatalo, K., Bacon, R., Blitz, L., Bois, M., Bournaud, F., Bureau, M., Davies, R. L.,

Davis, T. A., de Zeeuw, P. T., Duc, P.-A., Khochfar, S., Kuntschner, H., Lablanche, P.-Y., Morganti, R., Naab, T., Oosterloo, T., Sarzi, M., Serra, P., & Weijmans, A.-M. (2011a). The ATLAS^{3D} project - I. A volume-limited sample of 260 nearby early-type galaxies: science goals and selection criteria. ***MNRAS***, 413, 813–836.

Cappellari, M., Emsellem, E., Krajnović, D., McDermid, R. M., Serra, P., Alatalo, K., Blitz, L., Bois, M., Bournaud, F., Bureau, M., Davies, R. L., Davis, T. A., de Zeeuw, P. T., Khochfar, S., Kuntschner, H., Lablanche, P.-Y., Morganti, R., Naab, T., Oosterloo, T., Sarzi, M., Scott, N., Weijmans, A.-M., & Young, L. M. (2011b). The ATLAS^{3D} project - VII. A new look at the morphology of nearby galaxies: the kinematic morphology-density relation. ***MNRAS***, 416, 1680–1696.

Cappellari, M., McDermid, R. M., Alatalo, K., Blitz, L., Bois, M., Bournaud, F., Bureau, M., Crocker, A. F., Davies, R. L., Davis, T. A., de Zeeuw, P. T., Duc, P.-A., Emsellem, E., Khochfar, S., Krajnović, D., Kuntschner, H., Morganti, R., Naab, T., Oosterloo, T., Sarzi, M., Scott, N., Serra, P., Weijmans, A.-M., & Young, L. M. (2013a). The ATLAS^{3D} project - XX. Mass-size and mass-σ distributions of early-type galaxies: bulge fraction drives kinematics, mass-to-light ratio, molecular gas fraction and stellar initial mass function. ***MNRAS***, 432, 1862–1893.

Cappellari, M., Scott, N., Alatalo, K., Blitz, L., Bois, M., Bournaud, F., Bureau, M., Crocker, A. F., Davies, R. L., Davis, T. A., de Zeeuw, P. T., Duc, P.-A., Emsellem, E., Khochfar, S., Krajnović, D., Kuntschner, H., McDermid, R. M., Morganti, R., Naab, T., Oosterloo, T., Sarzi, M., Serra, P., Weijmans, A.-M., & Young, L. M. (2013b). The ATLAS^{3D} project - XV. Benchmark for early-type galaxies scaling relations from 260 dynamical models: mass-to-light ratio, dark matter, Fundamental Plane and Mass Plane. ***MNRAS***, 432, 1709–1741.

Carollo, C. M., Bschorr, T. J., Renzini, A., Lilly, S. J., Capak, P., Cibinel, A., Ilbert, O., Onodera, M., Scoville, N., Cameron, E., Mobasher, B., Sanders, D., & Taniguchi, Y. (2013). Newly Quenched Galaxies as the Cause for the Apparent Evolution in Average Size of the Population. ***ApJ***, 773, 112.

Cerulo, P., Couch, W. J., Lidman, C., Demarco, R., Huertas-Company, M., Mei, S., Sánchez-Janssen, R., Barrientos, L. F., & Muñoz, R. P. (2016). The accelerated build-up of the red sequence in high-redshift galaxy clusters. ***MNRAS***, 457, 2209–2235.

Chang, Y.-Y., van der Wel, A., Rix, H.-W., Holden, B., Bell, E. F., McGrath, E. J., Wuyts, S., Häussler, B., Barden, M., Faber, S. M., Mozena, M., Ferguson, H. C., Guo, Y., Galametz, A., Grogin, N. A., Kocevski, D. D., Koekemoer, A. M., Dekel, A., Huang, K.-H., Hathi, N. P., & Donley, J. (2013a). Structural Evolution of Early-type Galaxies to z = 2.5 in CANDELS. ***ApJ***, 773, 149.

Chang, Y.-Y., van der Wel, A., Rix, H.-W., Wuyts, S., Zibetti, S., Ramkumar, B., & Holden, B. (2013b). Shape Evolution of Massive Early-type Galaxies: Confirmation of Increased Disk Prevalence at z $>$ 1. ***ApJ***, 762, 83.

Choi, H. & Yi, S. K. (2017). On the Evolution of Galaxy Spin in a Cosmological Hydrodynamic Simulation of Galaxy Clusters. ***ApJ***, 837, 68.

Cimatti, A., Nipoti, C., & Cassata, P. (2012). Fast evolving size of early-type galaxies at $>$z $>$ 2 and the role of dissipationless (dry) merging. ***MNRAS***, 422, 62–66.

Ciotti, L. & Bertin, G. (1999). Analytical properties of the $R^{1/m}$ law. ***A&A***, 352, 447–451.

Ciotti, L., Lanzoni, B., & Renzini, A. (1996). The tilt of the fundamental plane of elliptical galaxies - I. Exploring dynamical and structural effects. ***MNRAS***, 282, 1–12.

Conselice, C. J. (2003). The Relationship between Stellar Light Distributions of Galaxies and Their Formation Histories. ***ApJS***, 147, 1–28.

Cooper, M. C., Griffith, R. L., Newman, J. A., Coil, A. L., Davis, M., Dutton, A. A., Faber, S. M., Guhathakurta, P., Koo, D. C., Lotz, J. M., Weiner, B. J., Willmer, C. N. A., & Yan, R. (2012). The DEEP3 Galaxy Redshift Survey: the impact of environment on the size evolution of massive early-type galaxies at intermediate redshift. ***MNRAS***, 419, 3018–3027.

Cox, T. J., Dutta, S. N., Di Matteo, T., Hernquist, L., Hopkins, P. F., Robertson, B., & Springel, V. (2006). The Kinematic Structure of Merger Remnants. ***ApJ***, 650, 791–811.

Daddi, E., Renzini, A., Pirzkal, N., Cimatti, A., Malhotra, S., Stiavelli, M., Xu, C., Pasquali, A., Rhoads, J. E., Brusa, M., di Serego Alighieri, S., Ferguson, H. C., Koekemoer, A. M., Moustakas, L. A., Panagia, N., & Windhorst, R. A. (2005). Passively Evolving Early-Type Galaxies at 1.4 <~ z <~ 2.5 in the Hubble Ultra Deep Field. ***ApJ***, 626, 680–697.

Damjanov, I., Abraham, R. G., Glazebrook, K., McCarthy, P. J., Caris, E., Carlberg, R. G., Chen, H.-W., Crampton, D., Green, A. W., Jørgensen, I., Juneau, S., Le Borgne, D., Marzke, R. O., Mentuch, E., Murowinski, R., Roth, K., Savaglio, S., & Yan, H. (2011). Red Nuggets at High Redshift: Structural Evolution of Quiescent Galaxies Over 10 Gyr of Cosmic History. ***ApJ***, 739, L44.

Davies, R. L., Efstathiou, G., Fall, S. M., Illingworth, G., & Schechter, P. L. (1983). The kinematic properties of faint elliptical galaxies. ***ApJ***, 266, 41–57.

Dawson, K. S., Aldering, G., Amanullah, R., Barbary, K., Barrientos, L. F., Brodwin, M., Connolly, N., Dey, A., Doi, M., Donahue, M., Eisenhardt, P., Ellingson, E., Faccioli, L., Fadeyev, V., Fakhouri, H. K., Fruchter, A. S., Gilbank, D. G., Gladders, M. D., Goldhaber, G., Gonzalez, A. H., Goobar, A., Gude, A., Hattori, T., Hoekstra, H., Huang, X., Ihara, Y., Jannuzi, B. T., Johnston, D., Kashikawa, K., Koester, B., Konishi, K., Kowalski, M., Lidman, C., Linder, E. V., Lubin, L., Meyers, J., Morokuma, T., Munshi, F., Mullis, C., Oda, T., Panagia, N., Perlmutter, S., Postman, M., Pritchard, T., Rhodes, J., Rosati, P., Rubin, D., Schlegel, D. J., Spadafora, A., Stanford, S. A., Stanishev, V., Stern, D., Strovink, M., Suzuki, N., Takanashi, N., Tokita, K., Wagner, M., Wang, L., Yasuda, N., Yee, H. K. C.,

& Supernova Cosmology Project, T. (2009). An Intensive Hubble Space Telescope Survey for z>1 Type Ia Supernovae by Targeting Galaxy Clusters. ***AJ***, 138, 1271–1283.

De Propris, R., Bremer, M. N., & Phillipps, S. (2015). Morphological evolution in situ: disc-dominated cluster red sequences at z $\sim$ 1.25. ***MNRAS***, 450, 1268–1278.

De Propris, R., Bremer, M. N., & Phillipps, S. (2016). Morphological evolution of cluster red sequence galaxies in the past 9 Gyr. ***MNRAS***, 461, 4517–4530.

de Propris, R., Eisenhardt, P. R., Stanford, S. A., & Dickinson, M. (1998). The Infrared Luminosity Function of Galaxies in the Coma Cluster. ***ApJ***, 503, L45–L48.

de Propris, R., Stanford, S. A., Eisenhardt, P. R., Dickinson, M., & Elston, R. (1999). The K-Band Luminosity Function in Galaxy Clusters to Z ~1. ***AJ***, 118, 719–729.

De Propris, R., Stanford, S. A., Eisenhardt, P. R., Holden, B. P., & Rosati, P. (2007). The Rest-Frame K-Band Luminosity Function of Galaxies in Clusters to z = 1.3. ***AJ***, 133, 2209–2215.

de Vaucouleurs, G. (1948). Recherches sur les Nebuleuses Extragalactiques. ***Annales d'Astrophysique***, 11, 247.

de Zeeuw, P. T., Bureau, M., Emsellem, E., Bacon, R., Carollo, C. M., Copin, Y., Davies, R. L., Kuntschner, H., Miller, B. W., Monnet, G., Peletier, R. F., & Verolme, E. K. (2002). The SAURON project - II. Sample and early results. ***MNRAS***, 329, 513–530.

Dekel, A. & Birnboim, Y. (2006). Galaxy bimodality due to cold flows and shock heating. ***MNRAS***, 368, 2–20.

Dekel, A. & Birnboim, Y. (2008). Gravitational quenching in massive galaxies and clusters by clumpy accretion. ***MNRAS***, 383, 119–138.

Dekel, A. & Burkert, A. (2014). Wet disc contraction to galactic blue nuggets and quenching to red nuggets. ***MNRAS***, 438, 1870–1879.

Delaye, L., Huertas-Company, M., Mei, S., Lidman, C., Licitra, R., Newman, A., Raichoor, A., Shankar, F., Barrientos, F., Bernardi, M., Cerulo, P., Couch, W., Demarco, R., Muñoz, R., Sánchez-Janssen, R., & Tanaka, M. (2014). Larger sizes of massive quiescent early-type galaxies in clusters than in the field at $0.8 < z < 1.5$. ***MNRAS***, 441, 203–223.

Demarco, R., Rosati, P., Lidman, C., Girardi, M., Nonino, M., Rettura, A., Strazzullo, V., van der Wel, A., Ford, H. C., Mainieri, V., Holden, B. P., Stanford, S. A., Blakeslee, J. P., Gobat, R., Postman, M., Tozzi, P., Overzier, R. A., Zirm, A. W., Benítez, N., Homeier, N. L., Illingworth, G. D., Infante, L., Jee, M. J., Mei, S., Menanteau, F., Motta, V., Zheng, W., Clampin, M., & Hartig, G. (2007). VLT and ACS Observations of RDCS J1252.9-2927: Dynamical Structure and Galaxy Populations in a Massive Cluster at z = 1.237. ***ApJ***, 663, 164–182.

D'Eugenio, F., Houghton, R. C. W., Davies, R. L., & Dalla Bontà, E. (2013). Fast and slow rotators in the densest environments: a FLAMES/GIRAFFE integral field spectroscopy study of galaxies in A1689 at z = 0.183. ***MNRAS***, 429, 1258–1266.

Djorgovski, S. & Davis, M. (1987). Fundamental properties of elliptical galaxies. ***ApJ***, 313, 59–68.

Doi, M., Fukugita, M., & Okamura, S. (1993). Morphological Classification of Galaxies Using Simple Photometric Parameters. ***MNRAS***, 264, 832.

Dressler, A. (1980). A catalog of morphological types in 55 rich clusters of galaxies. ***ApJS***, 42, 565–609.

Eisenhardt, P. R. M., Brodwin, M., Gonzalez, A. H., Stanford, S. A., Stern, D., Barmby, P., Brown, M. J. I., Dawson, K., Dey, A., Doi, M., Galametz, A., Jannuzi, B. T., Kochanek, C. S., Meyers, J., Morokuma, T., & Moustakas, L. A. (2008). Clusters of Galaxies in the First Half of the Universe from the IRAC Shallow Survey. ***ApJ***, 684, 905–932.

El-Zant, A., Shlosman, I., & Hoffman, Y. (2001). Dark Halos: The Flattening of the Density Cusp by Dynamical Friction. ***ApJ***, 560, 636–643.

Elmegreen, B. G., Bournaud, F., & Elmegreen, D. M. (2008). Bulge Formation by the Coalescence of Giant Clumps in Primordial Disk Galaxies. ***ApJ***, 688, 67–77.

Elston, R. J., Gonzalez, A. H., McKenzie, E., Brodwin, M., Brown, M. J. I., Cardona, G., Dey, A., Dickinson, M., Eisenhardt, P. R., Jannuzi, B. T., Lin, Y.-T., Mohr, J. J., Raines, S. N., Stanford, S. A., & Stern, D. (2006). The FLAMINGOS Extragalactic Survey. ***ApJ***, 639, 816–826.

Emsellem, E., Cappellari, M., Krajnović, D., Alatalo, K., Blitz, L., Bois, M., Bournaud, F., Bureau, M., Davies, R. L., Davis, T. A., de Zeeuw, P. T., Khochfar, S., Kuntschner, H., Lablanche, P.-Y., McDermid, R. M., Morganti, R., Naab, T., Oosterloo, T., Sarzi, M., Scott, N., Serra, P., van de Ven, G., Weijmans, A.-M., & Young, L. M. (2011). The ATLAS^{3D} project - III. A census of the stellar angular momentum within the effective radius of early-type galaxies: unveiling the distribution of fast and slow rotators. ***MNRAS***, 414, 888–912.

Emsellem, E., Cappellari, M., Krajnović, D., van de Ven, G., Bacon, R., Bureau, M., Davies, R. L., de Zeeuw, P. T., Falcón-Barroso, J., Kuntschner, H., McDermid, R., Peletier, R. F., & Sarzi, M. (2007). The SAURON project - IX. A kinematic classification for early-type galaxies. ***MNRAS***, 379, 401–417.

Emsellem, E., Cappellari, M., Peletier, R. F., McDermid, R. M., Bacon, R., Bureau, M., Copin, Y., Davies, R. L., Krajnović, D., Kuntschner, H., Miller, B. W., & de Zeeuw, P. T. (2004). The SAURON project - III. Integral-field absorption-line kinematics of 48 elliptical and lenticular galaxies. ***MNRAS***, 352, 721–743.

Epinat, B., Amram, P., Balkowski, C., & Marcelin, M. (2010). Evidence for strong dynamical evolution in disc galaxies through the last 11 Gyr. GHASP VIII - a local reference sample of rotating disc galaxies for high-redshift studies. ***MNRAS***, 401, 2113–2147.

Faber, S. M. (1973). Variations in Spectral-Energy Distributions and Absorption-Line Strengths among Elliptical Galaxies. ***ApJ***, 179, 731–754.

Faber, S. M. & Jackson, R. E. (1976). Velocity dispersions and mass-to-light ratios for elliptical galaxies. ***ApJ***, 204, 668–683.

Faber, S. M., Phillips, A. C., Kibrick, R. I., Alcott, B., Allen, S. L., Burrous, J., Cantrall, T., Clarke, D., Coil, A. L., Cowley, D. J., Davis, M., Deich, W. T. S., Dietsch, K., Gilmore, D. K., Harper, C. A., Hilyard, D. F., Lewis, J. P., McVeigh, M., Newman, J., Osborne, J., Schiavon, R., Stover, R. J., Tucker, D., Wallace, V., Wei, M., Wirth, G., & Wright, C. A. (2003). The DEIMOS spectrograph for the Keck II Telescope: integration and testing. In M. Iye & A. F. M. Moorwood (Eds.), ***Instrument Design and Performance for Optical/Infrared Ground-based Telescopes***, volume 4841 of ***Society of Photo-Optical Instrumentation Engineers (SPIE) Conference Series*** (pp. 1657–1669).

Fagioli, M., Carollo, C. M., Renzini, A., Lilly, S. J., Onodera, M., & Tacchella, S. (2016). Minor Mergers or Progenitor Bias? The Stellar Ages of Small and Large Quenched Galaxies. ***ApJ***, 831, 173.

Fan, L., Lapi, A., Bressan, A., Bernardi, M., De Zotti, G., & Danese, L. (2010). Cosmic Evolution of Size and Velocity Dispersion for Early-type Galaxies. ***ApJ***, 718, 1460–1475.

Fan, L., Lapi, A., De Zotti, G., & Danese, L. (2008). The Dramatic Size Evolution of Elliptical Galaxies and the Quasar Feedback. ***ApJ***, 689, L101.

Fisher, D. B. & Drory, N. (2008). The Structure of Classical Bulges and Pseudobulges: the Link Between Pseudobulges and SÉRSIC Index. ***AJ***, 136, 773–839.

Forbes, D. A., Ponman, T. J., & Brown, R. J. N. (1998). Dependence of the Fundamental Plane Scatter on Galaxy Age. ***ApJ***, 508, L43–L46.

Franx, M. & van Dokkum, P. G. (1996). Measuring the Evolution of the M%TL ratio from the Fundamental Plane in CL 0024+16 at Z =0.39. In R. Bender & R. L. Davies (Eds.), ***New Light on Galaxy Evolution***, volume 171 of ***IAU Symposium*** (pp. 233).

Freeman, K. C. (1970). On the Disks of Spiral and so Galaxies. ***ApJ***, 160, 811.

Fukugita, M., Nakamura, O., Okamura, S., Yasuda, N., Barentine, J. C., Brinkmann, J., Gunn, J. E., Harvanek, M., Ichikawa, T., Lupton, R. H., Schneider, D. P., Strauss, M. A., & York, D. G. (2007). A Catalog of Morphologically Classified Galaxies from the Sloan Digital Sky Survey: North Equatorial Region. ***AJ***, 134, 579–593.

Gargiulo, A., Bolzonella, M., Scodeggio, M., Krywult, J., De Lucia, G., Guzzo, L., Garilli, B., Granett, B. R., de la Torre, S., Abbas, U., Adami, C., Arnouts, S., Bottini, D., Cappi, A., Cucciati, O., Davidzon, I., Franzetti, P., Fritz, A., Haines, C., Hawken, A. J., Iovino, A., Le Brun, V., Le Fèvre, O., Maccagni, D., Małek, K., Marulli, F., Moutard, T., Polletta, M., Pollo, A., Tasca, L. A. M., Tojeiro, R., Vergani, D., Zanichelli, A., Zamorani, G., Bel, J., Branchini, E., Coupon, J., Ilbert, O., Moscardini, L., & Peacock, J. A. (2017). The VIMOS Public Extragalactic Redshift Survey (VIPERS). The distinct build-up of dense and normal massive passive galaxies. ***A&A***, 606, A113.

Genel, S., Vogelsberger, M., Springel, V., Sijacki, D., Nelson, D., Snyder, G., Rodriguez-Gomez, V., Torrey, P., & Hernquist, L. (2014). Introducing the Illustris project: the evolution of galaxy populations across cosmic time. ***MNRAS***, 445, 175–200.

Genzel, R., Burkert, A., Bouché, N., Cresci, G., Förster Schreiber, N. M., Shapley, A., Shapiro, K., Tacconi, L. J., Buschkamp, P., Cimatti, A., Daddi, E., Davies, R., Eisenhauer, F., Erb, D. K., Genel, S., Gerhard, O., Hicks, E., Lutz, D., Naab, T., Ott, T., Rabien, S., Renzini, A., Steidel, C. C., Sternberg, A., & Lilly, S. J. (2008). From Rings to Bulges: Evidence for Rapid Secular Galaxy Evolution at z ~ 2 from Integral Field Spectroscopy in the SINS Survey. ***ApJ***, 687, 59–77.

Genzel, R., Newman, S., Jones, T., Förster Schreiber, N. M., Shapiro, K., Genel, S., Lilly, S. J., Renzini, A., Tacconi, L. J., Bouché, N., Burkert, A., Cresci, G., Buschkamp, P., Carollo, C. M., Ceverino, D., Davies, R., Dekel, A., Eisenhauer, F., Hicks, E., Kurk, J., Lutz, D., Mancini, C., Naab, T., Peng, Y., Sternberg, A., Vergani, D., & Zamorani, G. (2011). The Sins Survey of z ~ 2 Galaxy Kinematics: Properties of the Giant Star-forming Clumps. ***ApJ***, 733, 101.

Gerhard, O. E. (1981). N-body simulations of disc-halo galaxies - Isolated systems, tidal interactions and merging. ***MNRAS***, 197, 179–208.

Gilbank, D. G., Yee, H. K. C., Ellingson, E., Hicks, A. K., Gladders, M. D., Barrientos, L. F., & Keeney, B. (2008). A z = 0.9 Supercluster of X-Ray Luminous, Optically Selected, Massive Galaxy Clusters. ***ApJ***, 677, L89–L92.

Gladders, M. D., Hoekstra, H., Yee, H. K. C., Hall, P. B., & Barrientos, L. F. (2003). The Incidence of Strong-Lensing Clusters in the Red-Sequence Cluster Survey. ***ApJ***, 593, 48–55.

Gnedin, O. Y. (2003). Tidal Effects in Clusters of Galaxies. ***ApJ***, 582, 141–161.

Graham, A. & Colless, M. (1997). Some effects of galaxy structure and dynamics on the Fundamental Plane. ***MNRAS***, 287, 221–239.

Graham, A. W. & Guzmán, R. (2003). HST Photometry of Dwarf Elliptical Galaxies in Coma, and an Explanation for the Alleged Structural Dichotomy between Dwarf and Bright Elliptical Galaxies. ***AJ***, 125, 2936–2950.

Green, A. W., Glazebrook, K., McGregor, P. J., Damjanov, I., Wisnioski, E., Abraham, R. G., Colless, M., Sharp, R. G., Crain, R. A., Poole, G. B., & McCarthy, P. J. (2014). DYNAMO - I. A sample of Hα-luminous galaxies with resolved kinematics. ***MNRAS***, 437, 1070–1095.

Greene, J. E., Leauthaud, A., Emsellem, E., Ge, J., Arag'on-Salamanca, A., Greco, J. P., Lin, Y.-T., Mao, S., Masters, K., Merrifield, M., More, S., Okabe, N., Schneider, D. P., Thomas, D., Wake, D. A., Pan, K., Bizyaev, D., Oravetz, D., Simmons, A., Yan, R., & van den Bosch, F. (2017a). SDSS-IV MaNGA: Uncovering the Angular Momentum Content of Central and Satellite Early-type Galaxies. ***ArXiv e-prints***.

Greene, J. E., Leauthaud, A., Emsellem, E., Goddard, D., Ge, J., Andrews, B. H., Brinkman, J., Brownstein, J. R., Greco, J. P., Law, D., Lin, Y.-T., Masters, K. L., Merrifield, M., More, S., Okabe, N., Schneider, D. P., Thomas, D., Wake, D. A., Yan, R., & Drory, N. (2017b). Probing the kinematic morphology-density relation of early-type galaxies with MaNGA. ***ArXiv e-prints***.

Hayashi, M., Kodama, T., Koyama, Y., Tanaka, I., Shimasaku, K., & Okamura, S. (2010). High star formation activity in the central region of a distant cluster at z = 1.46. ***MNRAS***, 402, 1980–1990.

Herpich, J., Stinson, G. S., Dutton, A. A., Rix, H.-W., Martig, M., Roškar, R., Macciò, A. V., Quinn, T. R., & Wadsley, J. (2015). How to bend galaxy disc profiles: the role of halo spin. ***MNRAS***, 448, L99–L103.

Hicks, A. K., Ellingson, E., Bautz, M., Cain, B., Gilbank, D. G., Gladders, M. G., Hoekstra, H., Yee, H. K. C., & Garmire, G. (2008). Chandra X-Ray Observations of the 0.6 < z < 1.1 Red-Sequence Cluster Survey Sample. ***ApJ***, 680, 1022–1041.

Hilton, M., Collins, C. A., Stanford, S. A., Lidman, C., Dawson, K. S., Davidson, M., Kay, S. T., Liddle, A. R., Mann, R. G., Miller, C. J., Nichol, R. C., Romer, A. K., Sabirli, K., Viana, P. T. P., & West, M. J. (2007). The XMM Cluster Survey: The Dynamical State of XMMXCS J2215.9-1738 at z = 1.457. ***ApJ***, 670, 1000–1009.

Hilton, M., Stanford, S. A., Stott, J. P., Collins, C. A., Hoyle, B., Davidson, M., Hosmer, M., Kay, S. T., Liddle, A. R., Lloyd-Davies, E., Mann, R. G., Mehrtens, N., Miller, C. J., Nichol, R. C., Romer, A. K., Sabirli, K., Sahlén, M., Viana, P. T. P., West, M. J., Barbary, K., Dawson, K. S., Meyers, J., Perlmutter, S., Rubin, D., & Suzuki, N. (2009). The XMM Cluster Survey: Galaxy Morphologies and the Color-Magnitude Relation in XMMXCS J2215.9 - 1738 at z = 1.46. ***ApJ***, 697, 436–451.

Hopkins, P. F., Bundy, K., Hernquist, L., Wuyts, S., & Cox, T. J. (2010). Discriminating between the physical processes that drive spheroid size evolution. ***MNRAS***, 401, 1099–1117.

Hopkins, P. F., Bundy, K., Murray, N., Quataert, E., Lauer, T. R., & Ma, C.-P. (2009). Compact high-redshift galaxies are the cores of the most massive present-day spheroids. ***MNRAS***, 398, 898–910.

Houghton, R. C. W., Davies, R. L., D'Eugenio, F., Scott, N., Thatte, N., Clarke, F., Tecza, M., Salter, G. S., Fogarty, L. M. R., & Goodsall, T. (2013). Fast and slow rotators in the densest environments: a SWIFT IFS study of the Coma cluster. ***MNRAS***, 436, 19–33.

Huertas-Company, M., Aguerri, J. A. L., Bernardi, M., Mei, S., & Sánchez Almeida, J. (2011). Revisiting the Hubble sequence in the SDSS DR7 spectroscopic sample: a publicly available Bayesian automated classification. ***A&A***, 525, A157.

Huertas-Company, M., Mei, S., Shankar, F., Delaye, L., Raichoor, A., Covone, G., Finoguenov, A., Kneib, J. P., Le, F. O., & Povic, M. (2013a). The evolution of the mass-size relation for early-type galaxies from z $\sim$ 1 to the present: dependence on environment, mass range and detailed morphology. ***MNRAS***, 428, 1715–1742.

Huertas-Company, M., Shankar, F., Mei, S., Bernardi, M., Aguerri, J. A. L., Meert, A., & Vikram, V. (2013b). No Evidence for a Dependence of the Mass-Size Relation of Early-type Galaxies on Environment in the Local Universe. ***ApJ***, 779, 29.

Ilbert, O., McCracken, H. J., Le Fèvre, O., Capak, P., Dunlop, J., Karim, A., Renzini, M. A., Caputi, K., Boissier, S., Arnouts, S., Aussel, H., Comparat, J., Guo, Q., Hudelot, P., Kartaltepe, J., Kneib, J. P., Krogager, J. K., Le Floc'h, E., Lilly, S., Mellier, Y., Milvang-Jensen, B., Moutard, T., Onodera, M., Richard, J., Salvato, M., Sanders, D. B., Scoville, N., Silverman, J. D., Taniguchi, Y., Tasca, L., Thomas, R., Toft, S., Tresse, L., Vergani, D., Wolk, M., & Zirm, A. (2013). Mass assembly in quiescent and star-forming galaxies since z $\simeq$ 4 from UltraVISTA. ***A&A***, 556, A55.

Illingworth, G. (1977). Rotation in 13 elliptical galaxies. ***ApJ***, 218, L43–L47.

Jedrzejewski, R. I. (1987). CCD surface photometry of elliptical galaxies. I - Observations, reduction and results. ***MNRAS***, 226, 747–768.

Jee, M. J., Dawson, K. S., Hoekstra, H., Perlmutter, S., Rosati, P., Brodwin, M., Suzuki, N., Koester, B., Postman, M., Lubin, L., Meyers, J., Stanford, S. A., Barbary, K., Barrientos, F., Eisenhardt, P., Ford, H. C., Gilbank, D. G., Gladders, M. D., Gonzalez, A., Harris, D. W., Huang, X., Lidman, C., Rykoff, E. S., Rubin, D., & Spadafora, A. L. (2011). Scaling Relations and Overabundance of Massive Clusters at z $>\sim$ 1 from Weak-lensing Studies with the Hubble Space Telescope. ***ApJ***, 737, 59.

Jee, M. J., Rosati, P., Ford, H. C., Dawson, K. S., Lidman, C., Perlmutter, S., Demarco, R., Strazzullo, V., Mullis, C., Böhringer, H., & Fassbender, R. (2009). Hubble Space Telescope Weak-lensing Study of the Galaxy Cluster XMMU J2235.3 - 2557 at z $\sim$ 1.4: A Surprisingly Massive Galaxy Cluster When the Universe is One-third of its Current Age. ***ApJ***, 704, 672–686.

Jesseit, R., Cappellari, M., Naab, T., Emsellem, E., & Burkert, A. (2009). Specific angular momentum of disc merger remnants and the λ_R-parameter. ***MNRAS***, 397, 1202–1214.

Jimmy, Tran, K.-V., Brough, S., Gebhardt, K., von der Linden, A., Couch, W. J., & Sharp, R. (2013). Angular Momenta, Dynamical Masses, and Mergers of Brightest Cluster Galaxies. ***ApJ***, 778, 171.

Jørgensen, I. & Chiboucas, K. (2013). Stellar Populations and Evolution of Early-type Cluster Galaxies: Constraints from Optical Imaging and Spectroscopy of z = 0.5-0.9 Galaxy Clusters. ***AJ***, 145, 77.

Jørgensen, I., Chiboucas, K., Toft, S., Bergmann, M., Zirm, A., Schiavon, R. P., & Grützbauch, R. (2014). RX J0848.6+4453: The Evolution of Galaxy Sizes and Stellar Populations in a z = 1.27 Cluster. ***AJ***, 148, 117.

Kashikawa, N., Aoki, K., Asai, R., Ebizuka, N., Inata, M., Iye, M., Kawabata, K. S., Kosugi, G., Ohyama, Y., Okita, K., Ozawa, T., Saito, Y., Sasaki, T., Sekiguchi, K., Shimizu, Y., Taguchi, H., Takata, T., Yadoumaru, Y., & Yoshida, M. (2002). FOCAS: The Faint Object Camera and Spectrograph for the Subaru Telescope. ***PASJ***, 54, 819–832.

Kassin, S. A., Weiner, B. J., Faber, S. M., Gardner, J. P., Willmer, C. N. A., Coil, A. L., Cooper, M. C., Devriendt, J., Dutton, A. A., Guhathakurta, P., Koo, D. C., Metevier, A. J., Noeske, K. G., & Primack, J. R. (2012). The Epoch of Disk Settling: z ∼ 1 to Now. ***ApJ***, 758, 106.

Khochfar, S. & Burkert, A. (2005). On the origin of isophotal shapes in elliptical galaxies. ***MNRAS***, 359, 1379–1385.

Khochfar, S., Emsellem, E., Serra, P., Bois, M., Alatalo, K., Bacon, R., Blitz, L., Bournaud, F., Bureau, M., Cappellari, M., Davies, R. L., Davis, T. A., de Zeeuw, P. T., Duc, P.-A., Krajnović, D., Kuntschner, H., Lablanche, P.-Y., McDermid, R. M., Morganti, R., Naab, T., Oosterloo, T., Sarzi, M., Scott, N., Weijmans, A.-M., & Young, L. M. (2011). The ATLAS^{3D} project - VIII. Modelling the formation and evolution of fast and slow rotator early-type galaxies within ΛCDM. ***MNRAS***, 417, 845–862.

Kodaira, K., Okamura, S., & Watanabe, M. (1983). Diameter versus surface brightness diagram of galaxies. ***ApJ***, 274, L49–L52.

Kodama, T. & Arimoto, N. (1997). Origin of the colour-magnitude relation of elliptical galaxies. ***A&A***, 320, 41–53.

Kormendy, J. (1977). Brightness distributions in compact and normal galaxies. II - Structure parameters of the spheroidal component. ***ApJ***, 218, 333–346.

Kormendy, J. & Bender, R. (1996). A Proposed Revision of the Hubble Sequence for Elliptical Galaxies. ***ApJ***, 464, L119.

Kormendy, J. & Bender, R. (2012). A Revised Parallel-sequence Morphological Classification of Galaxies: Structure and Formation of S0 and Spheroidal Galaxies. ***ApJS***, 198, 2.

Kormendy, J., Fisher, D. B., Cornell, M. E., & Bender, R. (2009). Structure and Formation of Elliptical and Spheroidal Galaxies. ***ApJS***, 182, 216–309.

Krajnović, D., Alatalo, K., Blitz, L., Bois, M., Bournaud, F., Bureau, M., Cappellari, M., Davies, R. L., Davis, T. A., de Zeeuw, P. T., Duc, P.-A., Emsellem, E., Khochfar, S., Kuntschner, H., McDermid, R. M., Morganti, R., Naab, T., Oosterloo, T., Sarzi, M., Scott, N., Serra, P., Weijmans, A.-M., & Young, L. M. (2013). The ATLAS^{3D} project - XVII. Linking photometric and kinematic signatures of stellar discs in early-type galaxies. ***MNRAS***, 432, 1768–1795.

Krajnović, D., Bacon, R., Cappellari, M., Davies, R. L., de Zeeuw, P. T., Emsellem, E., Falcón-Barroso, J., Kuntschner, H., McDermid, R. M., Peletier, R. F., Sarzi, M., van den Bosch, R. C. E., & van de Ven, G. (2008). The SAURON project - XII. Kinematic substructures in early-type galaxies: evidence for discs in fast rotators. ***MNRAS***, 390, 93–117.

Krajnović, D., Cappellari, M., de Zeeuw, P. T., & Copin, Y. (2006). Kinemetry: a generalization of photometry to the higher moments of the line-of-sight velocity distribution. ***MNRAS***, 366, 787–802.

Krajnović, D., Emsellem, E., Cappellari, M., Alatalo, K., Blitz, L., Bois, M., Bournaud, F., Bureau, M., Davies, R. L., Davis, T. A., de Zeeuw, P. T., Khochfar, S., Kuntschner, H., Lablanche, P.-Y., McDermid, R. M., Morganti, R., Naab, T., Oosterloo, T., Sarzi, M., Scott, N., Serra, P., Weijmans, A.-M., & Young, L. M. (2011). The ATLAS^{3D} project - II. Morphologies, kinemetric features and alignment between photometric and kinematic axes of early-type galaxies. ***MNRAS***, 414, 2923–2949.

Kuntschner, H., Emsellem, E., Bacon, R., Cappellari, M., Davies, R. L., de Zeeuw, P. T., Falcón-Barroso, J., Krajnović, D., McDermid, R. M., Peletier, R. F., Sarzi, M., Shapiro, K. L., van den Bosch, R. C. E., & van de Ven, G. (2010). The SAURON project - XVII. Stellar population analysis of the absorption line strength maps of 48 early-type galaxies. ***MNRAS***, 408, 97–132.

Lang, P., Wuyts, S., Somerville, R. S., Förster Schreiber, N. M., Genzel, R., Bell, E. F., Brammer, G., Dekel, A., Faber, S. M., Ferguson, H. C., Grogin, N. A., Kocevski, D. D., Koekemoer, A. M., Lutz, D., McGrath, E. J., Momcheva, I., Nelson, E. J., Primack, J. R., Rosario, D. J., Skelton, R. E., Tacconi, L. J., van Dokkum, P. G., & Whitaker, K. E. (2014). Bulge Growth and Quenching since z = 2.5 in CANDELS/3D-HST. ***ApJ***, 788, 11.

Lanzoni, B. & Ciotti, L. (2003). Projection effects on the FP thickness. A Monte-Carlo exploration. ***A&A***, 404, 819–830.

Lauer, T. R. (1985a). Boxy isophotes, discs and dust lanes in elliptical galaxies. ***MNRAS***, 216, 429–438.

Lauer, T. R. (1985b). High-resolution surface photometry of elliptical galaxies. ***ApJS***, 57, 473–502.

Lauer, T. R. (1985c). The cores of elliptical galaxies. ***ApJ***, 292, 104–121.

Lidman, C., Howell, D. A., Folatelli, G., Garavini, G., Nobili, S., Aldering, G., Amanullah, R., Antilogus, P., Astier, P., Blanc, G., Burns, M. S., Conley, A., Deustua, S. E., Doi, M., Ellis, R., Fabbro, S., Fadeyev, V., Gibbons, R., Goldhaber, G., Goobar, A., Groom, D. E., Hook, I., Kashikawa, N., Kim, A. G., Knop, R. A., Lee, B. C., Mendez, J., Morokuma, T., Motohara, K., Nugent, P. E., Pain, R., Perlmutter, S., Prasad, V., Quimby, R., Raux, J., Regnault, N., Ruiz-Lapuente, P., Sainton, G., Schaefer, B. E., Schahmaneche, K., Smith, E., Spadafora, A. L., Stanishev, V., Walton, N. A., Wang, L., Wood-Vasey, W. M., Yasuda, N., & Supernova Cosmology Project (2005). Spectroscopic confirmation of high-redshift supernovae with the ESO VLT. ***A&A***, 430, 843–851.

Lilly, S. J., Le Brun, V., Maier, C., Mainieri, V., Mignoli, M., Scodeggio, M., Zamorani, G., Carollo, M., Contini, T., Kneib, J.-P., Le Fèvre, O., Renzini, A., Bardelli, S., Bolzonella, M., Bongiorno, A., Caputi, K., Coppa, G., Cucciati, O., de la Torre, S., de Ravel, L., Franzetti, P., Garilli, B., Iovino, A., Kampczyk, P., Kovac, K., Knobel, C., Lamareille, F., Le Borgne, J.-F., Pello, R., Peng, Y., Pérez-Montero, E., Ricciardelli, E., Silverman, J. D., Tanaka, M., Tasca, L., Tresse, L., Vergani, D., Zucca, E., Ilbert, O., Salvato, M., Oesch, P., Abbas, U., Bottini, D., Capak, P., Cappi, A., Cassata, P., Cimatti, A., Elvis, M., Fumana, M., Guzzo, L., Hasinger, G., Koekemoer, A., Leauthaud, A., Maccagni, D., Marinoni, C., McCracken, H., Memeo, P., Meneux, B., Porciani, C., Pozzetti, L., Sanders, D., Scaramella, R., Scarlata, C., Scoville, N., Shopbell, P., & Taniguchi, Y. (2009). The zCOSMOS 10k-Bright Spectroscopic Sample. ***ApJS***, 184, 218–229.

Lilly, S. J., Le Fèvre, O., Renzini, A., Zamorani, G., Scodeggio, M., Contini, T., Carollo, C. M., Hasinger, G., Kneib, J.-P., Iovino, A., Le Brun, V., Maier, C., Mainieri, V., Mignoli, M., Silverman, J., Tasca, L. A. M., Bolzonella, M., Bongiorno, A., Bottini, D., Capak, P., Caputi, K., Cimatti, A., Cucciati, O., Daddi, E., Feldmann, R., Franzetti, P., Garilli, B., Guzzo, L., Ilbert, O., Kampczyk, P., Kovac, K., Lamareille, F., Leauthaud, A., Borgne, J.-F. L., McCracken, H. J., Marinoni, C., Pello, R., Ricciardelli, E., Scarlata, C., Vergani, D., Sanders, D. B., Schinnerer, E., Scoville, N., Taniguchi, Y., Arnouts, S., Aussel, H., Bardelli, S., Brusa, M., Cappi, A., Ciliegi, P., Finoguenov, A., Foucaud, S., Franceschini, A., Halliday, C., Impey, C., Knobel, C., Koekemoer, A., Kurk, J., Maccagni, D., Maddox, S., Marano, B., Marconi, G., Meneux, B., Mobasher, B., Moreau, C., Peacock, J. A., Porciani, C., Pozzetti, L., Scaramella, R., Schiminovich, D., Shopbell, P., Smail, I., Thompson, D., Tresse, L., Vettolani, G., Zanichelli, A., & Zucca, E. (2007). zCOSMOS: A Large VLT/VIMOS Redshift Survey Covering $0 < z < 3$ in the COSMOS Field. ***ApJS***, 172, 70–85.

Lin, Y.-T., Mohr, J. J., Gonzalez, A. H., & Stanford, S. A. (2006). Evolution of the K-Band Galaxy Cluster Luminosity Function and Scaling Relations. ***ApJ***, 650, L99–L102.

Lin, Y.-T., Mohr, J. J., & Stanford, S. A. (2003). Near-Infrared Properties of Galaxy Clusters: Luminosity as a Binding Mass Predictor and the State of Cluster Baryons. ***ApJ***, 591, 749–763.

Lin, Y.-T., Mohr, J. J., & Stanford, S. A. (2004). K-Band Properties of Galaxy Clusters and Groups: Luminosity Function, Radial Distribution, and Halo Occupation Number. ***ApJ***, 610, 745–761.

Lupton, R., Blanton, M. R., Fekete, G., Hogg, D. W., O'Mullane, W., Szalay, A., & Wherry, N. (2004). Preparing Red-Green-Blue Images from CCD Data. ***PASP***, 116, 133–137.

Maltby, D. T., Aragón-Salamanca, A., Gray, M. E., Barden, M., Häußler, B., Wolf, C., Peng, C. Y., Jahnke, K., McIntosh, D. H., Böhm, A., & van Kampen, E. (2010). The environmental dependence of the stellar-mass-size relation in STAGES galaxies. ***MNRAS***, 402, 282–294.

Mancini, C., Daddi, E., Renzini, A., Salmi, F., McCracken, H. J., Cimatti, A., Onodera, M., Salvato, M., Koekemoer, A. M., Aussel, H., Le Floc'h, E., Willott, C., & Capak, P. (2010). High-redshift elliptical galaxies: are they (all) really compact? ***MNRAS***, 401, 933–940.

Martig, M., Bournaud, F., Teyssier, R., & Dekel, A. (2009). Morphological Quenching of Star Formation: Making Early-Type Galaxies Red. ***ApJ***, 707, 250–267.

Martizzi, D., Jimmy, Teyssier, R., & Moore, B. (2014). Brightest cluster galaxies in cosmological simulations with adaptive mesh refinement: successes and failures. ***MNRAS***, 443, 1500–1508.

McDermid, R. M., Alatalo, K., Blitz, L., Bournaud, F., Bureau, M., Cappellari, M., Crocker, A. F., Davies, R. L., Davis, T. A., de Zeeuw, P. T., Duc, P.-A., Emsellem, E., Khochfar, S., Krajnović, D., Kuntschner, H., Morganti, R., Naab, T., Oosterloo, T., Sarzi, M., Scott, N., Serra, P., Weijmans, A.-M., & Young, L. M. (2015). The ATLAS^{3D} Project - XXX. Star formation histories and stellar population scaling relations of early-type galaxies. ***MNRAS***, 448, 3484–3513.

Mei, S., Blakeslee, J. P., Stanford, S. A., Holden, B. P., Rosati, P., Strazzullo, V., Homeier, N., Postman, M., Franx, M., Rettura, A., Ford, H., Illingworth, G. D., Ettori, S., Bouwens, R. J., Demarco, R., Martel, A. R., Clampin, M., Hartig, G. F., Eisenhardt, P., Ardila, D. R., Bartko, F., Benítez, N., Bradley, L. D., Broadhurst, T. J., Brown, R. A., Burrows, C. J., Cheng, E. S., Cross, N. J. G., Feldman, P. D., Golimowski, D. A., Goto, T., Gronwall, C., Infante, L., Kimble, R. A., Krist, J. E., Lesser, M. P., Menanteau, F., Meurer, G. R., Miley, G. K., Motta, V., Sirianni, M., Sparks, W. B., Tran, H. D., Tsvetanov, Z. I., White, R. L., & Zheng, W. (2006). Evolution of the Color-Magnitude Relation in High-Redshift Clusters: Blue Early-Type Galaxies and Red Pairs in RDCS J0910+5422. ***ApJ***, 639, 81–94.

Meyers, J., Aldering, G., Barbary, K., Barrientos, L. F., Brodwin, M., Dawson, K. S., Deustua, S., Doi, M., Eisenhardt, P., Faccioli, L., Fakhouri, H. K., Fruchter, A. S., Gilbank, D. G., Gladders, M. D., Goldhaber, G., Gonzalez, A. H., Hattori, T., Hsiao, E., Ihara, Y., Kashikawa, N., Koester, B., Konishi, K., Lidman, C., Lubin, L., Morokuma, T., Oda, T., Perlmutter, S., Postman, M., Ripoche, P., Rosati, P., Rubin, D., Rykoff, E., Spadafora, A., Stanford, S. A., Suzuki, N., Takanashi, N., Tokita, K., Yasuda, N., & Supernova Cosmology Project, T. (2012). The Hubble Space Telescope Cluster

Supernova Survey. III. Correlated Properties of Type Ia Supernovae and Their Hosts at 0.9 < Z < 1.46. ***ApJ***, 750, 1.

Mitsuda, K., Doi, M., Morokuma, T., Suzuki, N., Yasuda, N., Perlmutter, S., Aldering, G., & Meyers, J. (2017). Isophote Shapes of Early-type Galaxies in Massive Clusters at z $\sim$ 1 and 0. ***ApJ***, 834, 109.

Moore, B., Lake, G., & Katz, N. (1998). Morphological Transformation from Galaxy Harassment. ***ApJ***, 495, 139–151.

Moore, B., Lake, G., Quinn, T., & Stadel, J. (1999). On the survival and destruction of spiral galaxies in clusters. ***MNRAS***, 304, 465–474.

Morgan, W. W. (1958). A Preliminary Classification of the Forms of Galaxies According to Their Stellar Population. ***PASP***, 70, 364.

Morishita, T., Ichikawa, T., & Kajisawa, M. (2014). The Evolution of Galaxy Size and Morphology at z $\sim$ 0.5-3.0 in the GOODS-N Region with Hubble Space Telescope/WFC3 Data. ***ApJ***, 785, 18.

Morokuma, T., Tokita, K., Lidman, C., Doi, M., Yasuda, N., Aldering, G., Amanullah, R., Barbary, K., Dawson, K., Fadeyev, V., Fakhouri, H. K., Goldhaber, G., Goobar, A., Hattori, T., Hayano, J., Hook, I. M., Howell, D. A., Furusawa, H., Ihara, Y., Kashikawa, N., Knop, R. A., Konishi, K., Meyers, J., Oda, T., Pain, R., Perlmutter, S., Rubin, D., Spadafora, A. L., Suzuki, N., Takanashi, N., Totani, T., Utsunomiya, H., & Wang, L. (2010). Subaru FOCAS Spectroscopic Observations of High-Redshift Supernovae. ***PASJ***, 62, 19–.

Mullis, C. R., Rosati, P., Lamer, G., Böhringer, H., Schwope, A., Schuecker, P., & Fassbender, R. (2005). Discovery of an X-Ray-luminous Galaxy Cluster at z=1.4. ***ApJ***, 623, L85–L88.

Muzzin, A., Marchesini, D., Stefanon, M., Franx, M., McCracken, H. J., Milvang-Jensen, B., Dunlop, J. S., Fynbo, J. P. U., Brammer, G., Labbé, I., & van Dokkum, P. G. (2013). The Evolution of the Stellar Mass Functions of Star-forming and Quiescent Galaxies to z = 4 from the COSMOS/UltraVISTA Survey. ***ApJ***, 777, 18.

Muzzin, A., Wilson, G., Yee, H. K. C., Gilbank, D., Hoekstra, H., Demarco, R., Balogh, M., van Dokkum, P., Franx, M., Ellingson, E., Hicks, A., Nantais, J., Noble, A., Lacy, M., Lidman, C., Rettura, A., Surace, J., & Webb, T. (2012). The Gemini Cluster Astrophysics Spectroscopic Survey (GCLASS): The Role of Environment and Self-regulation in Galaxy Evolution at z $\sim$ 1. ***ApJ***, 746, 188.

Naab, T. & Burkert, A. (2003). Statistical Properties of Collisionless Equal- and Unequal-Mass Merger Remnants of Disk Galaxies. ***ApJ***, 597, 893–906.

Naab, T., Burkert, A., & Hernquist, L. (1999). On the Formation of Boxy and Disky Elliptical Galaxies. ***ApJ***, 523, L133–L136.

Naab, T., Johansson, P. H., & Ostriker, J. P. (2009). Minor Mergers and the Size Evolution of Elliptical Galaxies. ***ApJ***, 699, L178–L182.

Naab, T., Khochfar, S., & Burkert, A. (2006). Properties of Early-Type, Dry Galaxy Mergers and the Origin of Massive Elliptical Galaxies. ***ApJ***, 636, L81–L84.

Naab, T., Oser, L., Emsellem, E., Cappellari, M., Krajnović, D., McDermid, R. M., Alatalo, K., Bayet, E., Blitz, L., Bois, M., Bournaud, F., Bureau, M., Crocker, A., Davies, R. L., Davis, T. A., de Zeeuw, P. T., Duc, P.-A., Hirschmann, M., Johansson, P. H., Khochfar, S., Kuntschner, H., Morganti, R., Oosterloo, T., Sarzi, M., Scott, N., Serra, P., Ven, G. v. d., Weijmans, A., & Young, L. M. (2014). The ATLAS^{3D} project - XXV. Two-dimensional kinematic analysis of simulated galaxies and the cosmological origin of fast and slow rotators. ***MNRAS***, 444, 3357–3387.

Newman, A. B., Belli, S., & Ellis, R. S. (2015). Discovery of a Strongly Lensed Massive Quiescent Galaxy at z = 2.636: Spatially Resolved Spectroscopy and Indications of Rotation. ***ApJ***, 813, L7.

Newman, A. B., Ellis, R. S., Andreon, S., Treu, T., Raichoor, A., & Trinchieri, G. (2014). Spectroscopic Confirmation of the Rich z = 1.80 Galaxy Cluster JKCS 041 using the WFC3 Grism: Environmental Trends in the Ages and Structure of Quiescent Galaxies. ***ApJ***, 788, 51.

Newman, A. B., Ellis, R. S., Bundy, K., & Treu, T. (2012). Can Minor Merging Account for the Size Growth of Quiescent Galaxies? New Results from the CANDELS Survey. ***ApJ***, 746, 162.

Oesch, P. A., Brammer, G., van Dokkum, P. G., Illingworth, G. D., Bouwens, R. J., Labbé, I., Franx, M., Momcheva, I., Ashby, M. L. N., Fazio, G. G., Gonzalez, V., Holden, B., Magee, D., Skelton, R. E., Smit, R., Spitler, L. R., Trenti, M., & Willner, S. P. (2016). A Remarkably Luminous Galaxy at z=11.1 Measured with Hubble Space Telescope Grism Spectroscopy. ***ApJ***, 819, 129.

Oliva-Altamirano, P., Brough, S., Tran, K.-V., Jimmy, Miller, C., Bremer, M. N., Phillipps, S., Sharp, R., Colless, M., Lara-López, M. A., López-Sánchez, Á. R., Pimbblet, K., Kafle, P. R., & Couch, W. J. (2017). A Study of Central Galaxy Rotation with Stellar Mass and Environment. ***AJ***, 153, 89.

Oser, L., Ostriker, J. P., Naab, T., Johansson, P. H., & Burkert, A. (2010). The Two Phases of Galaxy Formation. ***ApJ***, 725, 2312–2323.

Pasquali, A., Ferreras, I., Panagia, N., Daddi, E., Malhotra, S., Rhoads, J. E., Pirzkal, N., Windhorst, R. A., Koekemoer, A. M., Moustakas, L., Xu, C., & Gronwall, C. (2006). The Structure and Star Formation History of Early-Type Galaxies in the Ultra Deep Field/GRAPES Survey. ***ApJ***, 636, 115–133.

Peng, C. Y., Ho, L. C., Impey, C. D., & Rix, H.-W. (2002). Detailed Structural Decomposition of Galaxy Images. ***AJ***, 124, 266–293.

Penoyre, Z., Moster, B. P., Sijacki, D., & Genel, S. (2017). The origin and evolution of fast and slow rotators in the Illustris simulation. ***MNRAS***, 468, 3883–3906.

Perlman, E. S., Horner, D. J., Jones, L. R., Scharf, C. A., Ebeling, H., Wegner, G., & Malkan, M. (2002). The WARPS Survey. VI. Galaxy Cluster and Source Identifications from Phase I. ***ApJS***, 140, 265–301.

Petrosian, V. (1976). Surface brightness and evolution of galaxies. ***ApJ***, 209, L1–L5.

Poggianti, B. M., Calvi, R., Bindoni, D., D'Onofrio, M., Moretti, A., Valentinuzzi, T., Fasano, G., Fritz, J., De Lucia, G., Vulcani, B., Bettoni, D., Gullieuszik, M., & Omizzolo, A. (2013). Superdense Galaxies and the Mass-Size Relation at Low Redshift. ***ApJ***, 762, 77.

Pohlen, M., Beckman, J. E., Hüttemeister, S., Knapen, J. H., Erwin, P., & Dettmar, R.-J. (2004). Stellar Disk Truncations: Where do we stand? In D. L. Block, I. Puerari, K. C. Freeman, R. Groess, & E. K. Block (Eds.), ***Penetrating Bars Through Masks of Cosmic Dust***, volume 319 of ***Astrophysics and Space Science Library*** (pp. 713).

Postman, M., Franx, M., Cross, N. J. G., Holden, B., Ford, H. C., Illingworth, G. D., Goto, T., Demarco, R., Rosati, P., Blakeslee, J. P., Tran, K.-V., Benítez, N., Clampin, M., Hartig, G. F., Homeier, N., Ardila, D. R., Bartko, F., Bouwens, R. J., Bradley, L. D., Broadhurst, T. J., Brown, R. A., Burrows, C. J., Cheng, E. S., Feldman, P. D., Golimowski, D. A., Gronwall, C., Infante, L., Kimble, R. A., Krist, J. E., Lesser, M. P., Martel, A. R., Mei, S., Menanteau, F., Meurer, G. R., Miley, G. K., Motta, V., Sirianni, M., Sparks, W. B., Tran, H. D., Tsvetanov, Z. I., White, R. L., & Zheng, W. (2005). The Morphology-Density Relation in z ~ 1 Clusters. ***ApJ***, 623, 721–741.

Postman, M., Lubin, L. M., & Oke, J. B. (1998). A Study of Nine High-Redshift Clusters of Galaxies. II. Photometry, Spectra, and Ages of Clusters 0023+0423 and 1604+4304. ***AJ***, 116, 560–583.

Postman, M., Lubin, L. M., & Oke, J. B. (2001). A Study of Nine High-Redshift Clusters of Galaxies. IV. Photometry and Spectra of Clusters 1324+3011 and 1604+4321. ***AJ***, 122, 1125–1150.

Prugniel, P. & Simien, F. (1996). The fundamental plane of early-type galaxies: stellar populations and mass-to-light ratio. ***A&A***, 309, 749–759.

Reiprich, T. H. & Böhringer, H. (2002). The Mass Function of an X-Ray Flux-limited Sample of Galaxy Clusters. ***ApJ***, 567, 716–740.

Rix, H.-W., Barden, M., Beckwith, S. V. W., Bell, E. F., Borch, A., Caldwell, J. A. R., Häussler, B., Jahnke, K., Jogee, S., McIntosh, D. H., Meisenheimer, K., Peng, C. Y., Sanchez, S. F., Somerville, R. S., Wisotzki, L., & Wolf, C. (2004). GEMS: Galaxy Evolution from Morphologies and SEDs. ***ApJS***, 152, 163–173.

Rodriguez-Gomez, V., Genel, S., Vogelsberger, M., Sijacki, D., Pillepich, A., Sales, L. V., Torrey, P., Snyder, G., Nelson, D., Springel, V., Ma, C.-P., & Hernquist, L. (2015). The merger rate of galaxies in the Illustris simulation: a comparison with observations and semi-empirical models. ***MNRAS***, 449, 49–64.

Rosati, P., Stanford, S. A., Eisenhardt, P. R., Elston, R., Spinrad, H., Stern, D., & Dey, A. (1999). An X-Ray-Selected Galaxy Cluster at Z = 1.26. ***AJ***, 118, 76–85.

Rosati, P., Tozzi, P., Ettori, S., Mainieri, V., Demarco, R., Stanford, S. A., Lidman, C., Nonino, M., Borgani, S., Della Ceca, R., Eisenhardt, P., Holden, B. P., & Norman, C. (2004). Chandra and XMM-Newton Observations of RDCS 1252.9-2927, A Massive Cluster at z=1.24. ***AJ***, 127, 230–238.

Saglia, R. P., Sánchez-Blázquez, P., Bender, R., Simard, L., Desai, V., Aragón-Salamanca, A., Milvang-Jensen, B., Halliday, C., Jablonka, P., Noll, S., Poggianti, B., Clowe, D. I., De Lucia, G., Pelló, R., Rudnick, G., Valentinuzzi, T., White, S. D. M., & Zaritsky, D. (2010). The fundamental plane of EDisCS galaxies. The effect of size evolution. ***A&A***, 524, A6.

Sandage, A. (1961). ***The Hubble atlas of galaxies***.

Sandage, A. & Tammann, G. A. (1981). ***A revised Shapley-Ames Catalog of bright galaxies***.

Schombert, J. M. (2015). The Structure of Galaxies. III. Two Structural Families of Ellipticals. ***AJ***, 150, 162.

Scott, N., Davies, R. L., Houghton, R. C. W., Cappellari, M., Graham, A. W., & Pimbblet, K. A. (2014). Distribution of slow and fast rotators in the Fornax cluster. ***MNRAS***, 441, 274–288.

Sereno, M. & Covone, G. (2013). The mass-concentration relation in massive galaxy clusters at redshift $\sim$1. ***MNRAS***, 434, 878–887.

Sérsic, J. L. (1968). ***Atlas de galaxias australes***.

Smethurst, R., Masters, K., Lintott, C., Weijmans, A.-M., Merrifield, M., Penny, S., Aragon Salamanca, A., Brownstein, J., Bundy, K., Drory, N., Law, D., & Nichol, R. (2017). SDSS-IV MaNGA: The Different Quenching Histories of Fast and Slow Rotators. ***ArXiv e-prints***.

Stanford, S. A., Eisenhardt, P. R., Brodwin, M., Gonzalez, A. H., Stern, D., Jannuzi, B. T., Dey, A., Brown, M. J. I., McKenzie, E., & Elston, R. (2005). An IR-selected Galaxy Cluster at z = 1.41. ***ApJ***, 634, L129–L132.

Stanford, S. A., Holden, B., Rosati, P., Eisenhardt, P. R., Stern, D., Squires, G., & Spinrad, H. (2002). An X-Ray-Selected Galaxy Cluster at z=1.11 in the ROSAT Deep Cluster Survey. ***AJ***, 123, 619–626.

Stanford, S. A., Romer, A. K., Sabirli, K., Davidson, M., Hilton, M., Viana, P. T. P., Collins, C. A., Kay, S. T., Liddle, A. R., Mann, R. G., Miller, C. J., Nichol, R. C., West, M. J., Conselice, C. J., Spinrad, H., Stern, D., & Bundy, K. (2006). The XMM Cluster Survey: A Massive Galaxy Cluster at z = 1.45. ***ApJ***, 646, L13–L16.

Suzuki, N., Rubin, D., Lidman, C., Aldering, G., Amanullah, R., Barbary, K., Barrientos, L. F., Botyanszki, J., Brodwin, M., Connolly, N., Dawson, K. S., Dey, A., Doi, M., Donahue, M., Deustua, S., Eisenhardt, P., Ellingson, E., Faccioli, L., Fadeyev, V., Fakhouri, H. K., Fruchter, A. S., Gilbank, D. G., Gladders, M. D., Goldhaber, G., Gonzalez, A. H., Goobar, A., Gude, A., Hattori, T., Hoekstra, H., Hsiao, E., Huang, X., Ihara, Y., Jee, M. J., Johnston, D., Kashikawa, N., Koester, B., Konishi, K., Kowalski, M., Linder, E. V., Lubin, L., Melbourne, J., Meyers, J., Morokuma, T., Munshi, F., Mullis, C., Oda, T., Panagia, N., Perlmutter, S., Postman, M., Pritchard, T., Rhodes, J., Ripoche, P., Rosati, P., Schlegel, D. J., Spadafora, A., Stanford, S. A., Stanishev, V., Stern, D., Strovink, M., Takanashi, N., Tokita, K., Wagner, M., Wang, L., Yasuda, N., Yee, H. K. C., & Supernova Cosmology Project, T. (2012). The Hubble Space Telescope Cluster Supernova Survey. V. Improving the Dark-energy Constraints above z > 1 and Building an Early-type-hosted Supernova Sample. ***ApJ***, 746, 85.

Tacconi, L. J., Genzel, R., Neri, R., Cox, P., Cooper, M. C., Shapiro, K., Bolatto, A., Bouché, N., Bournaud, F., Burkert, A., Combes, F., Comerford, J., Davis, M., Schreiber, N. M. F., Garcia-Burillo, S., Gracia-Carpio, J., Lutz, D., Naab, T., Omont, A., Shapley, A., Sternberg, A., & Weiner, B. (2010). High molecular gas fractions in normal massive star-forming galaxies in the young Universe. ***Nature***, 463, 781–784.

Tadaki, K.-i., Genzel, R., Kodama, T., Wuyts, S., Wisnioski, E., Förster Schreiber, N. M., Burkert, A., Lang, P., Tacconi, L. J., Lutz, D., Belli, S., Davies, R. I., Hatsukade, B., Hayashi, M., Herrera-Camus, R., Ikarashi, S., Inoue, S., Kohno, K., Koyama, Y., Mendel, J. T., Nakanishi, K., Shimakawa, R., Suzuki, T. L., Tamura, Y., Tanaka, I., Übler, H., & Wilman, D. J. (2017a). Bulge-forming Galaxies with an Extended Rotating Disk at z ~ 2. ***ApJ***, 834, 135.

Tadaki, K.-i., Kodama, T., Nelson, E. J., Belli, S., Förster Schreiber, N. M., Genzel, R., Hayashi, M., Herrera-Camus, R., Koyama, Y., Lang, P., Lutz, D., Shimakawa, R., Tacconi, L. J., Übler, H., Wisnioski, E., Wuyts, S., Hatsukade, B., Lippa, M., Nakanishi, K., Ikarashi, S., Kohno, K., Suzuki, T. L., Tamura, Y., & Tanaka, I. (2017b). Rotating Starburst Cores in Massive Galaxies at z = 2.5. ***ApJ***, 841, L25.

Taranu, D. S., Dubinski, J., & Yee, H. K. C. (2013). Mergers in Galaxy Groups. I. Structure and Properties of Elliptical Remnants. ***ApJ***, 778, 61.

Thomas, D., Maraston, C., Bender, R., & Mendes de Oliveira, C. (2005). The Epochs of Early-Type Galaxy Formation as a Function of Environment. ***ApJ***, 621, 673–694.

Thomas, D., Maraston, C., Schawinski, K., Sarzi, M., & Silk, J. (2010). Environment and self-regulation in galaxy formation. ***MNRAS***, 404, 1775–1789.

Toft, S., Zabl, J., Richard, J., Gallazzi, A., Zibetti, S., Prescott, M., Grillo, C., Man, A. W. S., Lee, N. Y., Gómez-Guijarro, C., Stockmann, M., Magdis, G., & Steinhardt, C. L. (2017). A massive, dead disk galaxy in the early Universe. ***Nature***, 546, 510–513.

Tomczak, A. R., Quadri, R. F., Tran, K.-V. H., Labbé, I., Straatman, C. M. S., Papovich, C., Glazebrook, K., Allen, R., Brammer, G. B., Kacprzak, G. G., Kawinwanichakij, L., Kelson, D. D., McCarthy, P. J., Mehrtens, N., Monson, A. J., Persson, S. E., Spitler, L. R., Tilvi, V., & van Dokkum, P. (2014). Galaxy Stellar Mass Functions from ZFOURGE/CANDELS: An Excess of Low-mass Galaxies since z = 2 and the Rapid Buildup of Quiescent Galaxies. ***ApJ***, 783, 85.

Trujillo, I., Burkert, A., & Bell, E. F. (2004). The Tilt of the Fundamental Plane: Three-Quarters Structural Nonhomology, One-Quarter Stellar Population. ***ApJ***, 600, L39–L42.

Trujillo, I., Conselice, C. J., Bundy, K., Cooper, M. C., Eisenhardt, P., & Ellis, R. S. (2007). Strong size evolution of the most massive galaxies since z ~ 2. ***MNRAS***, 382, 109–120.

Ubeda, L. e. (2012). ***Advanced Camera for Surveys Instrument Handbook for Cycle 21 v. 12.0***.

van de Sande, J., Bland-Hawthorn, J., Brough, S., Croom, S. M., Cortese, L., Foster, C., Scott, N., Bryant, J. J., d'Eugenio, F., Tonini, C., Goodwin, M., Konstantopoulos, I. S., Lawrence, J. S., Medling, A. M., Owers, M. S., Richards, S. N., Schaefer, A. L., & Yi, S. K. (2017). The SAMI Galaxy Survey: revising the fraction of slow rotators in IFS galaxy surveys. ***MNRAS***, 472, 1272–1285.

van der Kruit, P. C. (1979). Optical surface photometry of eight spiral galaxies studied in Westerbork. ***A&AS***, 38, 15–38.

van der Wel, A., Bell, E. F., van den Bosch, F. C., Gallazzi, A., & Rix, H.-W. (2009). On the Size and Comoving Mass Density Evolution of Early-Type Galaxies. ***ApJ***, 698, 1232–1243.

van der Wel, A., Franx, M., van Dokkum, P. G., Rix, H.-W., Illingworth, G. D., & Rosati, P. (2005). Mass-to-Light Ratios of Field Early-Type Galaxies at z ~ 1 from Ultradeep Spectroscopy: Evidence for Mass-dependent Evolution. ***ApJ***, 631, 145–162.

van der Wel, A., Franx, M., van Dokkum, P. G., Skelton, R. E., Momcheva, I. G., Whitaker, K. E., Brammer, G. B., Bell, E. F., Rix, H.-W., Wuyts, S., Ferguson, H. C., Holden, B. P., Barro, G., Koekemoer, A. M., Chang, Y.-Y., McGrath, E. J., Häussler, B., Dekel, A., Behroozi, P., Fumagalli, M., Leja, J., Lundgren, B. F., Maseda, M. V., Nelson, E. J., Wake, D. A., Patel, S. G., Labbé, I., Faber, S. M., Grogin, N. A., & Kocevski, D. D. (2014). 3D-HST+CANDELS: The Evolution of the Galaxy Size-Mass Distribution since z = 3. ***ApJ***, 788, 28.

van der Wel, A., Rix, H.-W., Wuyts, S., McGrath, E. J., Koekemoer, A. M., Bell, E. F., Holden, B. P., Robaina, A. R., & McIntosh, D. H. (2011). The Majority of Compact Massive Galaxies at z ~ 2 are Disk Dominated. ***ApJ***, 730, 38.

van der Wel, A. & van der Marel, R. P. (2008). Spatially Resolved Stellar Kinematics of Field Early-Type Galaxies at z = 1: Evolution of the Rotation Rate. ***ApJ***, 684, 260–269.

van Dokkum, P. G., Franx, M., Fabricant, D., Illingworth, G. D., & Kelson, D. D. (2000). Hubble Space Telescope Photometry and Keck Spectroscopy of the Rich Cluster MS 1054-03: Morphologies, Butcher-Oemler Effect, and the Color-Magnitude Relation at Z = 0.83. ***ApJ***, 541, 95–111.

van Dokkum, P. G., Franx, M., Kriek, M., Holden, B., Illingworth, G. D., Magee, D., Bouwens, R., Marchesini, D., Quadri, R., Rudnick, G., Taylor, E. N., & Toft, S. (2008). Confirmation of the Remarkable Compactness of Massive Quiescent Galaxies at z ~ 2.3: Early-Type Galaxies Did not Form in a Simple Monolithic Collapse. ***ApJ***, 677, L5–L8.

van Dokkum, P. G., Whitaker, K. E., Brammer, G., Franx, M., Kriek, M., Labbé, I., Marchesini, D., Quadri, R., Bezanson, R., Illingworth, G. D., Muzzin, A., Rudnick, G., Tal, T., & Wake, D. (2010). The Growth of Massive Galaxies Since z = 2. ***ApJ***, 709, 1018–1041.

Visvanathan, N. & Sandage, A. (1977). The color-absolute magnitude relation for E and S0 galaxies. I - Calibration and tests for universality using Virgo and eight other nearby clusters. ***ApJ***, 216, 214–226.

Vogelsberger, M., Genel, S., Springel, V., Torrey, P., Sijacki, D., Xu, D., Snyder, G., Nelson, D., & Hernquist, L. (2014). Introducing the Illustris Project: simulating the coevolution of dark and visible matter in the Universe. ***MNRAS***, 444, 1518–1547.

Wagner, C. R., Brodwin, M., Snyder, G. F., Gonzalez, A. H., Stanford, S. A., Alberts, S., Pope, A., Stern, D., Zeimann, G. R., Chary, R.-R., Dey, A., Eisenhardt, P. R. M., Mancone, C. L., & Moustakas, J. (2015). Star Formation in High-redshift Cluster Ellipticals. ***ApJ***, 800, 107.

Wang, T., Elbaz, D., Daddi, E., Finoguenov, A., Liu, D., Schreiber, C., Martín, S., Strazzullo, V., Valentino, F., van der Burg, R., Zanella, A., Ciesla, L., Gobat, R., Le Brun, A., Pannella, M., Sargent, M., Shu, X., Tan, Q., Cappelluti, N., & Li, Y. (2016). Discovery of a Galaxy Cluster with a Violently Starbursting Core at z = 2.506. ***ApJ***, 828, 56.

Weinmann, S. M., Kauffmann, G., van den Bosch, F. C., Pasquali, A., McIntosh, D. H., Mo, H., Yang, X., & Guo, Y. (2009). Environmental effects on satellite galaxies: the link between concentration, size and colour profile. ***MNRAS***, 394, 1213–1228.

White, S. D. M. (1979). Can mergers make slowly rotating elliptical galaxies. ***ApJ***, 229, L9–L13.

Wisnioski, E., Förster Schreiber, N. M., Wuyts, S., Wuyts, E., Bandara, K., Wilman, D., Genzel, R., Bender, R., Davies, R., Fossati, M., Lang, P., Mendel, J. T., Beifiori, A., Brammer, G., Chan, J., Fabricius, M., Fudamoto, Y., Kulkarni, S., Kurk, J., Lutz, D., Nelson, E. J., Momcheva, I., Rosario, D., Saglia, R., Seitz, S., Tacconi, L. J., & van Dokkum, P. G. (2015). The KMOS^{3D} Survey: Design, First Results, and the Evolution of Galaxy Kinematics from 0.7 <= z <= 2.7. ***ApJ***, 799, 209.

Worthey, G., Faber, S. M., & Gonzalez, J. J. (1992). MG and Fe absorption features in elliptical galaxies. ***ApJ***, 398, 69–73.

Wuyts, S., Cox, T. J., Hayward, C. C., Franx, M., Hernquist, L., Hopkins, P. F., Jonsson, P., & van Dokkum, P. G. (2010). On Sizes, Kinematics, M/L Gradients, and Light Profiles of Massive Compact Galaxies at z ~ 2. ***ApJ***, 722, 1666–1684.

Wuyts, S., Förster Schreiber, N. M., van der Wel, A., Magnelli, B., Guo, Y., Genzel, R., Lutz, D., Aussel, H., Barro, G., Berta, S., Cava, A., Graciá-Carpio, J., Hathi, N. P., Huang, K.-H., Kocevski, D. D., Koekemoer, A. M., Lee, K.-S., Le Floc'h, E., McGrath, E. J., Nordon, R., Popesso, P., Pozzi, F., Riguccini, L., Rodighiero, G., Saintonge, A., & Tacconi, L. (2011). Galaxy Structure and Mode of Star Formation in the SFR-Mass Plane from z ~ 2.5 to z ~ 0.1. ***ApJ***, 742, 96.

Xu, C. K., Zhao, Y., Scoville, N., Capak, P., Drory, N., & Gao, Y. (2012). Major-merger Galaxy Pairs in the COSMOS Field—Mass-dependent Merger Rate Evolution since z = 1. ***ApJ***, 747, 85.

Yamauchi, C., Ichikawa, S.-i., Doi, M., Yasuda, N., Yagi, M., Fukugita, M., Okamura, S., Nakamura, O., Sekiguchi, M., & Goto, T. (2005). Morphological Classification of Galaxies Using Photometric Parameters: The Concentration Index versus the Coarseness Parameter. ***AJ***, 130, 1545–1557.

Yasuda, N., Fukugita, M., Narayanan, V. K., Lupton, R. H., Strateva, I., Strauss, M. A., Ivezić, Ž., Kim, R. S. J., Hogg, D. W., Weinberg, D. H., Shimasaku, K., Loveday, J., Annis, J., Bahcall, N. A., Blanton, M., Brinkmann, J., Brunner, R. J., Connolly, A. J., Csabai, I., Doi, M., Hamabe, M., Ichikawa, S.-I., Ichikawa, T., Johnston, D. E., Knapp, G. R., Kunszt, P. Z., Lamb, D. Q., McKay, T. A., Munn, J. A., Nichol, R. C., Okamura, S., Schneider, D. P., Szokoly, G. P., Vogeley, M. S., Watanabe, M., & York, D. G. (2001). Galaxy Number Counts from the Sloan Digital Sky Survey Commissioning Data. ***AJ***, 122, 1104–1124.

York, D. G., Adelman, J., Anderson, Jr., J. E., Anderson, S. F., Annis, J., Bahcall, N. A., Bakken, J. A., Barkhouser, R., Bastian, S., Berman, E., Boroski, W. N., Bracker, S., Briegel, C., Briggs, J. W., Brinkmann, J., Brunner, R., Burles, S., Carey, L., Carr, M. A., Castander, F. J., Chen, B., Colestock, P. L., Connolly, A. J., Crocker, J. H., Csabai, I., Czarapata, P. C., Davis, J. E., Doi, M., Dombeck, T., Eisenstein, D., Ellman, N., Elms, B. R., Evans, M. L., Fan, X., Federwitz, G. R., Fiscelli, L., Friedman, S., Frieman, J. A., Fukugita, M., Gillespie, B., Gunn, J. E., Gurbani, V. K., de Haas, E., Haldeman, M., Harris, F. H., Hayes, J., Heckman, T. M., Hennessy, G. S., Hindsley, R. B., Holm, S., Holmgren, D. J., Huang, C.-h., Hull, C., Husby, D., Ichikawa, S.-I., Ichikawa, T.,

Ivezić, Ž., Kent, S., Kim, R. S. J., Kinney, E., Klaene, M., Kleinman, A. N., Kleinman, S., Knapp, G. R., Korienek, J., Kron, R. G., Kunszt, P. Z., Lamb, D. Q., Lee, B., Leger, R. F., Limmongkol, S., Lindenmeyer, C., Long, D. C., Loomis, C., Loveday, J., Lucinio, R., Lupton, R. H., MacKinnon, B., Mannery, E. J., Mantsch, P. M., Margon, B., McGehee, P., McKay, T. A., Meiksin, A., Merelli, A., Monet, D. G., Munn, J. A., Narayanan, V. K., Nash, T., Neilsen, E., Neswold, R., Newberg, H. J., Nichol, R. C., Nicinski, T., Nonino, M., Okada, N., Okamura, S., Ostriker, J. P., Owen, R., Pauls, A. G., Peoples, J., Peterson, R. L., Petravick, D., Pier, J. R., Pope, A., Pordes, R., Prosapio, A., Rechenmacher, R., Quinn, T. R., Richards, G. T., Richmond, M. W., Rivetta, C. H., Rockosi, C. M., Ruthmansdorfer, K., Sandford, D., Schlegel, D. J., Schneider, D. P., Sekiguchi, M., Sergey, G., Shimasaku, K., Siegmund, W. A., Smee, S., Smith, J. A., Snedden, S., Stone, R., Stoughton, C., Strauss, M. A., Stubbs, C., SubbaRao, M., Szalay, A. S., Szapudi, I., Szokoly, G. P., Thakar, A. R., Tremonti, C., Tucker, D. L., Uomoto, A., Vanden Berk, D., Vogeley, M. S., Waddell, P., Wang, S.-i., Watanabe, M., Weinberg, D. H., Yanny, B., Yasuda, N., & SDSS Collaboration (2000). The Sloan Digital Sky Survey: Technical Summary. ***AJ***, 120, 1579–1587.

Young, L. M., Bureau, M., Davis, T. A., Combes, F., McDermid, R. M., Alatalo, K., Blitz, L., Bois, M., Bournaud, F., Cappellari, M., Davies, R. L., de Zeeuw, P. T., Emsellem, E., Khochfar, S., Krajnović, D., Kuntschner, H., Lablanche, P.-Y., Morganti, R., Naab, T., Oosterloo, T., Sarzi, M., Scott, N., Serra, P., & Weijmans, A.-M. (2011). The ATLAS^{3D} project - IV. The molecular gas content of early-type galaxies. ***MNRAS***, 414, 940–967.

Zeimann, G. R., Stanford, S. A., Brodwin, M., Gonzalez, A. H., Mancone, C., Snyder, G. F., Stern, D., Eisenhardt, P., Dey, A., & Moustakas, J. (2013). Hα Star Formation Rates of z $>$ 1 Galaxy Clusters in the IRAC Shallow Cluster Survey. ***ApJ***, 779, 137.

Zhao, D. H., Jing, Y. P., Mo, H. J., & Börner, G. (2009). Accurate Universal Models for the Mass Accretion Histories and Concentrations of Dark Matter Halos. ***ApJ***, 707, 354–369.

Coffee break friends in the Institute of Astronomy. From left to right: Yuki Yoshimura, Noriaki Arima, Yui Yamashita, Akio Taniguchi, Tsuyoshi Ishida, Kazuma Mitsuda, Jian Jiang, Hideki Umehata, Masahito Uchiyama, and Masaki Yamaguchi. We also have two regular members in the coffee break in addition to above, Yuki Yamaguchi, Yuri Nishimura, Tao Wang, and Tatsuya Takegoshi.